CLINICAL APPLICATIONS OF PHYSIOME MODELS

EDITED BY: Eun Bo Shim, Thomas Heldt and Chae Hun Leem
PUBLISHED IN: Frontiers in Physiology

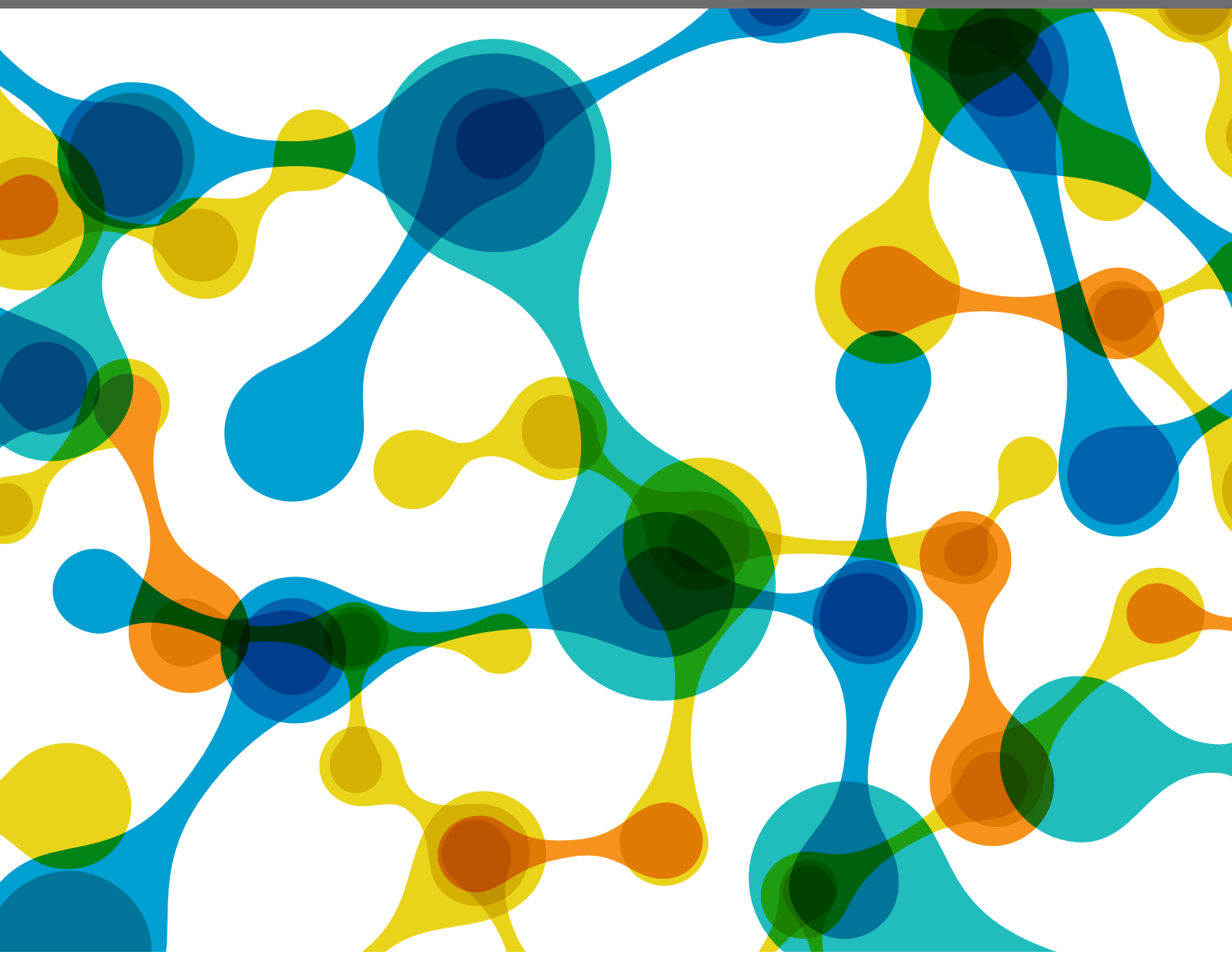

frontiers Research Topics

frontiers

Frontiers eBook Copyright Statement

The copyright in the text of individual articles in this eBook is the property of their respective authors or their respective institutions or funders. The copyright in graphics and images within each article may be subject to copyright of other parties. In both cases this is subject to a license granted to Frontiers.

The compilation of articles constituting this eBook is the property of Frontiers.

Each article within this eBook, and the eBook itself, are published under the most recent version of the Creative Commons CC-BY licence. The version current at the date of publication of this eBook is CC-BY 4.0. If the CC-BY licence is updated, the licence granted by Frontiers is automatically updated to the new version.

When exercising any right under the CC-BY licence, Frontiers must be attributed as the original publisher of the article or eBook, as applicable.

Authors have the responsibility of ensuring that any graphics or other materials which are the property of others may be included in the CC-BY licence, but this should be checked before relying on the CC-BY licence to reproduce those materials. Any copyright notices relating to those materials must be complied with.

Copyright and source acknowledgement notices may not be removed and must be displayed in any copy, derivative work or partial copy which includes the elements in question.

All copyright, and all rights therein, are protected by national and international copyright laws. The above represents a summary only. For further information please read Frontiers' Conditions for Website Use and Copyright Statement, and the applicable CC-BY licence.

ISSN 1664-8714
ISBN 978-2-88963-919-9
DOI 10.3389/978-2-88963-919-9

About Frontiers

Frontiers is more than just an open-access publisher of scholarly articles: it is a pioneering approach to the world of academia, radically improving the way scholarly research is managed. The grand vision of Frontiers is a world where all people have an equal opportunity to seek, share and generate knowledge. Frontiers provides immediate and permanent online open access to all its publications, but this alone is not enough to realize our grand goals.

Frontiers Journal Series

The Frontiers Journal Series is a multi-tier and interdisciplinary set of open-access, online journals, promising a paradigm shift from the current review, selection and dissemination processes in academic publishing. All Frontiers journals are driven by researchers for researchers; therefore, they constitute a service to the scholarly community. At the same time, the Frontiers Journal Series operates on a revolutionary invention, the tiered publishing system, initially addressing specific communities of scholars, and gradually climbing up to broader public understanding, thus serving the interests of the lay society, too.

Dedication to Quality

Each Frontiers article is a landmark of the highest quality, thanks to genuinely collaborative interactions between authors and review editors, who include some of the world's best academicians. Research must be certified by peers before entering a stream of knowledge that may eventually reach the public - and shape society; therefore, Frontiers only applies the most rigorous and unbiased reviews.
Frontiers revolutionizes research publishing by freely delivering the most outstanding research, evaluated with no bias from both the academic and social point of view. By applying the most advanced information technologies, Frontiers is catapulting scholarly publishing into a new generation.

What are Frontiers Research Topics?

Frontiers Research Topics are very popular trademarks of the Frontiers Journals Series: they are collections of at least ten articles, all centered on a particular subject. With their unique mix of varied contributions from Original Research to Review Articles, Frontiers Research Topics unify the most influential researchers, the latest key findings and historical advances in a hot research area! Find out more on how to host your own Frontiers Research Topic or contribute to one as an author by contacting the Frontiers Editorial Office: researchtopics@frontiersin.org

CLINICAL APPLICATIONS OF PHYSIOME MODELS

Topic Editors:
Eun Bo Shim, Kangwon National University, South Korea
Thomas Heldt, Massachusetts Institute of Technology, United States
Chae Hun Leem, University of Ulsan, South Korea

Citation: Shim, E. B., Heldt, T., Leem, C. H., eds. (2020). Clinical Applications of Physiome Models. Lausanne: Frontiers Media SA. doi: 10.3389/978-2-88963-919-9

Table of Contents

frontiers in Physiology

ORIGINAL RESEARCH
published: 11 October 2017
doi: 10.3389/fphys.2017.00792

Virtual *In-Silico* Modeling Guided Catheter Ablation Predicts Effective Linear Ablation Lesion Set for Longstanding Persistent Atrial Fibrillation: Multicenter Prospective Randomized Study

Jaemin Shim[1†], Minki Hwang[2†], Jun-Seop Song[2], Byounghyun Lim[2], Tae-Hoon Kim[2], Boyoung Joung[2], Sung-Hwan Kim[3], Yong-Seog Oh[3], Gi-Byung Nam[4], Young Keun On[5], Seil Oh[6], Young-Hoon Kim[1] and Hui-Nam Pak[2]*

[1] Cardiovascular Center, Korea University, Seoul, South Korea, [2] Division of Cardiology, Yonsei University Health System, Seoul, South Korea, [3] Division of Cardiology, Catholic University of Korea, Seoul, South Korea, [4] Asan Medical Center, University of Ulsan, Seoul, South Korea, [5] Samsung Medical Center, Sungkyunkwan University, Seoul, South Korea, [6] Division of Cardiology, Seoul National University, Seoul, South Korea

OPEN ACCESS

Edited by:
Eun Bo Shim,
Kangwon National University,
South Korea

Reviewed by:
Jae Boum Youm,
Inje University, South Korea
Seiryo Sugiura,
The University of Tokyo, Japan

***Correspondence:**
Hui-Nam Pak
hnpak@yuhs.ac

[†]These authors have contributed equally to this work.

Specialty section:
This article was submitted to Computational Physiology and Medicine, a section of the journal Frontiers in Physiology

Received: *25 May 2017*
Accepted: *27 September 2017*
Published: *11 October 2017*

Citation:
Shim J, Hwang M, Song J-S, Lim B, Kim T-H, Joung B, Kim S-H, Oh Y-S, Nam G-B, On YK, Oh S, Kim Y-H and Pak H-N (2017) Virtual In-Silico Modeling Guided Catheter Ablation Predicts Effective Linear Ablation Lesion Set for Longstanding Persistent Atrial Fibrillation: Multicenter Prospective Randomized Study. Front. Physiol. 8:792. doi: 10.3389/fphys.2017.00792

Objective: Radiofrequency catheter ablation for persistent atrial fibrillation (PeAF) still has a substantial recurrence rate. This study aims to investigate whether an AF ablation lesion set chosen using *in-silico* ablation (V-ABL) is clinically feasible and more effective than an empirically chosen ablation lesion set (Em-ABL) in patients with PeAF.

Methods: We prospectively included 108 patients with antiarrhythmic drug-resistant PeAF (77.8% men, age 60.8 ± 9.9 years), and randomly assigned them to the V-ABL ($n = 53$) and Em-ABL ($n = 55$) groups. Five different *in-silico* ablation lesion sets [1 pulmonary vein isolation (PVI), 3 linear ablations, and 1 electrogram-guided ablation] were compared using heart-CT integrated AF modeling. We evaluated the feasibility, safety, and efficacy of V-ABL compared with that of Em-ABL.

Results: The pre-procedural computing time for five different ablation strategies was 166 ± 11 min. In the Em-ABL group, the earliest terminating blinded *in-silico* lesion set matched with the Em-ABL lesion set in 21.8%. V-ABL was not inferior to Em-ABL in terms of procedure time ($p = 0.403$), ablation time ($p = 0.510$), and major complication rate ($p = 0.900$). During 12.6 ± 3.8 months of follow-up, the clinical recurrence rate was 14.0% in the V-ABL group and 18.9% in the Em-ABL group ($p = 0.538$). In Em-ABL group, clinical recurrence rate was significantly lower after PVI+posterior box+anterior linear ablation, which showed the most frequent termination during *in-silico* ablation (log-rank $p = 0.027$).

Conclusions: V-ABL was feasible in clinical practice, not inferior to Em-ABL, and predicts the most effective ablation lesion set in patients who underwent PeAF ablation.

Keywords: atrial fibrillation, catheter ablation, virtual ablation, *in-silico* modeling, recurrence

INTRODUCTION

The prevalence of AF increases with age, and ∼20% of all ischemic strokes are associated with AF (Goldstein et al., 2011). It is predicted that the prevalence of AF would more than double by the year 2050 (Ball et al., 2013). Although radiofrequency catheter ablation (RFCA) has been established as an effective rhythm control strategy, it still has a substantial long-term recurrence rate, especially in patients with persistent AF (Dewire and Calkins, 2013). AF catheter ablation introduces the risk of collateral damages, and a long duration of ablation procedure is associated with poor clinical outcomes (Shim et al., 2013). Moreover, the ablation strategy is selected largely based on the physician's experience, which bears the possibility of outcome differences depending on the physician. On the other hand, computer simulation has been widely used in the study of the mechanisms of AF (Hwang et al., 2014; Trayanova, 2014). Recently, a number of attempts have been made to use computer simulation for studying the effects of catheter ablation (Zhao et al., 2015). We previously conducted a retrospective study and reported that the earliest virtual AF terminating lesion set chosen by using a computer was commonly identical to that selected by the physician who performed the ablations in patients with persistent AF (Hwang et al., 2014). Because the computing speed for complicated *in-silico* modeling of AF is one of the limitations for the application of computer simulation in clinical practice, we have shortened the computing time for AF modeling by about 80 times compared with conventional modeling (Hwang et al., 2015; Zhao et al., 2015). This study was a prospective randomized trial to examine the applicability, safety, and efficacy of computer simulation for catheter ablation of AF. The ablation strategy was selected on the basis of computer simulation for one group of patients, and according to the physician's experience for the other group. Then, we evaluated the feasibility of *in-silico* ablation (computing time), and compared procedure time, procedure related complication rate, long-term rhythm outcome of both groups, and the most effective lesion set in *in-silico* ablation and empirical ablation (Em-ABL).

METHODS

Study Design

The study protocol adhered to the Declaration of Helsinki and was approved by the institutional review board of the Yonsei University Health System (clinicaltrials.gov; NCT 02171364). The enrolled patients were randomly assigned to either the virtual ablation (V-ABL) group or the Em-ABL group (**Figure 1**). For all patients in both groups, virtual ablations were performed by applying the following 5 strategies: (i) circumferential pulmonary vein isolation (CPVI), (ii) CPVI + posterior box lesion, (iii) CPVI + posterior box lesion + anterior line, (iv) CPVI + roof line + left lateral isthmus line, and (v) CPVI + complex fractionated atrial electrogram (CFAE)-guided ablation (Hwang et al., 2014; Song et al., 2016). For patients in the V-ABL group, the best virtual ablation strategy was applied in real ablation. The virtual ablation strategy that resulted in the earliest termination of AF after *in-silico* ablation was determined as the best *in-silico* ablation lesion set among the five ablation strategies. For patients in the Em-ABL group, the ablation strategy selected by the physician based on experience was applied in real ablation. The ablation outcomes were compared between the V-ABL and Em-ABL groups.

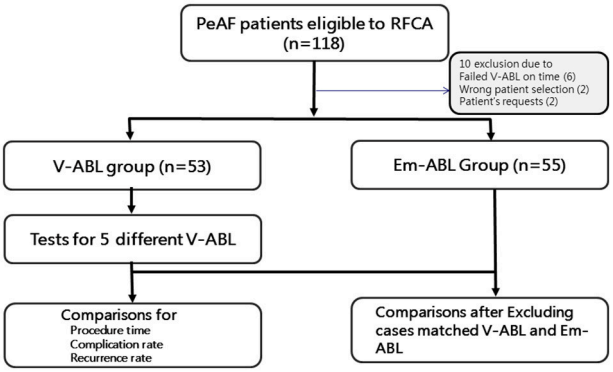

FIGURE 1 | Study flow chart. The enrolled patients were randomly assigned to either the virtual ablation (V-ABL) group or the empirical ablation (Em-ABL) group. Virtual ablations were performed for all patients in both groups, by applying five strategies. For patients in the V-ABL group, the best virtual ablation strategy was applied in real ablation. For patients in the Em-ABL group, the ablation strategy selected by the physician based on experience was applied in real ablation. The ablation outcomes were compared between the V-ABL and Em-ABL groups.

Study Population

In this study, we enrolled 118 patients with persistent AF (PeAF) who were eligible for RFCA. All patients provided written informed consent. The inclusion criteria were (i) age 19 years or older, (ii) antiarrhythmic drug resistance, and (iii) availability of three-dimensional (3D) computed tomography (CT) or magnetic resonance imaging (MRI) scans of the left atrium (LA). The exclusion criteria were (i) presence of significant structural heart disease, (ii) valvular AF, (iii) previous ablation or cardiac surgery, and (iv) presence of a cardiac implantable electronic device.

After receiving the patients' consent, DICOM files of heart CT were sent to the core laboratory a night before or in the early morning of the real AF ablation procedure. Patient randomization, *in-silico* AF modeling, and virtual AF ablation were done at the core laboratory during work hours (9.a.m.–6 p.m.). Among 118 patients, four were excluded owing to incorrect patient selection or patient request. Additional six patients were excluded because of failed *in-silico* AF ablation before the real ablation procedure, due to DICOM file error ($n = 2$) and communication error ($n = 4$). Finally, 108 patients (53 in the V-ABL group and 55 in the Em-ABL group) were enrolled in this study (**Figure 1**). The patient characteristics are shown in **Table 1**.

In-Silico Simulation of AF

Atrial geometries were reconstructed from the 3D CT merged NavX data (NavX; St. Jude Medical Inc., Minnetonka, MN, USA) defining the surface of the atrium. A triangular mesh was

TABLE 1 | Patient characteristics.

	Overall (*N* = 108)	V-ABL (*N* = 53)	Em-ABL (*N* = 55)	*p*-Value
Age (years)	60.8 ± 9.6	59.7 ± 10.1	61.9 ± 9.6	0.240
Male (%)	76.9	75.5	78.2	0.821
Longstanding persistent AF (%)	77.8	83.0	72.7	0.249
CHA2DS2-VASc score	1.97 ± 1.86	1.85 ± 1.65	2.09 ± 1.86	0.475
Heart failure (%)	12.0	9.4	14.5	0.557
Hypertension (%)	54.6	52.8	56.4	0.847
Age > 75 years (%)	9.3	3.8	14.5	0.094
Age 65–74 years (%)	25.0	28.3	21.8	0.508
Diabetes (%)	18.5	17.0	20.0	0.806
Previous stroke (%)	28.7	28.3	29.1	1
Previous TIA (%)	1.9	3.8	0	0.238
Vascular disease (%)	13.0	9.4	16.4	0.392
ECHOCARDIOGRAPHIC FINDINGS				
LA dimension (mm)	45.1 ± 4.4	46.1 ± 7.6	44.0 ± 4.4	0.086
EF (%)	59.3 ± 9.7	57.8 ± 7.8	60.7 ± 9.7	0.092
E/Em	10.2 ± 4.7	9.6 ± 3.0	10.7 ± 4.7	0.139

TIA, transient ischemic attack; LA, left atrium; EF, ejection fraction; E/Em, the ratio of early transmitral flow velocity (E) to early mitral annular velocity (Em).

generated on the surface of the 3D atrial geometry. The final number of grid elements was between 400,000 and 500,000. The LA appendage and myocardial sleeves were included in the mesh. For the simulation of cardiac wave propagation in the atrial wall, the following reaction-diffusion equation was solved numerically (Zozor et al., 2003):

$$\frac{\partial V_m}{\partial t} = \frac{1}{\beta C_m} \{\nabla \cdot D \nabla V_m - \beta (I_{ion} + I_s)\}, \quad (1)$$

where Vm is the membrane potential (Unit: volt); β is the membrane surface-to-volume ratio (Unit: meter^{-1}); C_m is the membrane capacitance per unit area (Unit: farad/meter^2); D is conductivity tensor (Unit: siemens/meter); and I_{ion} and I_s are the ion current and stimulation current, respectively (Unit: ampere/meter^2).

For the calculation of ionic currents, a mathematical model of human atrial action potential proposed by Courtemanche et al. (1998) was used. Electrical stimulation was applied at the location of Bachmann's bundle, and reentry was initiated by rapid pacing: a total of 24 pacings with pacing cycle lengths of 200, 190, and 180 ms. To induce self-sustained fibrillation, I_{to}, I_{CaL}, and I_{Kur} were reduced by 80, 40, and 50%, respectively, and I_{K1} was increased by 50% (Li et al., 2016). We chose a conduction velocity of 0.4 m/s based on real human patient data (Yonsei AF ablation cohort data; n = 1,980; mean CV = 0.43 ± 0.24 m/s) (Park et al., 2014) and previous simulation studies (Hwang et al., 2014; Li et al., 2016).

Virtual AF Ablation

Virtual ablation was conducted for all patients in both the V-ABL and Em-ABL groups. We developed a graphical user interface software with which the user can perform virtual ablation by mouse-clicking on the atrial geometry (CUVIA, Model: SH01, ver. 1.0; Laonmed Inc., Seoul, Korea; **Figure 2**). At the point where the mouse is clicked, a 2-mm-diameter circular region is virtually ablated, mimicking real ablation with a radiofrequency catheter. In the ablated region, no electrical flux condition was applied. The pattern of ablation was completed by serial mouse-clickings, similarly to real catheter ablation. For CFAE-guided ablations (Nademanee et al., 2004), the areas with CFAE cycle length < 120 ms were ablated as long as the total ablated area is < 5% of the whole atrial area. CFAE was observed in particular region in structurally homogenous simulation due to the three-dimensional geometrical variation. The area where the mitral annulus was located was also considered a non-conductive area. Virtual ablation was applied at 4 s after the end of pacings, and the simulation was run until 25 s from the start of the simulation. When all points in the atrial wall were repolarized by > 90%, the fibrillation was considered terminated. The duration until the termination of fibrillation was recorded for each ablation strategy for each patient. NavX potential map was not used in the virtual ablation. The physicians, however, utilized the endocardial potential map data in their decision makings. Fiber orientation was not considered in the simulation model, and conductivity was isotropic even though three-dimensional geometrical shape may have affected conductivity.

Real AF Ablation

The electrophysiological mapping method and the RFCA technique were as described previously (Mun et al., 2012). Briefly, we used an open irrigated-tip catheter (Celsius [Johnson & Johnson Inc., Diamond Bar, CA, USA] or Coolflex [St. Jude Medical]; 30–35 W, 47°C) to deliver radiofrequency energy for ablation under 3D electroanatomical mapping (NavX, St. Jude Medical; CARTO3, Johnson & Johnson) merged with 3D spiral CT. The procedure was completed when there was no immediate recurrence of AF after cardioversion with isoproterenol infusion (5 μg/min). All RFCA procedures were performed by an operator with > 10 years of experience.

Post-ablation Management and Follow-Up

As per RFCA procedure protocols, antiarrhythmic drugs were discontinued in all patients. The patients visited the outpatient clinic at 1, 3, 6, and 12 months after RFCA, or whenever symptoms occurred. All patients underwent electrocardiography at each visit, and 24-h Holter recording was done at 3, 6, and 12 months, according to the 2012 Heart Rhythm Society/European Heart Rhythm Association/European Cardiac Arrhythmia Society Expert Consensus Statement (Calkins et al., 2012). However, whenever patients reported palpitations, Holter monitor or event monitor recordings were obtained and evaluated to check for arrhythmia recurrence. We defined recurrence of AF as any episode of AF or atrial tachycardia lasting for at least 30 s. Any electrocardiography documentation of AF recurrence after 3 months of the blanking period was diagnosed as clinical recurrence.

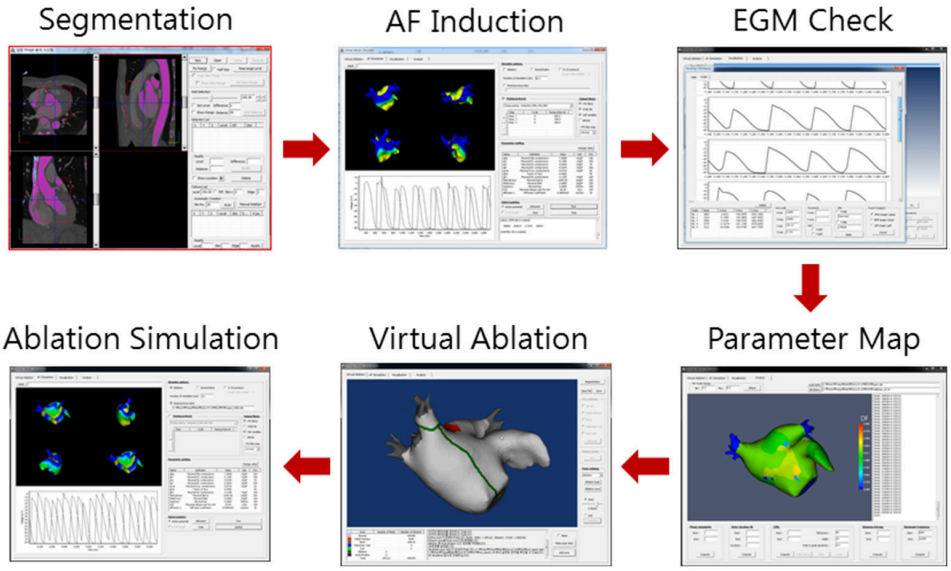

FIGURE 2 | Virtual ablation procedure. Computed tomography images are segmented to construct three-dimensional atrial geometry. Virtual atrial fibrillation (AF) is induced. The maps of cardiac wave dynamics parameters such as complex fractionated atrial electrogram (CFAE) are generated. Virtual ablation is performed on the atrial geometry. AF simulation is resumed. The cardiac wave propagation pattern is observed.

Statistical Analysis

Because the trial was conducted as a pilot study, the sample size was driven by the computation time and feasibility of recruiting eligible patients, and enrollment was open for 12 months. Results are expressed as mean values ± standard deviation for continuous variables, and absolute number and percentages for categorical variables. Continuous variables were compared by using Student's *t*-test, and categorical variables were compared by using either the chi-square test or Fisher's exact test as appropriate. The primary end point of the study was freedom from any atrial arrhythmias during follow-up after a 3-month blanking period. The time to recurrence and arrhythmia-free survival were assessed by using Kaplan-Meier analysis, and differences were calculated by using the log-rank test. A *p*-value of < 0.05 was considered statistically significant. All statistical analyses were performed by using SPSS version 18.0 software (SPSS Inc., Chicago, IL, USA).

RESULTS

Patient Characteristics

The patients' characteristics are summarized in **Table 1**. The mean age was 60.8 ± 9.6 years, and 76.9% were male patients. Among 108 patients with PeAF, 77.8% had longstanding PeAF (lasting for >1 year). More than 28% of patients had a history of stroke or transient ischemic attack; the mean left atrial dimension was 45.1 ± 4.4 mm and the mean ejection fraction was 59.3 ± 9.7%. Randomization was done well, and there was no statistically significant difference between the V-ABL and Em-ABL groups.

In-Silico Ablation Results

In-silico AF ablations were done in all included patients; however, the Em-ABL group was blinded to the *in-silico* ablation results. The pre-procedural computing time for the five virtual ablation strategies described in the Methods section was 166 ± 11 min. Heart CT segmentation with a semi-automatic method and five different *in-silico* ablation lesion settings with the manual method took about 1 h. Another 1 h was taken for computing the five different *in-silico* ablation protocols simultaneously, and additional 30 min was required for the calculation of the CFAE area.

Table 2 summarizes the outcome of *in-silico* AF ablation. After virtual ablation, we waited for 25 s, measuring the termination time. Among the five *in-silico* ablation strategies, [CPVI+Posterior box+Anterior linear ablation] showed the highest AF termination rate (81.5%, 88 of 108) and shortest time to AF termination (16.792 ± 5.672 ms). The AF termination rates within 25 s were 73.1% after [CPVI+Roof line+Left lateral isthmus] *in-silico* ablation, 28.7% after [CPVI+Posterior box] after *in-silico* ablation, 11.1% after [CPVI only], and 8.3% after [CPVI+CFAE] virtual ablation. Compared with virtual [CPVI only], virtual [CPVI+Posterior box+Anterior line] ($p < 0.001$) and virtual [CPVI+Roof line+Left lateral isthmus line] ($p < 0.001$) showed significantly higher virtual AF termination rates in both the V-ABL and Em-ABL groups. There was no significant difference in the *in-silico* ablation outcome between the V-ABL group and the Em-ABL group.

Comparison of V-ABL and Em-ABL

In the real ablation procedure, CPVI only was more commonly chosen in the Em-ABL group (30.9%) than in the V-ABL group (1.9%, $p < 0.001$; **Table 3**). Among patients in the V-ABL group, [CPVI+Roof+Left lateral isthmus] ablation was most commonly chosen (43.4%), although *in-silico* AF termination rate was highest in [CPVI+Posterior box+Anterior line] (**Table 2**). This

TABLE 2 | Virtual ablation outcome.

	Overall (*N* = 108)	V-ABL (*N* = 53)	Em-ABL (*N* = 55)	*p*-Value
Conduction velocity (m/s)	0.41 ± 0.11	0.40 ± 0.07	0.41 ± 0.14	0.615
APD_{90} (ms)	213 ± 2	213 ± 2	213 ± 3	0.618
AF TERMINATION RATE (%)				
CPVI	11.1 (12/108)	9.4 (5/53)	12.7 (7/55)	0.761
CPVI + PostBox	28.7 (31/108)*	34.0 (18/53)†	23.6 (13/55)	0.289
CPVI + PostBox + AL	81.5 (88/108)*	83.0 (44/53)†	80.0 (44/55)‡	0.806
CPVI + RL + LLI	73.1 (79/108)*	75.5 (40/53)†	70.9 (39/55)‡	0.667
CPVI + CFAE	8.3 (9/108)	7.5 (4/53)	9.1 (5/55)	1.000
TIME TO AF TERMINATION (MS)				
CPVI	23914 ± 3466	24017 ± 3354	23815 ± 3599	0.763
CPVI + PostBox	21893 ± 5471	21463 ± 5719	22307 ± 5240	0.426
CPVI + PostBox + AL	16792 ± 5672	16478 ± 5750	17094 ± 5633	0.575
CPVI + RL + LLI	17701 ± 5770	17199 ± 5949	18185 ± 5604	0.378
CPVI + CFAE	24170 ± 3041	24319 ± 2686	24018 ± 3385	0.619

*$p < 0.001$, †$p < 0.001$, ‡$p < 0.001$ compared with the CPVI of each group.
APD_{90}, action potential duration of 90% repolarization; CPVI, circumferential pulmonary vein isolation; PostBox, posterior box isolation; AL, anterior line; RL, roof line; LLI, left lateral isthmus line; CFAE, complex fractionated atrial electrogram guided ablation.*

TABLE 3 | Clinical outcome.

	Overall (*N* = 108)	V-ABL (*N* = 53)	Em-ABL (*N* = 55)	*p*-Value
PROCEDURAL LESION SET (%)				
CPVI	16.7 (18/108)	1.9 (1/53)	30.9 (17/55)	< 0.001
CPVI + PostBox	6.5 (7/108)	11.3 (6/53)	1.8 (1/55)	0.058
CPVI + PostBox + AL	38.0 (41/108)	39.6 (21/53)	36.4 (20/55)	0.843
CPVI + RL + LLI	33.3 (36/108)	43.4 (23/53)	23.6 (13/55)	0.041
CPVI + CFAE	5.6 (6/108)	3.8 (2/53)	7.1 (4/56)	0.679
Procedure time (min)	263.5 ± 88.5	256.2 ± 69.0	271.5 ± 104.7	0.403
Ablation time (min)	5121.9 ± 2574.6	4954.7 ± 2804.0	5272.8 ± 2368.2	0.510
Fluoroscopic time (min)	57 ± 30	59 ± 31	55 ± 30	0.523
Complication rate (%)	4.2	4.4	4.0	0.900
AAD utilization rate (%)	42.6	49.1	36.4	0.320
Early recurrence (%)	30.2	33.3	27.3	0.531
Clinical recurrence (%)	16.0	14.0	18.9	0.538

CPVI, circumferential pulmonary vein isolation; PostBox, posterior box isolation; AL, anterior line; RL, roof line; LLI, left lateral isthmus line; CFAE, complex fractionated atrial electrogram guided ablation; AAD, antiarrhythmic drug.

was because, when AF was terminated in both lesion sets (32 cases), we chose the earliest terminating virtual lesion set (16 in [CPVI+Roof+Left lateral isthmus] and 11 in [CPVI+Posterior box+Anterior line]). In the Em-ABL group, [CPVI+Posterior box+Anterior line] was selected most often (36.4%), followed by [CPVI only] (30.9%; $p = 0.687$) (**Table 3**). Among patients in the Em-ABL group, the earliest terminating *in-silico* lesion set, which was blinded to the operator, was identical to the empirically chosen real ablation lesion set in 21.8% (12 of 55).

The procedure-related acute outcomes are summarized in **Table 3**. There was no significant difference in procedure time ($p = 0.289$), ablation time ($p = 0.988$), complication rates ($p = 0.359$), and early recurrence rate within 3 months ($p = 1.000$) between the V-ABL group and the Em-ABL group.

Comparison of Rhythm Outcomes

During 12.6 ± 3.8 months of follow-up, the clinical recurrence rates were 14.0% in the V-ABL group and 20.9% in the Em-ABL group ($p = 0.411$). The maintenance rates of antiarrhythmic drugs were 49.1% in the V-ABL group and 39.5% in the Em-ABL group ($p = 0.840$). Kaplan-Meier analyses showed consistent findings in the overall patients (log-rank $p = 0.732$; **Figure 3A**) and after excluding patients who maintained antiarrhythmic drugs (log-rank $p = 0.751$; **Figure 3C**).

However, when we compared the clinical recurrence rate according to the ablation lesion set, the clinical recurrence rates were significantly lower in patients in the Em-ABL group who underwent [CPVI+Posterior box+Anterior line] ablation, which showed the most frequent termination and shortest AF maintenance duration in virtual ablation (log-rank $p = 0.027$; **Figure 4**).

DISCUSSION

Main Findings

In this prospective randomized trial, we investigated the feasibility of using a virtual ablation system in clinical practice and compared the clinical outcome of simulation-guided ablation (V-ABL) with empirical ablation (Em-ABL) in patients with PeAF. Patient-specific atrial geometry was used for finite element modeling, and five different virtual ablation patterns were tested for each patient. This is the first randomized study to validate the clinical outcomes of simulation-guided ablation, demonstrating the potential of *in-silico* computer models for planning individualized ablation strategies in clinical practice. We demonstrated that the most effective *in-silico* AF ablation lesion set showed the best clinical outcome in the Em-ABL group. The overall safety and efficacy of simulation-guided intervention was not inferior to empirical ablation of PeAF.

Unmet Clinical Needs in PeAF Ablation

Although pulmonary vein isolation is the cornerstone of catheter ablation for AF and effective in patients with paroxysmal AF, this was found to be insufficient to treat longstanding persistent AF. Even in the STAR AF II trial (Verma et al., 2015), which advocated CPVI alone for PeAF, a 41% recurrence rate within 18 months of CPVI procedure was not good enough for clinical

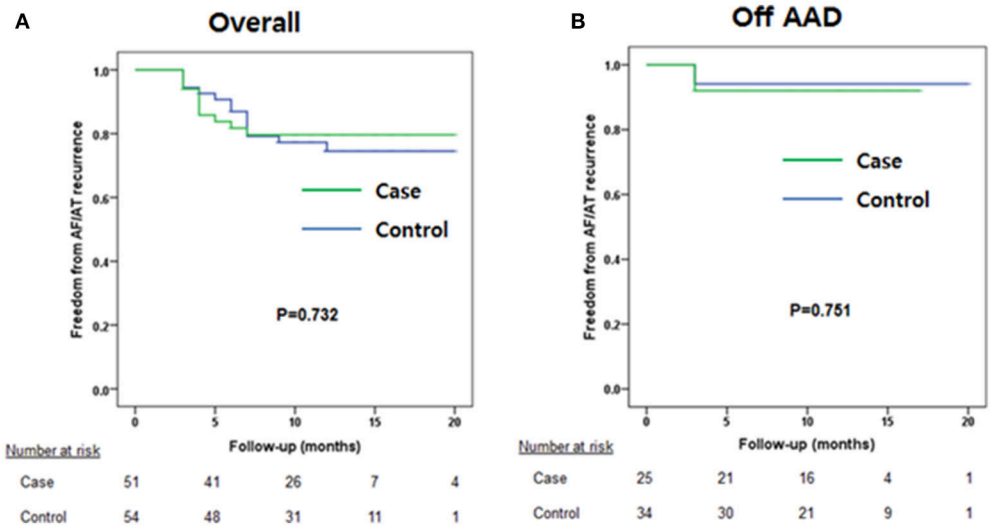

FIGURE 3 | Kaplan-Meier curves. **(A)** Overall patients. **(B)** Patients maintaining antiarrhythmic drug use were excluded.

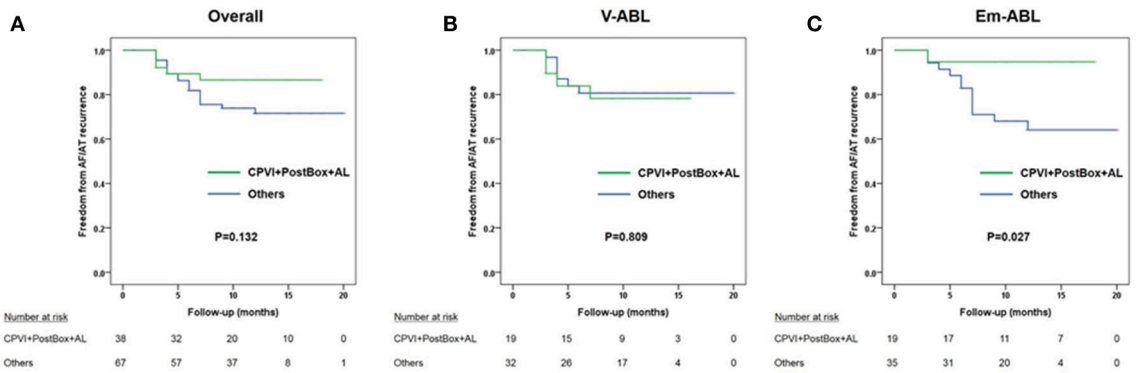

FIGURE 4 | Kaplan-Meier curves comparing the clinical recurrence rate of patients who underwent circumferential pulmonary vein isolation (CPVI) + posterior box lesion + anterior line with that of the other patients. **(A)** Overall patients. **(B)** V-ABL group. **(C)** Em-ABL group.

practice. However, there is no consensus on further ablation after CPVI in PeAF (Verma et al., 2015). Linear ablation modifies the atrial substrates and compartmentalizes the atrium into smaller regions to reduce critical mass and AF maintenance (Pak et al., 2011). The question on what is the best linear lesion set for individual patients remains unanswered. CFAE ablation has been reported to be effective for substrate modification in PeAF by some investigators (Nademanee et al., 2004; Verma et al., 2010); however, this positive outcome was not reproduced in other investigations (Oral et al., 2008). Other various ablation strategies targeting rotor (Narayan et al., 2012), driver (Haissaguerre et al., 2014), dominant frequency (Atienza et al., 2014), or Shannon entropy (Ganesan et al., 2013) remain to be validated in patients with PeAF. There are potential explanations for the lack of a "one-fits-all ablation protocol." First, PeAF is a progressive disease with various stages, and its nature is affected by the anatomy, histology, electrophysiology, and hemodynamic loading of individual patients. Second, the AF ablation procedure is operator dependent and the outcome is affected by the ablation lesion set; catheter stability; or ablation power, duration, and contact force. Third, it is not possible to test three different ablation designs in a patient because radiofrequency ablation causes irreversible tissue change. Therefore, *in-silico* AF ablation might be useful to test several different ablation lesion sets in a personalized modeling approach reflecting anatomy, histology, electrophysiology, and even genetic characteristics (Hwang et al., 2014).

Roles and Limitations of *In-Silico* AF Ablation

The advantage of computer simulation modeling is the potential for direct comparison of different ablation strategies for individual pre-procedural planning. As a result, modeling is emerging as a complementary approach to animal experiments and clinical trials in investigating more effective treatment (Winslow et al., 2012). Previously, Ruchat et al. (2007) compared

the success rates in converting AF to sinus rhythm for 19 different linear ablation patterns by using a single identical human atrial model. There have been six AF simulation studies of catheter ablation thus far (Jacquemet, 2016), and we previously reported on multiple virtual ablation protocols in 20 different personalized human atrial models (Hwang et al., 2014). In this study, we conducted *in-silico* ablations prospectively in 108 personalized LA models reflecting individual anatomy; however, it was also a single-layer homogeneous modeling approach without integrating local histology. The main reason for our use of over-simplified simulation modeling was to reduce the computing time. Unless AF simulation and virtual intervention can generate the result within a few hours, it is not acceptable for clinical application during intervention. Although we already made the computing time 80 times faster by using a graphics processing unit system, further innovation is still needed for sophisticated realistic AF modeling reflecting detailed histology and electrophysiology.

Another discrepancy of *in-silico* AF ablation and real catheter ablation is completeness and maintenance of conduction block after linear ablation. Although [CPVI+Posterior box+Anterior linear ablation] showed the highest antifibrillatory effect in both virtual ablation and Em-ABL, it was difficult to achieve complete and permanent transmural conduction block by using endocardial radiofrequency energy delivery in the clinical setting with a beating heart and respiratory motion. A non-transmural lesion or ablation gap provides one of the main reasons for AF recurrence after an ablation procedure, discordant to *in-silico* AF ablation.

Study Limitations

There are limitations in our simulation modeling. The mechanism of AF in this particular computer model is based exclusively on multiple wavelet theories (Moe et al., 1964), and other well-described mechanisms like rotors can be masked in this model. Although we used patient-specific atrial geometry for the AF ablation simulation, individual electrophysiological and structural characteristics such as regional differences in action potential morphology, and fiber orientation were not included. Clinical studies showed that atrial wall thickness affected AF wave dynamics (Song et al., 2017), but the wall thickness was not considered in the present model. We also did not model the right atrium, because AF drivers have been known to exist mostly in the LA in humans (Sanders et al., 2005). We assume that the predictability of AF intervention by using simulation will be improved remarkably by integrating high-resolution cardiac imaging modalities reflecting the remodeled scar area, pathological electro-anatomical information acquired during procedure, and more realistic multilayer bi-atrial modeling study.

Although our modeling protocol for virtual AF ablation may not reflect the mechanism of AF ablation precisely (whether virtual ablation stops an ongoing AF or whether it hinders the onset of new episode of AF, ectopic centers, rotor, or micro-reentry, etc.), it exhibits the antiarrhythmic effects of appropriate critical mass reduction, which is the main antiarrhythmic mechanism of linear ablation of AF or a surgical maze procedure. While CV may also change AF wave dynamics, we used a fixed CV based on real human patient data (Yonsei AF ablation cohort) (Park et al., 2014) and previous simulation studies (Hwang et al., 2014; Li et al., 2016). Because we tested five different virtual ablation protocols in every patient's LA modeling at the same CV condition, it did not affect the mechanism of critical mass reduction. For the model to show superiority to empirical ablation, individual patient's structural heterogeneity such as scar/fibrosis, fiber orientation, and wall thickness variation should be included in the model.

CONCLUSION

This is the first randomized multicenter study to demonstrate that simulation-guided ablation by using personalized models of LA was feasible, and the clinical outcome was not inferior to that of empirical ablation. Although there are limitations in applying virtual AF ablation to a personalized ablation strategy, our results showed that the virtual AF ablation system is capable of identifying the most effective ablation lesion set for individual patients. Advances in modeling technology might provide useful clinical insights for planning therapeutic interventions in the near future.

AUTHOR CONTRIBUTIONS

Conception and design of the study: HP. Acquisition of data: JS, TK, BJ, SK, YSO, GN, YKO, SO, YK, and HP. Analysis of data: JS, MH, JSS, and BL. Interpretation of data: JS and HP. Drafting the work: JS and MH. All authors contributed in revising the work, approved the final version to be published, and agreed to be accountable for all aspects of the work.

FUNDING

This research was supported by grants (A085136) from the Korea Health 21 R&D Project, the Ministry of Health and Welfare, [NRF-2017R1A2B4003983] from the Basic Science Research Program run by the National Research Foundation of Korea (NRF), and Basic Science Research Program through the National Research Foundation of Korea (NRF) funded by the Ministry of Education (2017R1D1A1B03030495).

REFERENCES

Atienza, F., Almendral, J., Ormaetxe, J. M., Moya, A., Martinez-Alday, J. D., Hernandez-Madrid, A., et al. (2014). Comparison of radiofrequency catheter ablation of drivers and circumferential pulmonary vein isolation in atrial fibrillation: a noninferiority randomized multicenter RADAR-AF trial. *J. Am. Coll. Cardiol.* 64, 2455–2467. doi: 10.1016/j.jacc.2014.09.053

Ball, J., Carrington, M. J., McMurray, J. J., and Stewart, S. (2013). Atrial fibrillation: profile and burden of an evolving epidemic in the 21st century. *Int. J. Cardiol.* 167, 1807–1824. doi: 10.1016/j.ijcard.2012.12.093

Calkins, H., Kuck, K. H., Cappato, R., Brugada, J., Camm, A. J., Chen, S. A., et al. (2012). 2012 HRS/EHRA/ECAS expert consensus statement on catheter and surgical ablation of atrial fibrillation: recommendations for patient selection, procedural techniques, patient management and follow-up, definitions, endpoints, and research trial design: a report of the Heart Rhythm Society (HRS) Task Force on Catheter and Surgical Ablation of Atrial Fibrillation. Developed in partnership with the European Heart Rhythm Association (EHRA), a registered branch of the European Society of Cardiology (ESC) and the European Cardiac Arrhythmia Society (ECAS); and in collaboration with the American College of Cardiology (ACC), American Heart Association (AHA), the Asia Pacific Heart Rhythm Society (APHRS), and the Society of Thoracic Surgeons (STS). Endorsed by the governing bodies of the American College of Cardiology Foundation, the American Heart Association, the European Cardiac Arrhythmia Society, the European Heart Rhythm Association, the Society of Thoracic Surgeons, the Asia Pacific Heart Rhythm Society, and the Heart Rhythm Society. *Heart Rhythm* 9, 632 e621–696 e621. doi: 10.1016/j.hrthm.2011.12.016

Courtemanche, M., Ramirez, R. J., and Nattel, S. (1998). Ionic mechanisms underlying human atrial action potential properties: insights from a mathematical model. *Am. J. Physiol.* 275(1 Pt 2), H301–H321.

Dewire, J., and Calkins, H. (2013). Update on atrial fibrillation catheter ablation technologies and techniques. *Nat. Rev. Cardiol.* 10, 599–612. doi: 10.1038/nrcardio.2013.121

Ganesan, A. N., Kuklik, P., Lau, D. H., Brooks, A. G., Baumert, M., Lim, W. W., et al. (2013). Bipolar electrogram shannon entropy at sites of rotational activation: implications for ablation of atrial fibrillation. *Circ. Arrhythm. Electrophysiol.* 6, 48–57. doi: 10.1161/CIRCEP.112.976654

Goldstein, L. B., Bushnell, C. D., Adams, R. J., Appel, L. J., Braun, L. T., Chaturvedi, S., et al. (2011). Guidelines for the primary prevention of stroke: a guideline for healthcare professionals from the American Heart Association/American Stroke Association. *Stroke* 42, 517–584. doi: 10.1161/STR.0b013e3181fcb238

Haissaguerre, M., Hocini, M., Denis, A., Shah, A. J., Komatsu, Y., Yamashita, S., et al. (2014). Driver domains in persistent atrial fibrillation. *Circulation* 130, 530–538. doi: 10.1161/CIRCULATIONAHA.113.005421

Hwang, M., Kwon, S. S., Wi, J., Park, M., Lee, H. S., Park, J. S., et al. (2014). Virtual ablation for atrial fibrillation in personalized *in-silico* three-dimensional left atrial modeling: comparison with clinical catheter ablation. *Prog. Biophys. Mol. Biol.* 116, 40–47. doi: 10.1016/j.pbiomolbio.2014.09.006

Hwang, M., Park, J., Lee, Y. S., Park, J. H., Choi, S. H., Shim, E. B., et al. (2015). Fibrillation number based on wavelength and critical mass in patients who underwent radiofrequency catheter ablation for atrial fibrillation. *IEEE Trans. Biomed. Eng.* 62, 673–679. doi: 10.1109/TBME.2014.2363669

Jacquemet, V. (2016). Lessons from computer simulations of ablation of atrial fibrillation. *J. Physiol.* 594, 2417–2430. doi: 10.1113/JP 271660

Li, C., Lim, B., Hwang, M., Song, J. S., Lee, Y. S., Joung, B., et al. (2016). The Spatiotemporal stability of dominant frequency sites in *in-silico* modeling of 3-dimensional left atrial mapping of atrial fibrillation. *PLoS ONE* 11:e0160017. doi: 10.1371/journal.pone.0160017

Moe, G. K., Rheinboldt, W. C., and Abildskov, J. A. (1964). A computer model of atrial fibrillation. *Am. Heart J.* 67, 200–220. doi: 10.1016/0002-8703(64) 90371-0

Mun, H. S., Joung, B., Shim, J., Hwang, H. J., Kim, J. Y., Lee, M. H., et al. (2012). Does additional linear ablation after circumferential pulmonary vein isolation improve clinical outcome in patients with paroxysmal atrial fibrillation? Prospective randomised study. *Heart* 98, 480–484. doi: 10.1136/heartjnl-2011-301107

Nademanee, K., McKenzie, J., Kosar, E., Schwab, M., Sunsaneewitayakul, B., Vasavakul, T., et al. (2004). A new approach for catheter ablation of atrial fibrillation: mapping of the electrophysiologic substrate. *J. Am. Coll. Cardiol.* 43, 2044–2053. doi: 10.1016/j.jacc.2003.12.054

Narayan, S. M., Krummen, D. E., Shivkumar, K., Clopton, P., Rappel, W. J., and Miller, J. M. (2012). Treatment of atrial fibrillation by the ablation of localized sources: CONFIRM (Conventional Ablation for Atrial Fibrillation With or Without Focal Impulse and Rotor Modulation) trial. *J. Am. Coll. Cardiol.* 60, 628–636. doi: 10.1016/j.jacc.2012.05.022

Oral, H., Chugh, A., Good, E., Crawford, T., Sarrazin, J. F., Kuhne, M., et al. (2008). Randomized evaluation of right atrial ablation after left atrial ablation of complex fractionated atrial electrograms for long-lasting persistent atrial fibrillation. *Circ. Arrhythm. Electrophysiol.* 1, 6–13. doi: 10.1161/CIRCEP.107.748780

Pak, H. N., Oh, Y. S., Lim, H. E., Kim, Y. H., and Hwang, C. (2011). Comparison of voltage map-guided left atrial anterior wall ablation versus left lateral mitral isthmus ablation in patients with persistent atrial fibrillation. *Heart Rhythm* 8, 199–206. doi: 10.1016/j.hrthm.2010.10.015

Park, J., Joung, B., Uhm, J. S., Young Shim, C., Hwang, C., Hyoung Lee, M., et al. (2014). High left atrial pressures are associated with advanced electroanatomical remodeling of left atrium and independent predictors for clinical recurrence of atrial fibrillation after catheter ablation. *Heart Rhythm* 11, 953–960. doi: 10.1016/j.hrthm.2014.03.009

Ruchat, P., Virag, N., Dang, L., Schlaepfer, J., Pruvot, E., and Kappenberger, L. (2007). A biophysical model of atrial fibrillation ablation: what can a surgeon learn from a computer model? *Europace* (Suppl. 6), 6, vi71–vi76. doi: 10.1093/europace/eum209

Sanders, P., Berenfeld, O., Hocini, M., Jais, P., Vaidyanathan, R., Hsu, L. F., et al. (2005). Spectral analysis identifies sites of high-frequency activity maintaining atrial fibrillation in humans. *Circulation* 112, 789–797. doi: 10.1161/CIRCULATIONAHA.104.517011

Shim, J., Joung, B., Park, J. H., Uhm, J. S., Lee, M. H., and Pak, H. N. (2013). Long duration of radiofrequency energy delivery is an independent predictor of clinical recurrence after catheter ablation of atrial fibrillation: over 500 cases experience. *Int. J. Cardiol.* 167, 2667–2672. doi: 10.1016/j.ijcard.2012.06.120

Song, J. S., Lee, Y. S., Hwang, M., Lee, J. K., Li, C., Joung, B., et al. (2016). Spatial reproducibility of complex fractionated atrial electrogram depending on the direction and configuration of bipolar electrodes: an *in-silico* modeling study. *Korean J. Physiol. Pharmacol.* 20, 507–514. doi: 10.4196/kjpp.2016.20.5.507

Song, J. S., Wi, J., Lee, H. J., Hwang, M., Lim, B., Kim, T. H., et al. (2017). Role of atrial wall thickness in wave-dynamics of atrial fibrillation. *PLoS ONE* 12:e0182174. doi: 10.1371/journal.pone.0182174

Trayanova, N. A. (2014). Mathematical approaches to understanding and imaging atrial fibrillation: significance for mechanisms and management. *Circ. Res.* 114, 1516–1531. doi: 10.1161/CIRCRESAHA.114.302240

Verma, A., Jiang, C. Y., Betts, T. R., Chen, J., Deisenhofer, I., Mantovan, R., et al. (2015). Approaches to catheter ablation for persistent atrial fibrillation. *N. Engl. J. Med.* 372, 1812–1822. doi: 10.1056/NEJMoa1408288

Verma, A., Mantovan, R., Macle, L., De Martino, G., Chen, J., Morillo, C. A., et al. (2010). Substrate and Trigger Ablation for Reduction of Atrial Fibrillation (STAR AF): a randomized, multicentre, international trial. *Eur. Heart J.* 31, 1344–1356. doi: 10.1093/eurheartj/ehq041

Winslow, R. L., Trayanova, N., Geman, D., and Miller, M. I. (2012). Computational medicine: translating models to clinical care. *Sci. Transl. Med.* 4, 158rv111. doi: 10.1126/scitranslmed.3003528

Zhao, J., Kharche, S. R., Hansen, B. J., Csepe, T. A., Wang, Y., Stiles, M. K., et al. (2015). Optimization of catheter ablation of atrial fibrillation: insights gained from clinically-derived computer models. *Int. J. Mol. Sci.* 16, 10834–10854. doi: 10.3390/ijms160510834

Zozor, S., Blanc, O., Jacquemet, V., Virag, N., Vesin, J. M., Pruvot, E., et al. (2003). A numerical scheme for modeling wavefront propagation on a monolayer of arbitrary geometry. *IEEE Trans. Biomed. Eng.* 50, 412–420. doi: 10.1109/TBME.2003.809505

Conflict of Interest Statement: The authors declare that the research was conducted in the absence of any commercial or financial relationships that could be construed as a potential conflict of interest.

Copyright © 2017 Shim, Hwang, Song, Lim, Kim, Joung, Kim, Oh, Nam, On, Oh, Kim and Pak. This is an open-access article distributed under the terms of the Creative Commons Attribution License (CC BY). The use, distribution or reproduction in other forums is permitted, provided the original author(s) or licensor are credited and that the original publication in this journal is cited, in accordance with accepted academic practice. No use, distribution or reproduction is permitted which does not comply with these terms.

frontiers in Physiology

ORIGINAL RESEARCH
published: 06 February 2018
doi: 10.3389/fphys.2018.00056

Absence of Rapid Propagation through the Purkinje Network as a Potential Cause of Line Block in the Human Heart with Left Bundle Branch Block

Jun-ichi Okada[1], Takumi Washio[1], Machiko Nakagawa[2], Masahiro Watanabe[2], Yoshimasa Kadooka[2], Taro Kariya[3], Hiroshi Yamashita[3], Yoko Yamada[4], Shin-ichi Momomura[4], Ryozo Nagai[3], Toshiaki Hisada[1] and Seiryo Sugiura[1]*

[1] Department of Human and Engineered Environmental Studies, Graduate School of Frontier Sciences, The University of Tokyo, Kashiwa, Japan, [2] Healthcare System Unit, Fujitsu Ltd., Tokyo, Japan, [3] Department of Cardiovascular Medicine, School of Medicine, The University of Tokyo, Tokyo, Japan, [4] Department of Cardiovascular Medicine, Saitama Medical Center, Jichi Medical University, Saitama, Japan

OPEN ACCESS

Edited by:
Eun Bo Shim,
Kangwon National University, South Korea

Reviewed by:
Arun V. Holden,
University of Leeds, United Kingdom
Jae-Sun Uhm,
Severance Hospital, South Korea

***Correspondence:**
Jun-ichi Okada
okada@sml.k.u-tokyo.ac.jp

Specialty section:
This article was submitted to Computational Physiology and Medicine, a section of the journal Frontiers in Physiology

Received: *01 November 2017*
Accepted: *17 January 2018*
Published: *06 February 2018*

Citation:
Okada J, Washio T, Nakagawa M, Watanabe M, Kadooka Y, Kariya T, Yamashita H, Yamada Y, Momomura S, Nagai R, Hisada T and Sugiura S (2018) Absence of Rapid Propagation through the Purkinje Network as a Potential Cause of Line Block in the Human Heart with Left Bundle Branch Block. Front. Physiol. 9:56. doi: 10.3389/fphys.2018.00056

Background: Cardiac resynchronization therapy is an effective device therapy for heart failure patients with conduction block. However, a problem with this invasive technique is the nearly 30% of non-responders. A number of studies have reported a functional line of block of cardiac excitation propagation in responders. However, this can only be detected using non-contact endocardial mapping. Further, although the line of block is considered a sign of responders to therapy, the mechanism remains unclear.

Methods: Herein, we created two patient-specific heart models with conduction block and simulated the propagation of excitation based on a cell model of electrophysiology. In one model with a relatively narrow QRS width (176 ms), we modeled the Purkinje network using a thin endocardial layer with rapid conduction. To reproduce a wider QRS complex (200 ms) in the second model, we eliminated the Purkinje network, and we simulated the endocardial mapping by solving the inverse problem according to the actual mapping system.

Results: We successfully observed the line of block using non-contact mapping in the model without the rapid propagation of excitation through the Purkinje network, although the excitation in the wall propagated smoothly. This model of slow conduction also reproduced the characteristic properties of the line of block, including dense isochronal lines and fractionated local electrocardiograms. Further, simulation of ventricular pacing from the lateral wall shifted the location of the line of block. By contrast, in the model with the Purkinje network, propagation of excitation in the endocardial map faithfully followed the actual propagation in the wall, without showing the line of block. Finally, switching the mode of propagation between the two models completely reversed these findings.

Conclusions: Our simulation data suggest that the absence of rapid propagation of excitation through the Purkinje network is the major cause of the functional line of block recorded by non-contact endocardial mapping. The line of block can be used to identify responders as these patients loose rapid propagation through the Purkinje network.

Keywords: multi-scale simulation, conduction block, non-contact mapping, line of block, Purkinje network, electrophysiology

INTRODUCTION

Although the therapeutic effects of cardiac resynchronization therapy (CRT) for patients with heart failure with conduction block have been confirmed by number of clinical trials, the existence of non-responders remains a major health and economic problem (Kirk and Kass, 2013; Prinzen et al., 2013; Yu and Hayes, 2013). Accordingly, there are numerous studies examining the mechanisms leading to electromechanical dyssynchrony in affected patients, to aid in the identification of individuals responding to treatment (Bax et al., 2005a,b). Indeed, electrophysiological studies have shown that a wide QRS on surface ECG, reflecting a long delay in propagation of activation, is a reliable marker of responders (Auricchio et al., 2003; Brignole et al., 2013). However, in a detailed analysis of the activation sequence in the left ventricle (LV) using the unipolar non-contact mapping system to assess the activation wave front, Auricchio et al. reported that the LV activation sequence in patients with heart failure and left bundle-branch block was blocked by a narrow region of slow conduction (line of block), which could not cross directly to the lateral wall from the anterior region (Auricchio et al., 2004). Similar observations were also reported, and the line of block was suggested as a biomarker of the response to CRT (Fung et al., 2004; Lambiase et al., 2004; Duckett et al., 2012). Nevertheless, bipolar contact mapping of the LV endocardium performed in the same patients revealed a continuous propagation of the activation wave front, and were thus unable to demonstrate a line of block (Auricchio et al., 2004). Unipolar signals by non-contact mapping were recorded by 64 electrodes mounted equidistantly on a 7.6 mL balloon (size 1.8 × 4.6 cm) placed in the LV cavity. From these signals, endocardial mapping was generated by solving the inverse problem using the boundary element method. An optimized regularization was required to produce accurate results, and a spline curve fit was used to produce 3,360 potential points on the endocardial surface. However, as the raw signals recorded in the LV cavity were far-field electrographic data, the generated non-contact endocardial map retains electrical information from the transmural thickness (Gornick et al., 1999). By contrast, the bipolar signals, recorded by pushing a pair of leads separated by 2 or 5 mm on the endocardial surface, represent the local information from the endocardium. The mapping procedure was performed for approximately 200 contact points equally distributed on the LV endocardial surface. Accordingly, the authors speculated that the line of block reflects the abnormal propagation pattern of intramural activation (Auricchio et al., 2004). However, this underlying mechanism has not been confirmed clinically.

Computer simulations are an indispensable tool for studying cardiac pathophysiology (Noble, 2002; Winslow et al., 2012). In particular, multi-scale simulations using a realistic three-dimensional heart model provide an opportunity to examine the normal and abnormal cardiac functions resulting from the complex interplay of molecular, cellular, and tissue-level activity. We also developed a multi-scale heart simulator (Watanabe et al., 2004; Washio et al., 2010, 2013; Sugiura et al., 2012), and reported its various applications including patient-specific electrophysiology of normal and diseased hearts (Okada et al., 2011, 2013), prediction of drug-induced arrhythmogenic risk (Okada et al., 2015), and CRT (Panthee et al., 2016; Okada et al., 2017). In our previous study, using CRT in patient-specific models of failing hearts with conduction block (Okada et al., 2017), we examined the intramural activation sequences of variably affected heart models, and found that either the absence or presence of the rapid propagation of activation through the Purkinje system in the endocardium determines the QRS width in the ECG of patients with left bundle branch block. We hypothesize that this difference in activation pattern within the ventricular wall may be also the cause of the line of block observed by non-contact mapping in left bundle-branch cases.

To test this hypothesis, in the present study we simulated non-contact mapping in our diseased heart models. We demonstrated that the slow propagation of activation without the involvement of the Purkinje system was recorded and processed by the algorithm of the non-contact mapping system to produce the line of block, thus supporting our hypothesis. This observation promotes our understanding on the pathophysiology of left bundle-branch block, and also characterizes the information retrievable from non-contact mapping of the heart.

MATERIALS AND METHODS

In this study, we used a number of models of heart failure with left bundle branch block using clinical data collected with written informed consent after approval by the institutional review board, as previously reported (Okada et al., 2017).

Multi-scale Simulation of the Cardiac Excitation and Propagation

Details of the multi-scale, multi-physics heart simulator were previously reported (Watanabe et al., 2004; Washio et al., 2010, 2013; Okada et al., 2011, 2013, 2015; Sugiura et al., 2012). In the present study, the simulation of electrophysiology was performed using only the finite element models of the ventricles and torso (Okada et al., 2017). In brief, the voxel model of the

heart (mesh size: 0.4 mm, number of elements: 32,768,000 and 36,126,720) and the torso (mesh size: 1.6 mm) were created from the three dimensional reconstruction of multi-slice computed tomography data. In the heart model, we mapped the fiber orientation using our rule-based method (Hisada et al., 2013), so that the fiber orientations changed across the wall depth from the endocardium to the epicardium (LV free wall: −90° to 60°, interventricular septum: −90° to 70°, RV wall: −60° to 60°). To each element, we implemented the human ventricular myocyte model of electrophysiology (Ten Tusscher et al., 2004), with three cell types with different action potential duration; i.e., endocardial, M-, and epicardial cells. The distribution of these sub-types of cells was similar to that we previously reported, in which M-cells were located at 10–40% from the endocardial surface (Okada et al., 2011). The conduction system was modeled by a thin layer on the surface of the endocardial region (thickness 0.8 mm) with a high conduction velocity (1.7 m/s (default)). For the simulation of sinus rhythm, we applied small currents to excite the earliest activation sites identified to reproduce the previously reported isochronal maps (Durrer et al., 1970) and body surface voltage maps (Taccardi, 1963; De Ambroggi et al., 1976; **Figure 1A**). Propagation of excitation in the heart domain was analyzed by solving the following bidomain equation.

$$\beta\left(C_m\frac{\partial V}{\partial t}+I_{ion}\right)=I_{stim}-\frac{\partial}{\partial x_i}\left(G_{ij}^{E}\frac{\partial \varnothing^{E}}{\partial x_j}\right)$$

$$\beta\left(C_m\frac{\partial V}{\partial t}+I_{ion}\right)=I_{stim}+\frac{\partial}{\partial x_i}\left(G_{ij}^{I}\frac{\partial \varnothing^{I}}{\partial x_j}\right),$$

where $\varnothing^E$ and $\varnothing^I$ are the extracellular and intracellular potentials, respectively, V= $\varnothing^I - \varnothing^E$ is the transmembrane voltage, β is the surface-to-volume ratio of the tissue, C_m is the membrane capacitance, t is time, G_{ij}^E and G_{ij}^I are the intra— and extracellular anisotropic conductivity tensors, respectively, x_i and x_j are the tensor notations of the x, y, and z coordinates, I_{stim} is the stimulation current, and I_{ion} is the sum of ionic transmembrane currents calculated by the ventricular myocyte model of electrophysiology. In the torso domain, the mono-domain equation was solved as follows.

$$-\frac{\partial}{\partial x_i}\left(G_{ij}\frac{\partial \varnothing}{\partial x_j}\right)=0,$$

where $\varnothing$ is the potential and G_{ij} is the anisotropic conductivity at each point. Detailed information on numerical methods can be seen in Supplementary Material. Simulations were performed for a heart rate of 1 Hz using only the ventricles. Default conductivity values used for the heart and torso were taken from reported literature (Camacho et al., 1995; Panescu et al., 1995; Keldermann et al., 2009) and are listed in **Table 1**. To reproduce the clinical ECG, we adjusted the conductivity for each patient.

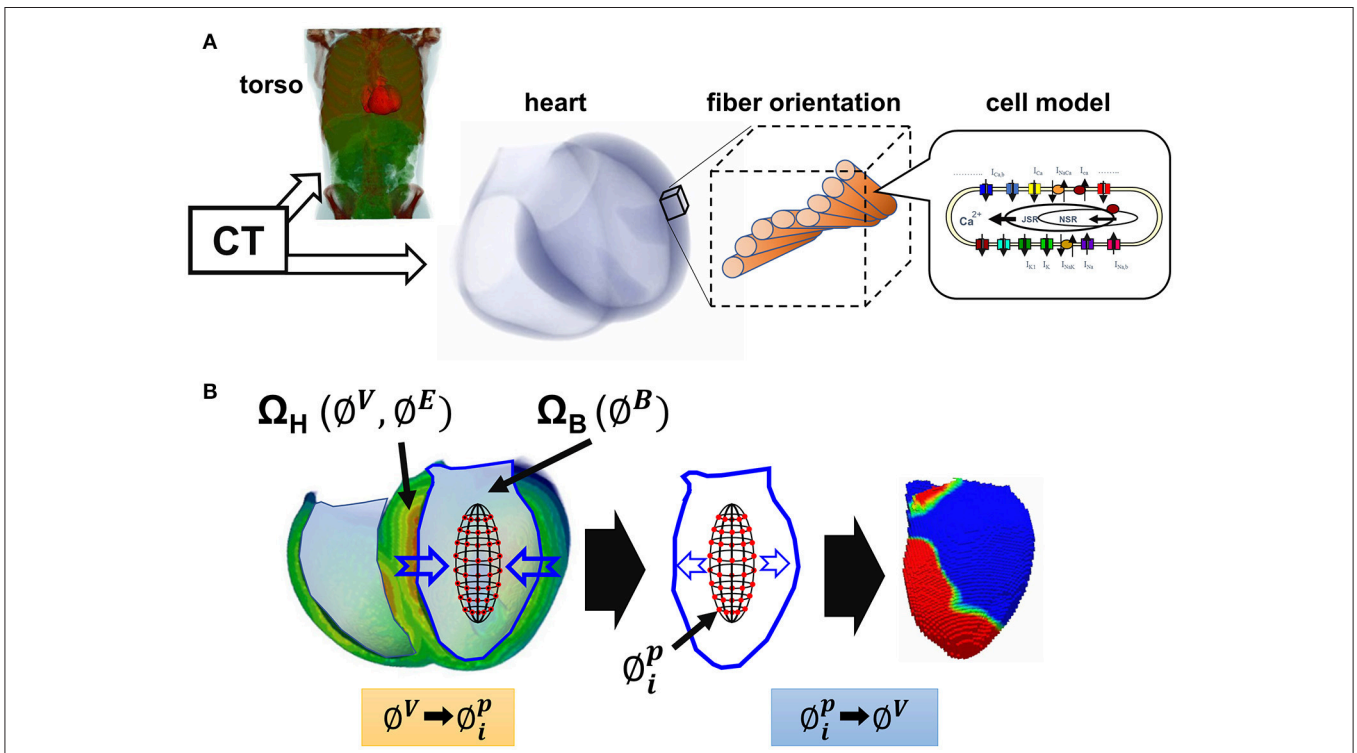

FIGURE 1 | Multi-scale simulation of cardiac excitation and propagation. **(A)** Schematic presentation of the multi-scale heart model. **(B)** Simulation of non-contact endocardial mapping. Ω_H, heart wall domain; Ω_B, ventricular cavity domain; $\varnothing^V$, membrane potential; $\varnothing^E$, potential in the extracellular space; $\varnothing^B$, potential in the cavity; $\varnothing_l^p$, l = 1 to 64: potential recorded by the 64 electrode array.

Simulation Model of Heart Failure with Left Bundle-Branch Block Model

We used two heart models. The model with the Purkinje layer was patient 8, and the model without the Purkinje layer was patient 3, from our previous study (Okada et al., 2017). In that study, the multi-scale heart model was created according to the method described above, and we introduced left bundle-branch block by allowing only the earliest activation sites in the right ventricle. However, after the left ventricular breakthrough, we needed to adopt either of two different modes of conduction, depending on the electrophysiological properties of the patients. While slow and homogeneous conduction in the left ventricular wall reproduced the clinical ECGs of patients exhibiting a wide QRS complex, we needed to account for rapid antidromic conduction through the Purkinje system in patients with a relatively narrow QRS complex. The selection of the conduction mode was dependent on the degree of agreement between the simulated and clinical ECGs. In general, the rapid conduction mode was applied for cases with a QRS width <150 ms.

TABLE 1 | Conductivity values used in the model.

Tissue	Conductivity (mS/cm)
HEART (INTRACELLULAR)	
Fiber direction	6.2
Fiber normal direction)	2.0
HEART (EXTRACELLULAR)	
Fiber direction	4.0
Fiber normal direction)	2.0
Purkinje fiber	30.0
Blood	7.8
Atrium, artery, vein	7.0
Muscle	2.56
Lung	0.83
Esophagus, stomach, bowel	2.0
Spleen, liver, kidney	1.67
Bone	0.1
Fat	0.5
Skin, body surface	80.0

Simulation of Non-contact Mapping

We simulated the unipolar non-contact mapping of the LV endocardium using a 64-electrode array, as used clinically (Gornick et al., 1999; Wang et al., 2013). The 64 electrodes were arranged concentrically and equidistantly around the surface of a prolate ellipsoid balloon (3.5 × 4.5 cm size). Details of the algorithm for obtaining the endocardial potential map are shown in Supplementary Material. In brief, we first solved the bidomain equations of the electrophysiology data in the domain consisting of the heart wall (Ω_H) and blood inside the ventricular cavity

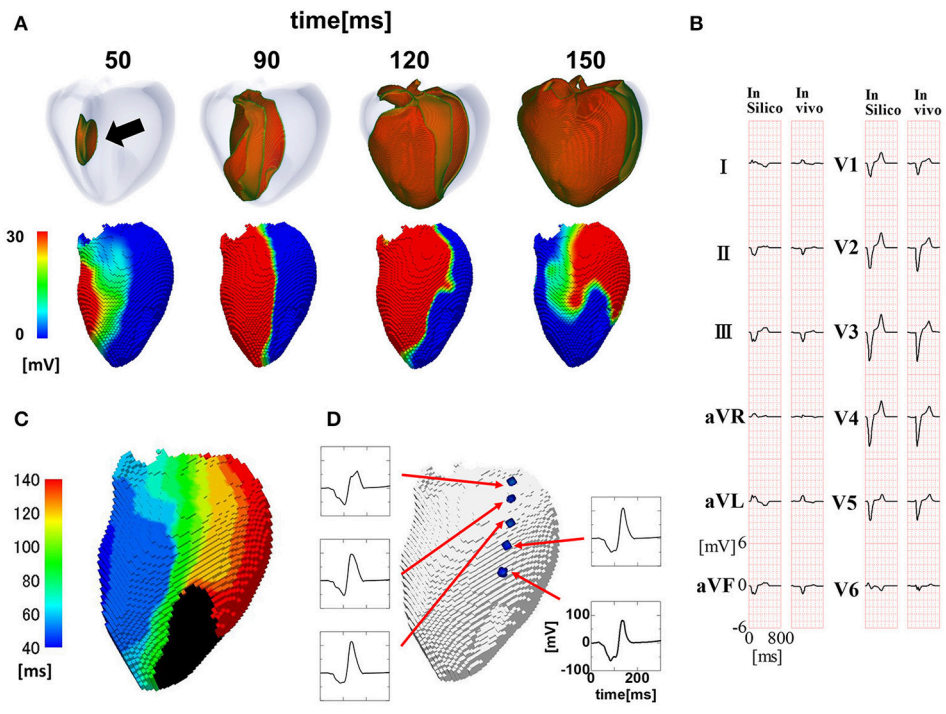

FIGURE 2 | Propagation of excitation in the heart with a narrow QRS width. **(A)** Time-lapse images of the activation in the ventricular wall (upper row: Region of ventricular wall where membrane voltage exceeds −50 mV is shown in color) and corresponding non-contact endocardial map (lower row). Numbers at the top indicate the time after the activation starts. Black arrow: left ventricular breakthrough; color bar: membrane potential. **(B)** Real (left column) and simulated (right column) 12 lead body surface electrocardiogram (ECG). **(C)** Color-coded isochronal map (left) and local unipolar electrocardiogram. **(D)** Local unipolar electrocardiogram.

containing blood (Ω_B). From this we obtained the membrane potential ($\varnothing^V$), and the potential in the extracellular space ($\varnothing^E$) in Ω_H and the potential in Ω_B ($\varnothing^B$) (**Figure 1B**, left). Potentials recorded by the 64 electrodes ($\varnothing_1^p$, $i = 1$ to 64) were sampled at the corresponding position in the blood domain, and were expressed by the following matrix equation.

$$\varnothing^p = \begin{pmatrix} \varnothing_1^p \\ \vdots \\ \varnothing_{64}^p \end{pmatrix} = B \cdot \begin{pmatrix} \varnothing_1^H \\ \vdots \\ \varnothing_N^H \end{pmatrix} = B \cdot \varnothing^H,$$

where N is the number of nodes in the heart domain. It is important to note that these potentials recorded by the electrode array reflected the electrical activity across the whole transmural thickness, not the mirror image of the endocardial potential. Finally, endocardial potentials were obtained as the inverse solution (**Figure 1B**, middle and right). However, as this is an ill-posed problem, we solved an optimization problem by minimizing the following function (Wang et al., 2013).

$$E\left(\varnothing^H\right) = \frac{1}{2} \| B \cdot \varnothing^H - \varnothing^p \|^2 + \frac{\varepsilon}{2} \left(\varnothing^H \cdot L \cdot \varnothing^H\right),$$

where L is the Laplacian operator. The second term on the right-hand side is a regularization term for stabilizing the minimization.

Computation

All program code was written in FORTRAN in our laboratory. Simulations were performed using a 2.6-GHz HP Blade System c7000 (Intel Xeon E5-2670; Intel, Santa Clara, CA, USA). With the total number of degrees of freedom set to approximately 60 million, it took 50 min to compute a single cardiac cycle using 127 cores. Numerical data were visualized using commercial software (MicroAVS; Advanced Visual Systems, Waltham, MA, USA).

RESULTS

Slow Propagation Excluding the Conduction System Introduces the Line of Block

The activation sequence in the entire ventricular wall (upper row) and the results of endocardial non-contact mapping (lower row) in the patient with a relatively narrow QRS complex (176 ms **Figure 2B**) are shown in **Figure 2A** (see also Supplemental Movie S1). During activation of the entire wall (upper row), activation of endocardial conduction system clearly preceded that of the

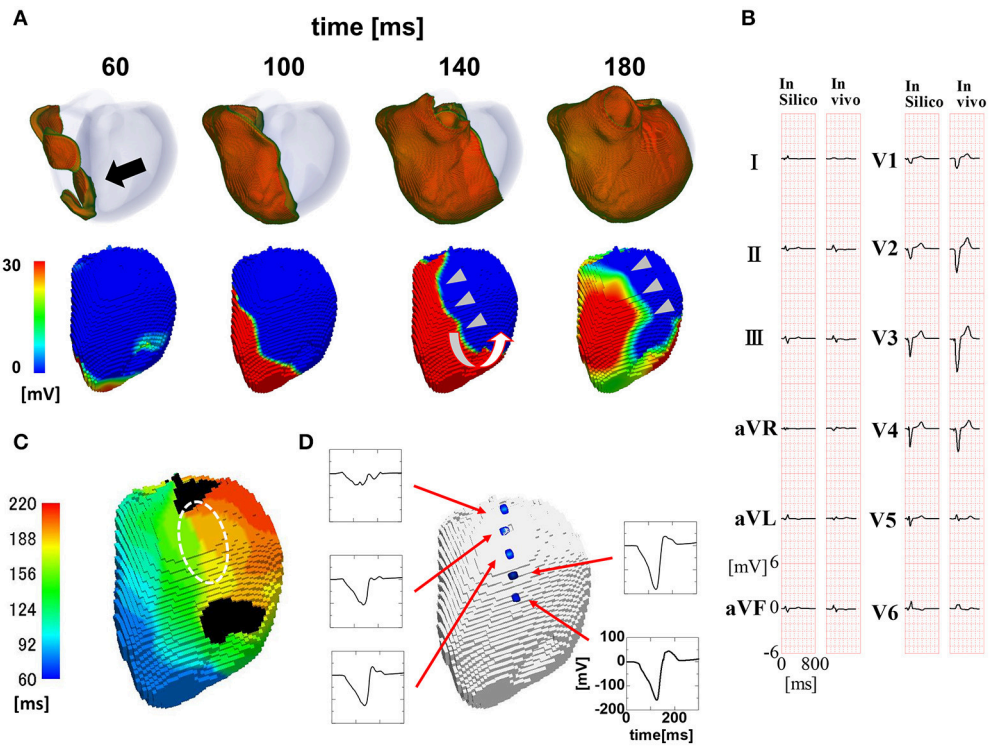

FIGURE 3 | Propagation of excitation in the heart with a wide QRS width. **(A)** Time-lapse images of the activation in the ventricular wall (upper row Region of ventricular wall where membrane voltage exceeds −50 mV is shown in color) and corresponding non-contact endocardial map (lower row). Numbers at the top indicate the time after the activation starts. Black arrow, left ventricular breakthrough; white U-shaped arrow, activation sequence; color bar, membrane potential. **(B)** Real (left column) and simulated (right column) 12 lead body surface ECG. **(C)** Color-coded isochronal map (left) and local unipolar electrocardiogram. White dotted circle indicates the region of dense isochronal lines. **(D)** Local unipolar electrocardiogram.

outer layer, while the activation pattern of the non-contact mapping (lower row) smoothly followed that of the conduction system. In this case, we could not identify the line of block in the endocardial isochronal map (**Figure 2C**) or the fractionated regional electrocardiogram (**Figure 2D**).

To reproduce the ECG with a wide QRS complex (200 ms; **Figure 3B**), we inhibited rapid conduction by omitting through the Purkinje network. In this case, the activation wave front started from the breakthrough point (black arrow), spanned the entire wall, and proceeded homogeneously to the free wall (**Figure 3A**, top row). However, the endocardial activation wave front stopped in the anterior region and turned around at the apex, thus showing a characteristic U-shaped pattern of activation sequence (white U-shaped arrow in **Figure 3A**, lower row) (see also Supplemental Movie S2). The isochronal map showed a region of dense isochronal lines (i.e., the line of block) at the base (white dotted circle in **Figure 3C**) We also identified fractionated local ECGs in the corresponding region, whereas the smooth local ECGs were observed in the apex (**Figure 3D**).

Simulation Model Reproduced the Characteristics of the Functional Line of Block

Auricchio et al. reported several findings supporting the functional nature of the line of block (Auricchio et al., 2004). We tested whether the current model of the line of block reproduced these findings. First, to determine whether the line of block in the left bundle branch block shifts from the left ventricular breakthrough point under intrinsic rhythm during pacing, we simulated the left ventricular pacing from the lateral wall (**Figure 4A**, red arrow). As shown in **Figure 4A** and the isochronal map (**Figures 4B,C**), the line of block shifted from the original location under pacing from the lateral wall (see also Supplemental Movie S3). The fractionated electrocardiograms identified in the region of slow conduction under intrinsic rhythm also disappeared during pacing (**Figure 4C**, broken line). Further, the amplitudes of both the unipolar and bipolar ECG in the region surrounding the line of block were similar to those in remote regions (i.e., near-normal; **Figure 4C**). Finally, the absence of scar tissue in the model of dilated cardiomyopathy excluded the possibility of morphologically-based conduction delay and block. Overall, these findings support that our simulation model reasonably reproduced the characteristics of the functional line of block observed in clinical studies (Auricchio et al., 2004; Fung et al., 2004, 2007).

Absence of Rapid Conduction through the Purkinje Network as the Predominant Cause of Line of Block

The activation sequence in the ventricle can be modified by multiple factors, including the electrophysiological property of myocytes, anisotropic conduction properties of tissue, and gross

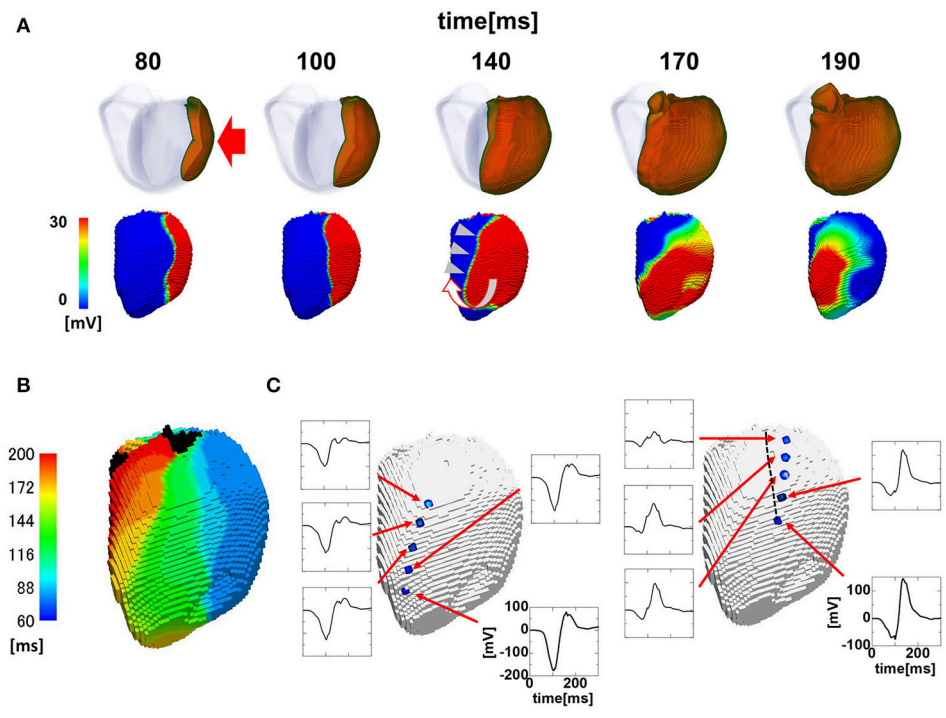

FIGURE 4 | Propagation of excitation in the paced heart with a wide QRS width. **(A)** Time-lapse images of the activation in the ventricular wall (upper row) and the corresponding non-contact endocardial map (lower row). Numbers at the top indicate the time after the activation starts. Red arrow: pacing site; white U-shaped arrow: activation sequence; color bar: membrane potential. **(B)** Isochronal map. **(C)** Local unipolar ECG near the line of block. The location of the line of block under the intrinsic rhythm (**Figure 3**) is shown by the black broken line.

morphology of the ventricle. Our multi-scale heart simulator reproduces these properties, some of which can be personalized. To exclude the possibility that these confounding factors may contribute to the genesis of the line of block, we switched the mode of conduction between the two models shown in **Figures 2**, **3**, and then repeated the simulations. When the rapid conduction through the endocardial Purkinje network was prevented in the model in **Figure 2** by omitting the network, the QRS width increased from 176 to 238 ms, and the line of block appeared in the anterior region of the endocardial surface. The activation wave front stopped at this line and turned around to show a U-shaped pattern of activation sequence (**Figures 5A,B**) (see also Supplemental Movie S4). By contrast, introduction of rapid conduction through the Purkinje network eliminated the line of block (**Figures 5C,D**) from the model in **Figure 3** (see also Supplemental Movie S5). These data suggest that the absence of rapid conduction through the Purkinje network is the predominant cause of the functional line of block observed in endocardial non-contact mapping.

DISCUSSION

Functional Characteristics of Line of Block

As unipolar non-contact mapping system can measure the global pattern of the left ventricular activation process, it has been previously used to assess the pathophysiology of heart failure patients with electromechanical abnormalities (Auricchio et al., 2004; Fung et al., 2004, 2007; Lambiase et al., 2004). For example, Fung et al. reported two patterns of activation sequence (type I and II) in heart failure patients with left bundle branch block by non-contact mapping, and patients with the type II pattern exhibiting conduction block had a more favorable response to CRT (Fung et al., 2004, 2007). The nature of conduction block was further investigated by Auricchio et al., with simultaneous application of contact and non-contact mappings (Auricchio et al., 2004). In that study, 23 out of 24 patients exhibited a U-shaped activation wave front turning around the line of block. Interestingly, however, the activation wave front proceeded smoothly by crossing the line of block in the simultaneous contact mapping. Based on the facts that (1) ventricular pacing from the coronary sinus or right ventricular apex shifted the line of block, (2) ischemic myocardial scarring was absent in two thirds of the studied patients, and (3) the amplitude of the local ECG was normal in the region surrounding the line of block, the authors concluded that the line of block identified by unipolar non-contact mapping was functional, and did not originate from the fixed scar tissue. As signals from unipolar non-contact mapping retain electrical information across the whole transmural thickness, in contrast to the bipolar contact mapping representing local electrical events, it was hypothesized that the functional line of block was caused by anisotropic conduction resulting from variation in alignment between the myocardial

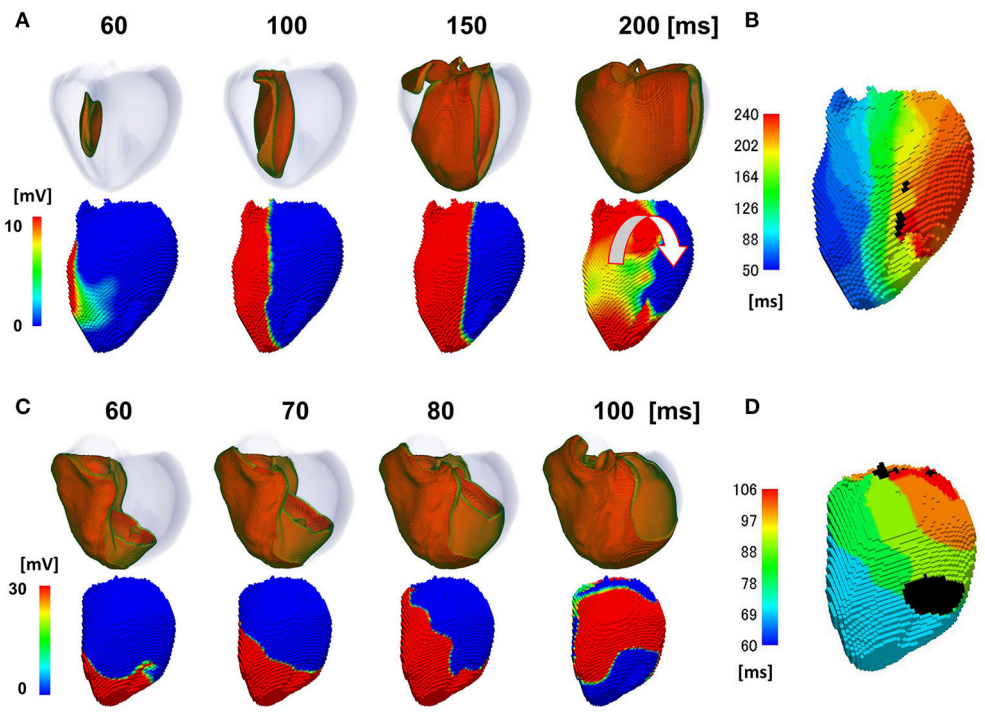

FIGURE 5 | Effects of switching the mode of conduction. In the model shown in **(A,B)**, rapid propagation through the Purkinje network was eliminated from the model in **Figure 2**. **(A)** Excitation of propagation in the wall (upper row) and non-contact mapping (lower row). White U-shaped arrow: activation pattern. **(B)** Isochronal map. In the model shown in **C,D**, rapid propagation through the Purkinje network was introduced to the model in **Figure 3**. **(C)** Excitation of propagation in the wall (upper row) and non-contact mapping (lower row). **(D)** Isochronal map. Color-code in the non-contact maps **(A,C)** indicates membrane potential, while color-code in the isochronal maps **(B,D)** indicates the time after the activation starts (black: root of papillary muscle).

layer in the ventricular wall. However, there are no prior studies that have confirmed the origin of the functional line of block.

Line of Block by the Simulation of Non-contact Mapping

We previously developed a multi-scale heart simulator in which the function and structure of the heart are reproduced at the microscopic to macroscopic levels (Sugiura et al., 2012; Washio et al., 2013). Using this technology, we also created tailor-made models of the failing heart with conduction block, with successful prediction of the responses to CRT (Okada et al., 2013, 2017; Panthee et al., 2016). Using the tailor-made failing heart models, in the present study we simulated non-contact mapping and found that the slow and homogeneous propagation of activation in the ventricular wall can cause the characteristic U-shaped activation wave front with a line of block. The presence of fragmented local ECG in the region of slow conduction, the shift of the line of block by pacing, and the disappearance of the line of block by the introduction of rapid propagation via the Purkinje network provide further support that our model reproduces the clinical observations. Overall, these findings support our hypothesis that the absence of rapid propagation via the conduction system is the major cause of the line of block in heart failure patients with conduction block.

Potential Mechanisms of Line of Block

What then, is the underlying mechanisms of the line of block only observed by non-contact mapping, and why does it appears in a specific position? As shown in **Figure 6A**, activated muscle tissue creates a field potential in the extra-cellular space centered around the activation wave front, which is measured by the non-contact electrodes. The field potential is symmetrical to the plane of the activation front (purple line), and if the electrode is placed near the plane of activation front, the electrode cannot sense the potential signal, despite its close proximity to the muscle tissue (red dot). In the real ventricle, the extracellular field potential varies in a complex manner depending on the tissue geometry and the activation sequence (**Figure 6B**). If the excitation propagates rapidly through the Purkinje network, the activation wave front always faces toward the epicardial surface (**Figure 7A**, top row), and the extracellular potential field efficiently covers the cavity throughout the ventricular activation (**Figure 7A**, bottom row). In this case, the basket electrode for non-contact mapping (dotted circle in the cavity) records the stable signal continuously, and this accurately reports the activation sequence. The activation sequence without rapid propagation through the Purkinje network under intrinsic rhythm is shown in **Figure 7B**. In this case, the activation wave front proceeds circumferentially in the wall (**Figure 7B**, top row), and the basket electrode cannot sense the potential field (**Figure 7B**, bottom row, dotted blue circle) during the ventricular activation. Under such conditions, the endocardial activation signal using non-contact mapping stalls, as the solution of the inverse problem cannot be obtained.

When the same heart was paced from the LV free wall, apparently symmetrical patterns were observed in both the activation sequence and extracellular field potential (**Figure 7C**). However, the timing and location of the line of block are different

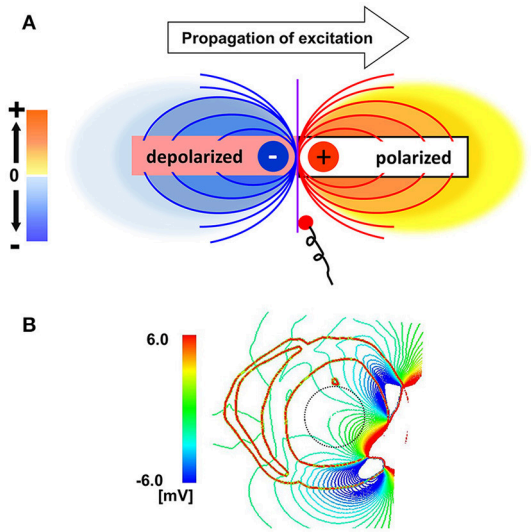

FIGURE 6 | Mechanisms of the functional line of block. **(A)** Extracellular field potential generated by the activated cardiac tissue. Purple line indicates the plane of the activation front. **(B)** Extracellular field potential in a realistic ventricular morphology.

(blue rectangle), because of the deviation of ventricular geometry from a perfect circle. The heterogeneity of the propagation velocity in the ventricular wall, reflecting the variation in fiber orientation, is also a determinant of the location of the line of block. By contrast, in the apical portion of the ventricle with a small radius, the extracellular potential covers the cavity, even under conditions in **Figures 7B,C**. Accordingly, endocardial activation using non-contact mapping proceeds smoothly, and shows a U-shaped pattern of activation sequence.

Clinical Implications

If our proposed mechanism is correct, the line of block may be simply an artifact. Nevertheless, the line of block provides an indication of slow conduction occurring outside of the endocardial Purkinje network, consistent with a prior clinical report (Fung et al., 2007), thus providing an indication of favorable response to CRT. Further, the line of block provides evidence for heterogeneous conduction within the ventricular wall.

LIMITATIONS

Although the heart models used in this study were based on clinical data, endocardial mapping was not performed in any of the patients. Thus, direct comparisons with endocardial mapping data should be performed in future studies to confirm our findings. The Purkinje network was modeled as an endocardial layer with a rapid propagation velocity and the distributions of the earliest activation sites, instead of explicitly modeling it. Although the good agreement with clinical ECG data confirmed in our previous study may rationalize this approach (Okada et al., 2013, 2017), future studies using more detailed models with the Purkinje network may provide further insight into

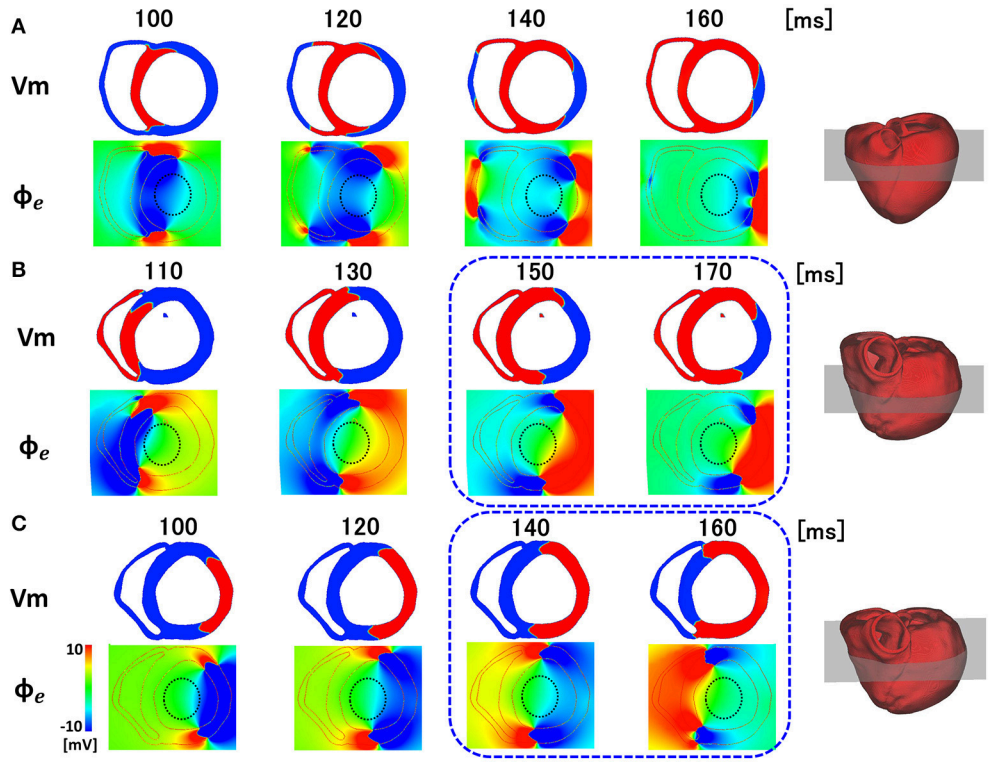

FIGURE 7 | Membrane potential (V_m) and extracellular potential field ($\varnothing_e$) in the various patterns of activation sequences. **(A)** Rapid propagation through the Purkinje network. **(B)** Slow propagation without the Purkinje network under the intrinsic rhythm. **(C)** Slow propagation without the Purkinje network under pacing rhythm.

the mechanism of the line of block in diseased hearts with conduction block.

AUTHOR CONTRIBUTIONS

JO, TH, and SS designed the study analyzed data and wrote the paper. JO and TW wrote the programs. MN, MW, and YK performed data processing. TK, HY, YY, SM, and RN collected data and were involved in study design.

FUNDING

This work was supported in part by MEXT (hp170233) as a social and scientific priority issue (Integrated computational life science to support personalized and preventive medicine) to be examined using post-K computers.

ACKNOWLEDGMENTS

We thank Edanz Group (www.edanzediting.com/ac) for editing a draft of this manuscript.

SUPPLEMENTARY MATERIAL

The Supplementary Material for this article can be found online at: https://www.frontiersin.org/articles/10.3389/fphys.2018.00056/full#supplementary-material

REFERENCES

Auricchio, A., Fantoni, C., Regoli, F., Carbucicchio, C., Goette, A., Geller, C., et al. (2004). Characterization of left ventricular activation in patients with heart failure and left bundle-branch block. *Circulation* 109, 1133–1139. doi: 10.1161/01.CIR.0000118502.91105.F6

Auricchio, A., Stellbrink, C., Butter, C., Sack, S., Vogt, J., Misier, A. R., et al. (2003). Clinical efficacy of cardiac resynchronization therapy using left ventricular pacing in heart failure patients stratified by severity of ventricular conduction delay. *J. Am. Coll. Cardiol.* 42, 2109–2116. doi: 10.1016/j.jacc.2003.04.003

Bax, J. J., Abraham, T., Barold, S. S., Breithardt, O. A., Fung, J. W. H., Garrigue, S., et al. (2005a). Cardiac resynchronization therapy: part 2—issues during and after device implantation and unresolved questions. *J. Am. Coll. Cardiol.* 46, 2168–2182. doi: 10.1016/j.jacc.2005.09.020

Bax, J. J., Abraham, T., Barold, S. S., Breithardt, O. A., Fung, J. W. H., Gorcsan, J. III, et al. (2005b). Cardiac resynchronization therapy: part 1—Issues before device implantation. *J. Am. Coll. Cardiol.* 46, 2153–2167. doi: 10.1016/j.jacc.2005.09.019

Brignole, M., Auricchio, A., Baron-Esquivias, G., Bordachar, P., Boriani, G., Breithardt, O., et al. (2013). 2013 ESC Guidelines on cardiac pacing and cardiac resynchronization therapy the task force on cardiac pacing and

resynchronization therapy of the European society of cardiology (ESC). developed in collaboration with the European heart rhythm association (EHRA). *Europace* 15, 1070–1118. doi: 10.1093/europace/eut206

Camacho, M. A., Lehr, J. L., and Eisenberg, S. R. (1995). A three-dimensional finite element 40 model of human transthoracic defibrillation: paddle placement and size. *IEEE Trans. Biomed. Eng.* 42, 572–578. doi: 10.1109/10.387196

De Ambroggi, L., Taccardi, B., and Macchi, E. (1976). Body-surface maps of heart potentials: tentative localization of pre-excited areas in forty-two Wolff-Parkinson-white patients. *Circulation* 54, 251–263. doi: 10.1161/01.CIR.54.2.251

Duckett, S. G., Camara, O., Ginks, M. R., Bostock, J., Chinchapatnam, P., Sermesant, M., et al. (2012). Relationship between endocardial activation sequences defined by high-density mapping to early septal contraction (septal flash) in patients with left bundle branch block undergoing cardiac resynchronization therapy. *Europace* 14, 99–106. doi: 10.1093/europace/eur235

Durrer, D., van Dam, R. T., Freud, G. E., Janse, M. J., Meijler, F. L., and Arzbaecher, R. C. (1970). Total excitation of the isolated human heart. *Circulation* 41, 899–912. doi: 10.1161/01.CIR.41.6.899

Fung, J. W. H., Chan, J. Y. S., Yip, G. W. K., Chan, H. C. K., Chan, W. W. L., Zhang, Q., et al. (2007). Effect of left ventricular endocardial activation pattern on echocardiographic and clinical response to cardiac resynchronization therapy. *Heart* 93, 432–437. doi: 10.1136/hrt.2007.115295

Fung, J. W.-H., Yu, C.-M., Yip, G., Zhang, Y., Chan, H., Kum, C.-C., et al. (2004). Variable left ventricular activation pattern in patients with heart failure and left bundle branch block. *Heart* 90, 17–19. doi: 10.1136/heart.90.1.17

Gornick, C. C., Adler, S. W., Pederson, B., Hauck, J., Budd, J., and Schweitzer, J. (1999). Validation of a new noncontact catheter system for electroanatomic mapping of left ventricular endocardium. *Circulation* 99, 829–835. doi: 10.1161/01.CIR.99.6.829

Hisada, T., Kurokawa, H., Oshida, M., Yamamoto, T., Washio, T., Okada, J., et al. (2013). *Modeling Device, Program, Computer-Readable Recording Medium, and Method of Establishing Correspondence*. USA patent application.

Keldermann, R. H., ten Tusscher, K. H. W. J., Nash, M. P., Bradley, C. P., Hren, R., Taggart, P., et al. (2009). A computational study of mother rotor VF in the human ventricles. *Am. J. Physiol.* 296, H370–H379. doi: 10.1152/ajpheart.00952.2008

Kirk, J. A., and Kass, D. A. (2013). Electromechanical dyssynchrony and resynchronization of the failing heart. *Circ. Res.* 113, 765–776. doi: 10.1161/CIRCRESAHA.113.300270

Lambiase, P. D., Rinaldi, A., Hauck, J., Mobb, M., Elliott, D., Mohammad, S., et al. (2004). Non-contact left ventricular endocardial mapping in cardiac resynchronisation therapy. *Heart* 90, 44–51. doi: 10.1136/heart.90.1.44

Noble, D. (2002). Modelling the heart: from genes to cells to the whole organ. *Science* 295, 1678–1682. doi: 10.1126/science.1069881

Okada, J., Sasaki, T., Washio, T., Yamashita, H., Kariya, T., Imai, Y., et al. (2013). Patient specific simulation of body surface ECG using the finite element method. *Pacing Clin. Electrophysiol.* 36, 309–321. doi: 10.1111/pace.12057

Okada, J., Washio, T., Maehara, A., Momomura, S., Sugiura, S., and Hisada, T. (2011). Transmural and apicobasal gradients in repolarization contribute to T-wave genesis in human surface ECG. *Am. J. Physiol.* 301, H200–H208. doi: 10.1152/ajpheart.01241.2010

Okada, J., Washio, T., Nakagawa, M., Watanabe, M., Kadooka, Y., Kariya, T., et al. (2017). Multi-scale, tailor-made heart simulation can predict the effect of cardiac resynchronization therapy. *J. Mol. Cell. Cardiol.* 108, 17–23. doi: 10.1016/j.yjmcc.2017.05.006

Okada, J., Yoshinaga, T., Kurokawa, J., Washio, T., Furukawa, T., Sawada, K., et al. (2015). Screening system for drug-induced arrhythmogenic risk combining a patch clamp and heart simulator. *Sci. Adv.* 1:e1400142. doi: 10.1126/sciadv.1400142

Panescu, D., Webster, J. G., Tompkins, W. J., and Stratbucker, R. A. (1995). Optimization of cardiac defibrillation by three-dimensional finite element modeling of the human thorax. *IEEE Trans. Biomed. Eng.* 42, 185–192. doi: 10.1109/10.341831

Panthee, N., Okada, J., Washio, T., Mochizuki, Y., Suzuki, R., Koyama, H., et al. (2016). Tailor-made heart simulation predicts the effect of cardiac resynchronization therapy in a canine model of heart failure. *Med. Image Anal.* 31, 46–62. doi: 10.1016/j.media.2016.02.003

Prinzen, F. W., Vernooy, K., and Auricchio, A. (2013). Cardiac resynchronization therapy state-of-the-art of current applications, guidelines, ongoing trials, and areas of controversy. *Circulation* 128, 2407–2418. doi: 10.1161/CIRCULATIONAHA.112.000112

Sugiura, S., Washio, T., Hatano, A., Okada, J.-I., Watanabe, H., and Hisada, T. (2012). Multi-scale simulations of cardiac electrophysiology and mechanics using the University of Tokyo heart simulator. *Prog. Biophys. Mol. Biol.* 110, 380–389. doi: 10.1016/j.pbiomolbio.2012.07.001

Taccardi, B. (1963). Distribution of heart potentials on the thoracic surface of normal human subjects. *Circ. Res.* 12, 341–352. doi: 10.1161/01.RES.12.4.341

Ten Tusscher, K. H. W. J., Noble, D., Noble, P. J., and Panfilov, A. V. (2004). A model for human ventricular tissue. *Am. J. Physiol.* 286, H1573–H1589. doi: 10.1152/ajpheart.00794.2003

Wang, D., Kirby, R. M., MacLeod, R. S., and Johnsona, C. R. (2013). Inverse electrocardiographic source localization of ischemia: an optimization framework and finite element solution. *J. Comput. Phys.* 250, 403–424. doi: 10.1016/j.jcp.2013.05.027

Washio, T., Okada, J., and Hisada, T. (2010). A parallel multilevel technique for solving the bidomain equation on a human heart with Purkinje fibers and a torso model. *SIAM Rev.* 52, 717–743. doi: 10.1137/100798429

Washio, T., Okada, J., Takahashi, A., Yoneda, K., Kadooka, Y., Sugiura, S., et al. (2013). Multiscale heart simulation with cooperative stochastic cross-bridge dynamics and cellular structures. *SIAM J. Multiscale Model. Simul.* 11, 965–999. doi: 10.1137/120892866

Watanabe, H., Sugiura, S., Kafuku, H., and Hisada, T. (2004). Multiphysics simulation of left ventricular filling dynamics using fluid-structure interaction finite element method. *Biophys. J.* 87, 2074–2085. doi: 10.1529/biophysj.103.035840

Winslow, R. L., Trayanova, N., Geman, D., and Miller, M. I. (2012). Computational medicine: translating models to clinical care. *Sci. Transl. Med.* 4, 158rv111–158rv111. doi: 10.1126/scitranslmed.3003528

Yu, C.-M., and Hayes, D. L. (2013). Cardiac resynchronization therapy: state of the art 2013. *Eur. Heart J.* 34, 1396–1403. doi: 10.1093/eurheartj/ehs454

Conflict of Interest Statement: JO, TW, TH, and SS have received grant support from Fujitsu Ltd. MW, YK, and MN was employed by company Fujitsu Ltd. The other authors declare that the research was conducted in the absence of any commercial or financial relationships that could be construed as a potential conflict of interest.

Copyright © 2018 Okada, Washio, Nakagawa, Watanabe, Kadooka, Kariya, Yamashita, Yamada, Momomura, Nagai, Hisada and Sugiura. This is an open-access article distributed under the terms of the Creative Commons Attribution License (CC BY). The use, distribution or reproduction in other forums is permitted, provided the original author(s) and the copyright owner are credited and that the original publication in this journal is cited, in accordance with accepted academic practice. No use, distribution or reproduction is permitted which does not comply with these terms.

frontiers in Physiology

ORIGINAL RESEARCH
published: 17 May 2018
doi: 10.3389/fphys.2018.00511

Computational Assessment of Blood Flow Heterogeneity in Peritoneal Dialysis Patients' Cardiac Ventricles

Sanjay R. Kharche[1,2], Aaron So[2,3], Fabio Salerno[1], Ting-Yim Lee[3], Chris Ellis[2], Daniel Goldman[2] and Christopher W. McIntyre[1,2]**

[1] Kidney Clinical Research Unit, Lawson's Health Research Institute, Victoria Hospital, London, ON, Canada, [2] Department of Medical Biophysics, Schulich School of Medicine and Dentistry, University of Western Ontario, London, ON, Canada, [3] Robarts Research Institute, University of Western Ontario, London, ON, Canada

Dialysis prolongs life but augments cardiovascular mortality. Imaging data suggests that dialysis increases myocardial blood flow (BF) heterogeneity, but its causes remain poorly understood. A biophysical model of human coronary vasculature was used to explain the imaging observations, and highlight causes of coronary BF heterogeneity. Post-dialysis CT images from patients under control, pharmacological stress (adenosine), therapy (cooled dialysate), and adenosine and cooled dialysate conditions were obtained. The data presented disparate phenotypes. To dissect vascular mechanisms, a 3D human vasculature model based on known experimental coronary morphometry and a space filling algorithm was implemented. Steady state simulations were performed to investigate the effects of altered aortic pressure and blood vessel diameters on myocardial BF heterogeneity. Imaging showed that stress and therapy potentially increased mean and total BF, while reducing heterogeneity. BF histograms of one patient showed multi-modality. Using the model, it was found that total coronary BF increased as coronary perfusion pressure was increased. BF heterogeneity was differentially affected by large or small vessel blocking. BF heterogeneity was found to be inversely related to small blood vessel diameters. Simulation of large artery stenosis indicates that BF became heterogeneous (increase relative dispersion) and gave multi-modal histograms. The total transmural BF as well as transmural BF heterogeneity reduced due to large artery stenosis, generating large patches of very low BF regions downstream. Blocking of arteries at various orders showed that blocking larger arteries results in multi-modal BF histograms and large patches of low BF, whereas smaller artery blocking results in augmented relative dispersion and fractal dimension. Transmural heterogeneity was also affected. Finally, the effects of augmented aortic pressure in the presence of blood vessel blocking shows differential effects on BF heterogeneity as well as transmural BF. Improved aortic blood pressure may improve total BF. Stress and therapy may be effective if they dilate small vessels. A potential cause for the observed complex BF distributions (multi-modal BF histograms) may indicate existing large vessel stenosis. The intuitive BF heterogeneity methods used can be readily used in clinical studies. Further development of the model and methods will permit personalized assessment of patient BF status.

Keywords: coronary vessels, cardiac physiology, mathematical modeling, computational physiology, integrative physiology

OPEN ACCESS

Edited by:
Eun Bo Shim,
Kangwon National University,
South Korea

Reviewed by:
Soroush Safaei,
University of Auckland, New Zealand
Ki Moo Lim,
Kumoh National Institute of Technology, South Korea

****Correspondence:***
Sanjay R. Kharche
sanjay.kharche@lhsc.on.ca
Christopher W. McIntyre
c.w.mcintyre@lhsc.on.ca

Specialty section:
This article was submitted to Computational Physiology and Medicine, a section of the journal Frontiers in Physiology

Received: *13 January 2018*
Accepted: *20 April 2018*
Published: *17 May 2018*

Citation:
Kharche SR, So A, Salerno F, Lee T-Y, Ellis C, Goldman D and McIntyre CW (2018) Computational Assessment of Blood Flow Heterogeneity in Peritoneal Dialysis Patients' Cardiac Ventricles. Front. Physiol. 9:511. doi: 10.3389/fphys.2018.00511

INTRODUCTION

Dialysis is a life prolonging treatment but significantly reduces quality of life due to its deleterious side effects on the heart. This mathematical modeling study explores some of the coronary vasculature based causes of myocardial blood flow (BF) heterogeneity.

Clinical Motivation

The over 20% mortality among end stage renal disease (ESRD) patients receiving dialysis treatment is often due to cardiovascular complications (Collins et al., 2015). Dialysis is a repetitive sub-lethal ischemia that is known to produce cardiac contractile dysfunction as observed clinically (Burton et al., 2009; McIntyre, 2010; Jefferies et al., 2011; Breidthardt et al., 2012). ESRD patients also experience significantly reduced coronary blood flow (BF) (Dasselaar et al., 2009). The reduced BF may often occur due to calcification (McIntyre et al., 2013; McIntyre and Odudu, 2014) that reduces arterial diameters. Experimental observations have led to the belief that an increased resistance of blood vessels in the sub-endocardium promotes increased transmural BF heterogeneity (Algranati et al., 2011). Although non-invasive interventions may not affect existing large vessel structural defects such as stenosis, it is thought that adenosine stress and dialysate cooling therapy may improve myocardial BF by vasodilation of the smaller blood vessels. The interventions may also improve myocardial BF by improving aortic pressure. The mechanisms by which BF heterogeneity is affected remain unclear. Knowledge of the cause-effect relationships may permit design of future clinical trials and augment the precision of medications given to this critically ill group of patients.

Previous Coronary Vasculature Theoretical Models, Extant Experimental Data

The predominantly dichotomous mammalian coronary architecture is complex with millions of arterial segments (Kassab et al., 1993, 1997a). The larger left and right coronary arteries (∼3 mm diameters, 80 mm lengths) forming aortic ostia give rise to arterial trees, which together constitute the arterial vasculature. A very large number of pre-capillary arterioles deliver blood to capillary beds (∼0.06 mm diameters, 0.15 mm lengths). A spectrum of biophysical and anatomical properties of vasculature has been studied to permit patho-physiological investigations. The topology of coronary arterial trees has been quantified by Kassab et al. (1993, 1997a,b) using silicon elastometer casts. In the absence of biophysical morphometry data, theoretical vasculature topologies can also be generated (Keelan et al., 2016). The topology data obtained from large animal hearts can be scaled to the human heart using clinical angiograms (Dodge et al., 1992). To permit generating a 3D geometry from the topology, the bifurcation properties of the network have been quantified. In accordance with Murray's law (Murray, 1926a,b), the relationship between artery segment lengths, diameters, and bifurcation angles and planes has been described by Zamir and Phipps (1988) and Zamir et al. (1983). Using the topology and Murray's law, algorithms that distributed the topology as uniformly as possible in 3D space were developed. The deterministic algorithm, which may overall be called "space filling algorithm," is based on the principles of self-avoidance and boundary avoidance and was developed by Beard and Bassingthwaighte (2000). Several studies further developed the space filling algorithm which optimizes vascular spatial distribution as well as delivery of BF to various parts of the heart (notably in Smith et al., 2000; Mittal et al., 2005; Kaimovitz et al., 2010), and have either generated the complete or partial epicardial vasculature networks. Whereas vascular resistance is regulated by geometry alone, the BF and pressure at each location in the network also depends on the properties of fluid flowing through the network. Blood is a biphasic fluid and alterations of its viscosity, dependent on haematocrit, have been quantified by Pries et al. (1996).The intricate problem of vasculature involves optimizing relative arterial diameters, bifurcation angles, providing of BF to potentially empty regions, and being as widely distributed in the myocardium as possible. In the absence of experimental data it may be possible to generate virtual vasculatures based on biophysical principles and computational optimization of cost functions (Karch et al., 1999; Kaimovitz et al., 2005; Keelan et al., 2016). The scientific problems arising in vasculature modeling based on available knowledge have been addressed in individual theoretical studies with particular aims. Alarcon et al. provide a design principle in light of complex blood rheology (Alarcón et al., 2005).

The effects of structural defects on hemodynamic distribution have been studied by Yang and Wang (2013). The availability of mathematical-computational tools such as the 3D coronary vasculature models has encouraged the investigation of specific disease conditions in the heart (Zhang et al., 2014). Similar to the present study, a detailed model by Fung et al. (2010, 2011) has been developed to assist in evaluation of imaging hearts with perfusion defects. An extension of previous and presented models will incorporate the multi-scale nature of delivery of oxygen (Goldman et al., 2017; Mason McClatchey et al., 2017) to myocardial tissue. Although several studies have characterized the properties of the coronary vasculature, the use of this vast basic science knowledge for clinical purposes remains acutely limited.

In this study, we endeavored to exploit organ level vasculature modeling to investigate potential causes for our clinical myocardial BF heterogeneity observations. This study developed our biophysically informed topology-geometry of the human coronary vasculature.

METHODS

Clinical Imaging

It is thought that peritoneal dialysis increases coronary BF heterogeneity in patients. CT imaging was performed to test whether adenosine, cooled dialysate, and adenosine combined with cooled dialysate can enhance myocardial BF, and reduce BF heterogeneity.

Patient Recruitment

Three chronic end stage renal failure patients, aged between 58-63 years, were recruited from the London Health Sciences

Centre Peritoneal Dialysis Program (London Ontario, Canada). Each patient had been on peritoneal dialysis for a minimum of 3 months prior to recruitment. All patients were informed regarding the study, after which written consents were obtained in accordance with the hospital and university procedures. All participants provided informed and written consent. The study protocol was approved by the research ethics board at Western University (London, Ontario, Canada).

Imaging Study Protocol

Briefly, each patient was scanned four times in two study visits. During the first visit, a glucose based peritoneal dialysate, according to their prescription, was administered at a physiological temperature of 37°C, after which they were scanned with and without adenosine stress. During the second visit, patients were administered the peritoneal dialysis dose but with a cooled dialysate (32.5°C), after which they were scanned with and without adenosine stress.

To assist the dynamic CT scanning, a contrast enhancing agent, lopamidol, was administered. The heart rate was reduced using a β-blocker, metoprolol, that permitted a longer diastolic phase in the left ventricle. The details of the imaging protocol and image processing that computed the BF maps are given in Section S1.

Patient Blood Pressure

The diastolic blood pressures values ranged between diastolic 71 and 85 mmHg, and systolic values between 130 and 210 mmHg. Other clinical laboratory measurements were not considered in this study.

3D Heart Segmentation

The 2D registered BF map slices were segmented by a physician semi-automatically using Fiji/ImageJ (Schindelin et al., 2012). Each slice was first segmented to remove non-myocardial tissue signals. Subsequently, the image was thresholded to between 0 and 600 ml/mg/min to selectively remove residual signals pertaining to intracardiac (left and right ventricle chambers) blood, while preserving signals providing coronary BF distribution. The slices were stacked to reconstruct each patients BF maps under each of the four clinical conditions (see section Imaging study protocol). The reconstruction was stored in a structured array of 0.5 (X) × 0.5 (Y) × 5 (Z) mm^3 array. The structured array representation was used to quantify BF heterogeneity (see below).

Model Construction

Human Ventricle Anatomy to Contain Vasculature Geometry

A representation of the human ventricles was constructed to permit generation of vascular geometry within it. An idealized representation bound by truncated ellipsoids was constructed (Göktepe and Kuhl, 2010). The dimensions of the anatomy are detailed in Section S2 and Figure S1. The coronary vasculature geometry was generated within the ventricular anatomy.

Topology of Coronary Vasculature Based on Morphometry Biophysical Data

The porcine coronary vasculature morphometry (Kassab et al., 1993) was used to construct arterial tree topology. The stochastic morphometry data consists of arterial segment connectivity matrices, segment lengths, and segment radii. In this study, two coronary arterial topologies were constructed as binary trees, one each for the right and left coronary arteries. The segments, defined as parts of arteries between two consecutive bifurcation nodes, in the trees were numbered according to the Strahler number (SN) ordering (Strahler, 1957). Within this numbering system the largest arteries are a series of segments of the same SN, namely the left anterior descending (LAD) and the right coronary artery (RCA), have a SN of 11. The left circumflex artery (LCX) which has a SN of 10 emerges at a bifurcation of the LAD, and provides BF to a sub-tree in the left ventricle. Whereas the larger vessels (SN 9–SN 11) are restricted to the epicardial surface, smaller vessels (SN 6–SN 8) provide BF transmurally (Kaimovitz et al., 2005). As a computationally manageable approximation that permitted simulation of whole heart BF, the arterial trees were generated for SN 6–SN 11, where SN 6 was identified based on its diameter and the number of bifurcations that would be needed to reach the capillary level (SN 0). First, arterial elements, defined as a series of connected segments of the same SN, were generated stochastically using the segment to element ratios in the morphometry data (Section S3). The elements were then assembled, again stochastically, using connectivity matrices (Section S3; Kassab et al., 1993) to stochastically generate multiple instances of the whole heart's coronary arterial binary tree topologies. Each element was assigned a constant radius along its length adapted from the experimental data of Kassab et al. (1993) and scaled to human using clinical data (Dodge et al., 1992) in accordance with previous modeling studies (Beard and Bassingthwaighte, 2000; Smith et al., 2000). Finally, the segments were assigned lengths stochastically (Section S3; Kassab et al., 1993). The total tree lengths were bounded to avoid non-physiologically short or long trees (Kaimovitz et al., 2005). The total tree length of RCA was limited to between 120 and 192 mm, and those of LAD and LCX were both limited to between 100 and 160 mm.

Using the segment lengths (L) and radius (r) information assigned during topology generation, and using a blood viscosity value of $\mu = 3.6 \times 10^{-3}$ Pa (Keelan et al., 2016), a value of resistance to flow (R) in each segment was assigned using the relationship:

$$R = \frac{8\mu L}{\pi r^4} \tag{1}$$

The downstream resistance at any bifurcation node was then computed recursively. Elements that include segments of SN 8–SN 11 constitute epicardial vessels (Kassab et al., 1993; Smith et al., 2000; Kaimovitz et al., 2005).

To permit generation of arterial geometry, pressure boundary conditions were imposed on the inlets and terminal nodes of the arterial tree topologies and BF in each segment and pressure at each internal node were computed recursively. At

the terminal nodes (SN 6), the pressure was set at 20 mmHg. At the inlets, the pressure was set at 100 mmHg under control conditions, and varied to simulate disease, stress, or therapy. The boundary conditions, conservation of flow at bifurcation nodes, and Poiseuille's law for steady state flow, ΔP (pressure) = R (resistance) × Q (BF) in each segment and in whole trees, permitted calculation of pressure at each bifurcation node, and BF through each segment of the arterial trees.

Generation of Arterial Tree Geometry

Each instance of the arterial tree topology was used to generate a corresponding coronary arterial geometry. The geometry structure was generated using a modification of the method developed by Fung et al. (2011). The method for assigning coordinates to distal nodes of daughter segments is illustrated in **Figure 1** which is inspired by Fung et al. (2011).

Placement of RCA, LAD, and LCX elements

The roots of the RCA and LAD arterial trees were placed approximately at their aortic ostia locations (Smith et al., 2000; Kaimovitz et al., 2005; Keelan et al., 2016). The largest arteries were placed either along the right or left epicardial surfaces (RCA and LCX respectively), or traversing from the base (AV border) to the apex (LAD). Doing so provided a starting point for the self-avoidance and boundary-avoidance algorithms as described by Beard and Bassingthwaighte (2000).

Initial daughter segment branching angles

The branching of a parent segment into two daughter segments is known to optimally minimize shear. As shown by Hacking et al. (1996) and Zamir (1976a,b), the initial left and right branching angles, $\theta_L$andθ_R respectively (see **Figure 1A**), were computed using the parent (denoted by subscript "p"), left (denoted by subscript "L"), and right (denoted by subscript "R") radii (r) and BFs (Q) as:

$$\theta_L = \cos^{-1}\left[\frac{Q_p{}^2/r_p{}^4 + Q_R{}^2/r_R{}^4 - Q_L{}^2/r_L{}^4}{2Q_pQ_L/r_p{}^2r_L{}^2}\right]$$
$$\theta_R = \cos^{-1}\left[\frac{Q_p{}^2/r_p{}^4 + Q_L{}^2/r_L{}^4 - Q_R{}^2/r_R{}^4}{2Q_pQ_R/r_p{}^2r_R{}^2}\right] \quad (2)$$

In conjunction with the combined branching vector (see below), these branching angles were used to assign initial locations of daughter segment distal nodes. The combined branching vector is a linear combination of the vascular supply and the boundary avoidance vectors.

Self-avoidance vector

To permit the child nodes to occupy a location within the tissue that was so far sub-optimally supplied with BF, a self-avoidance vector, $\vec{v}$, was computed as shown in **Figure 1B**. It was computed using Equation (3) as:

$$\vec{v}_s = \sum_i \frac{(L_s/d_i)^\xi}{1+(L_s/d_i)^\xi}\frac{\vec{s}_i}{d_i} \quad (3)$$

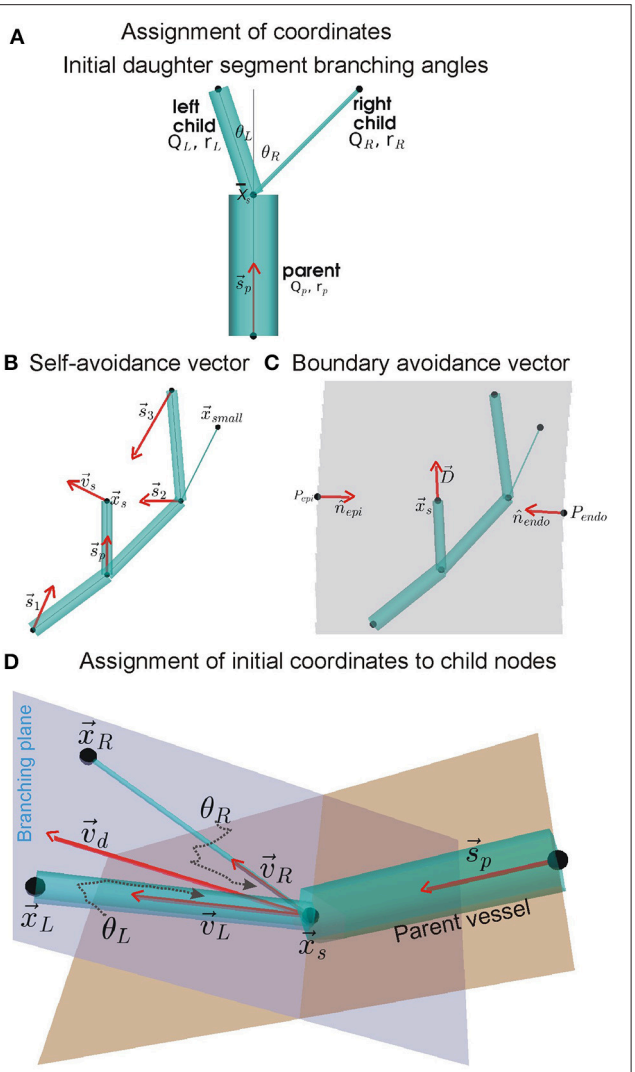

FIGURE 1 | Assignment of coordinates to distal nodes of daughter (or child) segments. **(A)** Initial branching angles between the left and right daughter segments, θ_L and θ_R, we computed using BF and radius (r) values of the parent and daughter segments (see Equation 1). The angles are subtended between centrelines (gray lines) of the parent segment and the daughter segments, all of which meet at $\vec{x}_S$ the upstream position of the current generating segment. **(B)** Simplified instance of the dependence of self-avoidance vector, $\vec{v}_S$, on supply vectors ($\vec{s}_i$) from distal nodes of larger segments. In the example network shown, the node $\vec{x}_{small}$ does not contribute to $\vec{v}_S$ because it belongs to a segment that has a smaller radius than both daughter segments being assigned coordinates (daughter segments are shown in **A**). **(C)** Same example network of **(B)** showing the boundary avoidance vector, $\vec{D}$, computed using boundary unit normals (n_j). **(D)** Using vectors $\vec{s}_p$ and $\vec{v}_d$ ($\vec{v}_d$ is a linear combination of $\vec{v}_S$ and $\vec{D}$), the initial coordinates of the distal nodes in the branching plane of daughter segments were computed using Equation (8).

where $\vec{s}_i = \vec{x}_c - \vec{x}_i$, $\vec{x}_i$ is upstream position of all segments of same or higher order with coordinates, $\vec{x}_c$ is the upstream position of the current generating segment; $d_i = |\vec{s}_i|$ is the magnitude of the vector $\vec{s}_i$, and ξ is the avoidance exponent with value 2 (Beard and Bassingthwaighte, 2000).

Boundary avoidance vector

The boundary avoidance vector permits the assignment of coordinates to child nodes such that they are contained within the predefined ventricle walls. A simple instance of the boundary avoidance vector, $\vec{D}$, is illustrated in **Figure 1C**. To compute $\vec{D}$, first the analytical equations for the unit normal vectors, $\hat{n}_j$, at each of the j ventricle walls were computed (Section S2, Equation S3). Then, the $\hat{n}_j$, distance of upstream position $\vec{x}_c$ to boundary j (d_j), and the expected length, L, of the segment being assigned to the daughter segment were used to compute $\vec{D}$ as:

$$\overrightarrow{D} = \sum_{\forall j} n_j e^{-d_j/2L} \tag{4}$$

Branching plane and assignment of initial coordinates to child nodes

The self-avoidance and boundary avoidance vectors were combined to generate a combined unit branching plane vector (**Figure 1D**; Fung et al., 2011; Yang and Wang, 2013; Tamaddon et al., 2016):

$$\vec{v}_d = c_s \frac{\vec{v}_s}{|\vec{v}_s|} + c_b \frac{\vec{D}}{|\vec{D}|} \tag{5}$$

where $c_s = c_b = 0.5$.

Which was used to generate a unit normal vector ($\hat{n}_b$) to the potential branching plane:

$$\hat{n}_b = (\vec{s}_p \times \vec{v}_d) \times \vec{v}_d \tag{6}$$

Rotation of $\vec{v}_d$ around $\hat{n}_b$, by θ_L for left and θ_R for right daughter segments, was performed to compute their respective direction vectors, $v_L and v_R$. The rotations were implemented using the rotation matrix detailed in Section S5. The initial coordinates of the left and right child nodes, as shown in **Figure 1D**, were then assigned as follows:

$$\begin{aligned} \vec{x}_L &= \vec{x}_c + L_L \vec{v}_L \\ \vec{x}_R &= \vec{x}_c + L_R \vec{v}_R \end{aligned} \tag{7}$$

In case the initially assigned locations (Equation 7) did not lie within ventricle tissue (or at least on the boundary), they were then incrementally moved away from the violating boundary using $\vec{D}$ till $\vec{x}_L and \vec{x}_R$ fell on or within the tissue. The incremental movement of the nodes was an iterative process and was performed for 200 iterations. Sub-trees that were not assigned positions were then pruned. Upon assignment of positions to all segments and their nodes in the trees, the pressure and BF were computed again using Poiseuille's law.

Generation of ensemble

As the arterial trees constructed in this study were limited to SN orders 6–11, any single instance of the geometry was unable to permit calculation of BF heterogeneity (see below). In addition, arterial tree topologies were generated stochastically. Therefore, an ensemble of 540 instances of the human coronary vasculature (consisting of RCA, LAD, and LCX sub-trees) were constructed to allow accurate estimation of BF in simulation experiments.

Construction of BF Map in 3D, Quantification of Heterogeneity

BF map construction

The model was divided into 1 mm^3 (high resolution) or 2 mm^3 (low resolution) voxels. BF to a given voxel contained within the ventricular walls was assigned as the sum of BF received through all SN 6 terminals that had coordinates belonging to the volume of that voxel. Such a vowelized distribution of BF was computed for each instance in the ensemble. An average over the complete ensemble was performed to give a BF map. This BF map was used in computing measures for heterogeneity.

BF histograms

The ranges of BF values in the vowelized BF maps were binned, or grouped, into 600 bins for the imaging data, and 100 bins for the modeling data. The numbers of values in each bin were counted and a BF histogram was constructed. The means and standard deviations of the BF histograms were computed.

Probability distribution function of relative BF, fractal dimension

Probability distribution functions (PDFs) of relative flow were calculated to permit estimation of relative dispersion (Bassingthwaighte et al., 1989). To do so, the vowelized BF values were first normalized as

$$d_j = \sum_j \frac{a_j/m_j}{A/M} \tag{8}$$

Where a_j is the perfusion in the piece, m_j is the mass of the piece, A is total perfusion in the 3D BF map or the imaging data, and M is the total mass of the ventricles. The d_j of Equation 8 is a different quantity from the d_j of Equation (4), which is a distance. The masses of 1 voxel in the imaging data, and 1 mm^3 voxel in the modeling data were assumed to be 1. The probability density of each bin was computed to give a probability density function (PDF) over a finite interval histogram. The area under this histogram and its mean were confirmed to be unity, to ensure that this histogram represented a PDF. The standard deviation of this PDF was taken to be the relative dispersion, RD. RD was computed at two resolutions and the lower resolution was taken to be the reference resolution. Fractal dimension, D, was computed using these two values of RD using the relationship (Bassingthwaighte et al., 1989):

$$RD(m(2mm^3)) = RD(m(1mm^3)) \left(\frac{m(2mm^3)}{m(1mm^3)} \right)^{1-D} \tag{9}$$

where m is the voxel mass at resolution 1 or 2 mm^3.

Transmural BF heterogeneity

To characterize transmural BF heterogeneity, the ventricles were divided into slices of 1 mm thickness that were equidistant from

endocardial surfaces. Starting with the structured grid of the BF map, the shortest distance of each 1 mm^3 voxels mid-point from the endocardial surfaces was computed. As the surfaces are idealized truncated ellipsoids, a geometric method detailed in Section S4 was implemented to generate distance maps. Using the distances, each voxel's BF was assigned to a 1 mm thick layer. In particular, the voxels with distances between 1 and 2 mm from the endocardial surface were considered as the sub-endocardial layer.

Simulation Experiments

After characterization of the baseline, or control, behavior of the model, simulation experiments were performed. To simulate the effect of adenosine or dialysate cooling, the boundary conditions in terms of inlet pressures were varied from low (30 mmHg) to high (200 mmHg) in steps of 10 mmHg, and BF distribution calculated for each value of inlet pressure. The range of pressures (30–200 mmHg) encompassed physiological and pathological aortic pressure. Further, the extreme pressures considered (30 and 200 mmHg) permitted clear demonstration of the cause-effect relationship in the simulated BF maps. To simulate the effect of dialysis or pre-existing structural conditions, vessels were constricted (stenosis). Stenosis of vessels consisted of either blocking the largest vessels, blocking of vessels that had a particular SN, or other structural characteristics. Finally, the combined effects of altered inlet pressure and blood vessel blocking were simulated.

Numerical Methods

The topology-geometry algorithms were implemented as a serial computer program using in house developed codes in C language, and ran on national High Performance Computing Services provided by Compute Canada. Simulation experiments and data analysis were performed using a local cluster. In both cases, the large number of simulations were optimally performed using serial farming job arrays which exploited the GNU parallel LINUX/UNIX utility (Tange, 2011).

RESULTS

CT Imaging Based BF Heterogeneity in Patient Ventricles

A representative 3D myocardial BF map which was reconstructed from thoracic CT images is shown in **Figure 2**, Row 1 and BF histograms in **Figure 2**, Row 2. The BF histograms were smoothed using Bezier smoothing and normalized to their respective maximum values to highlight the shifts in peaks. In comparison to control (red lines), adenosine (cyan lines) shifted the histogram peak to higher values. Dialysate cooling (green lines) shifted the histogram's peak in an inconclusive manner. Adenosine with dialysate cooling (blue lines) shifted the peaks to higher values. In case of patients 1 and 2, the histograms are unimodal whereas in case of patient 3, all histograms are bi-modal with one major peak at a high BF value, along with a secondary peak at a low BF value. The BF histograms were converted to PDFs of relative flow (see section Methods) (**Figure 2**, row 3). The standard deviations of these PDFs provided relative dispersions (RDs) at 1 voxel resolution. A similar PDF at a 4 voxel resolution was used to compute fractal dimensions (FDs) (**Figure 2**, Row 4). In case of all patients, adenosine reduced the 1 voxel RD and FD indicating a BF heterogeneity reducing effect. FD as regards dialysate cooling was either reduced in patients 1 and 2, or increased in case of patient 3. We noted that the BF histograms and PDFs for patient 3 were bi-modal. The bi-modality of the PDFs was enhanced by application of adenosine and dialysate cooling.

Modeling Results

Control *in Silico* BF Map and Transmural Heterogeneity

The control *in silico* BF map and its properties are illustrated in **Figure 3**. An instance of BF distribution in one of the 541 instances is shown in **Figure 3Ai**. The average of 541 instances, vowelized at resolution of 1 mm^3, was used to represent the control BF map (**Figure 3Aii**). Histogram of BF, based on the BF map, shows that the mean 1 mm^3 resolution BF was approximately 3.7 mm^3/s. Histograms at 1 and 2 mm^3 resolutions were used to construct the PDF of relative flow (**Figure 3Bii** shows the 1 mm^3 resolution PDF). The FD was found to be 1.18 showing a relatively low BF heterogeneity in the control BF map. The control *in silico* BF maps approximate error analysis was performed. FD was computed using an increasing number of instances. The values of FD were found to fit an exponential decay curve exactly (**Figure 3Biii**). From the fitted curve, it was found that the asymptotic value was 1.14. The difference between our control BF map and the asymptotic value was 7%, and therefore the error was deemed to be negligible.

Further, the transmural BF heterogeneity was quantified (**Figure 4**). BF within layers of 1 mm thickness, computed from the distances of each 1 mm^3 voxel from the endocardial surfaces (**Figure 4Ai**), in the right and left ventricles are shown in **Figures 4Bi,Bii** respectively. The epicardial layers in the right ventricle received significantly lower BF than in the left ventricle. The endocardial layers received a significant BF. In both the right and left ventricles, it was found that BF had a minimum in the sub-endocardial layers (**Figures 4Bi,Bii**, gray boxes).

Improved Aortic Pressure Improved Overall BF, Heterogeneity Unaltered

BF distributions under varying inlet pressure boundary conditions were simulated (**Figure 5**). The inlet boundary condition, representing aortic pressure, was taken to be 30, 40, 50, …, 200 mmHg and the BF maps calculated at each value of aortic pressure. **Figure 5A** shows three representative simulated BF maps at low (30 mmHg), control (100 mmHg), and high (200 mmHg) inlet pressures, representing aortic pressures. The BF histograms are shown in **Figure 5B**. At low pressure (sub-physiological to clearly show the effect), the histogram shows total BF to be low (area under curve of BF histogram). As inlet pressure was increased, the total BF

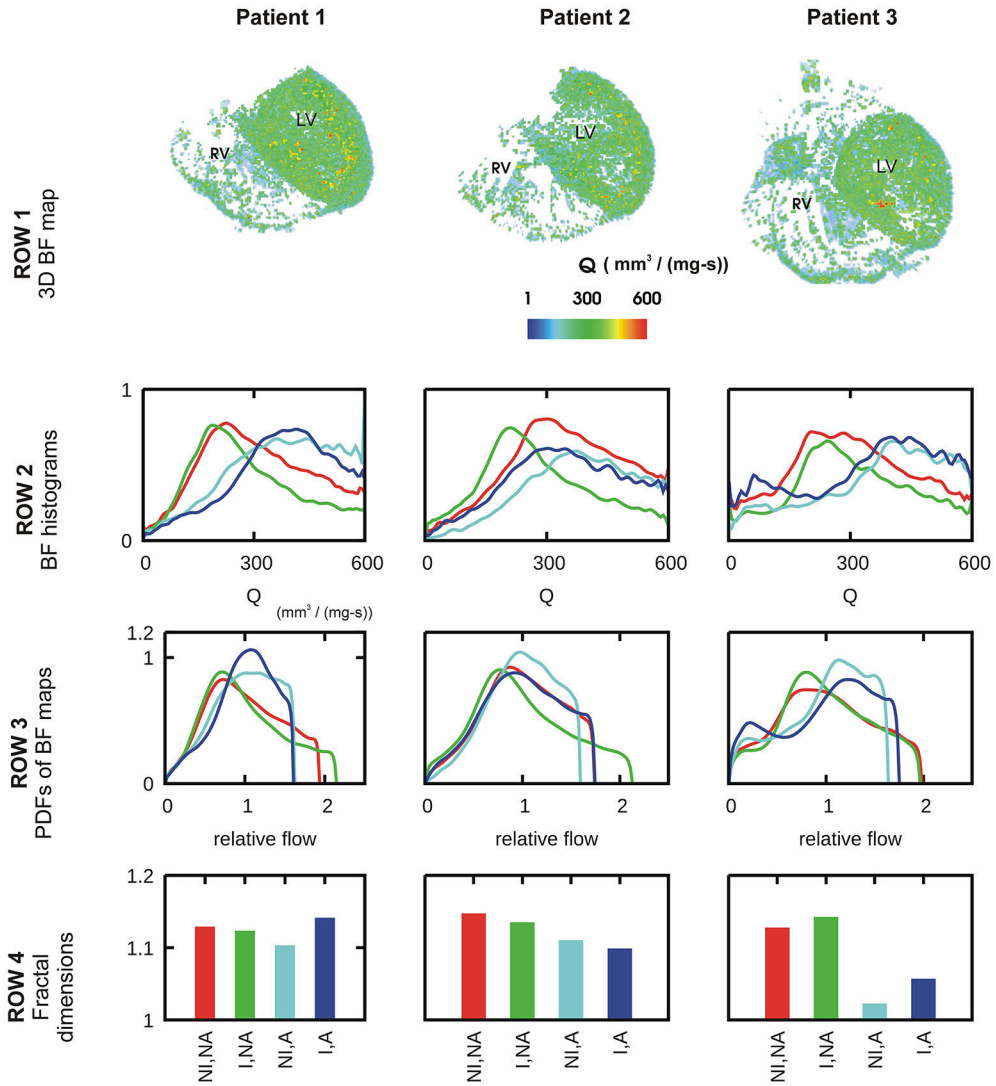

FIGURE 2 | Characteristics of BF heterogeneity in three patients. Row 1: 3D reconstruction of myocardial BF maps segmented from CT images of each of patient 1, 2, and 3. In rows 2–4, data for control (red), cooled dialysate (green), adenosine treated (cyan), and cooled dialysate with adenosine treated (blue) are shown. Row 2: Histograms of BFs in the 3D reconstructions. Row 3: PDFs of relative BF computed from corresponding histograms of row 2. Row 4: FDs computed using the corresponding PDFs.

also increased. The linear relationship between total BF and aortic pressure in **Figure 5C** shows the constant resistance of the unaltered vascular structure. PDFs of relative perfusion (**Figure 5D**) confirmed that the RD as well as the consequent FD remained unchanged, due to unaltered underlying coronary structure. The transmural BF was also unaltered (Figure S3).

Large Artery Blocking (Stenosis) Promotes BF Bi-Modality, Generates Low BF Distal Regions

The effects of blocking an arbitrarily chosen LAD segment are illustrated in **Figure 6**. Pressure distributions and BF maps under control ($r = 1.53$ mm, **Figure 6Ai**) and severe stenosis ($r = 0.01$ mm, **Figure 6Aii**) illustrate the emergence of low BF distal regions, distal to the severe stenosis. At mild stenosis ($r \geq 0.25$ mm), the PDFs of relative BF were found to be unimodal (**Figure 6Bi**). In contrast, at severe stenosis ($r < 0.25$ mm), the histograms became bimodal with two distinct peaks, one each at low and high BF values (**Figure 6Bi**). As the severity of stenosis was increased, the FD was found to progressively reduce from 1.18 (control) to 1.01 (severe stenosis) (Figure S4). Severe stenosis also reduced the total perfusion by approximately 15% (Figure S4). However, increased BF heterogeneity is reflected in the increase of RD as the severity of stenosis was increased (**Figure 6Bii**). The region of BF distal to the location of stenosis experienced a progressively reduced pressure gradient as shown in **Figure 6C**. As the stenosis segment was in the LAD and due to the approximate nature of the model (terminals at SN 6),

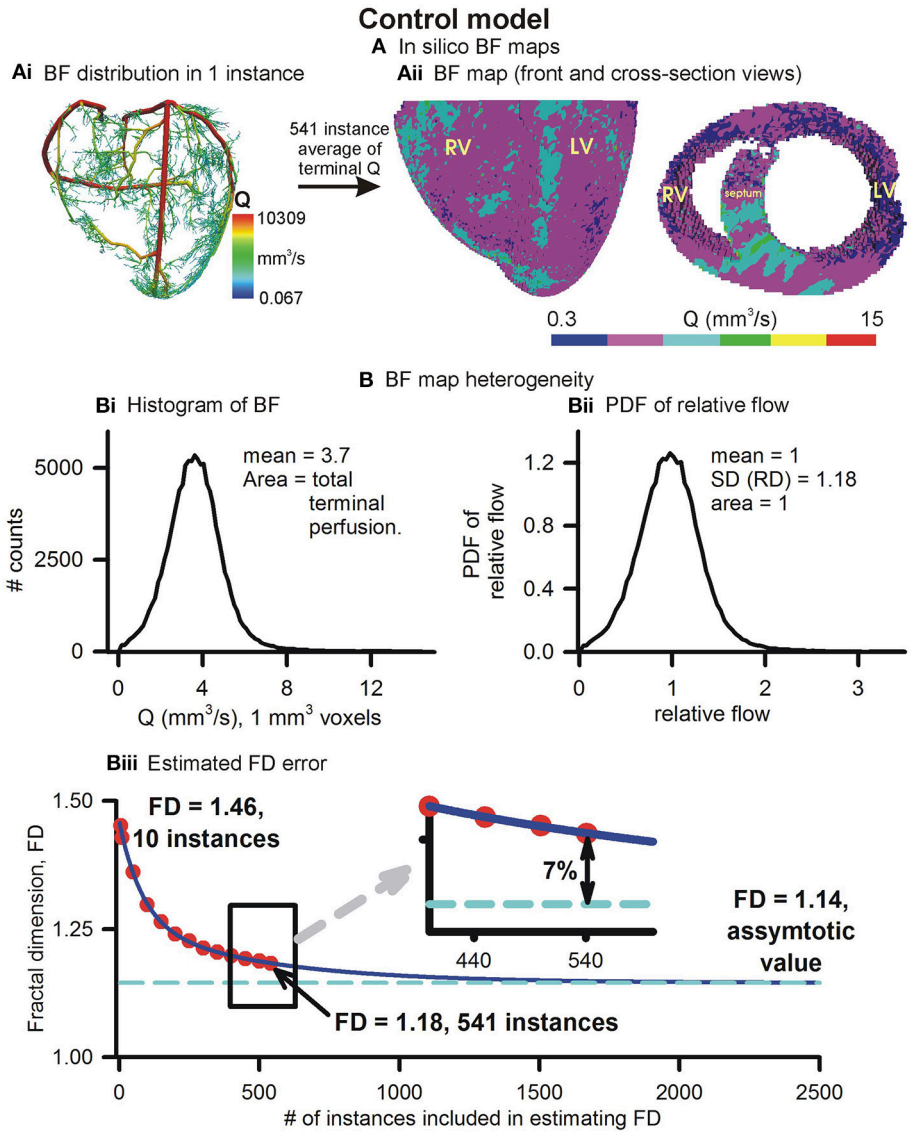

FIGURE 3 | Simulated BF map and quantification of BF heterogeneity. **(Ai)** An instance of vasculature structure showing BF distribution. **(Aii)** Front and cross-sectional views of simulated BF maps using the full 541 instances ensemble. **(Bi)** Histogram of simulated BF map. **(Bii)** PDF of relative perfusion which provides the relative dispersion (RD), also termed fractal dimension (FD). **(Biii)** Difference between FD using complete ensemble (1.18) and estimated asymptotic value (1.14).

the right ventricle transmural heterogeneity was unaffected (**Figure 6Di**). However, the amount of BF received by all layers in the left ventricle reduced progressively as severity of stenosis was increased. Further, the transmural heterogeneity was found to reduce as radius of chosen LAD segment was reduced (**Figure 6Dii**).

Blocking All Large Arteries (Stenosis) Promotes BF Bi-Modality, Blocking Smaller Arterioles Increase BF Heterogeneity

The roots of arterial sub-trees of a given SN order (SN 6–10) were blocked by 90% of their control radius to generate BF maps (**Figure 7Ai**). Blocking of root segments of SN 7–SN 10 sub-trees altered the BF patterns. Blocking of terminals (SN 6) caused an apparent overall reduction of BF. Instances of the corresponding pressure distributions are shown in **Figure 7Aii**. The BF maps and pressure gradients indicate that the volume of tissue affected is related to the SN order of the arterial sub-tree that was blocked. Relative dispersion of PDFs (**Figure 7B**) increased (RD = 1.22, also see Figure S5) when SN 6 terminals were blocked. The PDF was seen to be uni-modal. Blocking root segments of SN 7 or higher sub-trees also increased relative dispersion, but also gave rise to bi-modal PDFs with peaks at low and high values (**Figure 6B**). The amplitude of the lower relative flow peak was greater at SN 10 blocking as compared to SN 7 blocking. The total BF when each SN order was blocked is shown in **Figure 7C**.

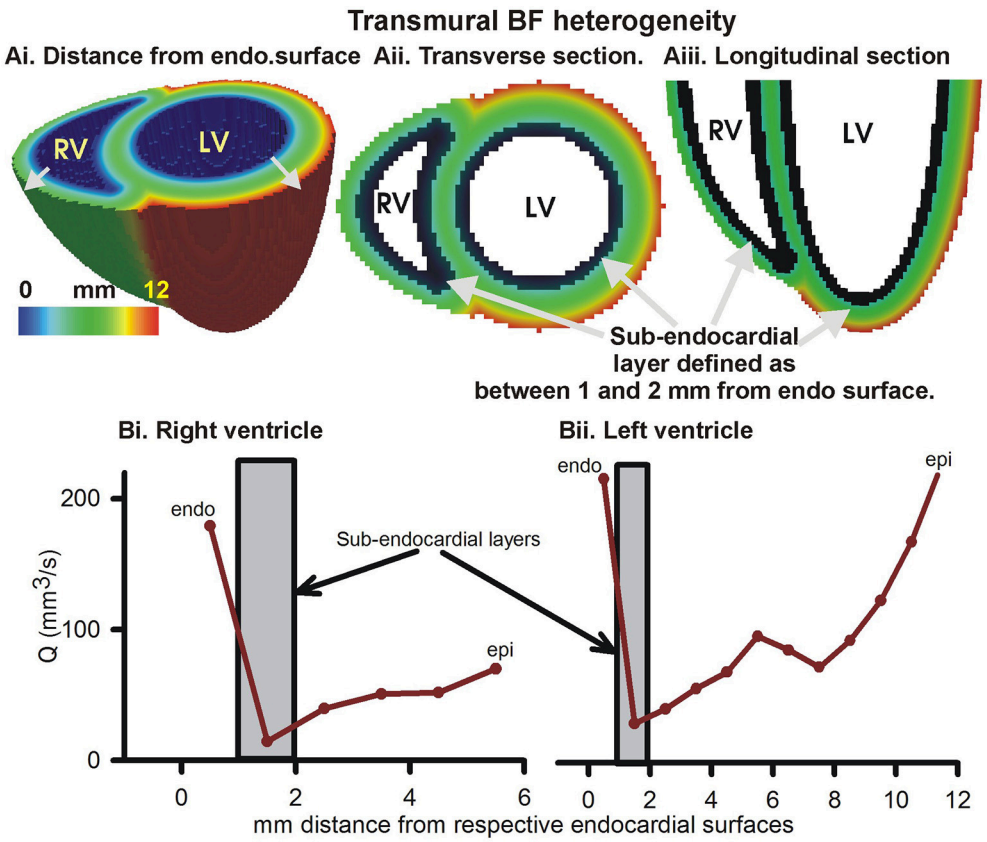

FIGURE 4 | Transmural BF heterogeneity in the simulated BF map. **(Ai)** Distance of each point in left and right ventricular tissue from respective endocardial surfaces. Increasing distance is shown by gray arrows. **(Aii)** Cross-section at the base showing distance from endocardial surface. **(Aiii)** Longitudinal section showing distance from endocardial layer. Black layer in **(Aii, Aiii)** shows sub-endocardial layer. **(Bi)** Measured total perfusion in each 1 mm thick layer of the model right ventricle. **(Bii)** Measured total perfusion in each 1 mm thick layer of the model left ventricle. Perfusion in sub-endocardial layer of RV and LV is shown in the gray boxes.

Blocking of the smallest arteries had the most significant effect of reducing total coronary BF. Blocking of SN 7-9 arteries had a relatively less impact. Blocking SN 10 arteries also reduced total coronary BF significantly. Blocking of arteries also affected transmural heterogeneity (**Figure 7D**). In the right ventricle, blocking SN 7 maximally increased transmural heterogeneity. On the other hand, blocking SN 6, or SN 8–10 reduced transmural heterogeneity. In the left ventricle, blocking SN 6 or SN 10 increased transmural heterogeneity maximally. Blocking of SN 7, 8, or 9 reduced heterogeneity.

Altered Inlet Perfusion in the Presence of Blocked Arteries

Simulation of diseased, or adenosine and dialysate cooling therapy induced alteration of aortic pressure in the presence of coronary structural defects are illustrated in **Figure 8**. Blocking of SN 6 terminals (70, 80, or 90% of control radius values) increased the FD (**Figure 8A**). In contrast, blocking of SN 10 sub-trees reduced the FD. Transmural heterogeneity was unaffected by blocking of SN 6 terminals (**Figure 8B**). However, as the severity of SN 10 blocking increased, the transmural heterogeneity was found to be increased. Blocking SN 6 vessels has a greater impact on reducing total BF in comparison to blocking SN 10 vessels (**Figure 8C**). BF reduced as aortic pressure reduced.

CONCLUSIONS AND DISCUSSION

The main conclusions of this study are:

a. Clinical imaging can provide information regarding BF alterations in patient ventricles. Total BF can become increased due to pharmacological (adenosine) and therapeutic (dialysate cooling) interventions. Although BF heterogeneity is also potentially affected by the interventions, the information is confounded by underlying vascular structural disease such as large vessel stenosis.
b. Computer modeling indicates that total coronary BF is increased by improved aortic pressure, and also by vasodilation of coronary blood vessels.
c. The causes of BF heterogeneity appear to be multi-fold. Small vessel constriction promoted increase of dispersion but maintained uni-modality of BF histograms. It may be the major cause of BF heterogeneity. Large vessel constriction promoted bi-modality in BF histograms. Constriction of large

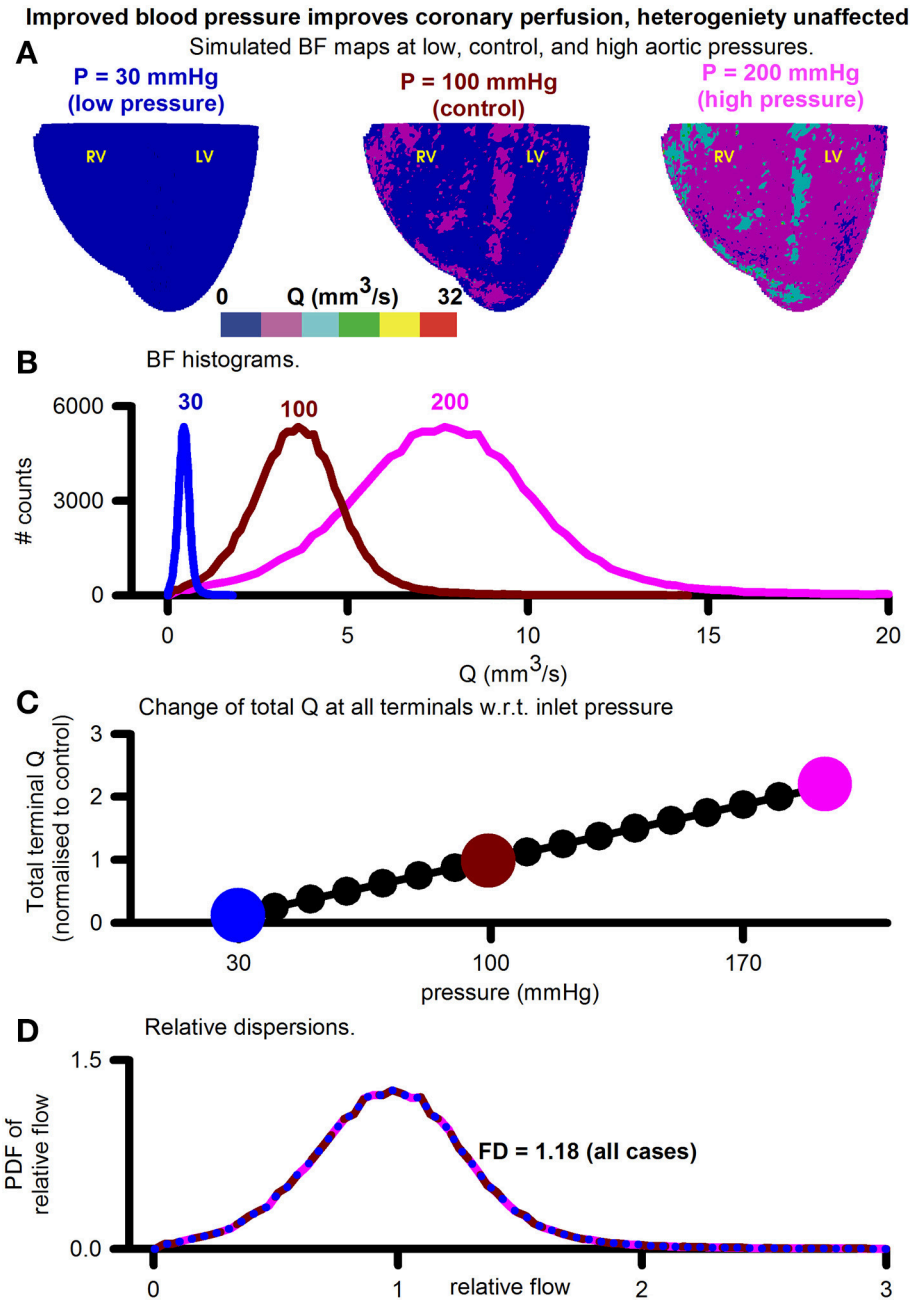

FIGURE 5 | Assessment of the effect of increasing aortic (inlets) pressure. **(A)** Simulated BF maps at 30 mmHg (left), 100 mmHg (center), and 200 mmHg (right). **(B)** BF histograms at 30 mmHg (blue), 100 mmHg (red), and 200 mmHg (pink) showing increase of total perfusion with increase of inlet pressure. **(C)** Total BF at terminals as a function of inlet pressure. Symbols show pressure values where simulations were performed. Large colored circles show the 30, 100, and 200 mmHg values. **(D)** Color coded PDFs of relative perfusion, which were found to be identical for all pressure values.

vessels had a greater impact on total transmural BF, as well as transmural BF heterogeneity in comparison to constriction of small vessels. The effect of therapy (adenosine or dialysate cooling) may arise from an increase of total BF, caused by an improved aortic pressure.

CT is now an advanced field of imaging that provides a wide spectrum of BF data in the heart (Schindler, 2016; Cademartiri et al., 2017). In this study, the patient hearts were imaged using a rest/stress protocol. It revealed that interventions have a significant effect. The difference between rest/stress also highlighted inherent vascular structural defects in the heart of patient 3 (**Figure 2**, second row, last column). Our CT protocols are being continually developed to fully exploit available technologies. However, the BF structure-function appears as a

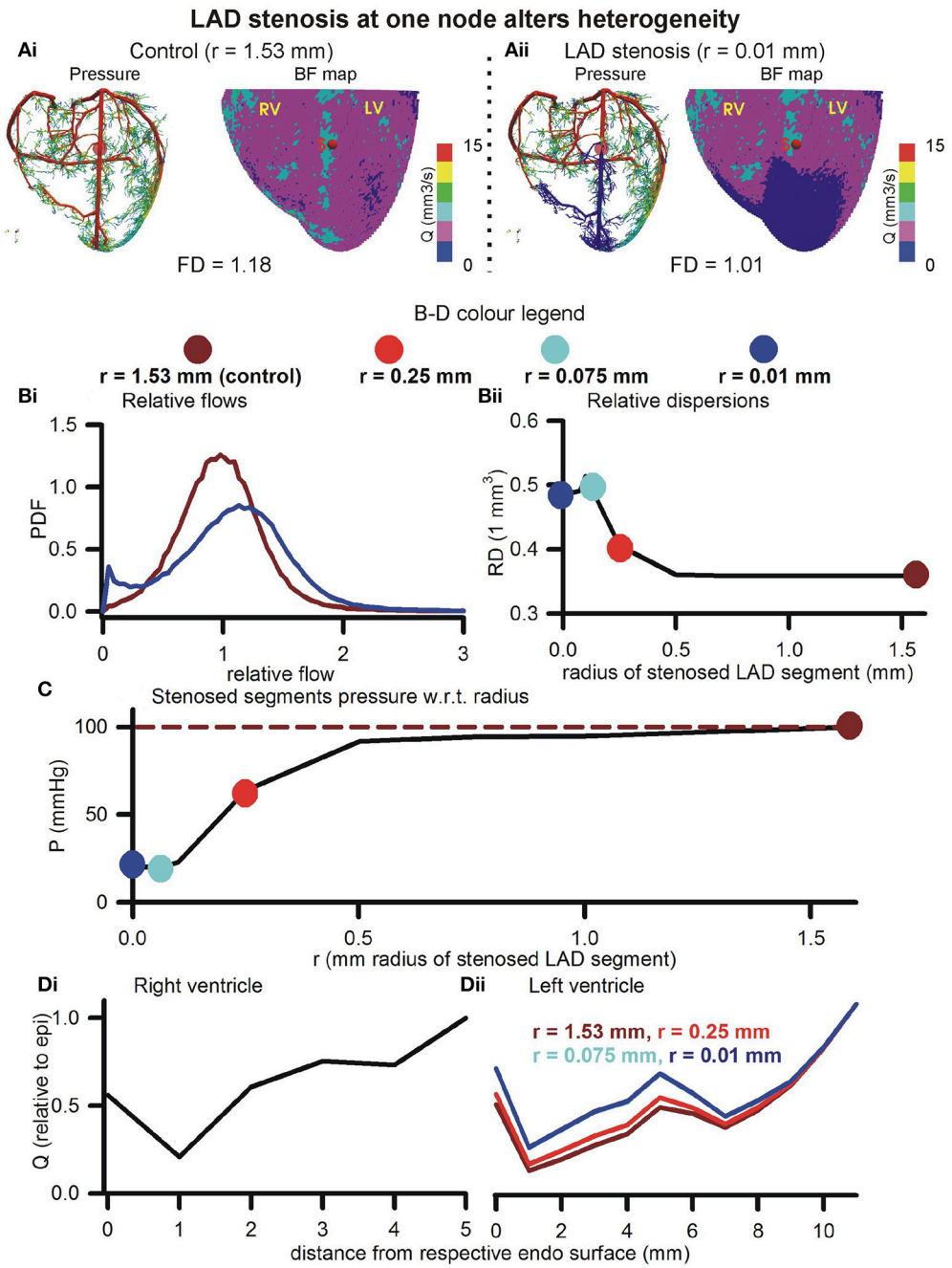

FIGURE 6 | Effect of stenosis in large artery segment. **(Ai)** Control pressure distribution in vasculature (Left) and BF map (Right). The control radius of the arbitrarily chosen LAD segment was $r = 1.53$ mm. **(Aii)** Pressure (Left) and BF map (Right) under severe stenosis at the chosen LAD segment was $r = 0.01$ mm. In **(B–D)**, the color coding is used to represent segment radii, $r = 1.53$ mm (dark red), $r = 0.25$ mm (red), $r = 0.075$ mm (cyan), and $r = 0.01$ mm (blue). **(Bi)** PDFs of relative perfusion. **(Bii)** Relationship between RD and stenosed segment radius. **(C)** Relationship between pressure at stenosed segment and its radius. **(Di,Dii)** Transmural BF heterogeneity in right (Left) and left (Right) ventricles.

combination of several factors in the imaging, making modeling investigation necessary.

Based on experimental measurements, our model incorporates morphometry data that gave realistic topologies of the coronary vasculature. The optimal assignment of 3D positions to the arterial tree nodes was performed using space filling algorithm (Beard and Bassingthwaighte, 2000). Accounting for limitations, an ensemble of instances was generated whose average hemodynamic properties are presented. The presented models BF heterogeneity (FD = 1.14) is in

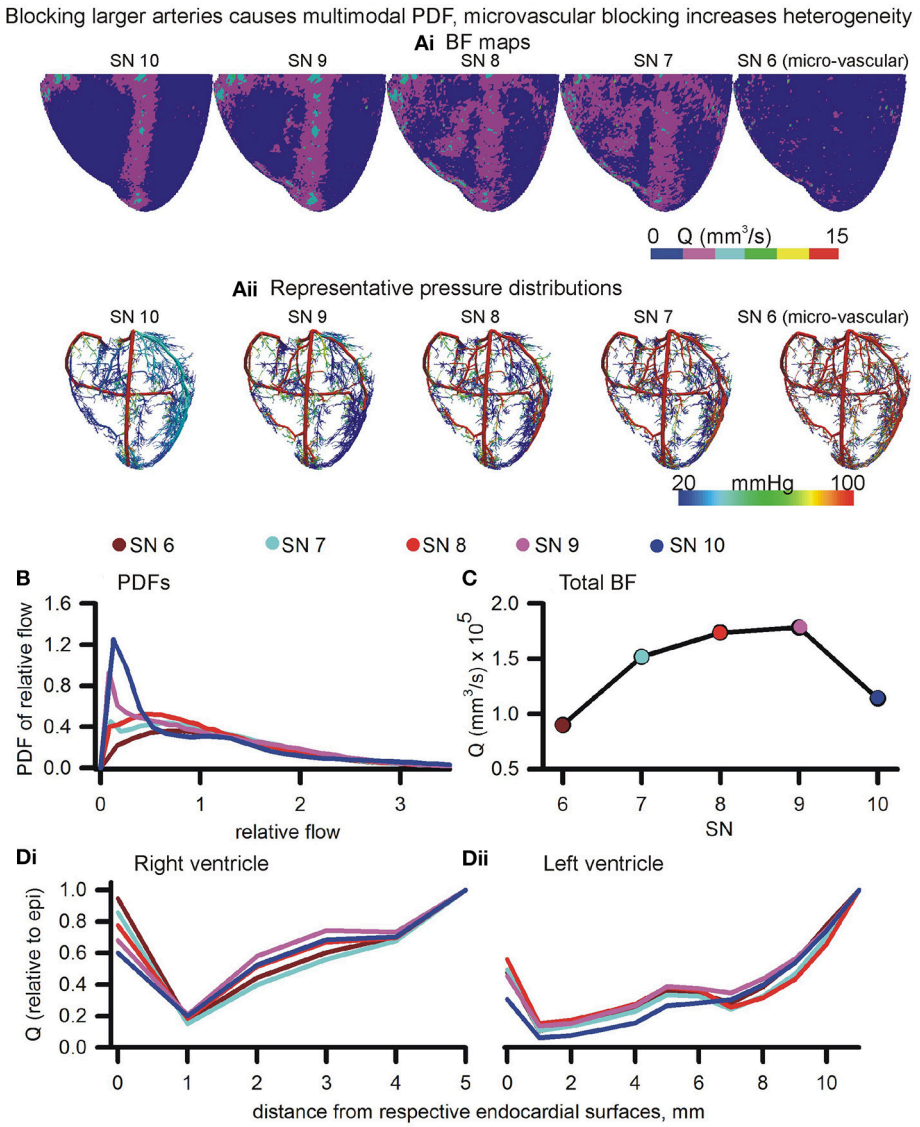

FIGURE 7 | Effects of blocking arteries at given order on perfusion and heterogeneity. **(Ai,Aii)** BF maps **(Ai)** and pressure distributions **(Aii)** when arteries of various orders were blocked. **(B)** PDFs of BF maps. **(C)** Total BF at terminals when that order arteries were blocked. **(Di,Dii)** Epi-endo heterogeneity alterations under blocking of various orders of arteries.

agreement with FD of 1.2 observed by VanBavel and Spaan in microcirculation SN 2–8 networks (VanBavel and Spaan, 1992). Others have used optimized models, where a spectrum of cost functions such as single arterial volume (Karch et al., 1999; Schreiner et al., 2006), or the combination of metabolic cost, volume, power (Kaimovitz et al., 2005; Keelan et al., 2016) have been optimized. Notwithstanding the relatively simple optimization used in this study, **Figure 4** shows that the BF is distributed throughout most of the myocardium almost uniformly (FD = 1.18). Our model has characteristic transmural BF heterogeneity. Whereas total path lengths of vessels were constrained, the combination of transmural path lengths and the space filling-boundary avoidance algorithm may explain model behavior. It is known that the myocardium is heterogeneously perfused transmurally (Huo et al., 2009). We therefore computed to alteration of our models transmural heterogeneity as an approximation, and we bear in mind that further development is required.

In this study, multi-modality in BF histograms due to large vessel severe stenosis was observed in the model, which agrees with the imaging data. However, single segment stenosis, or stenosis of high order segments, may be accompanied by an auto-regulatory response. Although overall BF became multi-modal, the FD (computed using the same methods as well as binning) was observed to be reduced. In contrast, the modeling study by Meier et al. (2004) which included autoregulation showed

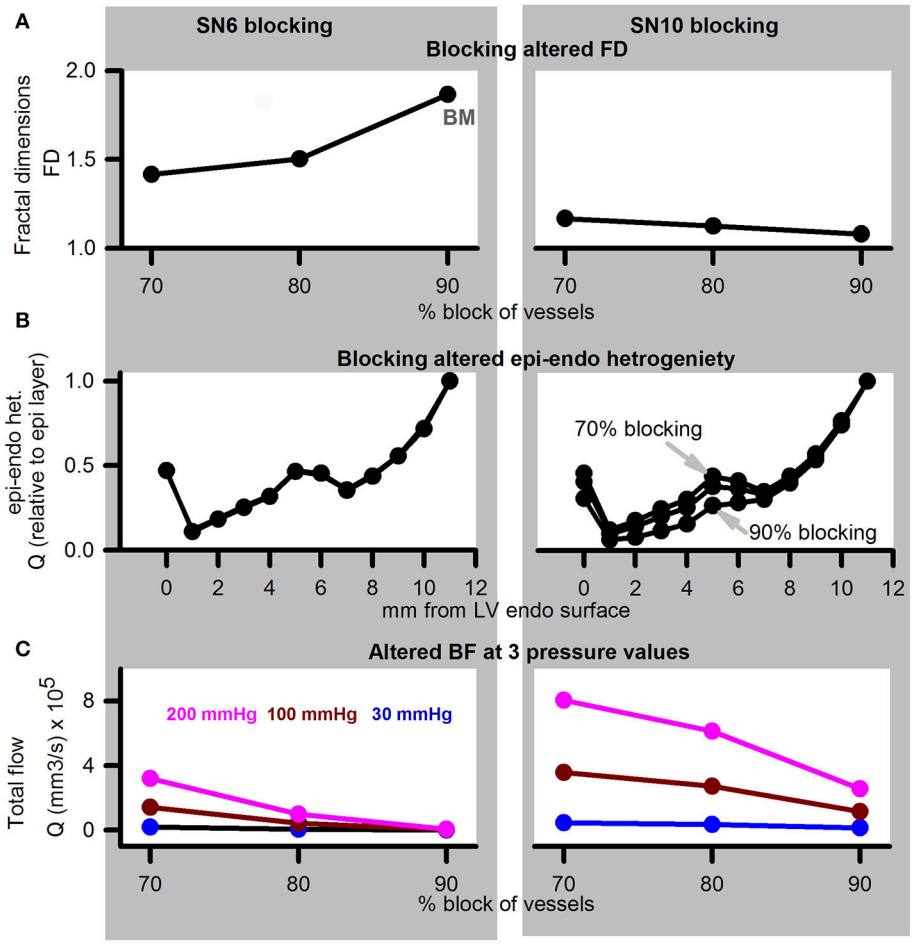

FIGURE 8 | Simulation of disease (reduced pressure) or adenosine and dialysate cooling (therapy) in the presence of structural defects. Left column shows data for SN 6 blocking, while right column shows data for SN 10 blocking. **(A)** FD when vessels were blocked by 70, 80, or 90% of their control values. **(B)** Transmural BF heterogeneity. **(C)** Total BF when vessels were blocked by 70, 80, or 90% when applied inlet pressure was 200 mmHg (pink), 100 mmHg (dark red), or 30 mmHg (blue).

that FD remained unchanged under stenosis. Remarkably, the inclusion of autoregulation in the above study maintained uni-modality of BF histograms, while increasing RD when low aortic pressure was applied.

The present model was constructed using a limited topology (SN 6–SN 11). It was also optimized using relatively straightforward space filling and boundary avoidance conditions. Nevertheless, transmural BF heterogeneity was observed, and it was affected by structural alterations. Specifically, blocking the larger (SN 7 or 8) vessels increased transmural heterogeneity more than blocking of the microvasculature (SN 6). Our finding is in line with that of Algranati et al. (2011) who have identified sub-endocardial compliance as a cause of BF redistribution. In the above study, they have also identified the contractile factors that may contribute to the sub-endocardial heterogeneity.

Although there have been significant advances in the experimental, theoretical, and imaging literature, we believe that this is one of a few studies that applies coronary vasculature models to indicatively explain clinical imaging observations. Previously developed models have generated 4-D XCAT Phantoms (Fung et al., 2011), or assist the clinician in identifying clinical defects (Fung et al., 2010). Further development of the presented model, at multi-scale and at multi-physics levels, will incorporate Cardiac Physiome models in a pre-clinical assessment tool to assist our clinical research. The model, in conjunction with detailed imaging (see Jogiya et al., 2014, as well as **Figure 1**), will expedite the assessment of patient BF status and consequently overall health assessment. The model is also capable of permitting investigation of specific artery bifurcation properties under health and disease conditions (Auricchio et al., 2014). Investigation of properties such as electrical wave propagation and their interaction with vascular structure (Bishop et al., 2010) can be further investigated using the presented model. Extension of the model will incorporate the multi-scale nature of delivery of oxygen to myocardial tissue (Goldman et al., 2017; Mason McClatchey et al., 2017).

LIMITATIONS

Imaging Limitations

Although a large amount of information is available in our clinical images, certain limitations remain. Firstly, only the diastolic phase was collected. During left ventricle's diastole, the right ventricle is still moving and therefore cannot be imaged. Using a 4D scanning protocol may alleviate this limitation in future studies that can capture right ventricle signals.

Another limitation is that of resolution. Due to the toxicity of the contrast agent and other factors, it is difficult to image the patient for longer durations. However, that results in significantly less number of slices and low 3D resolution. At the acquired resolution, it may not be possible to gain insights into the pre-capillary arteriole BF distributions. Apart from CT, other imaging modalities may be available for assessment of arterial defects (Gharib et al., 2008). The issues regarding toxicity of CT contrast agents may be reduced using magnetic resonance based imaging (Jogiya et al., 2014).

Modeling Limitations

Our model is limited to SN 6 (arterioles) to SN 11 (main coronary arteries) arterial segments. The ensemble of coronary trees generated in this work is based on the morphometric data by the Kassab group. However, the optimization algorithm in the uneven geometry of the heart is a compute intensive task and it was not possible to generate optimized structures within a short (48 h) duration. It is known that assigning spatial locations to the vasculature nodes is a large optimization problem where fractal models based on morphometry need to be combined with theoretical optimization methods (Schreiner et al., 2006). In future work, we will consider inclusion on further biophysical principles that permit use of cost functions to compute optimal locations of arteriole terminals (Zamir and Phipps, 1988; Kaimovitz et al., 2010; Keelan et al., 2016).

An important simplification of our model is that diameter asymmetry has been ignored. In our model, elements of the same order have a uniform radius. In addition, the bifurcations are assigned randomly where the daughter element radii are assigned according to morphometry rather than according to BF symmetry. Blood vessel diameter asymmetry has been observed in casting data (Huo et al., 2009) and shown to affect BF distributions significantly (Kaimovitz et al., 2008). Bifurcation asymmetry is known to promote increased RD (Sriram et al., 2014) and may be an important factor that contributes to BF heterogeneity in the critically ill groups of patients (Frisbee et al., 2016). It has been quantified in past studies (VanBavel and Spaan, 1992; Dankelman et al., 2007) and will be included in future versions of our model.

Both pulsatile BF (Huo and Kassab, 2006) and viscosity variability in micro-vessels (Pries et al., 1996; Pries and Secomb, 2009) have been ignored for simplicity in this study. As a first step toward constructing our model, the present study assumed steady state BF in line with the literature (Karch et al., 1999; Beard and Bassingthwaighte, 2000; Keelan et al., 2016), which includes studies that quantify BF heterogeneity (Schreiner et al., 2003). The coronary artery diameter (3.2 mm) is 10 times less than that of the ascending aorta during diastole (∼32 mm) (de Heer et al., 2011), thus partially justifying the present study's steady state BF assumption. It should also be appreciated that this study's CT imaging data were obtained during the diastole when pressure changes may be small. The overall qualitative results of this study regarding 3D structure based distribution of blood in the ventricles may remain unaffected with the inclusion of pulsatile BF, but also limit the applicability of the model. The pulsatile nature of blood flow in the coronary arteries stems from the pulsating pressure boundary conditions at the aorta, as well as the effects of myocardial motion-contraction. A number of previous theoretical and experiment-modeling studies (Womersley, 1955, 1958; Duan and Zamir, 1995; Huo and Kassab, 2006, 2007) may be adapted to incorporate pulsatile boundary conditions in the present model. The adaptation of previous knowledge entails significant model development and is out of scope of this study. In future studies, the inclusion of the time varying boundary conditions will permit application of model to address clinically relevant challenges such as calculation of fractional flow reserve (Yong et al., 2017) and vascular surgery assessment (Kouhi et al., 2008).

Generation of geometry is based on deterministic space filling, whereas optimization of energy expenditure or some measure is expected to give improved distribution in the future. In the future, we aim to develop a 4D XCT phantom that will permit a more in depth patient specific BF assessment along with other parameters (Fung et al., 2011).

The lack of autoregulation is a significant simplification in our study. The inclusion of autoregulation may affect results presented in this study (Meier et al., 2004). It will also permit testing of further factors that affect local and global flow, as shown recently by Namani et al. (2018).

Apart from structural changes, BF is also affected by several other factors, where metabolic demand of tissue and protein expression heterogeneity are prominent (Stoll et al., 2008). Autoregulation, as well as other patho-physiological factors will be incorporated into the model in future work.

CLINICAL SIGNIFICANCE OF THE STUDY

In this study, imaging data acquired from patients was analyzed. Whereas it is probably true that dialysis causes vascular dysfunction by affecting the micro-vasculature, this study's imaging observation combined with the modeling results, indicates that large vessel dysfunction may significantly affect patient's coronary perfusion.

In the process of quantifying BF heterogeneity, we have now developed algorithms that compute simple yet informative measures of BF heterogeneity. Such a tool will provide rapid assessment of whether imaging data reflect the effectiveness of therapy.

An important development during this study was the implementation of a method to generate organ level vascular structure. When combined with micro-vasculature, the vasculature model is being developed to become a pre-clinical trial *in silico* indicative outcome assessment tool.

AUTHOR CONTRIBUTIONS

SK, DG, and CM designed the study in consultation with CE. AS, and T-YL provided the texture analyzed CT data and related text. SK and FS segmented the hearts. SK developed the codes and performed the simulation experiments, acquired, curated, and analyzed the data. DG and CM provided expert comments. CE provided expert insights into clinical-modeling data interpretation. SK wrote the first draft. AS provided the draft of the imaging data analysis. All authors wrote and approved the final manuscript.

ACKNOWLEDGMENTS

We thank LHSC IT, Compute Canada, SHARCNet for IT and HPC resources. This study was supported by Heart and Stroke grant (G-17-0018311, PI: CM).

SUPPLEMENTARY MATERIAL

The Supplementary Material for this article can be found online at: https://www.frontiersin.org/articles/10.3389/fphys.2018.00511/full#supplementary-material

REFERENCES

Alarcón, T., Byrne, H. M., and Maini, P. K. (2005). A design principle for vascular beds: the effects of complex blood rheology. *Microvasc. Res.* 69, 156–172. doi: 10.1016/j.mvr.2005.02.002

Algranati, D., Kassab, G. S., and Lanir, Y. (2011). Why is the subendocardium more vulnerable to ischemia? A new paradigm. *Am. J. Physiol. Heart Circ. Physiol.* 300, H1090–1100. doi: 10.1152/ajpheart.00473.2010

Auricchio, F., Conti, M., Ferrazzano, C., and Sgueglia, G. A. (2014). A simple framework to generate 3D patient-specific model of coronary artery bifurcation from single-plane angiographic images. *Comput. Biol. Med.* 44, 97–109. doi: 10.1016/j.compbiomed.2013.10.027

Bassingthwaighte, J. B., King, R. B., and Roger, S. A. (1989). Fractal nature of regional myocardial blood flow heterogeneity. *Circ. Res.* 65, 578–590. doi: 10.1161/01.RES.65.3.578

Beard, D. A., and Bassingthwaighte, J. B. (2000). The fractal nature of myocardial blood flow emerges from a whole-organ model of arterial network. *J. Vasc. Res.* 37, 282–296. doi: 10.1159/000025742

Bishop, M. J., Boyle, P. M., Plank, G., Welsh, D. G., and Vigmond, E. J. (2010). Modeling the role of the coronary vasculature during external field stimulation. *IEEE Trans. Biomed. Eng.* 57, 2335–2345. doi: 10.1109/TBME.2010.2051227

Breidthardt, T., Burton, J. O., Odudu, A., Eldehni, M. T., Jefferies, H. J., and McIntyre, C. W. (2012). Troponin T for the detection of dialysis-induced myocardial stunning in hemodialysis patients. *Clin. J. Am. Soc. Nephrol.* 7, 1285–1292. doi: 10.2215/CJN.00460112

Burton, J. O., Jefferies, H. J., Selby, N. M., and McIntyre, C. W. (2009). Hemodialysis-induced repetitive myocardial injury results in global and segmental reduction in systolic cardiac function. *Clin. J. Am. Soc. Nephrol.* 4, 1925–1931. doi: 10.2215/CJN.04470709

Cademartiri, F., Seitun, S., Clemente, A., La Grutta, L., Toia, P., Runza, G., et al. (2017). Myocardial blood flow quantification for evaluation of coronary artery disease by computed tomography. *Cardiovasc. Diagn. Ther.* 7, 129–150. doi: 10.21037/cdt.2017.03.22

Collins, A. J., Foley, R. N., Gilbertson, D. T., and Chen, S. C. (2015). United States Renal Data System public health surveillance of chronic kidney disease and end-stage renal disease. Kid. *Int. Suppl.* 5, 2–7. doi: 10.1038/kisup.2015.2

Dankelman, J., Cornelissen, A. J., Lagro, J., Vanbavel, E., and Spaan, J. A. (2007). Relation between branching patterns and perfusion in stochastic generated coronary arterial trees. *Med. Biol. Eng. Comput.* 45, 25–34. doi: 10.1007/s11517-006-0139-9

Dasselaar, J. J., Slart, R. H., Knip, M., Pruim, J., Tio, R. A., McIntyre, C. W., et al. (2009). Haemodialysis is associated with a pronounced fall in myocardial perfusion. *Nephrol. Dial. Transplant* 24, 604–610. doi: 10.1093/ndt/gfn501

de Heer, L. M., Budde, R. P., Mali, W. P., de Vos, A. M., van Herwerden, L. A., and Kluin, J. (2011). Aortic root dimension changes during systole and diastole: evaluation with ECG-gated multidetector row computed tomography. *Int. J. Cardiovasc. Imaging* 27, 1195–1204. doi: 10.1007/s10554-011-9838-x

Dodge, J. T. Jr., Brown, B. G., Bolson, E. L., and Dodge, H. T. (1992). Lumen diameter of normal human coronary arteries. Influence of age, sex, anatomic variation, and left ventricular hypertrophy or dilation. *Circulation* 86, 232–246. doi: 10.1161/01.CIR.86.1.232

Duan, B., and Zamir, M. (1995). Pressure peaking in pulsatile flow through arterial tree structures. *Ann. Biomed. Eng.* 23, 794–803. doi: 10.1007/BF02584478

Frisbee, J. C., Goodwill, A. G., Frisbee, S. J., Butcher, J. T., Wu, F., and Chantler, P. D. (2016). Microvascular perfusion heterogeneity contributes to peripheral vascular disease in metabolic syndrome. *J. Physiol. (Lond).* 594, 2233–2243. doi: 10.1113/jphysiol.2014.285247

Fung, G. S., Segars, W. P., Gullberg, G. T., and Tsui, B. M. (2011). Development of a model of the coronary arterial tree for the 4D XCAT phantom. *Phys. Med. Biol.* 56, 5651–5663. doi: 10.1088/0031-9155/56/17/012

Fung, G. S., Segars, W. P., Lee, T. S., Higuchi, T., Veress, A. I., Gullberg, G. T., et al. (2010). Realistic simulation of regional myocardial perfusion defects for cardiac SPECT studies. *IEEE Nucl. Sci. Symp. Conf. Rec.* 2010, 3061–3064. doi: 10.1109/NSSMIC.2010.5874362

Gharib, A. M., Ho, V. B., Rosing, D. R., Herzka, D. A., Stuber, M., Arai, A. E., et al. (2008). Coronary artery anomalies and variants: technical feasibility of assessment with coronary MR angiography at 3 T. *Radiology* 247, 220–227. doi: 10.1148/radiol.2471070274

Göktepe, S., and Kuhl, E. (2010). Electromechanics of the heart: a unified approach to the strongly coupled excitation–contraction problem. *Comput. Mech.* 45, 227–243. doi: 10.1007/s00466-009-0434-z

Goldman, D., Zahra Farid, K. A. L., Jefferson, C., Frisbee, and D. N. J. (2017). "The microcirculation physiome: an approach using arteriolar-venular networks reconstructed from *in vivo* data," in *Cardiac Physiome Society Meeting* (Toronto, ON).

Hacking, W. J., VanBavel, E., and Spaan, J. A. (1996). Shear stress is not sufficient to control growth of vascular networks: a model study. *Am. J. Physiol.* 270, H364–H375. doi: 10.1152/ajpheart.1996.270.1.H364

Huo, Y., Kaimovitz, B., Lanir, Y., Wischgoll, T., Hoffman, J. I., and Kassab, G. S. (2009). Biophysical model of the spatial heterogeneity of myocardial flow. *Biophys. J.* 96, 4035–4043. doi: 10.1016/j.bpj.2009.02.047

Huo, Y., and Kassab, G. S. (2006). Pulsatile blood flow in the entire coronary arterial tree: theory and experiment. *Am. J. Physiol. Heart Circ. Physiol.* 291, H1074–H1087. doi: 10.1152/ajpheart.00200.2006

Huo, Y., and Kassab, G. S. (2007). A hybrid one-dimensional/Womersley model of pulsatile blood flow in the entire coronary arterial tree. *Am. J. Physiol. Heart Circ. Physiol.* 292, H2623–H2633. doi: 10.1152/ajpheart.00987.2006

Jefferies, H. J., Virk, B., Schiller, B., Moran, J., and McIntyre, C. W. (2011). Frequent hemodialysis schedules are associated with reduced levels of dialysis-induced cardiac injury (myocardial stunning). *Clin. J. Am. Soc. Nephrol.* 6, 1326–1332. doi: 10.2215/CJN.05200610

Jogiya, R., Morton, G., De Silva, K., Reyes, E., Hachamovitch, R., Kozerke, S., et al. (2014). Ischemic burden by 3-dimensional myocardial perfusion cardiovascular magnetic resonance: comparison with myocardial perfusion scintigraphy. *Circ. Cardiovasc. Imaging* 7, 647–654. doi: 10.1161/CIRCIMAGING.113.001620

Kaimovitz, B., Huo, Y., Lanir, Y., and Kassab, G. S. (2008). Diameter asymmetry of porcine coronary arterial trees: structural and functional implications. *Am. J. Physiol. Heart Circ. Physiol.* 294, H714–H723. doi: 10.1152/ajpheart.00818.2007

Kaimovitz, B., Lanir, Y., and Kassab, G. S. (2005). Large-scale 3-D geometric reconstruction of the porcine coronary arterial vasculature based on detailed anatomical data. *Ann. Biomed. Eng.* 33, 1517–1535. doi: 10.1007/s10439-005-7544-3

Kaimovitz, B., Lanir, Y., and Kassab, G. S. (2010). A full 3-D reconstruction of the entire porcine coronary vasculature. *Am. J. Physiol. Heart Circ. Physiol.* 299, H1064–H1076. doi: 10.1152/ajpheart.00151.2010

Karch, R., Neumann, F., Neumann, M., and Schreiner, W. (1999). A three-dimensional model for arterial tree representation, generated by constrained constructive optimization. *Comput. Biol. Med.* 29, 19–38. doi: 10.1016/S0010-4825(98)00045-6

Kassab, G. S., Berkley, J., and Fung, Y. C. (1997a). Analysis of pig's coronary arterial blood flow with detailed anatomical data. *Ann. Biomed. Eng.* 25, 204–217. doi: 10.1007/BF02738551

Kassab, G. S., Pallencaoe, E., Schatz, A., and Fung, Y. C. (1997b). Longitudinal position matrix of the pig coronary vasculature and its hemodynamic implications. *Am. J. Physiol.* 273, H2832–H2842. doi: 10.1152/ajpheart.1997.273.6.H2832

Kassab, G. S., Rider, C. A., Tang, N. J., and Fung, Y. C. (1993). Morphometry of pig coronary arterial trees. *Am. J. Physiol.* 265, H350–H365. doi: 10.1152/ajpheart.1993.265.1.H350

Keelan, J., Chung, E. M., and Hague, J. P. (2016). Simulated annealing approach to vascular structure with application to the coronary arteries. *R. Soc. Open Sci.* 3:150431. doi: 10.1098/rsos.150431

Kouhi, E., Morsi, Y. S., and Masood, S. H. (2008). Haemodynamic analysis of coronary artery bypass grafting in a non-linear deformable artery and Newtonian pulsatile blood flow. *Proc. Inst. Mech. Eng. H* 222, 1273–1287. doi: 10.1243/09544119JEIM459

Mason McClatchey, P., Wu, F., Olfert, I. M., Ellis, C. G., Goldman, D., Reusch, J. E., et al. (2017). Impaired tissue oxygenation in metabolic syndrome requires increased microvascular perfusion heterogeneity. *J. Cardiovasc. Transl. Res.* 10, 69–81. doi: 10.1007/s12265-017-9732-6

McIntyre, C. W. (2010). Haemodialysis-induced myocardial stunning in chronic kidney disease - a new aspect of cardiovascular disease. *Blood Purif.* 29, 105–110. doi: 10.1159/000245634

McIntyre, C. W., and Odudu, A. (2014). Hemodialysis-associated cardiomyopathy: a newly defined disease entity. *Semin. Dial.* 27, 87–97. doi: 10.1111/sdi.12197

McIntyre, N. J., Fluck, R. J., McIntyre, C. W., Fakis, A., and Taal, M. W. (2013). Determinants of arterial stiffness in chronic kidney disease stage 3. *PLoS ONE* 8:e55444. doi: 10.1371/journal.pone.0055444

Meier, J., Kleen, M., and Messmer, K. (2004). A computer model of fractal myocardial perfusion heterogeneity to elucidate mechanisms of changes in critical coronary stenosis and hypotension. *Bull. Math. Biol.* 66, 1155–1171. doi: 10.1016/j.bulm.2003.11.005

Mittal, N., Zhou, Y., Ung, S., Linares, C., Molloi, S., and Kassab, G. S. (2005). A computer reconstruction of the entire coronary arterial tree based on detailed morphometric data. *Ann. Biomed. Eng.* 33, 1015–1026. doi: 10.1007/s10439-005-5758-z

Murray, C. D. (1926a). The physiological principle of minimum work: I. the vascular system and the cost of blood volume. *Proc. Natl. Acad. Sci. U.S.A.* 12, 207–214. doi: 10.1073/pnas.12.3.207

Murray, C. D. (1926b). The physiological principle of minimum work: II. oxygen exchange in capillaries. *Proc. Natl. Acad. Sci. U.S.A.* 12, 299–304. doi: 10.1073/pnas.12.5.299

Namani, R., Kassab, G. S., and Lanir, Y. (2018). Integrative model of coronary flow in anatomically based vasculature under myogenic, shear, and metabolic regulation. *J. Gen. Physiol.* 150, 145–168. doi: 10.1085/jgp.201711795

Pries, A. R., and Secomb, T. W. (2009). Origins of heterogeneity in tissue perfusion and metabolism. *Cardiovasc. Res.* 81, 328–335. doi: 10.1093/cvr/cvn318

Pries, A. R., Secomb, T. W., and Gaehtgens, P. (1996). Biophysical aspects of blood flow in the microvasculature. *Cardiovasc. Res.* 32, 654–667. doi: 10.1016/S0008-6363(96)00065-X

Schindelin, J., Arganda-Carreras, I., Frise, E., Kaynig, V., Longair, M., Pietzsch, T., et al. (2012). Fiji: an open-source platform for biological-image analysis. *Nat. Methods* 9, 676–682. doi: 10.1038/nmeth.2019

Schindler, T. H. (2016). Myocardial blood flow: putting it into clinical perspective. *J. Nucl. Cardiol.* 23, 1056–1071. doi: 10.1007/s12350-015-0372-4

Schreiner, W., Karch, R., Neumann, M., Neumann, F., Roedler, S. M., and Heinze, G. (2003). Heterogeneous perfusion is a consequence of uniform shear stress in optimized arterial tree models. *J. Theor. Biol.* 220, 285–301. doi: 10.1006/jtbi.2003.3136

Schreiner, W., Karch, R., Neumann, M., Neumann, F., Szawlowski, P., and Roedler, S. (2006). Optimized arterial trees supplying hollow organs. *Med. Eng. Phys.* 28, 416–429. doi: 10.1016/j.medengphy.2005.07.019

Smith, N. P., Pullan, A. J., and Hunter, P. J. (2000). Generation of an anatomically based geometric coronary model. *Ann. Biomed. Eng.* 28, 14–25. doi: 10.1114/1.250

Sriram, K., Intaglietta, M., and Tartakovsky, D. M. (2014). Hematocrit dispersion in asymmetrically bifurcating vascular networks. *Am. J. Physiol. Heart Circ. Physiol.* 307, H1576–H1586. doi: 10.1152/ajpheart.00283.2014

Stoll, M., Quentin, M., Molojavyi, A., Thamer, V., and Decking, U. K. (2008). Spatial heterogeneity of myocardial perfusion predicts local potassium channel expression and action potential duration. *Cardiovasc. Res.* 77, 489–496. doi: 10.1093/cvr/cvm060

Strahler, A. N. (1957). Quantitative analysis of watershed geomorphology. *Am. Geophys. Union Trans.* 38, 913–920. doi: 10.1029/TR038i006p00913

Tamaddon, H., Behnia, M., and Kritharides, L. (2016). A new approach to blood flow simulation in vascular networks. *Comput. Methods Biomech. Biomed. Engin.* 19, 673–685. doi: 10.1080/10255842.2015.1058926

Tange, O. (2011). *GNU Parallel - The Command-Line Power Tool*. Berkeley, CA: The USENIX Magazine.

VanBavel, E., and Spaan, J. A. (1992). Branching patterns in the porcine coronary arterial tree. *Estim. Flow Heterog. Circ. Res.* 71, 1200–1212. doi: 10.1161/01.RES.71.5.1200

Womersley, J. R. (1955). Oscillatory flow in arteries: effect of radial variation in viscosity on rate of flow. *J. Physiol.* 127, 38P—39P.

Womersley, J. R. (1958). Oscillatory flow in arteries. III. Flow and pulse-velocity formulae for a liquid whose viscosity varies with frequency. *Phys. Med. Biol.* 2, 374–382. doi: 10.1088/0031-9155/2/4/307

Yang, J., and Wang, Y. (2013). Design of vascular networks: a mathematical model approach. *Int. J. Numer. Method. Biomed. Eng.* 29, 515–529. doi: 10.1002/cnm.2534

Yong, A. S. C., Javadzadegan, A., Fearon, W. F., Moshfegh, A., Lau, J. K., Nicholls, S., et al. (2017). The relationship between coronary artery distensibility and fractional flow reserve. *PLoS ONE* 12:e0181824. doi: 10.1371/journal.pone.0181824

Zamir, M. (1976a). Optimality principles in arterial branching. *J. Theor. Biol.* 62, 227–251. doi: 10.1016/0022-5193(76)90058-8

Zamir, M. (1976b). The role of shear forces in arterial branching. *J. Gen. Physiol.* 67, 213–222. doi: 10.1085/jgp.67.2.213

Zamir, M., and Phipps, S. (1988). Network analysis of an arterial tree. *J. Biomech.* 21, 25–34. doi: 10.1016/0021-9290(88)90188-1

Zamir, M., Wrigley, S. M., and Langille, B. L. (1983). Arterial bifurcations in the cardiovascular system of a rat. *J. Gen. Physiol.* 81, 325–335. doi: 10.1085/jgp.81.3.325

Zhang, J. M., Zhong, L., Luo, T., Huo, Y., Tan, S. Y., Wong, A. S., et al. (2014). Numerical simulation and clinical implications of stenosis in coronary blood flow. *Biomed Res. Int.* 2014:514729. doi: 10.1155/2014/514729

Conflict of Interest Statement: The authors declare that the research was conducted in the absence of any commercial or financial relationships that could be construed as a potential conflict of interest.

Copyright © 2018 Kharche, So, Salerno, Lee, Ellis, Goldman and McIntyre. This is an open-access article distributed under the terms of the Creative Commons Attribution License (CC BY). The use, distribution or reproduction in other forums is permitted, provided the original author(s) and the copyright owner are credited and that the original publication in this journal is cited, in accordance with accepted academic practice. No use, distribution or reproduction is permitted which does not comply with these terms.

frontiers in Physiology

ORIGINAL RESEARCH
published: 18 May 2018
doi: 10.3389/fphys.2018.00404

Atrial Fibrosis Hampers Non-invasive Localization of Atrial Ectopic Foci From Multi-Electrode Signals: A 3D Simulation Study

*Eduardo Jorge Godoy[1], Miguel Lozano[1], Ignacio García-Fernández[1], Ana Ferrer-Albero[1], Rob MacLeod[2], Javier Saiz[3] and Rafael Sebastian[1]**

[1] Computational Multiscale Simulation Lab, Department of Computer Science, Universitat de Valencia, Valencia, Spain, [2] Department of Bioengineering, Scientific Computing and Imaging Institute, University of Utah, Salt Lake City, UT, United States, [3] Centro de Investigación en Bioingeniería, Universitat Politécnica de Valencia, Valencia, Spain

OPEN ACCESS

Edited by:
Thomas Heldt,
Massachusetts Institute of Technology, United States

Reviewed by:
Olaf Doessel,
Karlsruher Institut für Technologie, Germany
Chris Patrick Bradley,
University of Auckland, New Zealand

***Correspondence:**
Rafael Sebastian
rafael.sebastian@uv.es

Specialty section:
This article was submitted to Computational Physiology and Medicine, a section of the journal Frontiers in Physiology

Received: 22 December 2017
Accepted: 04 April 2018
Published: 18 May 2018

Citation:
Godoy EJ, Lozano M, García-Fernández I, Ferrer-Albero A, MacLeod R, Saiz J and Sebastian R (2018) Atrial Fibrosis Hampers Non-invasive Localization of Atrial Ectopic Foci From Multi-Electrode Signals: A 3D Simulation Study. Front. Physiol. 9:404. doi: 10.3389/fphys.2018.00404

Introduction: Focal atrial tachycardia is commonly treated by radio frequency ablation with an acceptable long-term success. Although the location of ectopic foci tends to appear in specific hot-spots, they can be located virtually in any atrial region. Multi-electrode surface ECG systems allow acquiring dense body surface potential maps (BSPM) for non-invasive therapy planning of cardiac arrhythmia. However, the activation of the atria could be affected by fibrosis and therefore biomarkers based on BSPM need to take these effects into account. We aim to analyze the effect of fibrosis on a BSPM derived index, and its potential application to predict the location of ectopic foci in the atria.

Methodology: We have developed a 3D atrial model that includes 5 distributions of patchy fibrosis in the left atrium at 5 different stages. Each stage corresponds to a different amount of fibrosis that ranges from 2 to 40%. The 25 resulting 3D models were used for simulation of Focal Atrial Tachycardia (FAT), triggered from 19 different locations described in clinical studies. BSPM were obtained for all simulations, and the body surface potential integral maps (BSPiM) were calculated to describe atrial activations. A machine learning (ML) pipeline using a supervised learning model and support vector machine was developed to learn the BSPM patterns of each of the 475 activation sequences and relate them to the origin of the FAT source.

Results: Activation maps for stages with more than 15% of fibrosis were greatly affected, producing conduction blocks and delays in propagation. BSPiMs did not always cluster into non-overlapped groups since BSPiMs were highly altered by the conduction blocks. From stage 3 (15% fibrosis) the BSPiMs showed differences for ectopic beats placed around the area of the pulmonary veins. Classification results were mostly above 84% for all the configurations studied when a large enough number of electrodes were used to map the torso. However, the presence of fibrosis increases the area of the ectopic focus location and therefore decreases the utility for the electrophysiologist.

Conclusions: The results indicate that the proposed ML pipeline is a promising methodology for non-invasive ectopic foci localization from BSPM signal even when fibrosis is present.

Keywords: atrial tachycardia, body surface potential map, structural remodeling, ectopic focus location, optimal electrode location, machine-learning

1. INTRODUCTION

Focal atrial tachycardia (FAT) is a supraventricular tachycardia that triggers fast atrial rhythms from a location outside the sinoatrial node (Saoudi et al., 2001). FAT is commonly treated by radiofrequency ablation (RFA) with a high long-term success rate. The catheter ablation treatment targets the arrhythmogenic electrical drivers and terminates them by localized energy delivery. The end point of catheter based ablation is to eliminate the triggers with the least amount of ablation necessary (Santangeli and Marchlinski, 2017). In the case of FAT, the localization of those drivers tends to appear in specific hot-spots (Kistler et al., 2006), for example the pulmonary veins (PV) ostia are the most common sites of origin of focal tachycardias within the left atrium (LA) (Hoffmann et al., 2002), however they can be found virtually in any region of the atria, which makes their treatment difficult. The prevalence and distribution of focal triggers in persistent and long-standing atrial fibrillation has also been studied, showing a higher prevalence in the pulmonary veins for most groups, although non-PV triggers were observed in 11% of the cases (Santangeli et al., 2016). Electro-anatomical 3D mapping (EAM) is the standard technique used to obtain detailed intra-atrial activation sequences with the aim of bounding the source of the tachycardia (Bhakta and Miller, 2008; Santangeli and Marchlinski, 2017; Santoro et al., 2018).

Some factors might coexist with the tachycardia such as heart disease, hypertension or diabetes that could induce a structural remodeling process and the proliferation of fibrosis. Atrial fibrosis increases also with age and grows in conjunction with cardiomyopathy and heart failure (Go et al., 2001). Fibrosis has been linked to an increased incidence of rhythm disturbances via interaction with healthy tissue (Spach and Boineau, 1997). In addition, fibrosis distribution and density have been proposed as a predictor of recurrence in patients after a pulmonary vein isolation procedure by RFA (Oakes et al., 2009).

Detailed biophysical and anatomical models of the atria and torso have been successfully employed to reproduce complex electrical activation patterns observed in experiments and clinics (Trayanova and Boyle, 2014). Most of these studies, however, have focused on understanding the mechanisms that maintain certain types of arrhythmia such as atrial fibrillation (Zhao et al., 2015; Guillem et al., 2016), or spiral wave dynamics (Jalife, 2011), rather than providing solutions to tailor their treatment. In the last years, the analysis of arrhythmic patterns from non-invasive recordings such as multi-electrode surface ECGs using multi-scale biophysical models is starting to draw some attention as an alternative to EAMs (Shah et al., 2013; Giffard-Roisin et al., 2016).

The use of multi-electrode surface ECG systems allows for dense body surface potential maps (BSPM) with the aim of improving diagnosis of cardiac arrhythmia. A few attempts have been already carried out in clinics to relate BSPM-derived indices with atrial arrhythmic events induced artificially from an intracardiac catheter (Shah et al., 2013). From the modeling perspective, algorithms have been developed, mainly based on decision trees, to help identify the source of FAT from BSPM data (Kistler et al., 2006). In most of the previous studies, the presence of fibrosis has been neglected or not considered in the models. Ignoring the effects of fibrosis is a clear limitation since current-resistant fibrotic tissue affects the activation patterns.

In this study, we aim to predict the triggering site of a FAT using only BSPM data to help electrophysiologists pre- and intra-operatively, reducing the time to find and ablate the source. To achieve this goal, we have to be able to relate a BSPM-derived index with the source of a FAT even in the face of fibrosis patches that are present in different distributions and densities. In addition, we set out to ascertain the effect of fibrosis on the BSPM-derived indices. The proposed method uses machine learning techniques to develop a prediction pipeline that should be able to learn the relationship between BSPMs and ectopic foci location. We trained this system with a simulation database, generated by means of a detailed biophysical model of 3D human atria, in which we have control of the input parameters, and can simulate the desired scenarios.

2. MATERIALS AND METHODS

2.1. Anatomical Model

The 3D geometrical model of the atria and torso used in this study was previously developed (Ferrer et al., 2015). It consists of a highly detailed 3D geometric model of the atria (754,893 nodes and 515,005 hexahedral elements with a homogeneous resolution of 300 μm) coupled to a torso model (254,976 nodes and 1.5 M tetrahedral elements) made up of lungs, bones, liver, ventricles, blood, and general torso, see **Figure 1A**. The atrial model includes specific fiber orientations in 21 different atrial regions, heterogeneous tissue conductivity and anisotropy ratios and heterogeneous cellular properties adjusted following the model by Ferrer-Albero et al. (2017) and summarized in **Table 1**.

On the base atrial model, we included 5 different random distributions of patchy fibrosis in the left atrium. To define the fibrotic regions we included 50 seeds distributed among the following LA regions: Pulmonary veins, coronary sinus, ring fosa ovalis, and posterior LA wall in different proportions as in Zhao et al. (2013). Following, we grew each of the seeds using the region growing technique, so that fibrosis expanded forming patches. However, to avoid unrealistic perfect spherical fibrotic regions, we randomly reassign patchy elements back to healthy in the

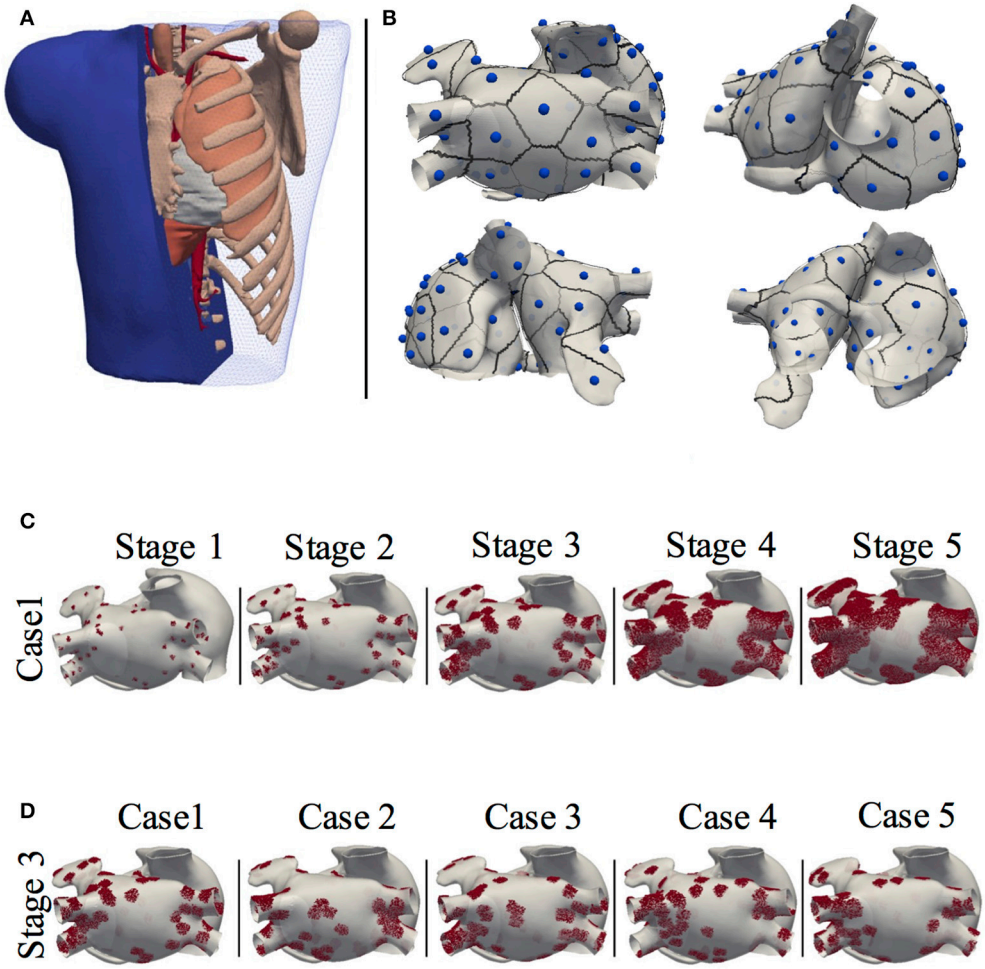

FIGURE 1 | Model of the human atria and torso. **(A)** 3D torso model of tetrahedral elements, made up of lungs, bones, liver, ventricles, blood and general torso; **(B)** Localization of the 57 ectopic foci on the atria, together with their region of influence or patch. **(C)** The 3D atria including stages of patchy fibrosis. Case 1 shown for the 5 stages of fibrosis; **(D)** Stage 3 shown for the 5 different cases.

TABLE 1 | Parameters used to reproduce cellular and tissue atrial heterogeneity.

Prop.	RA	PM	CT/BB	TVR	RAA	LA	FO	MVR	LAA	PV	CS
g_{to}	1.00	1.00	1.00	1.00	0.68	1.00	1.00	1.00	0.68	1.00	1.00
g_{CaL}	1.00	1.00	1.67	0.67	1.00	1.00	1.00	0.67	1.00	1.00	1.00
g_{Kr}	1.00	1.00	1.00	1.53	1.00	1.60	1.60	2.44	1.60	2.20	1.60
σ_l	0.003	0.0075	0.0085	0.003	0.003	0.003	0.000	0.003	0.003	0.0017	0.006
σ_t/σ_l	0.35	0.15	0.15	0.35	0.35	0.35	1.00	0.35	0.35	0.5	0.5
CV_L	63.3	115.4	100.0	63.3	63.3	63.3	0.0	62.9	63.3	75.0	97.2

contours of the growing patch in each iteration, forming random fibrotic tissue shapes that might include surviving healthy tissue surrounded by fibrosis.

The fibrotic areas were grown according to the Utah classification (Oakes et al., 2009; Daccarett et al., 2011), that defines up to four levels of LA remodeling (quartiles) of fibrosis associated to the ratio of fibrosis to atrial volume [Utah stage I: $<$ 8.1% (Q1); Utah Stage II: $<$ 16% (Q2); Utah Stage III: $<$ 21% (Q3) ; Utah Stage IV: $>$ 21% (Q4)]. Therefore, from the initial 5 fibrotic distributions, fibrosis was grown, as describe above, generating a total of 25 3D models. Note that for each of the 5 initial distributions we developed two models for quartile Q4 that we called Stage IV and Stage V. **Figure 1C** shows the atrial model for one of the 5 fibrotic distributions (Case 1) with fibrotic

patches at each of the stages, and **Figure 1D** shows the atrial model for Stage 3, and for the 5 cases of fibrotic distribution. The figure shows how fibrotic areas can have any shape and include small islands of surviving tissue within the patches. Figure S2 shows the 25 distributions of patchy fibrosis used.

2.2. Electrophysiology Modeling

For the electrophysiology simulations, we considered electrophysiological cellular heterogeneity in 10 different regions by adjusting I_{to}, I_{CaL}, and I_{Kr} in the Courtemanche-Ramirez-Nattel (CRN) ionic model (Courtemanche et al., 1998), plus the well-established fibroblast cell model by MacCannell et al. (2007) coupled to the CRN model. The tissue conductivities for each region defined together with their anisotropy ratios were obtained from Ferrer-Albero et al. (2017) and summarized in **Table 1**. The first three rows are the multiplicative factors used for the maximum conductance of three (g_{to}, g_{CaL}, and g_{Kr}) ion channels with respect to the base Courtemanche-Ramirez-Nattel (CRN) ionic model (Courtemanche et al., 1998), and the next three rows are the longitudinal conductivity (σ_l), the ratio between the transverse and longitudinal conductivities (σ_t/σ_l), and the longitudinal conduction velocity (CV_L).

Propagation of excitation in the atria was calculated solving the reaction-diffusion, mono-domain equations, Equations (1) and (2), given by Geselowitz and Miller (1983) with the finite element method using the operator splitting numerical scheme by ELVIRA software (Heidenreich et al., 2010),

$$\nabla \cdot \left(\mathbf{D}\nabla V\right) = C_m \cdot \frac{\partial V}{\partial t} + I_{ion} \quad in \quad \Omega_H \tag{1}$$

$$\mathbf{n} \cdot \left(\mathbf{D}\nabla V\right) = 0 \quad in \quad \partial\Omega_H \tag{2}$$

where $\mathbf{D}$ is the equivalent conductivity tensor, $I_{ion}$is the transmembrane ionic current that depends on the cellular model, $C_m$is the membrane capacitance and Ω_H is the heart domain.

The extracellular potentials V_e in the torso model coupled to the atria were calculated using an approximation of the bidomain model. The first step was to interpolate the transmembrane potentials (V) obtained in the hexahedral mesh nodes of the atria to the tetrahedral torso mesh, overlapping the atrial region. The second step corresponds to the calculation of the extracellular potential by solving the passive term of the bidomain model (Keller et al., 2010), Equation (3), using the finite element method with Dirichlet and Neumann boundary conditions (Weber et al., 2011).

$$\nabla \cdot \left(\mathbf{D}\nabla V\right) + \nabla \cdot \left(\left(\mathbf{D}_i + \mathbf{D}_e\right)\nabla V_e\right) = 0 \tag{3}$$

where $\mathbf{D_i}$ and $\mathbf{D_e}$ are the volume-average conductivity tensors of the intra and extracellular domains (Niederer et al., 2011).

2.2.1. Analysis of Cell Coupling

In order to analyze the coupling of the different cell models with the fibrosis, we performed a preliminary analysis on a 3D slab of tissue that combined healthy atrial tissue and fibrotic tissue to assess: (i) changes in action potential duration (APD), and (ii) conduction velocities. The 3D slab dimensions were 50 × 50 × 0.3 mm and were built with voxel elements of 300 μm in size. Several configurations of the fibrotic tissue were designed to evaluate: (i) the minimum amount of fibrosis required to produce a conduction block in a wavefront advancing perpendicular to the line of fibrosis; (ii) the minimum conduction channel (healthy tissue surrounded by fibroblast) necessary to allow the propagation of the electrical impulse.

2.3. Simulation of BSPM During Focal Atrial Tachycardia

The 3D atrial models were prepared for simulation of FAT from 19 different triggering locations (including sinus rhythm) following clinical studies (SippensGroenewegen et al., 2004). See Figure S1 for a graphical description of the 19 triggered locations selected out of the 57 initial locations included in **Figure 1A**. Triggering points were present in both the left and right atria, and were chosen to cover most of the atrial wall, in regions prone to elicit ectopic activity. Only in the case of the atrial model without fibrosis, did we consider an additional set of 38 extra triggering points in order to have more information on the healthy activation maps as in Ferrer-Albero et al. (2017). **Figure 1B** shows the 57 ectopic locations used. For a more detailed description, see Table S1, in which the different anatomical regions in the atria with simulated ectopic foci are shown. Figure S3 shows the LATs for all ectopic foci (Case 1), while Figure S4 shows their corresponding BSPiMs.

Before triggering the FAT, all 3D models were stabilized by simulating 20 heart beats in sinus rhythm with a basic cycle length (BCL) of 500 ms. This was necessary to homogenize the coupling of the different cellular populations and the fibrotic tissue, smoothing differences between neighboring regions. Next, simulations corresponding to each of the 19 ectopic beat locations were carried out for each fibrotic configuration which resulted in 475 simulations in the 3D atrial models with fibrosis, plus 57 simulations in the non-fibrotic model.

Body surface potential maps (BSPM) were obtained for all the simulations by calculating the extracellular potential at all the nodes of the torso surface. To obtain more realistic results, we added white Gaussian noise to simulate the effect of noise from muscles or other sources on the BSPM. An average P wave had a mean power of 0.003 mW (i.e., −55.2 dBW), and we added white Gaussian noise with a mean power of 0.001 mW (i.e., −60.0 dBW), yielding an approximate power ratio of 3 and S/N ratio of 4.8 dB. Afterward, we filtered the signal using a Savitzky-Golay smoothing filter that minimizes the least-square error in fitting a polynomial to frames of noisy data. It is optimal in the sense that performs much better than the standard FIR filters, which tend to filter out a significant portion of high frequency content along with the noise (Orfanidis, 1995).

Once all the filtered noisy BSPMs were obtained, the body surface potential integral maps (BSPiM) were calculated, as described in SippensGroenewegen et al. (2004). As a result, for each ectopic focus simulated we summarized each P-wave signal on the torso surface into a single value obtained from integrating the corresponding P-waves at each torso point, which resulted in the BSPiM. The integration of the BSPiM is equivalent to the average of the electrical cardiac vector over time, and therefore

describes how the depolarization wavefront advances during the activation. The BSPiMs were all normalized in the range [−1,1].

2.4. Machine Learning Pipeline

The simulation of ectopic foci allowed us to obtain a data set formed by the ectopic locations on the atria (3D points) and the corresponding BSPiMs they produced on the torso. Using this data set, machine learning techniques could be applied to establish a relationship between the location of an ectopic focus and the BSPiM map it produced. Following this idea, we designed the pipeline shown in **Figure 2** to solve the ectopic localization problem. This pipeline had five main steps. Firstly, we performed the simulations for every ectopic focus on the atria and obtained the corresponding BSPiM. Next, we performed a dimensionality reduction on the BSPiMs, followed by a clustering of BSPiMs. We validated all the clusters obtained to evaluate their *quality*. Finally, we performed a stratified cross-validation, to assess the classification accuracy of the ectopic foci into the different clusters defined. Note that in this context, a cluster of ectopic foci corresponds to a region on the atria.

The first two steps in the pipeline can be considered as a pre-processing stage, and they were necessary to generate and reduce the resolution of the raw BSPiMs, which originally had more samples than those in a real clinical setting. In this pipeline, we used two datasets, one corresponding to the 57 ectopic foci simulated without fibrosis, which contained 57 activation sequences. The second data set corresponded to the 25 fibrotic configurations × 19 triggering locations containing 475 activation sequences.

Step 1 - Atria/Torso Model simulation: In this step the simulation of ectopic foci was performed by solving Equation (1) in the atria domain and Equation (3) in the torso domain, which generated the BSPMs. After adding noise to the P-wave signals for all the computational nodes, we filtered the resulting signals. We performed a trapezoidal integration of the noisy P-wave to obtain the BSPiMs. As an example, **Figure 2** (step 1) contains the activation patterns produced by the ectopic focus LA1 (located on the left atrium (LA) posterior wall), for a configuration with fibrosis remodeling in stage III, together with the corresponding BSPiM with and without noise (frontal views) for the same ectopic focus.

Step 2 - Dimension reduction and BSPiM clustering: This step corresponded to an unsupervised learning phase to classify the filtered noisy BSPiMs that result from the activation of the different ectopic foci (457 + 57 simulations).

The computational torso model used in this pipeline had 14,157 surface nodes, and therefore provided BSPiMs with that resolution. Before the clustering phase, these dense BSPiM data sets were reduced to a more feasible clinical scenario, since current BSPM vest system technologies allow a maximum of about 256 electrodes placed on the torso of a patient (Shah et al., 2013). Therefore, the dimension of each input data set of filtered noisy BSPiM, was homogeneously reduced to a maximum of 256 nodes, (i.e., features) (see **Figure 2**, step 2, top). To select the nodes, we divided the torso domain into 256 equally-sized patches (55 nodes per patch in average), and choose randomly one of the nodes in each patch to represent the whole region. This is a sensible approach since in a clinical BSPM acquisition system the exact location and spacing of the mapping electrodes may not be perfectly preserved across patients.

The unsupervised clustering of the 256-dimensional BSPiM patterns was performed using hierarchical/agglomerative clustering. One of the benefits of hierarchical clustering is that one does not need to know in advance the number of clusters K in the dataset, assigning each sample to its natural class. We used the Ward et al. variance minimization algorithm (Ward, 1963). We started with a single cluster for each sample and iterated by finding, at each step, the pair of clusters that, after merging, produced the minimum increase in the total within-cluster variance.

We also used dendrograms for visualization in the form of trees showing the order and distances of merges during the hierarchical clustering process. We repeated this phase imposing a distance limit in the algorithm, obtaining K clusters ranging from 2 to 10 clusters (see **Figure 2**, step 2, down).

Step 3 - Clusters validation on the atrial surface: The assignation of every BSPiMs to a cluster induced a clustering on the set of ectopic foci that produced the corresponding BSPiM; if a certain BSPiM was assigned a label j by the clustering algorithm, then we assigned the same label to the ectopic location that produced that BSPiM. Now, the question to resolve was whether the clustering that was mapped onto the atria had some geometrical meaning to identify the location of the ectopic focus. To analyze this, we associated to each ectopic focus a region or patch formed by the points in the atria closer to that focus than to any other. From the clustering induced in the atria, we could associate also a patch to every BSPiM cluster, built as the union of the patches of the associated ectopic foci. In **Figure 2** (step 3, top) we show an example of the clustering generated on the atria surface. Each atrial patch associated to an ectopic focus has a color that corresponds to its class. In the example, ectopic LA1 (for $K = 6$ groups and fibrosis Stage III) was associated to the purple class.

Recall that our goal was to build a system that takes a measured BSPiM and predicts the location of the ectopic focus that generated it or, at least, a region where it could be located. Thus, the ideal situation would be that two BSPiM that are in the same cluster are the result of the same ectopic focus or, at least, of two ectopic foci that are in nearby patches in the atria. By contrast, an adverse situation would happen when similar BSPiM would be clustered together due to their similarity, but the ectopic foci that generated them were distributed along the atria and did not form a connected region on the surface. We defined a well formed region/cluster as a union of ectopic patches that was connected and only included ectopic foci from the same cluster.

Thus, we sought to assess the quality of the patches formed from the BSPiM clustering. To be able to verify this requirement we created an ectopic graph, where the nodes represent the ectopic foci and are connected by an edge if their associated patches share a border. The geodesic distances on the atria were obtained by a Fast Marching algorithm (Kimmel and Sethian, 1996). According to the ectopic graph created, a well formed patch could be identified as a connected subgraph containing all the ectopic foci of a class (see **Figure 2**, step 3, down). In this way,

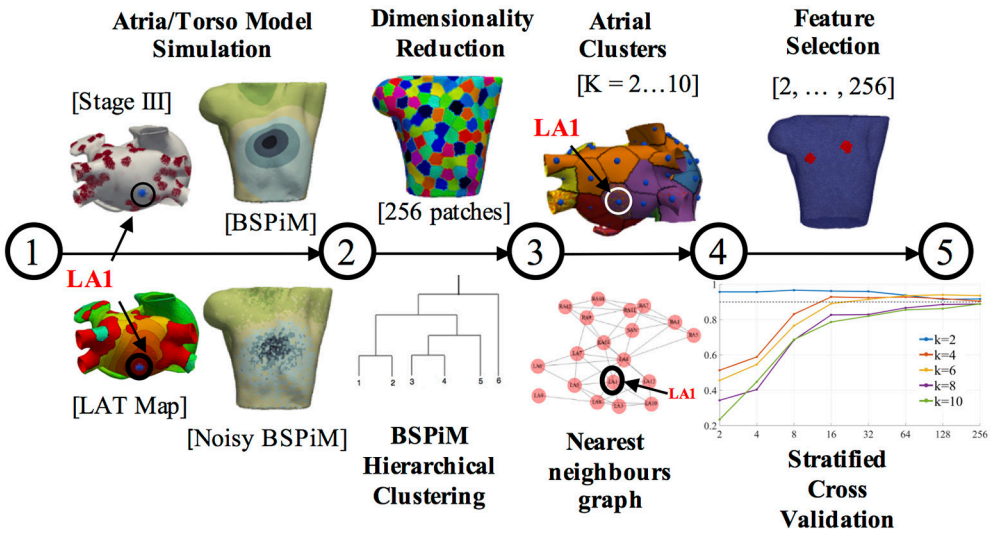

FIGURE 2 | Machine learning pipeline. The pipeline consists of 5 steps. Steps 1 and 2 are performed for each ectopic focus and fibrosis configuration. Steps 3, 4, and 5 are the training and validation phases and carried out with all the simulation results. The different torso and atrium figures shown correspond to ectopic focus LA1, located on the LA posterior wall.

we reduced the problem of deciding if a cluster is well formed to a connectivity test on the associated subgraph.

It is important to note that for each ectopic location we had 25 simulations (5 different fibrosis configurations × 5 different fibrosis stages) with differing fibrosis distribution. An ideal result would be that all the BSPiM simulations produced by the same ectopic focus end up in the same cluster, regardless of the fibrosis configuration or stage. However, due to the changes in LAT due to fibrosis such a result would have been highly unlikely.

Considering K as the number of clusters, we define the *persistence* of an ectopic location x as the number of different clusters that contains ectopic foci located at x, divided by the number of clusters, K. The best situation for an ectopic is produced when it only appears in one class (fully persistent), with a persistence value of $1/K$, while the worst situation occurs when it appears in all the classes, with a persistence value of 1. Ectopic locations with a poor value of persistence would indicate that several cluster patches overlap on that ectopic patch. This situation will be represented in our figures with regions that have spots of more than one color.

It is noteworthy, however, that a poor persistence value does not necessarily lead to a bad prediction situation. Although an ectopic location is in, say, three clusters, if the three clusters are well formed the system will still be able to indicate a meaningful region for the ectopic when a BSPiM is processed.

Step 4 - Feature selection: In addition to the dimensionality reduction carried out before the clustering step, we performed a feature selection step, in this case to select the best features among the 256 (see **Figure 2**, step 4, top). The reason for this further selection is that in many clinical procedures the number of available electrodes is far below 256. We wished to establish the minimum number of electrodes necessary to build a successful prediction system and to determine what their optimal locations are.

In our context, we will consider that a feature (representing an electrode location) is less relevant than another when its value is independent of the classification of the sample, from a probabilistic point of view. We performed a hypothesis contrast on the data set to assess the dependence of each component of the BSPiMs data with the class distribution of the samples. Given a feature, we consider its value and the class of the samples in the data set as random variables. Using the chi-square (χ^2) test, if a small p-value is found for a given feature, it shows statistical evidence that the value of that feature is not independent from the class of the sample. Then, we keep the N best features and disregard those that are most likely to be independent of the class label. This process is repeated for $N = 2, 4, 8, 16, 32, 64, 128, 256$, which permits us to compare the performance of the system as a function of the final number of features selected.

Step 5 - Ectopic foci Classification: As a result of the cluster validation process, the generated clusters can be viewed as groups of patches on the atrial surface that relate to BSPiMs patterns. We trained a classifier able to classify any BSPiM into one of the clusters defined, that would point to a patch group [atrial region(s)]. For each number of clusters ($K = 2$,...10), we constructed a supervised learning model using a support vector machine (SVM) using the implementation in Pedregosa et al. (2011) and Buitinck et al. (2013). The SVM does the classification of the data finding the best hyperplane that separates all data points of one class from those of other classes. We used a 4-fold stratified cross validation process where different SVMs were trained to avoid over-fitting and to evaluate the prediction accuracy and the generalization level obtained. We adjusted the parameters (i.e., a regularization term) of a radial basis kernel

for the decision function. Folds were selected so that the mean response value was approximately equal in all of them. Each fold contains the same proportion of ectopic foci from each cluster, and all the ectopic foci were tested. Having 4-folds leaves 75% of samples for training and 25% of samples for testing in each fold.

3. RESULTS

3.1. Simulations on a 3D Slab of Tissue

In a first evaluation, we analyzed the amount of fibrosis required to produce a conduction block. We included in the slab modeled as LA posterior wall tissue, a cross-wise line of fibroblast cells with different width (x-axis) to evaluate the effect on the propagation (see **Figures 3A–D**). We stimulated the slab with a cross-wise flat impulse that progressed activating the full width of the slab from bottom to top. **Figure 3A** shows a slab configuration free of fibrosis. The time required for the wavefront to travel the full size of the slab was 59 ms. **Figure 3B**, shows a slab that includes a cross-wise line of 0.3 mm modeled as fibroblast cells. The activation time was 62 ms, therefore the fibroblasts introduced a delay in the propagation wavefront of 3 ms (5% increase). When the fibrotic barrier was 0.6 mm, the wavefront took 71 ms to reach the top of the slab, that is a 12 ms delay (20% increase) with respect to the healthy configuration (see **Figure 3C**). When the barrier was increased to three voxels, i.e., 0.9 mm width, there was a conduction blockage (see **Figure 3D**). The results clearly show that the effect of fibrosis on the propagation wavefront in our model is not linear.

In a second evaluation, we inverted the configuration of the tissue types of the slab, that is, all tissue was modeled as fibroblast, except a conduction channel modeled as healthy atrial tissue, with different width {[1.4, 1.5, 1.8, 2.4, and 2.7 mm] (x-axis) × [0.3 mm] (z-axis)}. The goal was to determine the minimum width required for a conducting channel to propagate the electrical impulse when it is surrounded by fibrotic tissue. **Figure 3E** shows a slab of fibrosis tissue with a conduction channel of 1.8 × 0.3 mm, where we studied the AP at 4 locations distributed along the conduction channel. **Table 2** summarizes the results obtained. Location 1 (trace in red color) shows the largest AP amplitude, since it is closer to the initial electrical shock delivered. Resting potential is elevated in all cases, but the effect is larger at locations 2, 3, and 4. **Table 2** shows the AP values for locations 1 and 4, and for each channel width tested. The channel with a width of 1.2 mm produced a propagation block a few millimeters from the initial impulse. The intermediate channel (1.5 mm), propagated the signal, but the amplitude of the signal at the channel exit (location 4) was reduced by 54%, whereas in the wider channel (1.8 mm) it was reduced by 48%. All the $APDs_{90}$ measured, for all locations in the conduction channel, were greatly reduced with respect to the APD for the original model. With respect to the delay, it was clear that the electrotonic coupling affected the AP rising time, with an increase of 40 ms in the propagation delay when channels were reduced to 1.5 mm. That delay equates to a decrease in conduction velocity from 0.85 to 0.50 m/s, due only to the effect of fibrosis coupling. Channels larger than 3.0 mm permitted a normal propagation of the signal in the center of the channel, with respect to conduction velocity and APD morphology.

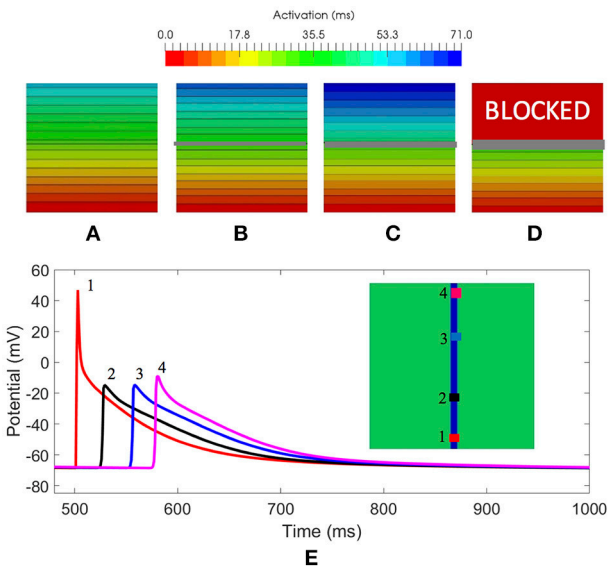

FIGURE 3 | 3D slabs of left atrial tissue including fibrosis barriers. **(A)** Shows a slab free of fibrosis with an activation time of 59 ms; **(B)** a slab with the same properties and a cross-wise barrier of one voxel element width (x-axis) of fibroblast cell model, taking a time for activation of 62 ms; **(C)** 3D slab including a cross-wise barrier of two voxel elements width (x-axis) of fibroblast cell model, taking a time for activation of 71 ms; **(D)** 3D slab including a barrier of three voxel elements width (x-axis) of fibrosis tissue model where the propagation front is blocked; **(E)** Study of the effect on the AP at 4 locations along a conduction channel of healthy atrial tissue with a width y-axis of 1.8 and 0.3 mm, on a slab of fibrosis tissue.

Finally, using the same size and number of voxel elements, we analyzed the propagation changes as a function of the 5 different stages of patchy fibrosis, from less dense (Stage I) to more dense (Stage V) of fibrosis (see **Figure 4A**). The figure shows that as we increase the level of fibrosis, paths are formed by the fibrosis patches.

We also assessed the influence of the electrotonic interactions between atrial tissue myocytes and random shape and size fibrotic patches on the AP, APD, and the resting membrane potential (RMP); with that purpose, we used six probes located in different positions within the 3D slab of tissue with Stage IV of fibrosis. Those locations were selected to go across different areas of the slab, from a channel free of fibrosis to an area well inside a higher density zone of fibrosis, see **Figure 4A**, labeled Stage IV.

To appreciate the changes in the AP when coupling myocytes to fibroblasts, and the cell-to-cell electrotonic interaction, we overlapped the AP signals measured at each probe, together with an AP measured in a healthy myocyte, as control. **Figure 4B** together with **Table 3** show those effects.

Electrophysiological effects on the Courtemanche-Ramirez-Nattel myocytes when coupling to the active formulation of MacCannell fibroblast model due to the cell-to-cell electrotonic interaction, caused a reduction of AP amplitude which can be appreciated with respect to the control trace as soon as the

TABLE 2 | Properties of AP in the entrance and exit [locations (1)/(4)] of a conduction channel.

Channel width	1.2 mm	1.5 mm	1.8 mm	2.4 mm	2.7 mm	>3.0 mm
RMP (mV)	−63.6/–	−66.3/−65.8	−68.5/−68.0	−71.4/−71.0	−72.7/−72.2	−79.91
Peak value (mV)	39.4/–	43.0/−15.2	46.7/−9.0	50.7/−1.7	52.9/0.2	0.73
APD90 (ms)	65.0/–	104/122	127/168	153/189	161/195	252
Delay (4)-(1) (ms)	–	99.0	76.0	60.0	60.0	59.0

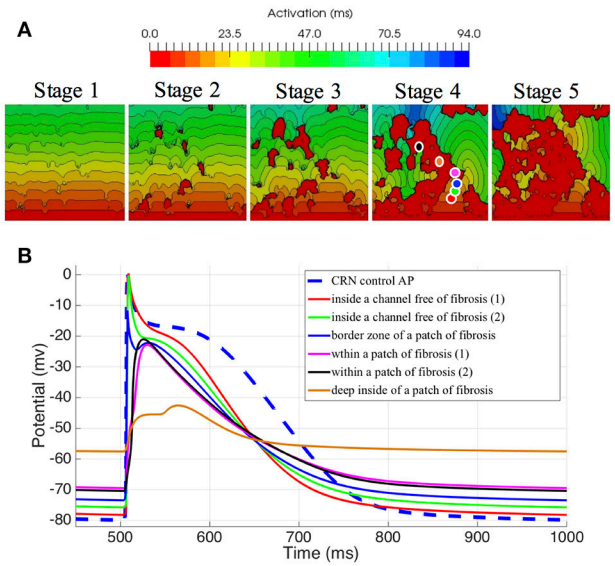

FIGURE 4 | Electrophysiological effects on the Courtemanche-Ramirez-Nattel myocytes when coupling to the active formulation of MacCannell fibroblast model. **(A)** shows the local activation time map on 3D slabs of tissue that include fibrotic tissue in increasing amount (left to right). The color corresponds to the local activation time in ms. **(B)** shows the action potential on specific locations obtained from the 3D slab with fibrosis in Stage 4. Note that the color of each plot refers to the corresponding color-coded disc in the figure above.

probe was near a more dense patchy fibrosis area. It produced a reduction of AP plateau, and a clear shortening of the myocyte APD90 with respect to the control AP and variable depending the location of the probe and the density of fibrosis. APD50 showed a more constant reduction of the APD as we went deep inside fibrotic areas showing a clear deformation of the AP profile. Also, it produced a prolonged repolarization of the AP compared to the uncoupled myocyte, and more significantly, fibroblasts had a higher resting membrane potential (RMP) and hence affected directly the myocyte RMP, which was constantly elevated (see **Figure 4B**).

3.2. Simulations on the Atria-Torso Model

Once the atrial simulations were completed, from the 475 simulations that included fibrosis, 54 of them were excluded because they did not trigger the FAT activity due to the proximity between the ectopic location and the fibrotic tissue. The excluded simulations were 5 from the Stage 3, 20 from the stage 4, and 29 from the stage 5. Activation maps for stages with more than 15% of fibrosis showed both conduction blockades and delays in propagation, fundamentally around the pulmonary veins, but also in some critical areas that prevented the electrical communication between both atria through standard pathways. As expected the larger changes in LAT maps were for stages 4 and 5 due to the conduction delays and blockades that changed the standard activation sequences (see **Figure 5A** and Figure S3). **Figure 5** shows the LAT maps and BSPiM for two ectopic foci, LA1 located in the posterior LA wall and LA10 located in the area of the bicuspid mitral valve ring embraced by the coronary sinus. LA1 activation sequence was not greatly affected by the fibrosis along the different stages, except for the left atrial appendage and the pulmonary veins which did show very low voltage potentials that did not contribute to the activation sequence (**Figure 5A**, red regions). The corresponding BSPiM patterns showed little differences where the maximum values drifted slightly and the isochrones expanded. On the other side, LA10 showed important differences between stages for several reasons. Firstly, the communication between atria through Bachmann's Bundle was compromised, delaying the activation of the RA. Second, the activation of the LA appendage was also delayed as happened with LA1. As a result, LA10 BSPiM for stages 4 and 5 resembled LA1 more than LA10, which could hamper the training system that classifies ectopic foci.

3.2.1. Clustering of BSPiM Maps

For the clustering, learning, and classification of the ectopic foci we created six different subsets of BSPiMs named M0, …, M5. **Table 4** summarizes the data included in each of those models. Model M0 includes the control data set without fibrosis, where FAT is triggered from 57 ectopic foci. The rest of models M1–M5 include fibrosis and are triggered from 19 locations. For instance, model M1 includes cases 1 to 5 with fibrosis stage 1 which makes 95 simulations. In some models simulations that did not propagate were excluded: 5 for M3, 20 for M4, and 29 for M5.

The clustering of the BSPiM maps obtained with the hierarchical/agglomerative clustering predicted a number of groups. **Figure 6** shows, as an example of the performed hierarchical/agglomerative algorithm, the dendrograms for the model M1. The hierarchy levels (from 1 to 9) as a function of the separation distance (green arrow) are indicated by the horizontal dotted lines, and the clusters (K) being formed at each iteration, which are shown on the y right axis from $K = 2$ to $K = 10$. At each iteration the clusters being split have the smallest distance according to the Ward et. al. linkage algorithm (Ward, 1963).

TABLE 3 | Effects of fibroblast-myocyte interaction on the Action Potential (Shown for the Stage 4 of fibrosis).

AP measurement/trace	Control	Red	Green	Blue	Magenta	Black	Orange
RMP (mV)	−79.9	−78.2	−75.7	−73.4	−69.4	−70.3	−57.5
Peak value (mV)	0.73	0.39	−0.16	−11.67	−22.85	−21.04	−42.58
Amplitude (mV)	80.66	78.59	75.60	61.77	46.63	49.33	14.97
APD90 (ms)	252	209	212	224	219	218	200
APD50 (ms)	153	105	94	101	85	87	52

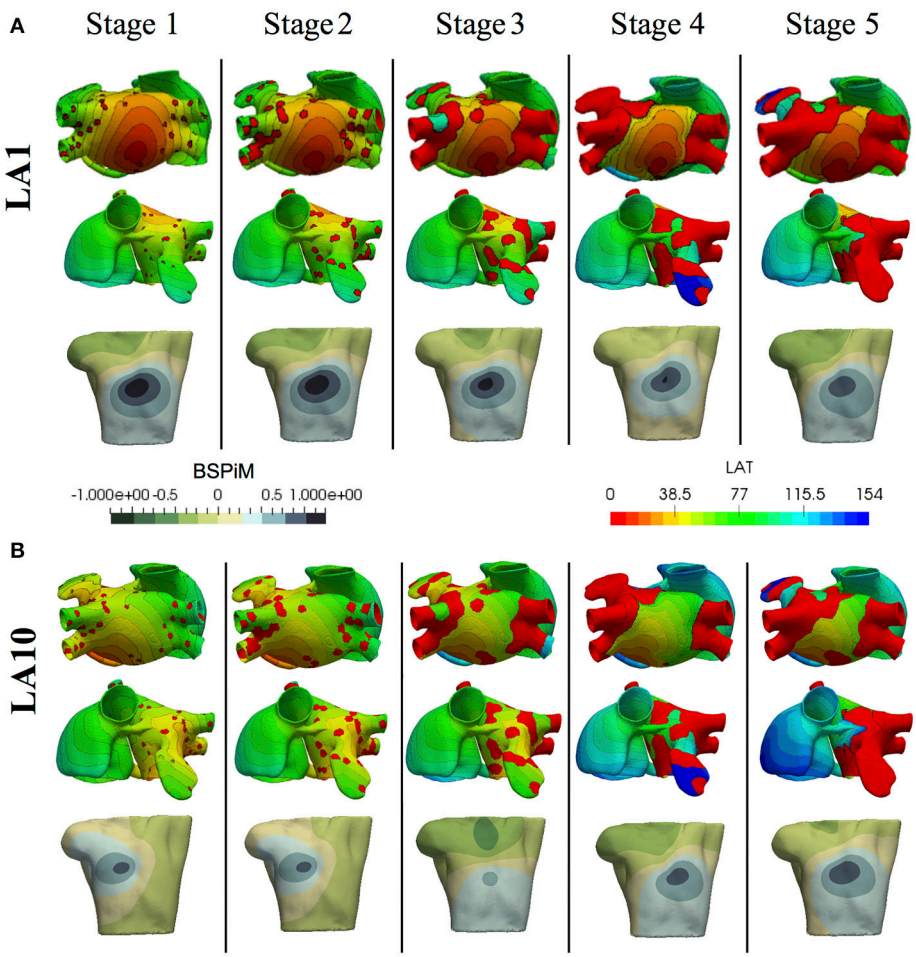

FIGURE 5 | Local activation time (LAT) maps and BSPiMs generated by ectopic foci **(A)** LA1 and **(B)** LA10 for the 5 Stages of fibrosis and simulated for case 1, and the 5 stages of fibrosis.

Figure 6 shows how in its first iteration the linkage algorithm decided to split the 95 original samples of model M1 in two clusters ($K = 2$), one with 30 samples (number of samples per cluster shown in blue) and the other with 65 samples, with a large separation distance. In the second iteration, the cluster with 65 samples was divided by the algorithm in two clusters, generating 3 clusters in total with 30, 25 and 40 samples respectively ($K = 3$). Following iterations keep dividing and merging the data set, up to the imposed limit of level 9 and $K = 10$, where the clusters formed had few samples and a quite small separation distance, making further iterations pointless in terms of the subsequent classification stage.

The x axis shows the color coded labels of the ectopic foci grouped for $K = 10$ (i.e., level 9 and last iteration). It is important to recall that a particular ectopic focus should be the same for any of the 5 different distributions of fibrosis (i.e., Case 1 to Case 5). The groups formed are shown separated by a thick black vertical line. At this hierarchy level, the simulations for ectopic focus LA5 (simulated 5 times for M1, corresponding to Case 1 to Case 5) did not fall in the same cluster, but 3 BSPiMs were classified

into Class 3, and 2 BSPiMs to Class 4 (see **Figure 6**, encircled labels). This fact indicates how the presence of fibrosis, already in Model M1, starts to affect the BSPiM profiles, and consequently the clustering process.

The clustering of the BSPiM maps obtained above corresponds to groups formed by ectopic locations on the atria. When we choose $K = 2$, for example, all ectopics were arranged into cluster 1 or 2, if we chose $K = 6$, all ectopics were then distributed into clusters 1–6.

3.2.2. Association of BSPiM Clusters to Regions on the Atria

After clustering the BSPiM maps, we associated to each cluster the ectopic beats that generated the corresponding BSPiM in the cluster. Next, for each cluster, we summed the areas on the atria surface that were linked to each ectopic beat, i.e., the ectopic patches. We obtained this measure for $K = 2$ to $K = 10$. For example in the case of $K = 2$ we had the area of cluster 1 and cluster 2, and then calculated the mean area, and the standard deviation in the areas, to obtain a single representative measure of the atrial regions. Note that if a given patch in the atria had two labels (it was expected to have a single label), its area would be summed twice to take into account the existence of region overlaps.

This measure is shown in **Table 5** as $\hat{x} \pm \sigma$ (cm^2). The results show, as expected, a decrease in the mean and standard deviation of the region area as we incremented the number of clusters from $K = 2$ to $K = 10$ (row wise). When we analyzed those areas moving from M1 to M5 (column wise), there was an increase of the areas as the level of fibrosis increased. This finding is due to the region label overlap, since when a patch is labeled with more than one label it contributes to the sum of areas of more than one region. Therefore, the sum of all areas of all regions is larger than the area of the atria surface when there is label overlap. This increment is explained with another measure which is the ectopic persistence within the clustering process.

Figure 7 shows the 19 atrial patches for the models M1, M3, and M5 (an increasing level of fibrosis) color-coded with the assigned label for $K = 6$ and $K = 8$ (in three different atrial views). Patches with the same color form a unique region that relates to a group of BSPiM patterns. When a patch within a region shows more than one color or label (a region with different colored dots), it means that two different BSPiM could be mapped to the same patch due to the variability introduced by the fibrosis.

TABLE 4 | Models created for the clustering, learning, and classification steps of the pipeline.

Model	Fibrosis	Stages	# BSPiMs
M0	No	–	57
M1	Yes	[1]	95
M2	Yes	[1,2]	190
M3	Yes	[1,..,3]	280
M4	Yes	[1,..,4]	355
M5	Yes	[1,..,5]	421

The table shows the levels of fibrosis and the number of BSPiMs included in each model as data set.

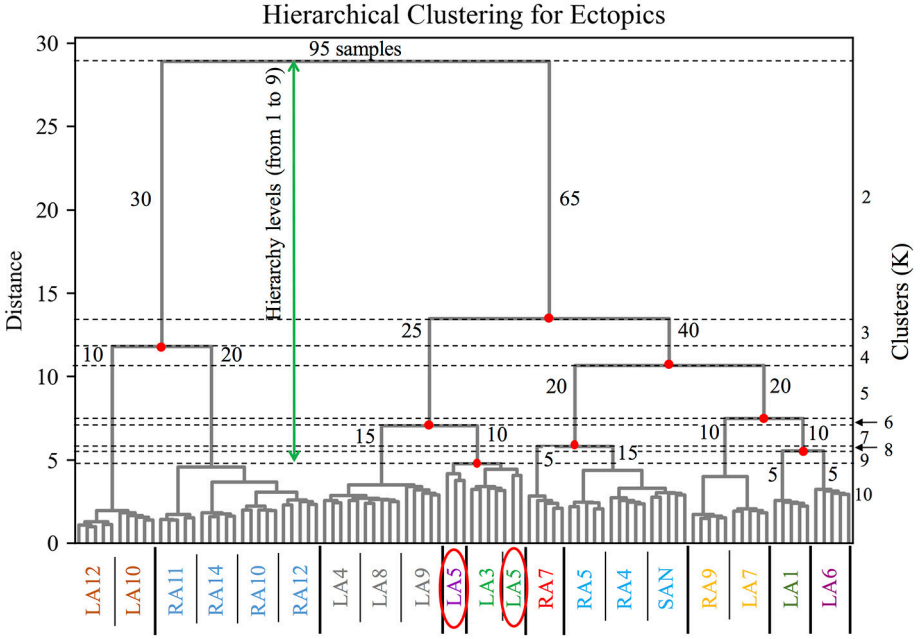

FIGURE 6 | Dendrogram of the hierarchical/agglomerative clustering algorithm for the model M1. Hierarchical levels are indicated by the horizontal dotted lines from 1 to 9 (green arrow), the *y* axis on the left shows the distance between levels, and on the right the clusters being formed after merging and splitting samples (number of samples) at each level from $K = 2$ to $K = 10$. The *x* axis shows the color coded groups of ectopic labels separated by the thick vertical black line. The red ellipses show the particular case of the BSPiM produced by the ectopic LA5, being grouped in two different clusters, 3 samples to cluster 3, and 2 samples in cluster 4.

TABLE 5 | Clustering performance results for the models M0–M5.

K_i	Measure	M0	M1	M2	M3	M4	M5
K2	$\hat{x} \pm \sigma$	66 ± 41	68 ± 39	78 ± 53	81 ± 49	68 ± 67	84 ± 44
	OR	–	–	10.53	15.79	–	21.05
	CR	100	100	100	100	100	100
	CA	0.98	1.00	1.00	0.99	0.97	0.91
K4	$\hat{x} \pm \sigma$	33 ± 14	34 ± 16	39 ± 22	40 ± 30	52 ± 28	61 ± 17
	OR	–	–	10.53	15.79	42.11	52.63
	CR	100	100	100	100	100	100
	CA	0.94	0.85	0.93	0.84	0.90	0.90
K6	$\hat{x} \pm \sigma$	22 ± 10	22 ± 13	27 ± 14	32 ± 20	42 ± 25	44 ± 25
	OR	–	–	15.79	36.84	63.16	68.42
	CR	100	89.4	100	94.7	94.7	94.7
	CA	0.91	1.00	0.96	0.97	0.96	0.93
K8	$\hat{x} \pm \sigma$	16 ± 9	17 ± 7	20 ± 13	27 ± 15	37 ± 20	43 ± 19
	OR	–	–	15.79	47.37	68.42	73.68
	CR	100	84.2	89.4	94.7	89.4	89.4
	CA	0.92	1.00	0.98	0.96	0.93	0.88
K10	$\hat{x} \pm \sigma$	13 ± 8	14 ± 8	17 ± 11	24 ± 15	32 ± 17	37 ± 17
	OR	–	5.26	21.05	52.63	78.95	78.95
	CR	100	78.9	84.2	89.4	89.4	89.4
	CA	0.85	1.00	0.98	0.96	0.89	0.88

$\hat{x} \pm \sigma$: Mean Area ± Standard Deviation (cm^2).
OR: Overlapped ratio (%).
CR: Connectivity ratio (%).
CA: Classification Accuracy - Results for 256 characteristics.

Therefore, patches colored as "red" and patches with "red dots" were all considered as a single region. However, our goal was to create regions that were as small as possible, in order to reduce the search area of the ectopic focus.

3.2.3. Ectopic Focus Persistence Within a Clustering Process

When models with fibrosis were included, they did not cluster properly into non-overlapped groups since BSPiM were highly altered by the conduction blocks. From stage 3 (i.e., 15% fibrosis) onwards the BSPiMs showed large differences for ectopic beats placed in the pulmonary veins, as can be seen in the example of **Figure 5B**, where the LATs of ectopic LA10, from Stage 3 to Stage 5 of fibrosis, show clear blockades at the pulmonary veins and left atrial appendage, and consequently completely different BSPiMs with a lesser level of fibrosis.

From the dendrogram of **Figure 6** we observed that for the Model M1, when $K = 10$, due to the variability among these BSPiMs, we found that 3 of the LA5 BSPiMs were grouped into cluster 3 while the 2 remaining BSPiMs (with more fibrosis) were in cluster 4. This result indicates that samples of the ectopic LA5 have been spread into two clusters, so the corresponding atrial patches will overlap on the atria surface exactly on LA5. In **Figure 7**, ectopic foci locations with poor persistence values show regions that have spots of more than one color, indicating overlap. Figure S5 shows, as an example, the BSPiM together with their labels for model M3 and $K = 6$. A given ectopic focus can be classified into two different classes as a function of the fibrosis, e.g., class green and red for LA1.

For the results of the persistence analysis, we calculated the ratio of ectopics that appear in more than one cluster with respect to the total number of ectopic foci in the atria, (i.e., 57 ectopics for model M0, and 19 ectopics for models M1 to M5); **Table 5** displays this measure as Overlapped Regions (OR).

The Model M0 (no fibrosis), showed, as expected, no overlap, given that there was no more than one label per ectopic focus (i.e., OR = 0). Results are summarized in **Table 5**. For the models with fibrosis, there was an increase of overlap as we incremented the level of fibrosis from M1 to M5 (column wise) and an increase of overlap as K increased from 2 to 5 (row wise), with the particular case of M1 with no overlap except for $K = 10$ with LA5 being spread in two clusters and OR = 5.26.

3.2.4. Geometrical Consistence of Clusters

The analysis of the cluster connectivity using graphs permitted us to identify which clusters were not well formed, i.e., were not connected. We always preferred connected regions without holes or islands over the atria surface, otherwise when we associated an ectopic focus to a cluster, the cluster was scattered in several regions of the atria instead of having a connected and delimited one.

We calculated the ratio of well-formed clusters or connected clusters (i.e., well formed over all clusters) as the measure

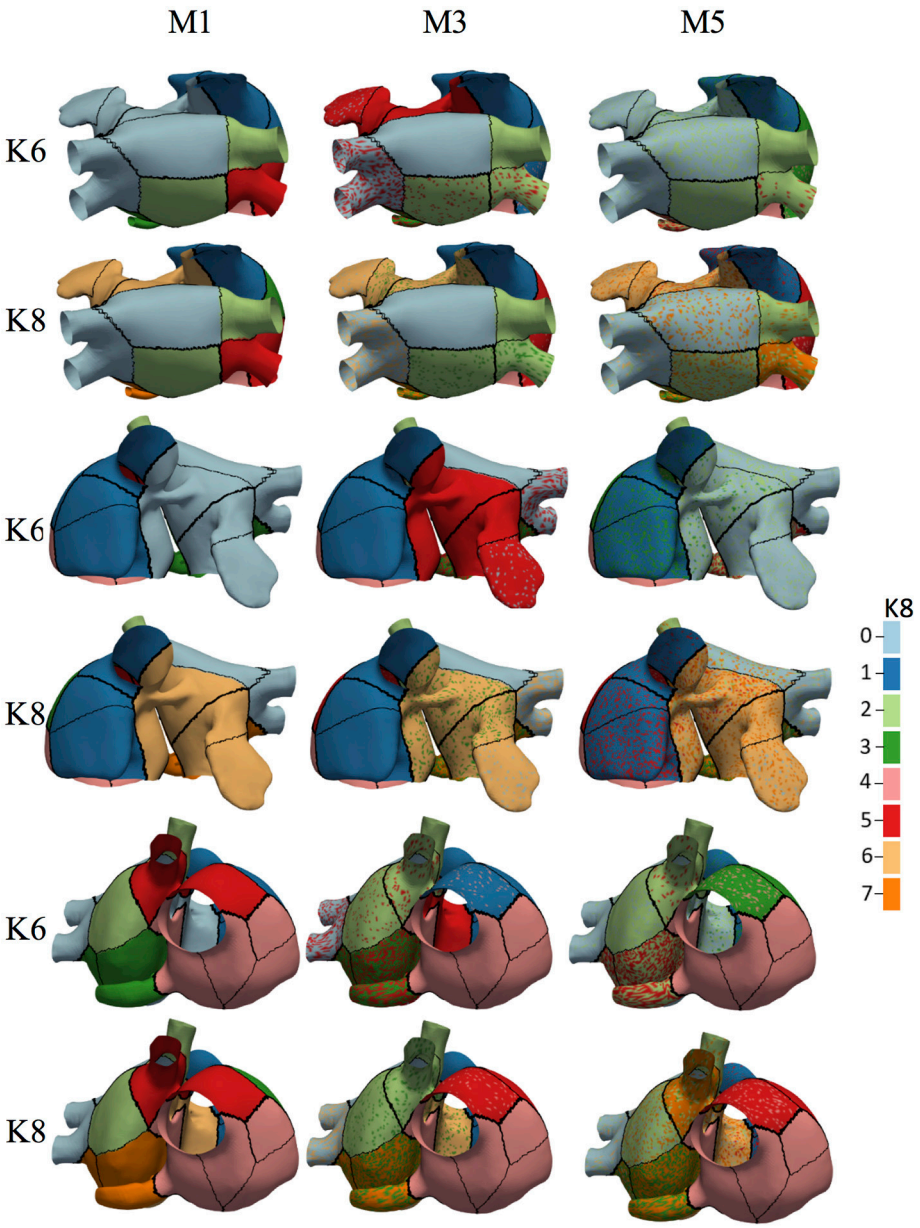

FIGURE 7 | Associated BSPiM clusters for models M1, M3, and M5, for $K = 6$ and $K = 8$ (color coded) to the 19 patches defined by the atrial ectopic foci simulated with fibrosis (three different views). Regions including colored dots indicate that samples of a particular ectopic focus have spread into two or more clusters, and the corresponding atrial patches overlapped on the atrial surface exactly at that ectopic focus. Model M1 shows no overlapping for $K = 6$ and $K = 10$, and models M3 and M5 show an intensification of overlapping as the fibrosis stage increased. The color legend indicates the class/cluster number assigned to each atria patch.

Connection Ratio (CR) from the validation process of the model M0 without fibrosis, and the five model configurations (M1–M5) with fibrosis, for K ranging from 2 to 10 clusters. Results are summarized in the **Table 5**.

For the Model M0 (no fibrosis), from $K = 2$ to 10, the Connection Ratio (CR) was 100%. The results for the model M1 (with fibrosis), for $K = 2$ and $K = 4$ show that the connection ratio was 100% and maintained with all models and levels of fibrosis (column wise). When we increased the number of groups from $K = 6$ to $K = 10$ (row wise), but also with the increase of fibrosis from M1 to M5 (column wise) there was a variable decrease of the ratio CR, implying the loss of connection or isolation of some ectopics from the groups. This effect depended on the different configurations of the patchy fibrosis (see **Table 5**).

As an example, the **Figure 8** depicts at the top row, on the left, the complete ectopic graph of the atria with the nodes representing the 19 ectopic foci connected by edges; the rest of the figure shows the 6 subgraphs of each class, formed after clustering the model M1 for $K = 6$. The subgraph in the middle row, on the right, shows the ectopic

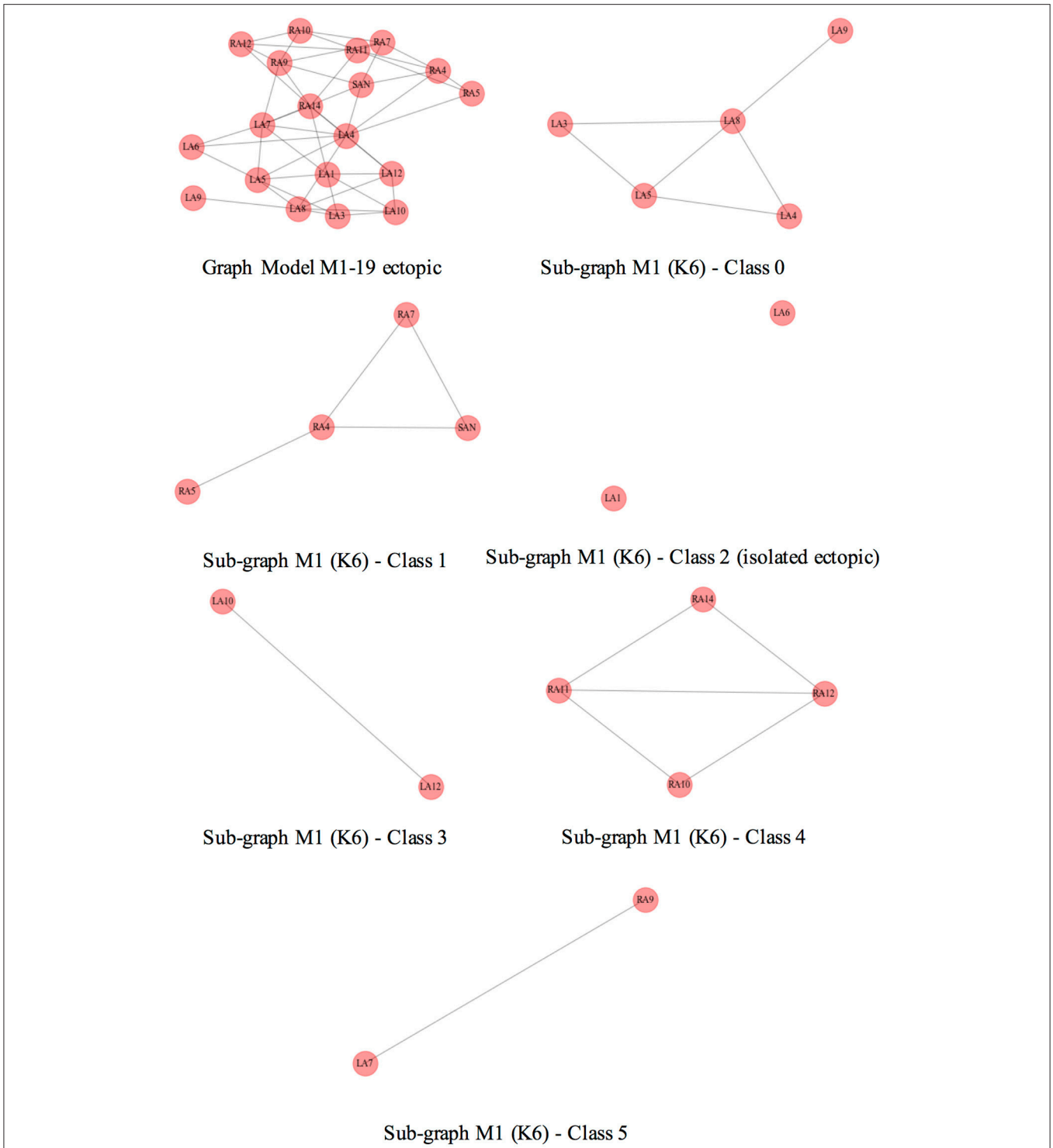

FIGURE 8 | Geometrical consistence of clusters. Top row, on the left, shows the complete graph of the atria where the nodes represent the ectopic foci connected by edges. The rest of the figure shows all the subgraphs that represent the classes of the model M1 and $K = 6$. All of them are well formed connected subgraphs, except for the one at the middle row, on the right, representing ectopic foci LA1 and LA6 of the class 2 and indicating no connected nodes.

foci LA1 and LA6 with no connection, (i.e., 2 isolated nodes with respect to 19 total nodes, therefore a CR of 89.4%).

We observed that the isolated ectopics for the particular case of model M1 were mainly the LA1 and LA5, both located at the center of the posterior wall of the left atrium, lower and upper

regions, respectively, and LA6 at the upper Right pulmonary vein. More ectopics were located in the right atrium, RA7 and RA11, right above the pectinate muscles. In the case of the model M2, the isolated ectopics were the same as in model M1, except for LA1; for the models M3 to M5, the isolated ectopics were LA7, at the lower right pulmonary vein, and LA9 at the left appendage.

3.3. Classification of Atrial Ectopic Focus

After the analysis of the persistence and geometrical consistence of the clustering process, we performed a classification of the ectopic foci, according to the step 5 of our pipeline. The **Figure 9** gives an example of the calculation of the accuracy for the model M0, no-fibrosis, and the extreme case of the model M5 that includes all the stages of fibrosis. The values obtained came from the cross-validation process which averages the accuracy obtained for each fold and summarizes the result. We used 4-folds to split and stratify homogeneously the training set and the test set. We have also included in the plot a dotted line (accuracy $= 0.90$) that is the minimum level of accuracy that we considered necessary to use the model in a clinical environment.

3.3.1. Classification of Non-fibrotic Cases

Table 5 shows the measured classification accuracy (CA) for 256 features for the model M0 (i.e., no-fibrosis) and for $K = 2$ to $K = 10$. The results show that for this case of no-fibrosis we obtained an accuracy CA > 0.90 for $K = 2$ to $K = 8$, and a minimum accuracy CA $= 0.85$ for $K = 10$. **Figure 9A**, shows the complete accuracy obtained by the classification of the model M0 for features or electrodes from 2 to 256. In the cases $K = 2$ to $K = 8$ we recorded an accuracy of CA $>$ 0.90 even with only 64 features or electrodes, and for $K = 10$ the accuracy was entirely below the dotted line of CA $= 0.90$. Inset **Figure 9A**, shows a torso with an example of the optimal electrode locations selected from the 256-electrode BSPiM to perform the ectopic foci classification in groups. For example, yellow spheres correspond to the best set of 2 electrodes, whereas yellow together with green spheres correspond to the best set of 4 electrodes. Larger sets of optimal electrodes always contained smaller sets. There were no intersecting classes, and all the ectopic groups were associated to different regions.

3.3.2. Classification of Fibrotic Cases

We introduced incrementally in the training phase for classification those fibrotic cases from model M1 to model M5 (i.e., data from all FAT simulations, and all configurations of fibrosis). **Table 5**, shows the measured CA for the models M1 to M5 for $K = 2$ to $K = 10$ and 256 features, where the values of accuracy remained almost all above CA > 0.90 for all the models with slight variations, except for model M3 and $K = 4$, that showed a minimum of CA $= 0.84$.

Figure 9B shows the complete accuracy obtained for the extreme case of M5 (i.e., Stage 5 of fibrosis). We see, in this case, from $K = 2$ to $K = 6$ that we need a minimum of 16 features to obtain an accuracy CA $= 0.90$, and a maximum of CA $= 0.93$ with 256 features for $K = 6$. From $K = 8$ to $K = 10$ the values of accuracy are below the dotted line of 0.90, obtaining values of CA $= 0.8$ for both, $K = 8$ and $K = 10$. Figure S6 includes accuracy plots for all the models, M0–M5.

4. DISCUSSION

4.1. Coupling Atrial Myocytes and Fibroblast

Several modeling studies have illustrated the impact of fibrosis on atrial electrophysiology and conduction as well as on ECGs and showed in a realistic atrial anatomy that increased anisotropy in the atria due to fibrosis can be responsible for the breakup of PV ectopic waves into multiple re-entrant circuits. Maleckar et al. (2009) coupled a human atrial myocyte to a variable number of fibroblasts and investigated the effect of altering the intercellular coupling conductance, electrophysiological fibroblast properties, and stimulation rate on the atrial AP. The results demonstrated that the myocyte resting potential and AP waveform are modulated strongly by the properties and number of coupled fibroblasts, the degree of coupling, and the pacing frequency. Jacquemet et al. developed a 2D model of atrial tissue including microfibrosis incorporated as a set of thin collagenous septa (sheets) of cardiac muscle to determine whether they, like thick collagenous septa, could affect electrical impulse propagation and disconnect transverse coupling (Jacquemet, 2012). The density and length of these septa were varied and the analysis of unipolar electrograms showed that the septa decreased conduction velocity (CV) by up to 75%. Another important aspect to be considered is the existence of collagen layers in the fibrosis model. Atrial models incorporating transverse collagen deposition have underlined the significant interruption and disorder in atrial conduction patterns (Boyle et al., 2016). Not only the total amount of collagen was important, but also the specific spatial distribution of collagen deposition, which governed the occurrences of conduction block. Another novel arrhythmic mechanism being considered in models is percolation (slow and difficult fluid flow through a porous medium). It has been shown that simulation of conduction obstacles derived from LGE-MR images of AF patient atria, give rise to excitation patterns resembling near-threshold percolation (Vigmond et al., 2016). In this context, the percolation threshold is the fraction of lattice points that must be filled to create a continuous path of nearest neighbors from one side to another.

In our study, we evaluated the degree to which coupling fibroblasts to atrial myocytes altered the electrophysiology of the normal myocytes. Our simulations confirmed that the coupling of fibroblasts to myocytes significantly affects the electrophysiological properties of the myocytes, as described by MacCannell et al. (2007), Maleckar et al. (2009), and Morgan et al. (2016).

The coupling of the CRN (Courtemanche et al., 1998) atrial myocyte model to the active formulation of the MacCannell fibroblast model (i.e., 4 membrane currents including, the time and voltage dependent fibroblast current I_{Kv}, the inward rectifying current I_{K1}, the Na^+-K^+ pump current I_{NaK}, and the background Na^+ current $I_{b,Na}$) (MacCannell et al., 2007), and the cell-to-cell electrotonic interaction, caused: (i) a reduction

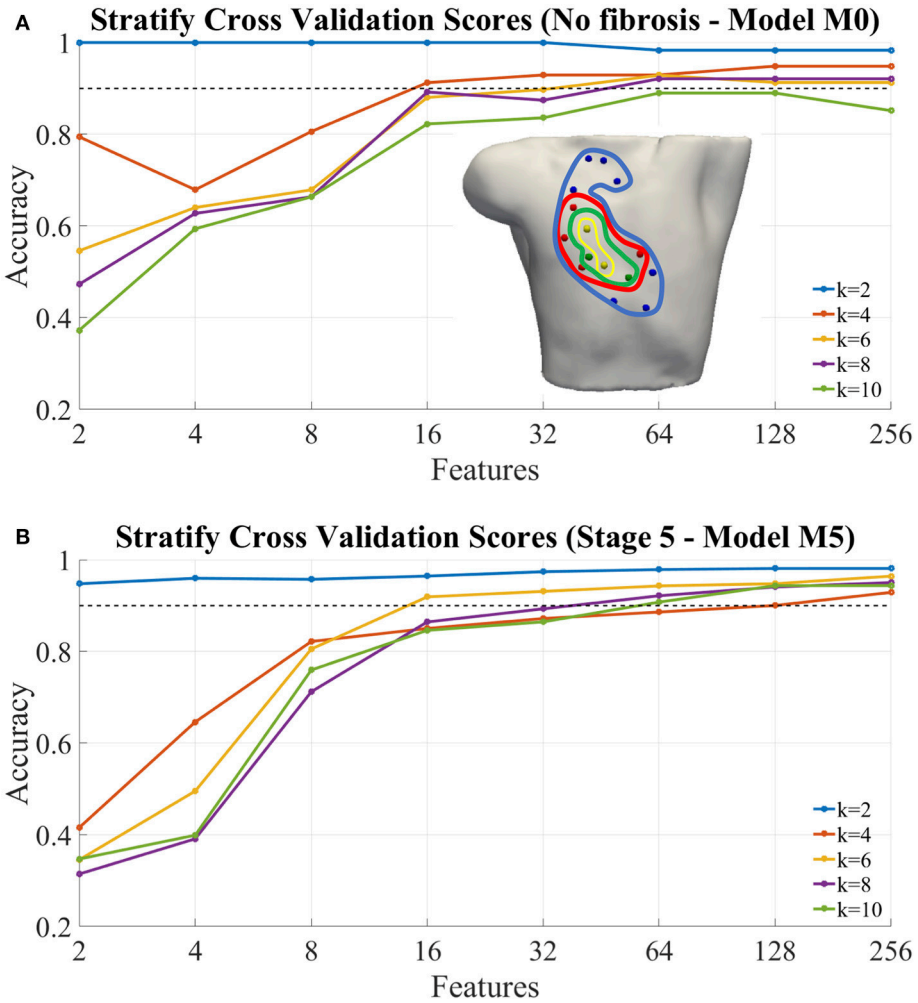

FIGURE 9 | Classification of ectopic foci. **(A)** Accuracy of classification for the model M0, no fibrosis; **(B)** Accuracy of classification for the model M5, extreme case of fibrosis (i.e., from Stage1 to Stage 5). In both cases, the graphs were performed for different number of ectopic clusters (from $K = 2$ to $K = 10$), and different number N of features used (i.e., 2, 4, 8, 16, 32, 64, 128, and 256). Inset **(A)**, example of optimal selected features (electrodes) for: 2 (yellow), 4 (+green), 8 (+red), 16 (+blue) features.

of myocyte APD; (ii) a prolonged repolarization of the AP compared to the uncoupled myocyte control model AP; and importantly since fibroblasts have a higher resting membrane potential (RMP), (iii) changes of the myocyte RMP, see **Figure 4B**.

Furthermore, this shortening of the APD generates a spatial heterogeneity within the atrial tissue due to variations in the fibroblast density and the number of coupled fibroblasts to myocytes, generating a variation of the APD that depends, to a great extent, on the point where the measurement is taken in our virtual human atrial mesh. Although there were variations in the $APDs_{90}$, dependent on the test location, density of fibrosis, and the number of coupled fibroblast to that point, all the APDs were shorter than the uncoupled myocyte control case, see **Figure 4B**.

4.2. Ectopic Foci Localization

Computational modeling of the human atria has changed during the last 15 years, evolving from very simple structures to very detailed models including atrial wall and fiber directions (Doessel et al., 2012). Several models exist today that include structures of intracellular compartments and atrial heterogeneity, and furthermore they include pathological structures, modeling atrial remodeling and fibrotic tissue.

MacLeod et al. (2008) emphasized the importance of including information about structural changes of the atrial myocardium into geometrical models. Previous results from Kistler et al. (2006) suggest that FATs have a particular electrical pattern on the torso (Morton et al., 2001; Kistler et al., 2003a,b, 2005), and that those patterns have a singular P wave morphology in specific locations providing a potential way to predict the origin of FATs. They developed a decision tree algorithm based on the P-wave morphology in specific surface ECG leads to provide some help in the search for ectopic foci sources to allow for the identification of the origin of the tachycardia. Therefore, using only the P wave morphology, they prospectively evaluated the algorithm with a number of patients, finding a predictive

accuracy of 93% for a few focal trigger locations that could be distinguishable.

Other biomarkers such as P-wave integral maps (SippensGroenewegen et al., 1998) have been recommended to summarize different atrial activation sequences and relate them to ectopic foci. In the ventricles, other complex techniques such as electrocardiographic imaging (ECGi), have been widely studied in the last few decades to directly compute the cardiac action potentials by solving an ill-posed inverse problem (Ramanathan et al., 2003; Van Oosterom, 2012). However, many of those approaches use a priori information to improve their results, such as constraints in spatial and temporal domains, physiological knowledge about the activation sequence or localization of activation onset. In addition, those methods need a segmentation of the atria and torso models from an image sequence stack, and the construction of a finite element model to simulate cardiac electrophysiology. All those requirements, which are very time consuming, hamper the use of those tools in clinical environments.

In our previous work Ferrer-Albero et al. (2017), we used machine learning techniques to spatially cluster and classify ectopic atrial foci into clearly differentiated atrial regions by using the body surface P-wave integral map (BSPiM) as a biomarker. Ectopic foci with similar BSPiM naturally clustered into differentiated, non-intersected atrial regions and new patterns could be correctly classified with an accuracy of 97% when considering 2 clusters and 96% for 4 clusters (Ferrer-Albero et al., 2017). However, we only considered non-fibrotic cases, which are not very common cases clinically.

To learn this association, (i.e., ectopic location-BSPiM), regression techniques could appear to be a reasonable approach. However, as the total number of ectopic locations is reduced (i.e., $57 = 19$ with fibrosis $+$ 38 without fibrosis), there are not enough ectopic locations to apply regression techniques.

In this multi-scale biophysical 3D model simulation study, we used machine learning techniques to focus also on the localization of the arrhythmogenic electrical drivers (i.e., ectopic foci), that contribute to the generation of focal atrial tachycardia (FAT) with regional LA patchy fibrosis as a variable of structural remodeling according to the Utah classification scale (Oakes et al., 2009). This study introduces a new methodology which improves previous results and obtains an accuracy above 90% for classifying ectopics into 6 different atrial regions (i.e., from $K = 2$ to $K = 6$). In addition, we reduced the dimensionality of the BSPiM patterns and included noise to obtain data similar to that acquired in a clinical environment. It is important to remark that our simulated P-waves do not include QRS complex and are not affected by baseline wandering. In a real scenario, it will be fundamental to use filters such as bidirectional high-pass Butterworth filter to correct baseline wandering, or Template Matching Subtraction to eliminate the QRS complex. Feature selection analysis was used to find the minimum number of electrodes required to predict, with high accuracy, the location of ectopic foci during FAT. For cases without fibrosis, we could obtain predictions (dividing the atria in $K = 4$ regions) with an accuracy of 0.90 with only 16 features or electrodes placed on the torso front. When detection considered more and smaller regions (from $K = 6$ to $K = 10$), the accuracy was reduced to a minimum accuracy of 0.81 for $K = 10$, and a maximum of 256 electrodes.

As soon as LA patchy fibrosis comes into play, (i.e., Stage 1 to Stage 5), together with an increase in the number of regions analyzed, (i.e., $K = 2$ to $K = 10$), the measure of overlapped regions ratio increases, confirming that overlapping (see Figure S6), and the ratio of well formed clusters, or convexity, decreases, demonstrating the presence of ectopics disconnected or isolated from their group. However, the classification accuracy, remained above the value of 0.90 for numbers electrodes ranging from 128 to 256, even for the most extreme case, which is the model M5. The high accuracy was obtained because we allowed the clusters of patches to be disconnected. Therefore, if the model predicts that a given BSPiM relates to class n, the patches that form the class could belong to more than one single atrial region. From a clinical point of view, the location of the atrial trigger will not be so efficient since the area of search increases, but still the method improves current clinical practice. A positive point is that in cases in which a given atrial patch has more than one label, the main patches associated with the label are in general neighbors. That means that patches in the borders of two regions sometimes are classified as label "a" and sometimes a neighboring region "b."

4.3. Study Limitations

There are several limitations of the proposed methodology that need to be acknowledged. The most important is that although the activation patterns were validated against a clinical database, they have been simulated and do not correspond to real patients. In addition, patient atrial shape variability could introduce slight differences in the P wave morphology that in turn will affect the BSPiM patterns in some cases. Finally, the localization of ectopic focus is based on regions, and therefore the electrophysiologist still has to determine where exactly the focal point is within the predicted region.

5. CONCLUSIONS

The methodology presented here could be useful to help an electrophysiologist to reduce the search area of an ectopic focus non-invasively and plan the intervention a priori. The pipeline presented can produce results in real time, since all the simulations and the training phase are performed offline and a priori. The effect of fibrosis on the atrial activation and BSPiM is large when stage 3 (>15% fibrosis) is used. The machine learning system obtains high accuracy at the expense of increasing the size of the region where the ectopic focus is located. The most complex locations determined in our simulation study were in certain pulmonary veins when the stages of fibrosis were 3, 4, or 5. However, patients that show a stage of fibrosis higher than 3 are not recommended for treatment.

AUTHOR CONTRIBUTIONS

All authors have made substantial contributions to this study. EG and RS conceived and designed the study, and drafted the manuscript, EG performed the investigation and simulation work. EG, ML, and RS contributed to data analysis, computer simulations and the software development. IG-F, AF-A, RM and JS contributed to the interpretation of the results and have revised the document critically. All authors have also approved the final version to be published while agreeing to be accountable for all aspects of the work in ensuring that questions related to the accuracy or integrity of any part of the work are appropriately investigated and resolved.

FUNDING

This work was partially supported by Ministerio de Economia y Competitividad and Fondo Europeo de Desarrollo Regional (FEDER) DPI2015-69125-R and TIN2014-59932-JIN (MINECO/FEDER, UE).

SUPPLEMENTARY MATERIAL

The Supplementary Material for this article can be found online at: https://www.frontiersin.org/articles/10.3389/fphys.2018.00404/full#supplementary-material

REFERENCES

Bhakta, D., and Miller, J. M. (2008). Principles of electroanatomic mapping. *Ind. Pacing Electrophysiol. J.* 8, 32–50.

Boyle, P. M., Zahid, S., and Trayanova, N. A. (2016). Towards personalized computational modelling of the fibrotic substrate for atrial arrhythmia. *EP Europace* 18(Suppl. 4):iv136–iv145. doi: 10.1093/europace/euw358

Buitinck, L., Louppe, G., Blondel, M., Pedregosa, F., Mueller, A., Grisel, O., et al. (2013). "API design for machine learning software: experiences from the scikit-learn project," in *ECML PKDD Workshop: Languages for Data Mining and Machine Learning* (Prague), 108–122.

Courtemanche, M., Ramirez, R. J., and Nattel, S. (1998). Ionic mechanisms underlying human atrial action potential properties: insights from a mathematical model. *Am. J. Physiol. Heart Circul. Physiol.* 275, H301–H321. doi: 10.1152/ajpheart.1998.275.1.H301

Daccarett, M., Badger, T. J., Akoum, N., Burgon, N. S., Mahnkopf, C., Vergara, G., et al. (2011). Association of left atrial fibrosis detected by delayed-enhancement magnetic resonance imaging and the risk of stroke in patients with atrial fibrillation. *J. Am. Coll. Cardiol.* 57, 831–838. doi: 10.1016/j.jacc.2010.09.049

Doessel, O., Krueger, M. W., Weber, F. M., Wilhelms, M., and Seemann, G. (2012). Computational modeling of the human atrial anatomy and electrophysiology. *Med. Biol. Eng. Comput.* 50, 773–799. doi: 10.1007/s11517-012-0924-6

Ferrer, A., Sebastián, R., Sánchez-Quintana, D., Rodríguez, J. F., Godoy, E. J., Martínez, L., et al. (2015). Detailed anatomical and electrophysiological models of human atria and torso for the simulation of atrial activation. *PLoS ONE* 10:e0141573. doi: 10.1371/journal.pone.0141573

Ferrer-Albero, A., Godoy, E. J., Lozano, M., Martínez-mateu, L., Atienza, F., Saiz, J., et al. (2017). Non-invasive location of atrial ectopic beats by using Body Surface P-wave integral Maps. *PLoS ONE* 12:e0181263. doi: 10.1371/journal.pone.0181263

Geselowitz, D. B., and Miller, W. (1983). A bidomain model for anisotropic cardiac muscle. *Ann. Biomed. Eng.* 11, 191–206. doi: 10.1007/BF02363286

Giffard-Roisin, S., Jackson, T., Fovargue, L., Lee, J., Delingette, H., Razavi, R., et al. (2016). Non-invasive personalisation of a cardiac electrophysiology model from body surface potential mapping. *IEEE Trans. Biomed. Eng.* 64, 2206–2218. doi: 10.1109/TBME.2016.2629849

Go, A. S., Hylek, E. M., Phillips, K. A., Chang, Y., Henault, L. E., Selby, J. V., et al. (2001). Prevalence of diagnosed atrial fibrillation in adults. *JAMA* 285:2370. doi: 10.1001/jama.285.18.2370

Guillem, M. S., Climent, A. M., Rodrigo, M., Fernandez-Aviles, F., Atienza, F., and Berenfeld, O. (2016). Presence and stability of rotors in atrial fibrillation: evidence and therapeutic implications. *Cardiovasc. Res.* 109, 480–492. doi: 10.1093/cvr/cvw011

Heidenreich, E. A., Ferrero, J. M., Doblaré, M., and Rodríguez, J. F. (2010). Adaptive macro finite elements for the numerical solution of monodomain equations in cardiac electrophysiology. *Ann. Biomed. Eng.* 38, 2331–2345. doi: 10.1007/s10439-010-9997-2

Hoffmann, E., Reithmann, C., Nimmermann, P., Elser, F., Dorwarth, U., Remp, T., et al. (2002). Clinical experience with electroanatomic mapping of ectopic atrial tachycardia. *Pacing Clin. Electrophysiol.* 25, 49–56. doi: 10.1046/j.1460-9592.2002.00049.x

Jacquemet, V. (2012). An eikonal-diffusion solver and its application to the interpolation and the simulation of reentrant cardiac activations. *Comput. Methods Prog. Biomed.* 108, 548–558. doi: 10.1016/j.cmpb.2011.05.003

Jalife, J. (2011). Déjà vu in the theories of atrial fibrillation dynamics. *Cardiovasc. Res.* 89, 766–775. doi: 10.1093/cvr/cvq364

Keller, D. U., Weber, F. M., Seemann, G., and Dossel, O. (2010). Ranking the influence of tissue conductivities on forward-calculated ecgs. *IEEE Trans. Biomed. Eng.* 57, 1568–1576. doi: 10.1109/TBME.2010.2046485

Kimmel, R., and Sethian, J. (1996). *Fast Marching Methods for Computing Distance Maps Shortest Paths*. Technical report, SCAN-9605127.

Kistler, P. M., Fynn, S. P., Haqqani, H., Stevenson, I. H., Vohra, J. K., Morton, J. B., et al. (2005). Focal atrial tachycardia from the ostium of the coronary sinus: electrocardiographic and electrophysiological characterization and radiofrequency ablation. *J. Am. Coll. Cardiol.* 45, 1488–1493. doi: 10.1016/j.jacc.2005.01.042

Kistler, P. M., Roberts-Thomson, K. C., Haqqani, H. M., Fynn, S. P., Singarayar, S., Vohra, J. K., et al. (2006). P-wave morphology in focal atrial tachycardia. Development of an algorithm to predict the anatomic site of origin. *J. Am. Coll. Cardiol.* 48, 1010–1017. doi: 10.1016/j.jacc.2006.03.058

Kistler, P. M., Sanders, P., Fynn, S. P., Stevenson, I. H., Hussin, A., Vohra, J. K., et al. (2003a). Electrophysiological and electrocardiographic characteristics of focal atrial tachycardia originating from the pulmonary veins: acute and long-term outcomes of radiofrequency ablation. *Circulation* 108, 1968–1975. doi: 10.1161/01.CIR.0000095269.36984.75

Kistler, P. M., Sanders, P., Hussin, A., Morton, J. B., Vohra, J. K., Sparks, P. B., et al. (2003b). Focal atrial tachycardia arising from the mitral annulus: electrocardiographic and electrophysiologic characterization. *J. Am. Coll. Cardiol.* 41, 2212–2219. doi: 10.1016/S0735-1097(03)00484-4

MacCannell, K. A., Bazzazi, H., Chilton, L., Shibukawa, Y., Clark, R. B., and Giles, W. R. (2007). A mathematical model of electrotonic interactions between ventricular myocytes and fibroblasts. *Biophys. J.* 92, 4121–4132. doi: 10.1529/biophysj.106.101410

MacLeod, R., Kholmovski, E., DiBella, E., Oakes, R., Blauer, J., Fish, E., et al. (2008). Integration of MRI in evaluation and ablation of atrial fibrillation. *Comput. Cardiol.* 35, 77–80. doi: 10.1109/CIC.2008.4748981

Maleckar, M. M., Greenstein, J. L., Giles, W. R., and Trayanova, N. A. (2009). Electrotonic coupling between human atrial myocytes and fibroblasts alters myocyte excitability and repolarization. *Biophys. J.* 97, 2179–2190. doi: 10.1016/j.bpj.2009.07.054

Morgan, R., Colman, M. A., Chubb, H., Seemann, G., and Aslanidi, O. V. (2016). Slow conduction in the border zones of patchy fibrosis stabilizes the drivers for atrial fibrillation: insights from multi-scale human atrial modeling. *Front. Physiol.* 7:474. doi: 10.3389/fphys.2016.00474

Morton, J. B., Sanders, P., Das, A., Vohra, J. K., Sparks, P. B., and Kalman, J. M. (2001). Focal atrial tachycardia arising from the tricuspid annulus: electrophysiologic and electrocardiographic characteristics. *J. Cardiovasc. Electrophysiol.* 12, 653–659. doi: 10.1046/j.1540-8167.2001.00653.x

Niederer, S. A., Kerfoot, E., Benson, A. P., Bernabeu, M. O., Bernus, O., Bradley, C., et al. (2011). Verification of cardiac tissue electrophysiology simulators using an n-version benchmark. *Philos. Trans. R. Soc. A* 369, 4331–4351. doi: 10.1098/rsta.2011.0139

Oakes, R. S., Badger, T. J., Kholmovski, E. G., Akoum, N., Burgon, N. S., Fish, E. N., et al. (2009). Detection and quantification of left atrial structural remodeling with delayed-enhancement magnetic resonance imaging in patients with atrial fibrillation. *Circulation* 119, 1758–1767. doi: 10.1161/CIRCULATIONAHA.108.811877

Orfanidis, S. J. (1995). *Introduction to Signal Processing*. Upper Saddle River, NJ: Prentice-Hall, Inc.

Pedregosa, F., Varoquaux, G., Gramfort, A., Michel, V., Thirion, B., Grisel, O., et al. (2011). Scikit-learn: machine learning in Python. *J. Mach. Learn. Res.* 12, 2825–2830.

Ramanathan, C., Jia, P., Ghanem, R., Calvetti, D., and Rudy, Y. (2003). Noninvasive electrocardiographic imaging (ECGI): application of the generalized minimal residual (GMRes) method. *Ann. Biomed. Eng.* 31, 981–994. doi: 10.1114/1.1588655

Santangeli, P., and Marchlinski, F. E. (2017). Techniques for the provocation, localization, and ablation of non–pulmonary vein triggers for atrial fibrillation. *Heart Rhythm* 14, 1087–1096. doi: 10.1016/j.hrthm.2017.02.030

Santangeli, P., Zado, E. S., Hutchinson, M. D., Riley, M. P., Lin, D., Frankel, D. S., et al. (2016). Prevalence and distribution of focal triggers in persistent and long-standing persistent atrial fibrillation. *Heart Rhythm* 13, 374–382. doi: 10.1016/j.hrthm.2015.10.023

Santoro, F., Heeger, C. H., Metzner, A., Brunetti, N. D., Biase, M. D. I., Kuck, K.-H., et al. (2018). Targeting ablation strategies and electro-anatomical systems for different atrial fibrillation patterns. *Minerva Cardioangiol.* 65, 63–74. doi: 10.23736/S0026-4725.17.04430-9

Saoudi, N., Cosío, F., Waldo, A., Chen, S. A., Iesaka, Y., Lesh, M., et al. (2001). A classification of atrial flutter and regular atrial tachycardia according to electrophysiological mechanisms and anatomical bases: a statement from a joint expert group from the working group of arrhythmias of the European society of cardiology and the North American society of pacing and electrophysiology. *Eur. Heart J.* 22, 1162–1182. doi: 10.1053/euhj.2001.2658

Shah, A. J., Hocini, M., Pascale, P., Roten, L., Komatsu, Y., Daly, M., et al. (2013). Body surface electrocardiographic mapping for non-invasive identification of arrhythmic sources. *Arrhyth. Electrophysiol. Rev.* 2, 16–22. doi: 10.15420/aer.2013.2.1.16

SippensGroenewegen, A., Natale, A., Marrouche, N. F., Bash, D., and Cheng, J. (2004). Potential role of body surface ECG mapping for localization of atrial fibrillation trigger sites. *J. Electrocardiol.* 37, 47–52. doi: 10.1016/j.jelectrocard.2004.08.017

SippensGroenewegen, A., Roithinger, F. X., Peeters, H. A. P., Linnenbank, A. C., Van Hemel, N. M., Steiner, P. R., et al. (1998). Body surface mapping of atrial arrhythmias: atlas of paced P wave integral maps to localize the focal origin of right atrial tachycardia. *J. Electrocardiol.* 31, 85–91. doi: 10.1016/S0022-0736(98)90298-9

Spach, M. S., and Boineau, J. P. (1997). Microfibrosis produces electrical load variations due to loss of side- to-side cell connections: a major mechanism of structural heart disease arrhythmias. *Pacing Clin. Electrophysiol.* 20, 397–413. doi: 10.1111/j.1540-8159.1997.tb06199.x

Trayanova, N. A., and Boyle, P. M. (2014). Advances in modeling ventricular arrhythmias: from mechanisms to the clinic. *Wiley Interdiscip. Rev. Syst. Biol. Med.* 6, 209–224. doi: 10.1002/wsbm.1256

Van Oosterom, A. (2012). *The Inverse Problem of Bioelectricity: An Evaluation*. Philadelphia: Elsevier Inc., Heart Rhythm Society.

Vigmond, E., Pashaei, A., Amraoui, S., Cochet, H., and Hassaguerre, M. (2016). Percolation as a mechanism to explain atrial fractionated electrograms and reentry in a fibrosis model based on imaging data. *Heart Rhythm* 13, 1536–1543. doi: 10.1016/j.hrthm.2016.03.019

Ward, J. H. Jr. (1963). Hierarchical grouping to optimize an objective function. *J. Am. Stat. Assoc.* 58, 236–244. doi: 10.1080/01621459.1963.10500845

Weber, F. M., Keller, D. U., Bauer, S., Seemann, G., Lorenz, C., and Dossel, O. (2011). Predicting tissue conductivity influences on body surface potentials—an efficient approach based on principal component analysis. *IEEE Trans. Biomed. Eng.* 58, 265–273. doi: 10.1109/TBME.2010.2090151

Zhao, J., Kharche, S. R., Hansen, B. J., Csepe, T. A., Wang, Y., Stiles, M. K., et al. (2015). Optimization of catheter ablation of atrial fibrillation: insights gained from clinically-derived computer models. *Int. J. Mol. Sci.* 16, 10834–10854. doi: 10.3390/ijms160510834

Zhao, J., Stephenson, R. S., Sands, G. B., LeGrice, I. J., Zhang, H., Jarvis, J. C., et al. (2013). "Atrial fibrosis and atrial fibrillation: a computer simulation in the posterior left atrium," in *Lecture Notes in Computer Science (Including Subseries Lecture Notes in Artificial Intelligence and Lecture Notes in Bioinformatics)*, Vol. 7945, eds S. Ourselin, D. Rueckert, and N. Smith (London, UK: Springer-Verlag Berlin Heidelberg), 400–408.

Conflict of Interest Statement: The authors declare that the research was conducted in the absence of any commercial or financial relationships that could be construed as a potential conflict of interest.

Copyright © 2018 Godoy, Lozano, García-Fernández, Ferrer-Albero, MacLeod, Saiz and Sebastian. This is an open-access article distributed under the terms of the Creative Commons Attribution License (CC BY). The use, distribution or reproduction in other forums is permitted, provided the original author(s) and the copyright owner are credited and that the original publication in this journal is cited, in accordance with accepted academic practice. No use, distribution or reproduction is permitted which does not comply with these terms.

frontiers in Physiology

ORIGINAL RESEARCH
published: 30 May 2018
doi: 10.3389/fphys.2018.00648

Comparative Effectiveness of ICA and PCA in Extraction of Fetal ECG From Abdominal Signals: Toward Non-invasive Fetal Monitoring

Radek Martinek[1], Radana Kahankova[1], Janusz Jezewski[2], Rene Jaros[1], Jitka Mohylova[3], Marcel Fajkus[4], Jan Nedoma[4], Petr Janku[5] and Homer Nazeran[6]*

[1] Department of Cybernetics and Biomedical Engineering, Faculty of Electrical Engineering and Computer Science, VSB-Technical University of Ostrava, Ostrava, Czechia, [2] Institute of Medical Technology and Equipment ITAM, Zabrze, Poland, [3] Department of General Electrical Engineering, Faculty of Electrical Engineering and Computer Science, VSB-Technical University of Ostrava, Ostrava, Czechia, [4] Department of Telecommunications, Faculty of Electrical Engineering and Computer Science, VSB-Technical University of Ostrava, Ostrava, Czechia, [5] Department of Obstetrics and Gynecology, Masaryk University and University Hospital Brno, Brno, Czechia, [6] Department of Electrical and Computer Engineering, University of Texas El Paso, El Paso, TX, United States

OPEN ACCESS

Edited by:
Thomas Heldt, Massachusetts Institute of Technology, United States

Reviewed by:
Arun V. Holden, University of Leeds, United Kingdom
Andrea Fanelli, Massachusetts Institute of Technology, United States

***Correspondence:**
Radek Martinek
radek.martinek@vsb.cz

Specialty section:
This article was submitted to Computational Physiology and Medicine, a section of the journal Frontiers in Physiology

Received: *05 December 2017*
Accepted: *11 May 2018*
Published: *30 May 2018*

Citation:
Martinek R, Kahankova R, Jezewski J, Jaros R, Mohylova J, Fajkus M, Nedoma J, Janku P and Nazeran H (2018) Comparative Effectiveness of ICA and PCA in Extraction of Fetal ECG From Abdominal Signals: Toward Non-invasive Fetal Monitoring. Front. Physiol. 9:648. doi: 10.3389/fphys.2018.00648

Non-adaptive signal processing methods have been successfully applied to extract fetal electrocardiograms (fECGs) from maternal abdominal electrocardiograms (aECGs); and initial tests to evaluate the efficacy of these methods have been carried out by using synthetic data. Nevertheless, performance evaluation of such methods using real data is a much more challenging task and has neither been fully undertaken nor reported in the literature. Therefore, in this investigation, we aimed to compare the effectiveness of two popular non-adaptive methods (the ICA and PCA) to explore the non-invasive (NI) extraction (separation) of fECGs, also known as NI-fECGs from aECGs. The performance of these well-known methods was enhanced by an adaptive algorithm, compensating amplitude difference and time shift between the estimated components. We used real signals compiled in 12 recordings (real01–real12). Five of the recordings were from the publicly available database (PhysioNet-Abdominal and Direct Fetal Electrocardiogram Database), which included data recorded by multiple abdominal electrodes. Seven more recordings were acquired by measurements performed at the Institute of Medical Technology and Equipment, Zabrze, Poland. Therefore, in total we used 60 min of data (i.e., around 88,000 R waves) for our experiments. This dataset covers different gestational ages, fetal positions, fetal positions, maternal body mass indices (BMI), etc. Such a unique heterogeneous dataset of sufficient length combining continuous Fetal Scalp Electrode (FSE) acquired and abdominal ECG recordings allows for robust testing of the applied ICA and PCA methods. The performance of these signal separation methods was then comprehensively evaluated by comparing the fetal Heart Rate (fHR) values determined from the extracted fECGs with those calculated from the fECG signals recorded directly by means of a reference FSE. Additionally, we tested the possibility of non-invasive ST analysis (NI-STAN) by determining the T/QRS ratio. Our results

demonstrated that even though these advanced signal processing methods are suitable for the non-invasive estimation and monitoring of the fHR information from maternal aECG signals, their utility for further morphological analysis of the extracted fECG signals remains questionable and warrants further work.

Keywords: electronic fetal monitoring (EFM), fetal electrocardiogram (fECG), non-invasive fetal heart rate (NI-fHR) estimation, non-invasive fetal ECG (NI-fECG), nonadaptive methods, independent component analysis (ICA), principal component analysis (PCA), non-invasive ST analysis (NI-STAN)

1. INTRODUCTION

Electronic fetal monitoring (EFM) is a routine monitoring modality during labor and delivery in developed countries. Currently, Doppler ultrasound and fetal electrocardiography (both invasive and non-invasive) are recognized as reliable and proven techniques for monitoring the Fetal Heart Rate (fHR) (Jezewski et al., 2017). The monitoring of fHR using Doppler ultrasound, also called Cardiotocography (CTG), is well established as it is considered effective and is therefore widely used in clinics. However, the fetal Electrocardiogram-based (fECG-based) EFM seems to offer a more promising approach Jezewski et al. (2017) and Hasan et al. (2009b), as it significantly outperforms the Doppler-based CTG, especially during the early stages of labor (Reinhard et al., 2012). Moreover, Reinhard et al. (2013) have concluded that the intrapartum fHR monitoring using the CTG has the disadvantage of more maternal and fetal HR ambiguity compared to the ECG, which additionally provides the maternal Heart Rate (mHR) information.

The non-invasive variants of fECG signals are sensed by abdominal electrodes, amplified and filtered by proper analog signal processing circuitry with adequate gain and bandwidth. Nevertheless, besides the desired fECG signal, there are many other unwanted components originating from biological sources (maternal and fetal muscles, stomach, uterus) as well as technical noise from the powerlines and their surrounding electrical devices that contaminate the recorded abdominal ECG (aECG) signals. Most of these unwanted signals can be eliminated by conventional signal processing techniques (linear filtering) because their frequency ranges are different from the spectrum of the desired (fECG) signals (Sameni and Clifford, 2010). The main challenge in fECG signal processing is suppressing the maternal component, i.e., the maternal electrocardiogram (mECG). Since both signals overlap in the time and frequency domains, advanced signal processing methods must be used to extract the fECG signals.

There are several methods that can be used for extracting fECG component from aECG signals. Generally, they can be divided into two main groups: adaptive and non-adaptive. In our previous research reported elsewhere (Martinek and Zidek, 2012; Martinek et al., 2016a, 2017a,b; Fajkus et al., 2017) we used the adaptive methods and achieved good results in suppressing the mECG signals present in the aECG signals. In spite of producing good outcomes, these methods have the disadvantage of requiring additional thoracic electrodes to provide reference mECG signals. This fact affects the patient's comfort, and complicates its usage in clinical practice. Furthermore, the efficiency of the adaptive methods is closely connected with the adaptive filter's settings. The optimal settings vary with gestational age, fetal position in the uterus, etc. (Martinek et al., 2017a).

From a practical clinical point of view, non-adaptive methods offer the advantage of using ECG signals acquired from the abdominal electrodes alone. In addition, there is a trend toward using SMART technologies in medicine. Thus a multisource system, where the electrodes are embedded within a flexible garment (one electrode grid/strip for the abdominal area) seems to be very promising for the future of continuous fetal monitoring. In such a system, the ICA and PCA methods presented in this article could prove to be the most suitable for implementation. Consequently, to complement our previous work and compare the effectiveness of non-adaptive signal processing methods in suppressing the mECG signals, we carried out the current investigation focusing on the Independent Component Analysis (ICA) and Principal Component Analysis (PCA). The results of our initial experiments applying the popular PCA and ICA methods to synthetic data are presented and reported elsewhere (Kahankova et al., 2017a). The next logical step was to expand our previous work and perform our experiments using real data. The main difference between using synthetic versus real data is in the evaluation of the results. In case of synthetic data, we can benefit from the fact that the ideal fECG signal is available to be used as the reference for objective quality assessment based on metrics such as: Signal-to-Noise Ratio (SNRin, SNRout), Percentage Root Difference (PRD), Root Mean Square Error (RMSE), etc. However, for the experiments with real data, the efficacy of the applied methods can only be evaluated based on the reference signal recorded by the FSE, which is considered as a "gold standard" for fHR determination.

In this investigation, we evaluated the comparative efficacy of the ICA and PCA methods by using real data from a publicly available database (Jezewski et al., 2012) as well as those acquired at the Institute of Medical Technology and Equipment, Zabrze, Poland. Our results show that these non-adaptive methods are suitable for the extraction of fetal heart rate (fHR) information from fECG signals. However, their utility for further morphological analysis of these signals is questionable.

Nevertheless, the results of morphological analysis showed that it is possible to extract relevant information such as the T/QRS ratio from the estimated fECG signals contingent upon ensuring the acquisition of high quality data (elimination of the motion artifacts, correct electrode placement,

suffient electrode-skin contact, etc.). In other words, reliable morphological analysis of high quality fECG signals offers the possibility of introducing the non-invasive STAN (NI-STAN) to clinical practice, which would in turn lead to a significant reduction in unnecessary C-sections due to misrepresented EFM results.

2. STATE OF THE ART

The fetal heart rate undergoes dynamic adjustments as it responds to the fetal environment and other stimuli. The changes in fHR can reflect both physiological and pathological influences. Physiological changes are associated with fetal movements and also with maternal contractions during labor (the so-called accelerations and decelerations Williams and Arulkumaran, 2004). A decrease or an increase in fHR which is not a response to physiological events may be a sign of pathology such as fetal hypoxia, i.e., the inadequate supply of oxygen to the fetus (Chandraharan and Arulkumaran, 2007). Therefore, it is essential to monitor fHR, fetal movements and uterine contractions simultaneously. In other words, Electronic Fetal Monitoring (EFM) is a method for observing and controlling a variety of underlying physiological measures at the same time and therefore it enables the detection of any unusual changes in fHR.

2.1. Electronic Fetal Monitoring Instrumentation

Electronic fetal monitoring (EFM) using Cardiotocography (CTG) is the most frequently used tool to assess fetal well-being during labor and delivery. The fHR and uterine contractions are detected by two external transducers placed on the maternal abdomen. One of the transducers, placed above the fetal heart, uses Doppler ultrasound to detect fetal heart motion. The second transducer, placed at the fundus of the uterus, measures the frequency of the uterine contractions (Sweha et al., 1999).

The disadvantage of CTG is that it tends to produce false-positive (FP) results. These in turn lead to increased rates of unnecessary caesarian sections, thereby increasing labor and delivery costs Vintzileos et al. (1995). One of the reasons for the production of FP results is the problematic interpretation of CTG, which suffers from large inter-observer disagreement (see Bernardes et al., 1997; Blix et al., 2003; Vayssière et al., 2010; Blackwell et al., 2011; Hruban et al., 2015). This is clearly noticeable when we compare the clinical expert interpretation of the fetal Heart Rate Variability (fHRV) with those generated by computerized systems (Jezewski et al., 2002). The accuracy of the CTG method can be increased by using an internal probe that measures the fetal heart rate directly from the fetal scalp (Amer-Wåhlin et al., 2001; Jezewski et al., 2012). This is, however, inconvenient for the mother and the fetus. Some authors have suggested that fetal heart rate signal interpretation can be improved by applying advanced signal processing techniques (Wróbel et al., 2013; Wrobel et al., 2015; Jezewski et al., 2016).

In addition to CTG, fHR can be obtained from fECG signals. Recent studies show that this method is the most promising one (Jezewski et al., 2017). The monitoring of fECG is performed by internal or external means. The internal monitoring of fHR is performed by attaching a screw-type Fetal Scalp Electrode (FSE) on the fetus forehead. At the same time, uterine contractions are recorded by using an Intrauterine Pressure Catheter (IUPC) placed in the uterus through the cervix. This approach ensures accuracy; however, it poses a risk of infection for the mother and the fetus (Peters et al., 2001; Neilson, 2006). Moreover, its utilization is limited by several factors. The fetal membranes have to be ruptured and the cervix must be at least partially dilated before the FSE can be placed on the fetal scalp.

External fetal monitoring is performed by using surface electrodes that are placed on the maternal abdomen. The internal monitoring of fHR is performed by attaching a screw-type Fetal Scalp Electrode (FSE) on the examiner (Burattini et al., 2015). However, the placement of the electrodes significantly influences the quality of the signal as well as the demands on the system that processes it Martinek et al. (2017b). Compared to internal monitoring, this approach is less stressful and dangerous for the mother and her fetus (Neilson, 2006). Moreover, it can be theoretically used from quite early stages of pregnancy (Kahankova et al., 2017c). Nevertheless, the drawback of this method is that the desired signal (fECG) is contaminated by a large amount of noise. The main source of the noise is of course the maternal body. These biological signals include breathing and muscular activity, motion artifacts and maternal ECG (mECG). Most of these unwanted signals may be reduced by classical filtering methods because frequency ranges of these contaminating signals are different from those of the fECG signal. However, as the mECG signals overlap with fECG signals in the time and frequency domains, they cannot be filtered out by using conventional methods.

2.2. Non-invasive Fetal Electrocardiogarm (NI-fECG) Signal Extraction Methods

Fetal ECG signals can be extracted from either single-channel or multi-channel sources. These signals can be processed by means of adaptive or non-adaptive methods. Even though many different techniques have been implemented to extract the fECG signals (Viunytskyi and Shulgin, 2017), researchers still strive for more accurate and improved non-invasive fetal ECG (NI-fECG) extraction (separation) methods.

Adaptive methods use filters that are able to automatically self-adjust their coefficients (control parameters) according to the information in the filtered signal. These methods are often utilized for noise suppression in a variety of applications, where the source of the signal is known and measurable, such as Channel Equalization (Martinek and Zidek, 2014; Martinek et al., 2015c), Speech Noise Removal (Martinek et al., 2015a), and others. In NI-fECG signal extraction, the maternal component is considered to be the noise in the composite aECG signal, which is comprised of fECG as well as the mECG in addition to other unwanted biological and technical contaminating components. Therefore, adaptive methods can be used for the mECG signal suppression, where the aECG is the primary output and the mECG, recorded by means of the maternal thoracic leads, is the reference input.

2.2.1. Adaptive Methods

Adaptive methods can be divided into two groups: Linear and Nonlinear. Linear adaptive methods that have been applied to the NI-fECG signal extraction problem include algorithms based on Kalman Filtering (KF), (Niknazar et al., 2013), Adaptive Voltera Filtering (Shadaydeh et al., 2008), Comb Filtering (Wei et al., 2013), Stochastic Gradient Adaptation, i.e., the Least Mean Squares (LMS) method (Poularikas and Zayed, 2006; Swarnalatha and Prasad, 2010; Kahankova et al., 2018), and algorithms based on optimal recursive adaptation, i.e., the Recursive Least Squares (RLS) method (Poularikas and Zayed, 2006; Swarnalatha and Prasad, 2010; Martinek et al., 2016a; Kahankova et al., 2017d). Adaptive Linear Neuron or Adaptive Linear Element (ADALINE) (Reaz and Wei, 2004; Jia et al., 2010; Amin et al., 2011), and so on.

Nonlinear methods are based on Artificial Intelligence (AI) and those that have been applied to extract the NI-fECG signals include: Adaptive Neural Networks (ANN), Hasan et al. (2009a), Hybrid Neural Networks (HNN), Assaleh (2007), Genetic Algorithms and Bayesian Adaptive Filtering Frameworks Talha et al. (2010), Kam and Cohen (1999), as well as techniques utilizing Adaptive Neuro-Fuzzy Interference System (ANFIS), Assaleh (2007), Al-Zaben and Al-Smadi (2006), Martinek et al. (2016c), and Martinek and Zidek (2012). In addition, Artificial Neural Networks based on Logical Interpretation of fuzzy if-then Rules (ANBLIR) has been introduced as an approach to classify fetal cardiotocograms Czabanski et al. (2008). The main difference between the Linear and Nonlinear approaches is that the latter methods capture the underlying nonlinear characteristics of the body and thus are theoretically more suitable for NI-fECG extraction.

2.2.2. Non-adaptive Methods

Non-adaptive filtering methods eliminate the undesired signals to yield the fECG signal without filter adaptation. More specifically, in some of these methods, filter weights are determined by using some initial training data and remain constant. These methods can use either a single-channel or multi-channel signal source. Techniques utilizing a multi-channel signal source include multiple and single-source methods. Single-channel signal source methods are based on for example Wavelet Transform (WT), Karvounis et al. (2004), Datian and Xuemei (1996), Hassanpour and Parsaei (2007), Bsoul (2015), Ivanushkina et al. (2014), Abburi and Chandrasekhara Sastry (2012), Bensafia et al. (2017), Castillo et al. (2013), Correlation Techniques De Araujo et al. (2005), Averaging Techniques (AT) Hon and Lee (1963), Hon and Lee (1964), Template Subtraction Tsui et al. (2017), Singular Value Decomposition (SVD) Kanjilal et al. (1997), Adaptive Noise Canceler (ANC) Zhang et al. (2017), and so on.

The multi-source methods are based on Subspace Denoising Fatemi and Sameni (2017) or Blind Source Separation (BSS), namely: Independent Component Analysis (ICA), Martín-Clemente et al. (2011), Vrins et al. (2004), Najafabadi et al. (2006), Mochimaru et al. (2004), Sameni et al. (2007), De Lathauwer et al. (2000), Marossero et al. (2003), Gurve et al. (2017), Billeci and Maurizio (2017); Principal Component Analysis (PCA), Gurve et al. (2017), Kahankova et al. (2017b), and so on. BSS is a frequently used method for fECG signal filtering. It assumes the statistical independence of the two processed signals: fECG and mECG. It can be applied in the case of multi-channel abdominal recording with the assumption that the signals from different leads are a linear combination of independent signal sources generated by the maternal and fetal hearts (Sameni et al., 2007). The challenge, however, is that the relationship between the mECG recorded on the maternal chest and the mECG in the abdominal signal is rather nonlinear in nature. It is important to emphasize that the greater the number of channels, the better the quality of the extracted fECG signal. However, a large number of electrodes is clinically difficult to use and, moreover, they are unpleasant for the patient (Burattini et al., 2015).

De Lathauwer et al. applied the ICA method to fECG signal processing and explained that it is a rather demanding approach (De Lathauwer et al., 2000). They focused on the direct reconstruction of various statistically independent bioelectric signal sources while considering both the maternal and fetal hearts as important sources of diagnostic information, and paid special attention to the propagation characteristics of these signals toward the recording electrodes. Their solution is nonparametric and it is not based on sample averaging, which may be a problem while detecting and analyzing atypical changes in heart rate.

Marrosero et al. compared three ICA-based methods: the Mermaid algorithm, Infomax, and Fast Independent Component Analysis (FastICA), Marossero et al. (2003). By detecting fHR from both real and synthetic records, they showed that the Mermaid method outperforms the other two algorithms. It also appears that this method is more efficient in batch and on-line operating modes, which is vital for real-time implementation.

Sameni et al. applied the ICA method to extract fECG signals, while taking into account the dimensionality of these signals and the theory of the heart dipole (Sameni et al., 2007). In their work, the interpretation of the independent components obtained from multiple leads was closely related to the representation of vectorcardiograms of individual signals. The subspaces of the fetal and maternal ECG signals are not completely different. By using dynamic filters, it should be possible to use a dynamic model that is time-synchronous with mECG and thereby to remove the maternal component while preserving the fetal one.

3. METHODS

Figure 1 shows a block diagram of the experimental setup used for our investigation. The main aim of this investigation was to process aECG signals in order to extract fECG signals from them by applying and comparing two popular non-adapative signal processing (ICA and PCA) methods and then successfully determine the fetal Heart Rate fHR, which is one of the main indicators used to detect and diagnose fetal hypoxia (Hyvarinen and Oja, 2000).

The aECG signals were first pre-processed by FIR bandpass filtering to remove baseline wander, and subsequently applied to the ICA and PCA signal processing blocks to extract the fECG

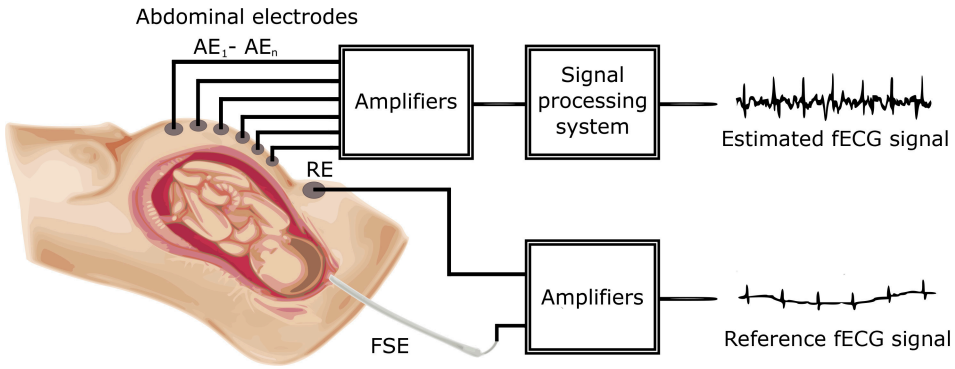

FIGURE 1 | Block diagram of the experimental setup for fECG signal extraction and quality assessment.

signals. The filtered fECG signals were then compared with the direct (reference) fECG signals recorded by means of the FSE using the fHR values determined from the extracted as well as direct fECG signals. The FSE recordings were quality assured by clinical experts resulting in a set of reference markers precisely indicating the time of occurrence of the R-waves. Thus these transvaginal records could be considered as a "gold standard" for fHR determination and a relevant reference for validating the outcomes of our experiments. Additionally, the results were statistically evaluated by means of the Bland-Altman method. We also provide the graphical interpretation of the results to facilitate the visual evaluation of the fECG signal separation process.

In addition to fHR determination, this article also focuses on testing possible morphological analysis (MA) of the fECG signals, namely non-invasive ST analysis (NI-STAN). We analyzed the estimated as well as the reference fECG signals and also carried out the evaluation of the MA as well.

Non-adaptive methods have been applied to the fECG signal extraction problem (Kahankova et al., 2017b), and initial investigations have been carried out by using synthetic data from a novel signal generator (Martinek et al., 2015b, 2016b). Nevertheless, performance verification of the applied methods using real data is a more complex task than testing them with synthetic signals.

In this research, we used abdominal ECG signals from a publicly available database as well as data acquired in Poland (for details please see section 5). Each recording in the Polish data included four aECG signals. One recording could be tested by:(1) using 11 possible combinations of electrodes; (2) 6 possible combinations when utilizing 2 signal channels; (3) 4 possible combinations when using 3 channels; and (4) 1 combination when using all of the channels simultaneously.

3.1. Independent Component Analysis (ICA)

Figure 2 shows the block diagram for the optimized ICA method. The pre-processing block includes a bandpass FIR filter (with a bandwidth from 3 to 150 Hz) for isoline drift (baseline wander) correction. The pre-processed signals were subsequently applied to the ICA signal processing block, which produced the estimated aECG* signals (with increased amplitude and enhanced fetal and mECG* components, respectively). There was a time shift between the estimated aECG* and mECG* components which needed to be centered. Moreover, it was necessary to equalize the amplitudes of both components in order to ensure that the maternal components had the same amplitude. For this task, we developed an adaptive algorithm that was able to correct the amplitude and phase shifts (see block called Compensation of samples and amplitude in **Figure 2**). This led to a significant increase in the fECG extraction performance. Finally, the fECG signals were extracted by subtracting the mECG* from aECG* signals. Beside fHR determination, this article also focuses on testing possible morphological analysis (MA) of fECG, namely non-invasive ST analysis. We analyzed the estimated as well as the reference fECG signal and evaluated results (MA evaluation).

Figure 3 shows a depiction of the BSS extraction method based on the 'Cocktail Party Problem' adapted for pregnant women as signal sources. There are two signal sources in the maternal body, maternal and fetal heart, producing signals that can be measured by means of electrodes placed on the maternal abdomen. Abdominal electrodes measure both maternal and fetal signals. The signal from the first electrode is marked as $x_1(t)$ and the second as $x_2(t)$. Each of these recorded signals was generated by weighing the signals $s_1(t)$ and $s_2(t)$ of the individual signal sources (hearts). The relationship between the signals obtained from the electrodes $x_i(t)$ and the signals generated by the individual hearts $s_i(t)$ can be expressed as follows:

$$x_1(t) = a_{11}(t)s_1(t) + a_{12}(t)s_2(t), \quad (1)$$

$$x_2(t) = a_{21}(t)s_1(t) + a_{22}(t)s_2(t). \quad (2)$$

3.1.1. ICA Data Model

Independent Component Analysis (ICA) is a statistical analysis technique used to decompose a multivariable signal into a set of mutually independent, non-Gaussian components, assuming that the measured signals are a combination of independent source signals described mathematically by the ICA model (Karhunen, 1996; Hyvärinen and Oja, 1997; Hyvarinen and Oja, 2000; Černošek et al., 2000; Mohylova et al., 2001):

$$\mathbf{x} = \mathbf{As}, \quad (3)$$

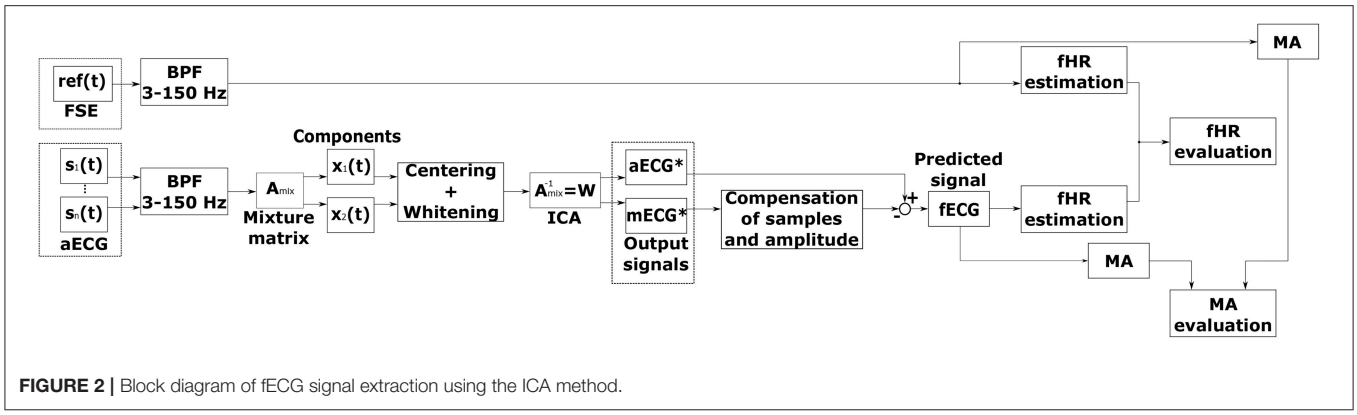

FIGURE 2 | Block diagram of fECG signal extraction using the ICA method.

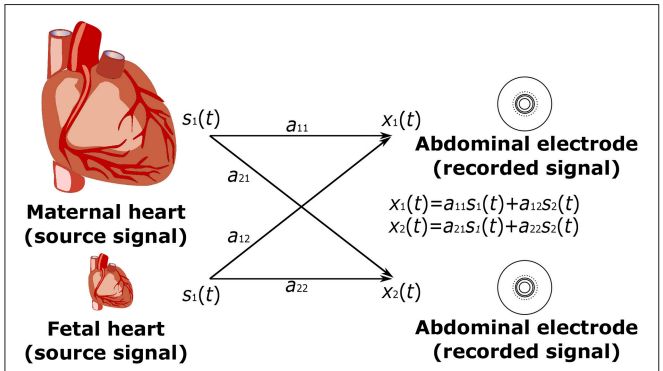

FIGURE 3 | Principle of the ICA method: linear mixture of the unobserved independent source signals - $s_1(t)$, $s_2(t)$: source signals; and $x_1(t)$, $x_2(t)$: recorded signals.

where again $\mathbf{x} = [x_1, x_2, \cdots, x_n,]^{\mathrm{T}}$ is the observed multivariate signal, $\mathbf{s} = [s_1, s_2, \cdots, s_m,]^{\mathrm{T}}$ is the original unknown multivariate source signal, m is the number of observed signals, n is the number of sources and $\mathbf{A}$ is the mixing matrix. The values of the signals are considered samples (instantiations) of the random variables, not functions of time. The aim of ICA is to return the linear unmixing matrix $\mathbf{W}$ in order to acquire the estimated independent components $\mathbf{y}$ such that:

$$\mathbf{y} = \mathbf{W}\mathbf{x}. \tag{4}$$

We assumed here that the number of independent components $\mathbf{s}$ is equal to the number of observed variables; this is a simplifying assumption that is not completely necessary. If the unknown mixing matrix $\mathbf{A}$ is square and non-singular, then $\mathbf{W}$ is the inverse matrix $\mathbf{W} = \mathbf{A}^{-1}$. Otherwise, the best unmixing matrix, that separates sources as independent as possible, is given by the generalized inverse Penrose-Moore matrix:

$$\mathbf{W} = \mathbf{A}^{+} \text{ and } \left\|\mathbf{y} - \mathbf{s}\right\| = \min. \tag{5}$$

3.1.2. Preprocessing for ICA

The primary reasons for pre-processing are:

- simplification of algorithms,
- reduction of dimensionality of the problem,
- reduction of number of parameters to be estimated,
- highlighting features of the data set not readily explained by the mean and covariance.

There are two main pre-processing strategies in ICA, namely centering and whitening/sphering.

a) Centering Centered vectors have zero mean. Centering is a very simple operation and simply refers to subtracting the mean $E\{\mathbf{x}\}$:

$$\mathbf{x}_c = \mathbf{x} - E\{\mathbf{x}\}. \tag{6}$$

b) Whitening Whitened vectors have unit variance. Whitening can be performed by using the eigenvalue decomposition of the covariance matrix:

$$E\left\{\mathbf{x}_c\mathbf{x}_c^{\mathrm{T}}\right\} = \mathbf{V}\mathbf{D}\mathbf{V}^{\mathrm{T}}, \tag{7}$$

where $\mathbf{V}$ is the orthogonal matrix of eigenvectors and $\mathbf{D}$ is the diagonal matrix of its eigenvalues. A new whitened vector is created as follows:

$$\mathbf{x}_w = \mathbf{V}\mathbf{D}^{-1/2}\mathbf{V}^{\mathrm{T}}\mathbf{x}_c. \tag{8}$$

3.1.3. Limitations of ICA

There are four basic limitations of the ICA method Lee et al. (1998):

1. Only one original independent component can have Gaussian distribution. If multiple Gaussian sources exist, the ICA method is not able to extract these sources (independent components) from the data (x).
2. If we have an n-dimensional data vector, then we can find a maximum of n-independent components using the ICA method.
3. Some (or all) calculated y components can be multiplied by -1 with respect to the original components.
4. The order of the original independent components cannot be determined by the ICA method.

3.2. Principal Component Analysis (PCA)

The PCA (Soong and Koles, 1995; Diamantaras and Kung, 1996; Jolliffe, 2002; Lhotská et al., 2009) is a useful statistical technique for finding patterns in data of high dimensionality. It is a way of identifying patterns in data, and expressing the data in such a way as to highlight their similarities and differences. Since patterns can be hard to find in data of high dimension, where the luxury of graphical representation is not available, PCA is a powerful tool for analyzing data.

Figure 4 shows the block diagram for the PCA method. Similarly to the ICA method (see **Figure 2**), this diagram includes a pre-processing stage, fECG signal estimation as well as the evaluation of the results by comparing it with the data recorded by means of the FSE. The time shift between the estimated aECG* and mECG* components and amplitude difference was compensated using the same adaptive algorithm as in the previous case. Additionally, further morphological analysis (MA) is provided for both reference and estimated data.

The other main advantage of the PCA method is that we can find patterns in the data and then we can compress the data, i.e., by reducing the number of dimensions, without much loss of information. The input data vector is represented by the column vector $\mathbf{x} = [x_1, x_2, \cdots, x_n]^{\mathrm{T}}$, with dimension n. We have a set of data that consists of m input vectors. The entire ensemble is compactly represented by the $n \times m$ data matrix $\mathbf{X} = [x_1, x_2, \cdots, x_m]$. The purpose of PCA is to find those $m\,(m < n)$ components of the elements of $\mathbf{X}$, which reduce the dimensionality of the input vector in a mean squared error sense. One of the approaches to this solving problem is the projection of the data along orthogonal basis vectors through eigen decomposition of the covariance estimate of the input.

If we let $\mathbf{x}$ vector have a zero mean value, $E\{\mathbf{x}\} = 0$, then the transformation of vector $\mathbf{x}$ can be defined as:

$$\mathbf{s} = \mathbf{x}^{\mathrm{T}}\mathbf{U} = \mathbf{U}^{\mathrm{T}}\mathbf{x}. \tag{9}$$

Or also

$$\mathbf{s}_i = \mathbf{x}^{\mathrm{T}}\mathbf{u}_i = \mathbf{U}_i^{\mathrm{T}}\mathbf{x}, \tag{10}$$

where matrix $\mathbf{U} = [u_1, u_2, \cdots, u_n]$ is the transformation matrix with the condition:

$$\|\mathbf{u}_i\| = \sqrt{\mathbf{u}_i^{\mathrm{T}}\mathbf{u}_i} = 1. \tag{11}$$

That means that the module of the base vector $\mathbf{u}_i$ is equal to one. Equation (12) is also called the PCA data model. The value $\mathbf{s}_i$ is the projection of the input data $\mathbf{x}$ to the orthogonal base vectors $\mathbf{u}_i$. The vector $\mathbf{s} = [s_1, s_2, \cdots, s_n]^{\mathrm{T}}$ is the principal component vector and the values $\mathbf{s}_i$ are the principal components.

We can also do the opposite approach. After PCA's main components $\mathbf{s}_i$ (i.e., U-matrix coefficients,) have been found, the data vector $\mathbf{x}$ can be reconstructed as follows:

$$\mathbf{x} = \mathbf{U}\mathbf{s} = \sum_{i=1}^{n} \mathbf{s}_i\mathbf{u}_i. \tag{12}$$

The aim of the PCA method is to find a linear orthogonal transformation represented by the $\mathbf{U}$ matrix so that the variance of $\mathbf{s}_i$ projection is maximum. The variance can be defined as:

$$\sigma_s^2 = E\{\mathbf{s}^2\} = E\left\{\left(\mathbf{u}^{\mathrm{T}}\mathbf{x}\right)\left(\mathbf{x}^{\mathrm{T}}\mathbf{u}\right)\right\} = \mathbf{u}^{\mathrm{T}}\mathbf{C}\mathbf{u}_i, \tag{13}$$

where $\mathbf{C} = E\{\mathbf{x}\mathbf{x}^{\mathrm{T}}\} = \mathbf{C}^{\mathrm{T}}$ is a symmetric covariance matrix of random vector $\mathbf{x}$. From equation (14) it follows that the variance of the s projection is a function of the unit vector $\mathbf{u}_i$.

$$\psi(\mathbf{u}) = \sigma_s^2 = \mathbf{u}^{\mathrm{T}}\mathbf{C}\mathbf{u}, \tag{14}$$

where $\psi(\mathbf{u})$ is the variance probe.

The aim of the PCA method is to find the base vectors $\mathbf{u}_i$ for which the variation probe $\psi(\mathbf{u})$ is maximal under the condition expressed in Equation (12).

3.3. Principal Components Estimation

The problem about estimating the base vectors $\mathbf{u}_i$ is based on solving equation (16):

$$\mathbf{C}\mathbf{u}_i = \lambda_i\mathbf{u}_i;\ \ i = 1, 2, \cdots, n. \tag{15}$$

The solution of the equation is to find the actual numbers λ_i (the numbers of the covariance
matrix $\mathbf{C}$) and the vectors of the covariance matrix $\mathbf{C}$.

The $\mathbf{C}$ matrix's eigenvalues are ordered from the largest value to the smallest value $\lambda_1 > \lambda_2 > \cdots > \lambda_n$; $\lambda_1 = \lambda_{max}$ and by the ordered vectors $\mathbf{u}_i$ it is possible to create the matrix $\mathbf{U} = [\mathbf{u}_1, \mathbf{u}_2, \cdots, \mathbf{u}_n]$, then the equation (15) can be expressed as:

$$\mathbf{C} \cdot \mathbf{U} = \mathbf{U} \cdot \Lambda, \tag{16}$$

where Λ denotes the diagonal matrix with the eigenvalues $\lambda_1, \cdots, \lambda_n$. Respective column vectors u_i satisfy the orthogonality condition:

$$\mathbf{u}_i^{\mathrm{T}} \cdot \mathbf{u}_j = \begin{cases} 1, i = j, \\ 0, i \neq j. \end{cases} \tag{17}$$

That means that $\mathbf{U}$ is an identity matrix (15) and can be expressed as:

$$\mathbf{U}^{\mathrm{T}} \cdot \mathbf{C} \cdot \mathbf{U} = \mathbf{U}\Lambda. \tag{18}$$

By comparing equations (14) and (19) we can assume that:

$$\psi(\mathbf{u}_i) = \lambda_i;\ \ i = 1, 2, \cdots, n. \tag{19}$$

This means that the variance probes $\psi(\mathbf{u}_i)$ seek the maximum variance and the matrix's eigenvalues are identical.

The PCA principle is illustrated in **Figure 5** for the two-dimensional set of input data, depicted as points marked with the letter 'A'. The data is expressed by the matrix $\mathbf{X}$, $\mathbf{X} = [x_{1i}, x_{2i}]^{\mathrm{T}}$, $i = 1, 2, \cdots, p$; where p is the number of points and x_{ji} is the i-th value of the j-random variable. On the horizontal axis, the values x_1 are plotted, whereas x_2 values are plotted on the

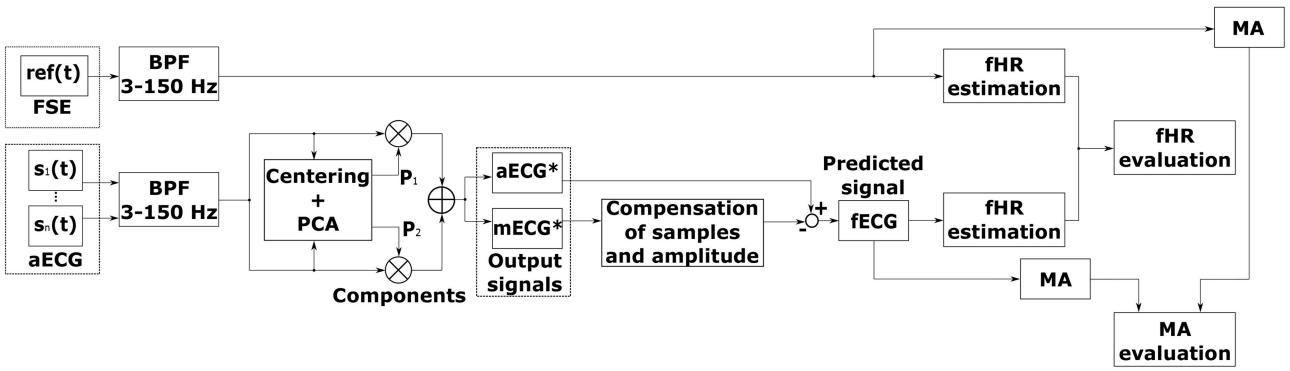

FIGURE 4 | Block diagram for fECG signal extraction using the PCA method.

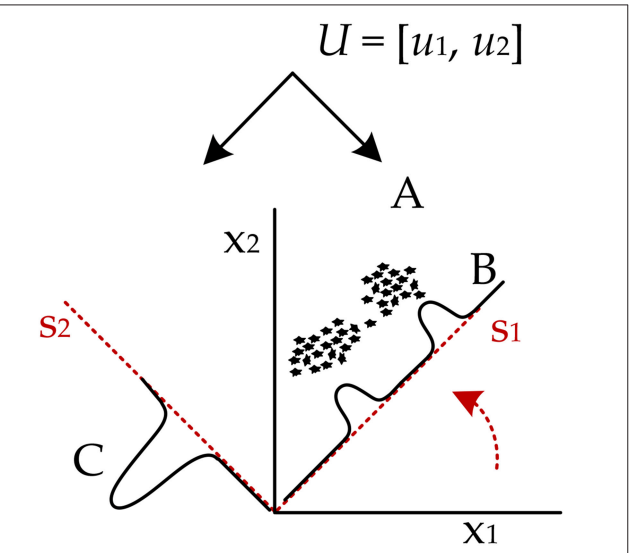

FIGURE 5 | The principle of PCA method.

vertical axis. The PCA method caused the rotation of the axes from the original position x_1 and x_2 to a position that is denoted by the letters s_1 and s_2. The axes rotated in the direction of the vectors of the covariance matrix. The rotation is represented by a dotted arrow in **Figure 5**. By projecting the dataset on an axis that is in the direction of the first vector, we capture the exact data structure that represents 2 clusters in this structure ("B"). The variation of this projection is the maximum of all possible directions (rotations). When projection is made to the s_2 ("C") axis, the information about 2 clusters is hidden.

4. DATASET

The research material consisted of multichannel fetal electrocardiograms obtained from 12 different women at ITAM in Zabrze, Poland during established labors, between 38 and 41 weeks of gestation and saved in 12 different recordings. Five of these recordings constitute the Abdominal and Direct Fetal Electrocardiogram Database (AD FECG) available to the public on the PhysioNet website (Matonia et al., 2006; Jezewski et al., 2012).

In all cases the additional scalp electrode was placed for a clinical indication and all patients consented to participate in this study. The signals were recorded using a system for acquisition and analysis of fetal electrocardiogram KOMPOREL (ITAM Institute, Zabrze, Poland), in the Department of Obstetrics at the Medical University of Silesia. Each individual recording was comprised of signals acquired from four differential channels using electrodes placed on a maternal abdomen, and a direct electrocardiogram was registered from a fetal head as a reference signal (please see **Figure 6**).

The abdominal electrodes configuration was comprised of four electrodes placed around the navel, a reference electrode positioned above the pubic symphysis and a common mode reference electrode (with active-ground signal) placed on the left leg. To reduce the skin impedance, the areas under the Ag-AgCl electrodes (3M Red Dot 2271) were abraded (3M Red Dot Trace Prep 2236). It is important to emphasize that the acquisition of abdominal fECG signals during labor presents additional challenges we had to be aware of. Firstly, during labor the strongest signal was observed when the fetus was fully developed. On the other hand, the quality of abdominal signals acquired during labor was contaminated by considerable muscular activity of the uterus. Moreover, during signal acquisition the scalp electrode very often lost contact with the fetal head, causing temporary signal loss. Some fragments of the direct fECG signals were also distorted by interferences caused by maternal movements. Consequently, we had to select only those short fragments of the recordings for which there were no signal loss periods in the direct (reference) fECG signal. The acquisition of direct fetal electrocardiogram was carried out with a typical spiral electrode, commonly used in the direct fECG channel of popular bedside fetal monitors. The R-wave peaks were then automatically determined from the direct fECG signals by means of an on-line analysis algorithm applied in the KOMPOREL system. The accurate occurrence of these peaks was then verified (off-line) by a group of cardiologists, resulting in a set of reference

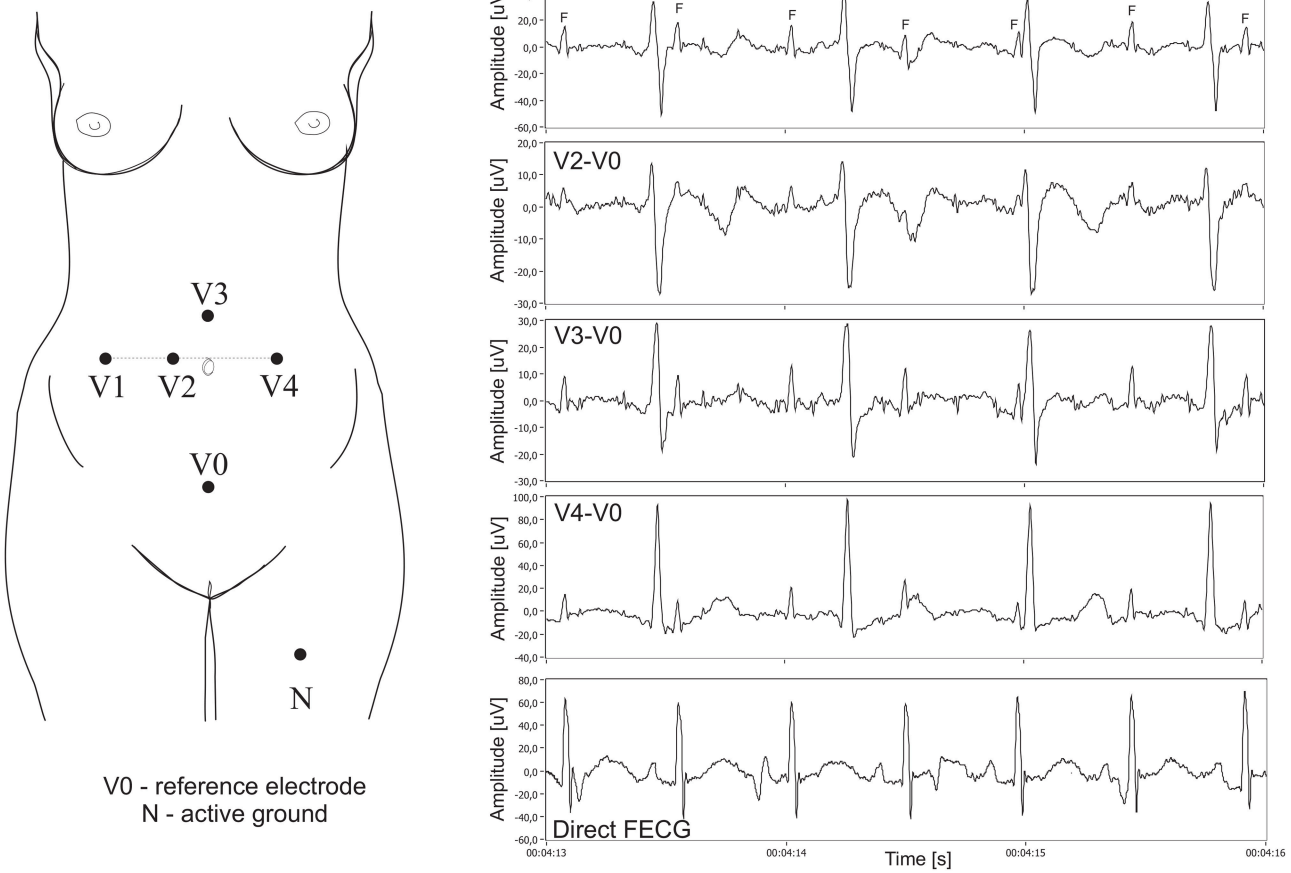

FIGURE 6 | Left: Electrode placement system for recording and analysis of bioelectric signals acquired from the maternal abdominal wall, the direct electrode attached to the fetus head (sampling rate of 1 kHz, bandwidth 1 Hz–150 Hz and resolution of 16 bits). **Right:** Plots for 4 differential signals acquired from the maternal abdomen and the reference direct fECG signal (M, maternal QRS complexes; F, fetal QRS complexes).

markers precisely indicating the location of the R-waves. These markers were then stored together with the direct and indirect fECG signals. In 12 5-min recordings, a total of 5,165 maternal QRS complexes as well as 7,863 fetal QRS complexes were detected. Assuming the maximum width of the maternal QRS complex as 100 ms and that of the fetal as 40 ms, the number of complexes without feto-maternal coincidence was 2,415 maternal and 5,142 fetal.

4.1. Performance Evaluation Measures

We used quantitative measures (dedicated evaluation indices) related to the Signal-to-Noise Ratio (SNR) to evaluate the sufficiency and diversity of the research data to clearly distinguish between useful signal components and contaminating interferences in the abdominal signals. These indices allow the evaluation of the mutual amplitude dependencies of maternal and fetal components on each other and their relation to other noise components in the aECG signals (**Figure 7**).

Assuming that the signal powers of P and T waves in the fetal and maternal complexes are negligible, the average power of interferences P_N in the abdominal signal can be presented as an average signal power outside the QRS complex locations given by:

$$P_N = \frac{\sum_{k=1}^{L} x^2(k)}{L}, \tag{20}$$

where L is the number of samples in the abdominal signal $x(k)$ that are not associated with any QRS complex.

Additionally, assuming that there is no correlation between the useful signal and the noise component, the average power of the maternal signal P_M is given by:

$$P_M = \frac{\sum_{i=1}^{J} \sum_{k=FP_M(i)-S_M/2}^{FP_M(i)+S_M/2} x^2(k)}{J(S_M+1)} - P_N, \tag{21}$$

where J is the number of detected maternal QRSs that do not overlap the fetal QRSs; S_M is the width of the maternal QRS

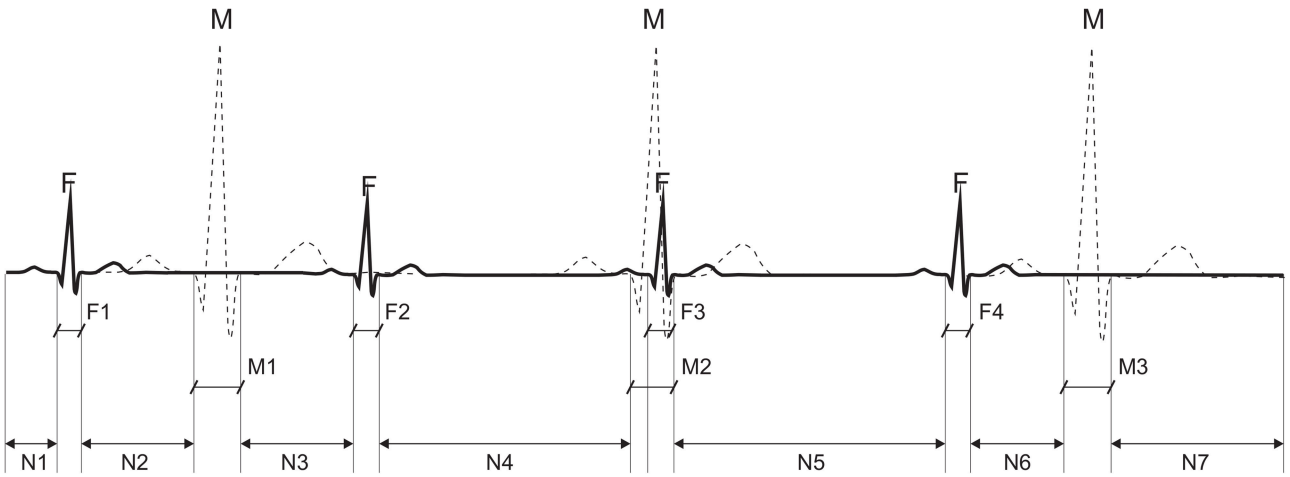

FIGURE 7 | Calculation of an average power for particular components of the abdominal ECG signal: the average power of interference N is calculated from segments: N1 + N2 + N3 + N4 + N5 + N6 + N7, the maternal signal power M from M1 + M3, and fetal from: F1 + F2 + F4.

(100 ms); and $FP_M(i)$ is the timing of the i-th maternal QRS occurrence.

Similarly, the average power of the fetal signal P_F is:

$$P_F = \frac{\sum_{i=1}^{J} \sum_{k=FP_F(i)-S_F/2}^{FP_F(i)+S_F/2} x^2(k)}{I(S_F+1)} - P_N, \quad (22)$$

where I is the number of detected fetal QRSs that do not overlap the maternal ones, S_F is the fetal QRS width (40 ms), and $FP_F(i)$ is the timing of the i-th fetal QRS occurrence.

Based on these values, the WMF index relating the maternal and fetal components can be defined as follows:

$$WMF = 10 \log \frac{P_M}{P_F}, \quad (23)$$

and similarly, the WM and WF indices describing the mECG signal and fECG signal powers in relation to the power of the interfering components, can be respectively defined as follows:

$$WM = SNR_{MECG} = 10 \log \frac{P_M}{P_N}, \quad (24)$$

$$WF = SNR_{FECG} = 10 \log \frac{P_F}{P_N}. \quad (25)$$

From the analysis of these indices based on the results obtained from the four abdominal signal channels, it could clearly be seen that for the research data used, the dominant signal was the mECG, whose amplitude was always more than three times higher than that of the noise component signal (mean WM is 10.9 dB, with a range from 5 to 12.6 dB). Similarly, its relation to the fetal signal, as indicated by the WMF index, exceeded 7 dB on average (range from 1.8 to 11.9 dB). The WF indicator, informing the relationship between fetal QRSs and the noise component, varied very considerably. Its average value was 3.9 dB, but there were cases where the WF oscillated within almost 7 dB (the fetal QRS amplitude was more than twice as high as that of the noise component), and in cases when WF was close to only 0.5 dB the fetal QRS level was comparable to the amplitude of interferences.

5. RESULTS

5.1. Fetal Heart Rate Determination

In this section, we present our evaluation results of the fECG signals extracted from aECG signals acquired by using 4 abdominal electrodes. The fECG signals acquired by means of the Fetal Scalp Electrode (FSE) were used as reference. This direct signal was used for the verification of the extracted signal by comparing the fHR values determined from each of them.

In the reference and extracted fECG signals, the R waves were detected and the intervals between subsequent peaks (RR intervals) were determined. Fetal HR was then calculated as the number of the RR intervals in 1 min.

Figure 8 presents an overview of the dataset used in fHR determination. It includes the mean fHR waveform calculated for all of the available data. This figure shows that 60 min of ECG data (i.e., around 8,000 R waves) in total were available for our experiments. This dataset covers different gestation ages, fetal positions, maternal body mass indexes (BMI), etc. Such a unique heterogeneous dataset with sufficient length combining continuous FSE and abdominal ECG recordings allows for robust testing of the applied ICA and PCA methods.

In this study, we used two types of moving average filters (MAF). For the dataset overview depicted in **Figure 8**, the most suitable values for the MAF window size was 30 as it produced the best visual results and enhanced the fHR waveform trend. However, for the rest of the determined fHR waveforms, we used a MAF window size of 10 since the data length was significantly lower (5 min). The following figures (**Figures 9–14**) show the details of the fHR waveforms shown in **Figures 8**, **9–11**, which reveal good agreement between the fHR values determined from

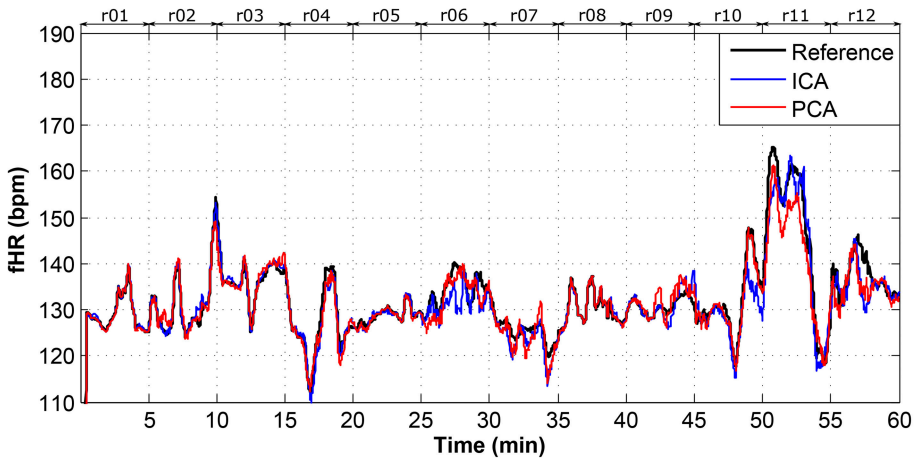

FIGURE 8 | Dataset overview of real01 to real12 fHR determination.

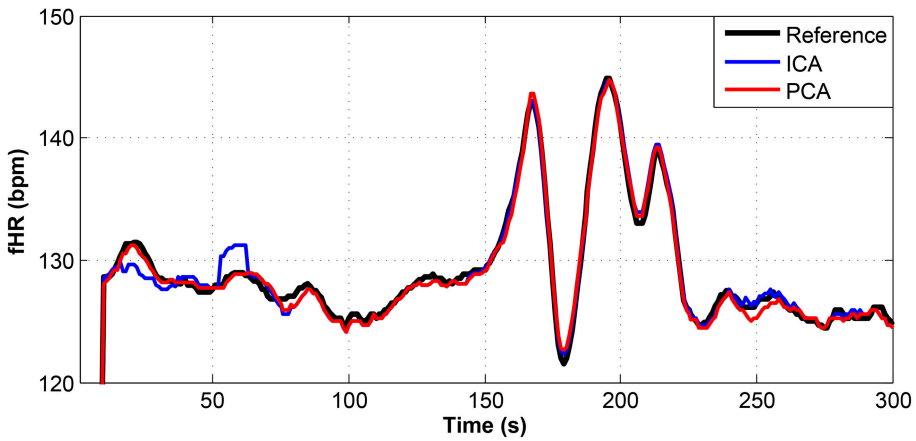

FIGURE 9 | Comparison of the fHR values determined from the fECG signals extracted from recording real01 by using the ICA and PCA methods with the reference fECG signal recorded by means of the FSE.

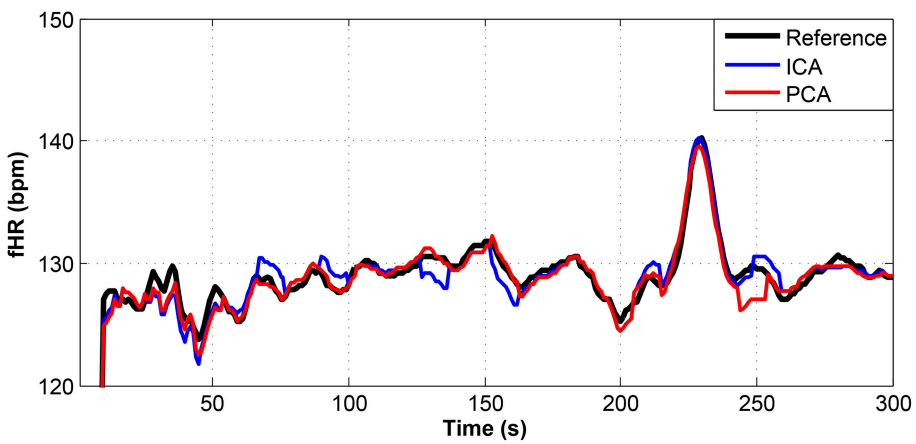

FIGURE 10 | Comparison of the fHR values determined from the fECG signals extracted from recording real05 by using the ICA and PCA methods with the reference fECG signal recorded by means of the FSE.

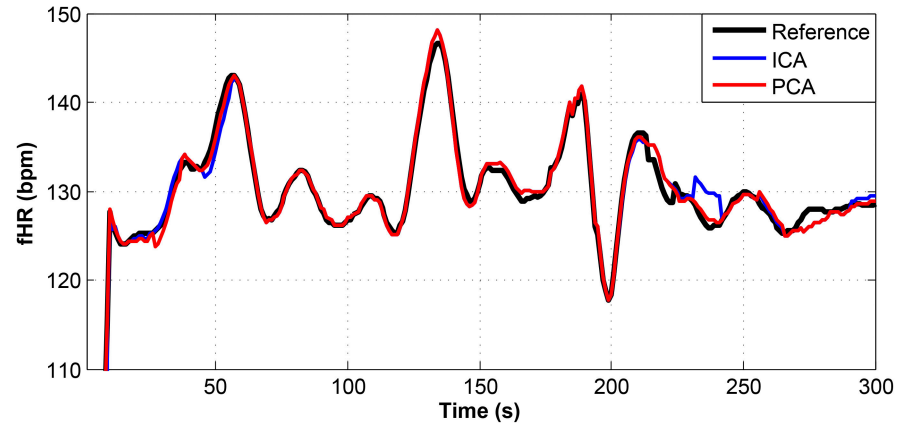

FIGURE 11 | Comparison of the fHR values determined from the fECG signals extracted from recording real08 by using the ICA and PCA methods with the reference fECG signal recorded by means of the FSE.

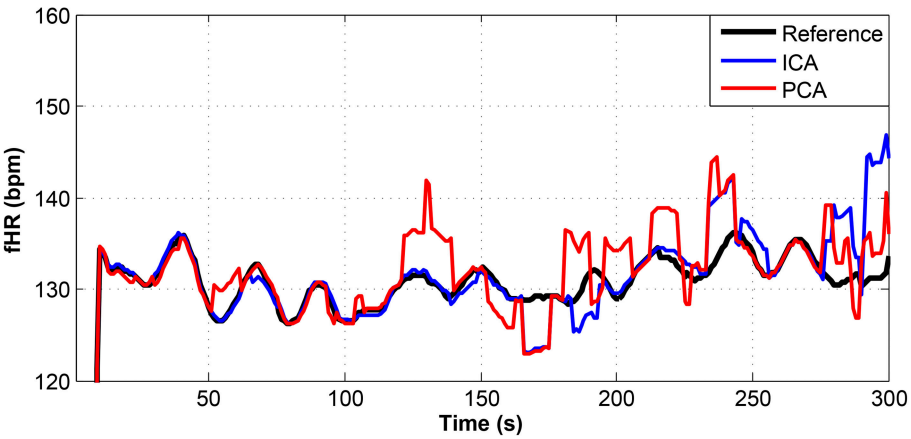

FIGURE 12 | Comparison of the fHR values determined from the fECG signals extracted from recording real09 by using the ICA and PCA methods with the reference fECG signal recorded by means of the FSE.

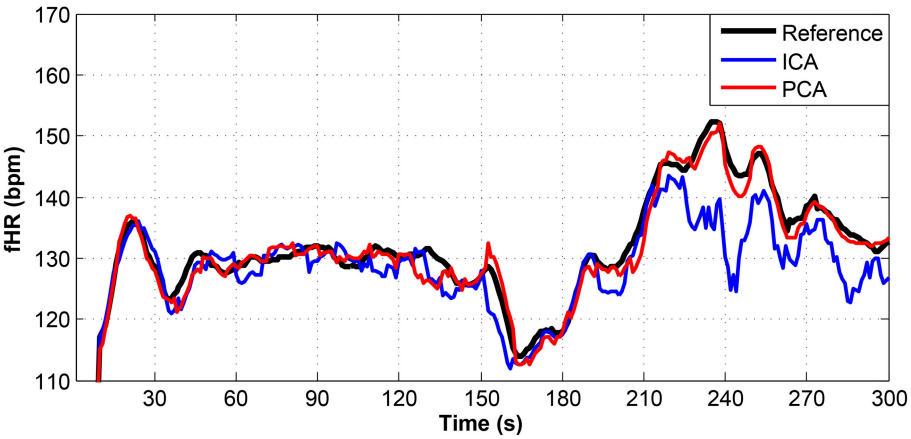

FIGURE 13 | Comparison of the fHR values determined from the fECG signals extracted from recording real10 by using the ICA and PCA methods with the reference fECG signal recorded by means of the FSE.

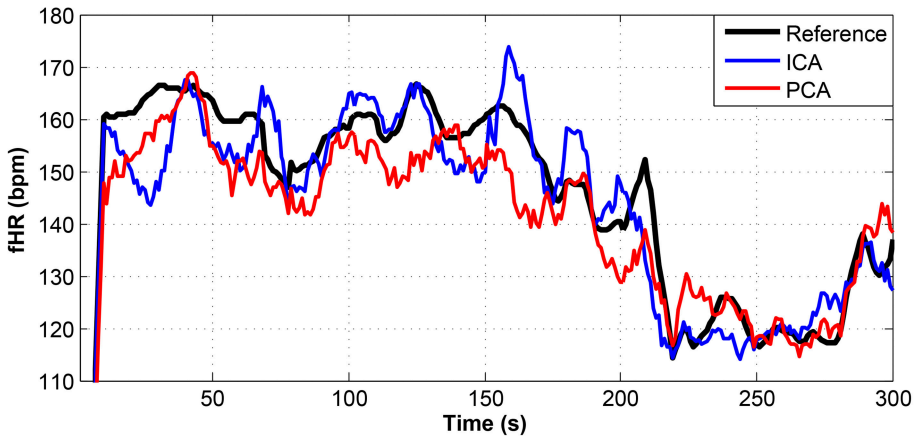

FIGURE 14 | Comparison of the fHR values determined from the fECG signals extracted from recording real11 by using the ICA and PCA methods with the reference fECG signal recorded by means of the FSE.

the reference fECG signals and those calculated by applying the ICA and PCA methods to the aECG signals (recordings real01, real05, real08) to extract fECG signals, whereas **Figures 12–14** show fragments with sufficient quality for fHR detection (recording real09, real10, real11), however, these fragments were insufficient for advanced morphological fECG signal analysis.

Figures 9–11 show the comparison of the fHR values (in bpm) determined from the fECG signals extracted from recordings real01 and real05, real08, respectively, as well as those calculated from the direct or reference fECG signals. We can observe that the fHR values determined from the extracted signals (especially those by the PCA method) were comparable to those calculated from the reference signal (acquired by means of the FSE).

For other recordings, however, the results were different. In the case of the real09, real10, and real11 recordings (**Figures 12–14**, respectively), the fHR values determined from the fECG signals extracted by the ICA method significantly differed from those fHR values calculated by using the reference fECG signals. It was observed that the fHR values determined by the PCA method were significantly more accurate than those determined by the ICA method. This could be caused by several factors that will be discussed in more detail (see section 6.4).

5.2. Statistical Analysis

In this section, we present the statistical evaluation of the accuracy of the ICA and PCA methods in the extraction of fECG signals compared to the reference fECG signal measured by means of the FSE. We use the following metrics and equations (26–29) to achieve this task: Sensitivity (Se), Positive Predictive Value (PPV), Accuracy (ACC), and F1 (the overall probability that the fQRS complex is correctly detected) (Samuel et al., 2017). In these equations, TP represents True Positive (correct detection of fQRS complexes when they are present in the fECG signals), FN stands for False Negative (incorrect detection of fQRS complexes when they are not present in the fECG signal), FP symbolizes False Positive (incorrectly indicates the presence of fQRS complexes in the fECG signals), and TN (true detection of the absence of fQRS complexes in the fECG signals). **Tables 1**, **2** show the calculated values of these parameters for the analyzed records. For the detection of the fQRS complexes, we used an extended version of the Pan and Tompkins algorithm (Pan and Tompkins, 1985); and the accuracy of the fECG estimation was evaluated by a beat-to-beat comparison of the extracted fQRS complexes by means of the ICA or PCA methods and the reference fQRS complexes detected in the reference fECG signal acquired by the FSE (Zhang et al., 2017).

$$\mathrm{Se} = \frac{\mathrm{TP}}{\mathrm{TP} + \mathrm{FN}} \cdot 100. \tag{26}$$

$$\mathrm{PPV} = \frac{\mathrm{TP}}{\mathrm{TP} + \mathrm{FP}} \cdot 100. \tag{27}$$

$$\mathrm{ACC} = \frac{\mathrm{TP}}{\mathrm{TP} + \mathrm{FP} + \mathrm{FN}} \cdot 100. \tag{28}$$

$$\mathrm{F1} = 2 \cdot \frac{\mathrm{PPV} \cdot \mathrm{Se}}{\mathrm{PPV} + \mathrm{Se}} = \frac{2 \cdot \mathrm{TP}}{2 \cdot \mathrm{TP} + \mathrm{FP} + \mathrm{FN}} \cdot 100. \tag{29}$$

5.3. Bland-Altman Statistical Analysis

For further evaluation of the accuracy of the determined fHR values, the Bland-Altman method was utilized. This method is based on calculating the mean difference between two methods of measurement (so-called bias), and 95 % of the limits of agreement as the mean difference (2 SD), or more precisely, (1.96 SD). It is expected that the chosen limit of 95 % contains 95 % of the variances between the two tested methods: the reference and estimated fHR values in our case. Therefore, the fHR values determined from the extracted fECG signals are assumed to be accurate, such that 95% of all of them fall in the range of $\pm$ 1.96 SD (Myles and Cui, 2007).

Figures 15–17 show the plots based on the Bland-Altman statistical analysis technique for both methods with 12 different data recordings. In these plots, there are 3 lines: 2 of them

TABLE 1 | Statistical evaluation of fQRS detection by ICA method.

Recordings	TP	FP	FN	± 1.96 SD	Se (%)	PPV (%)	ACC (%)	F1 (%)
real01	644	2	3	98.33	99.54	99.69	99.23	99.61
real02	663	9	5	95.33	99.25	98.66	97.93	98.96
real03	686	14	7	93.00	98.99	98.00	97.03	98.49
real04	643	11	19	90.00	97.13	98.32	95.54	97.72
real05	645	5	7	96.00	98.93	99.23	98.17	99.08
real06	676	12	15	91.00	97.83	98.26	96.16	98.04
real07	626	6	24	90.00	96.31	99.05	95.43	97.66
real08	651	4	3	97.67	99.54	99.39	98.94	99.47
real09	657	5	4	97.00	99.39	99.24	98.65	99.32
real10	635	3	24	91.00	96.36	99.53	95.92	97.92
real11	719	10	17	91.00	97.69	98.63	96.38	98.16
real12	688	10	15	91.67	97.87	98.57	96.49	98.22
Total	7,933	91	143	93.50	98.23	98.87	97.13	98.55

TABLE 2 | Statistical evaluation of fQRS detection by PCA method.

Recordings	TP	FP	FN	± 1.96 SD	Se (%)	PPV (%)	ACC (%)	F1 (%)
real01	644	1	2	99.00	99.69	99.84	99.54	99.77
real02	663	14	13	91.00	98.08	97.93	96.09	98.00
real03	686	14	9	92.33	98.71	98.00	96.76	98.35
real04	643	12	17	90.33	97.42	98.17	95.68	97.79
real05	645	3	8	96.33	98.77	99.54	98.32	99.15
real06	676	9	16	91.67	97.69	98.69	96.43	98.18
real07	626	10	17	91.00	97.36	98.43	95.87	97.89
real08	651	2	2	98.67	99.69	99.69	99.39	99.69
real09	657	13	6	93.67	99.10	98.06	97.19	98.57
real10	635	6	14	93.33	97.84	99.06	96.95	98.45
real11	719	3	21	92.00	97.16	99.58	96.77	98.36
real12	688	5	16	93.00	97.73	99.28	97.04	98.50
Total	7,933	92	141	93.53	98.27	98.86	97.17	98.56

indicate the chosen limit of 95%, whereas the 3rd one is bold and denotes the state when the signals match. The closer to zero the results are, the better correlation between the fHR determined from the reference signal and the one determined from the signals extracted by the PCA or ICA methods.

Figure 15 shows the Bland-Altman plot of whole dataset depicted in **Figure 8**. The results show that these methods are effective for recordings real01, real05, and real08 as only for these recordings the value of SD exceeded 95% (see **Tables 1**, **2**). Most of the data are thus highly uncorrelated in the Bland-Altman plot. That is caused by the unsatisfactory results achieved by some of the recordings as discussed above.

The results in **Figure 16** show a good correlation in case of recordings real01, real05, and real08, whereas recordings real09, real10, and real11 are highly uncorrelated (see **Figure 17**). This further confirms the results included in **Tables 1**, **2**.

5.4. Challenge 2013 Results Comparison

To present a better implementation of the aforementioned techniques, we compared the performance of our approach to competitive algorithms available in literature. We tested the algorithms on the open source Fetal ECG database on Physionet.org (set A, see phy, 2014), and compared the performance in fECG extraction with the results that were presented at the Computing in Cardiology Conference in 2013, summarizing the competition "Noninvasive Fetal ECG Challenge." Since HRMSE and RRRMSE Scoring parameters for the effectiveness evaluation proposed in the competition turned out to be too controversial, we primarily focused on the comparison of PPV, Se, ACC, and F1 index (see **Table 3**).

TABLE 3 | Performance of the tested algorithms on set a.

Method	± 1.96 SD	Se (%)	PPV (%)	ACC (%)	F1 (%)
ICA	79.71	84.45	99.71	84.26	91.16
PCA	75.98	82.05	99.45	81.68	89.63

Behar et al. presented the possibility of using ICA and PCA (with various combinations of these methods) for the

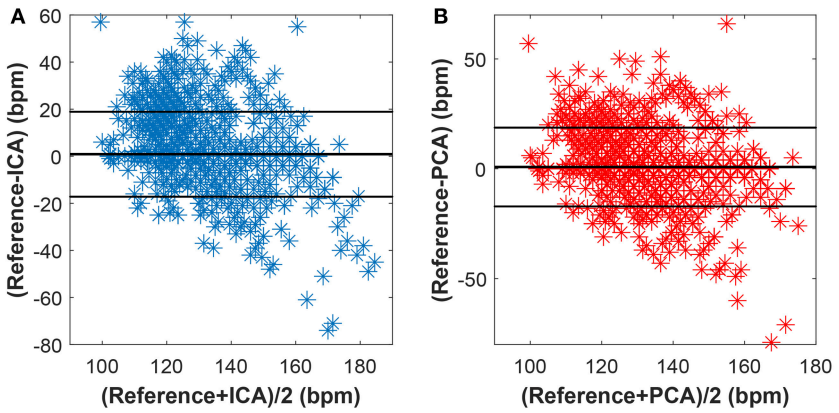

FIGURE 15 | Bland-Altman plot for the entire dataset using **(A)** the ICA and **(B)** the PCA methods.

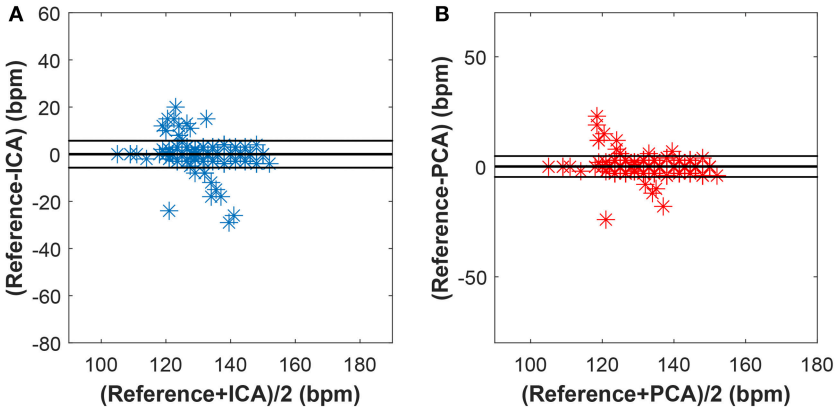

FIGURE 16 | Bland-Altman plot for recordings real01, real05, and real08 using **(A)** the ICA and **(B)** the PCA methods.

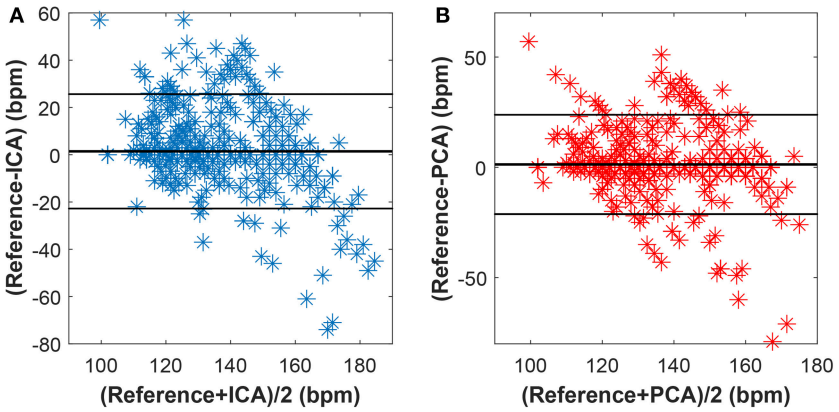

FIGURE 17 | Bland-Altman plot for recordings real09, real10, and real11 using **(A)** the ICA and **(B)** the PCA methods.

extraction of the fECG signal (Behar et al., 2013, 2014). The results showed that the algorithms used in combination with other algorithms perform significantly better than if used separately. Our adaptive algorithm was able to enhance the quality of the fECG extraction compared to the results of ICA and PCA being used separately (improvement of

approximately 27 and 38% in terms of F1 for ICA and PCA, respectively).

5.5. Graphical Interpretation of the Results

To keep our paper to a reasonable length, in this part, we provide the graphical interpretation of the some of the output signals as examples to facilitate their visual evaluation and discuss the unsatisfactory results achieved for some of the recordings. **Figure 18** includes the reference signal recorded by means of the FSE (**Figure 18A**), and the fECG signals extracted by the ICA (**Figure 18B**) and PCA (**Figure 18C**) methods. These results show that the maternal R waves were successfully suppressed while fetal R waves remained unchanged. This is a vital requirement for accurate fHR detection. In terms of the estimated fECG signal morphology, the shape and the duration of P waves were unchanged. However, S and Q waves were deformed (lowered) by the applied signal processing methods. It is important to note that these satisfactory results were mainly achieved due to the high quality of the input ECG signal recordings (see **Figure 19**).

On the contrary, in some records, the determined fHR was lower than the fHR calculated from the reference signal. **Figure 20** (input data on **Figure 21**) presents some examples of the signals that produced unsatisfactory results. It is noticeable that some of the fetal R peaks were suppressed, which could subsequently lead into missed R-peak detection and thus a decreased value of the fHR.

In some time intervals, the fHR waveforms determined from the signals estimated by PCA and ICA methods exceeded the waveform of the fHR determined from the reference signal recorded by means of FSE (see **Figure 12**). An analysis of the estimated signals in these particular fragments reveals maternal residues (see **Figure 22**). These artifacts produce false positively detected fetal peaks and thus increase the mean fHR value. One of the reasons that the PCA and ICA methods performed worst can be noticed in **Figure 23**, which includes the input data in the same time intervals. The quality of the recordings is significantly lower than in the case of the signals depicted in **Figure 19**, especially in the case of abdominal signals called record 2 where the motion artifacts distorted the signal.

5.6. Non-invasive ST-Analysis

In addition to fHR determination and its variability (HRV), we focused on the morphological analysis of the estimated fECG signals extracted from the abdominal records, with primary emphasis on ST segment Analysis (STAN) and T/QRS determination. These capabilities have the potential to improve the diagnosis of fetal hypoxia (sensitivity, specificity) and decrease the number of unnecessary surgical terminations of pregnancy (cesarean sections). Besides, as currently there are no gold standards available for STAN, we are unfortunately unable to perform the quantitative verification and evaluation of the efficacy of our results. Consequently, our initial tests in this article include only the results for the T/QRS determination without deeper statistical analysis. The ST segment is considered to be the most variable part of the fECG signal. The changes in its duration and morphology may indicate pathological states. In particular, the elevation of the ST segment and the T-wave amplitude increase occur when the cardiovascular adaptation to hypoxia is no longer sufficient. STAN automatically detects and alerts changes that are related to the risk of fetal hypoxia (Rosen et al., 1992). In most cases, the method is used in combination with Cardiotocography (CTG) during labor and the interpretations follow the FIGO guidelines and recommendations (Ayres-De-Campos et al., 2015). It is based on calculating the ratio between T-waves and QRS complexes (T/QRS). The analysis of T/QRS in this paper was carried out in the fECG diagnostic tool that we have developed in our laboratory. **Figure 24** shows the Graphical User Interface (GUI) of the application with some examples of the fECG signal analysis results. In our system, the STAN involved three different steps:

1. Localization of the R and S waves in the fECG signals followed by QRS complex detection and amplitude determination;
2. Detection of the R-peaks in the entire fECG signals by using the Continuous Wavelet Transform (CWT) based method;
3. Detection of the T-waves and their amplitude calculations. It is important to emphasize that due to the very low T-wave amplitudes, the mean of 30 Heartbeats (Cardiac Cycles) was used to calculate the T/QRS ratios.

Figure 24 shows the Graphical User Interface (GUI) of our application. It includes the part to load the File (data channel) to be analyzed as well as the sampling frequency. The user is able to load any file in the *.edf or *.mat formats. The panel Heart rate detection allows the user the R-peak detection and HRV calculation on previously loaded fECG data. The user can select between 6 available algorithms based on, for example, the Non-adaptive and Adaptive threshold for heartbeat detection, Discrete and Continuous WT, Neural network, and so on. There is a special panel to visualize the T/QRS analysis since it is a more advanced method for ECG feature analysis. To run a T/QRS ratio analysis (or STAN) the user must select one of the graphs to be analyzed. The details for samples from different recordings used for the experiments carried out in this paper are shown in **Figure 26**.

The graphs in **Figure 25** include 3 types of graphs for 2 recordings (real01 and real09): the fECG estimated by the ICA and PCA methods and the reference signal sensed by FSE. All of the graphs include details needed for STAN: the amplitudes of the T wave and QRS complex and the corresponding T/QRS ratio. The graphs prove that the morphological analysis is achievable in the case of high quality input data. Although the amplitudes of detected T waves and QRS complexes are lower than in the case of the signal from FSE (since the fECG signal is decreased while spreading toward the maternal abdomen) the T/QRS ratios remained unchanged. That means that improving the quality of fECG extraction techniques would allow a unique chance to provide STAN non-invasively in the future.

6. DISCUSSION

The results presented in section 6 prove that the extracted fECG signals fom aECG signals could serve as a valuable

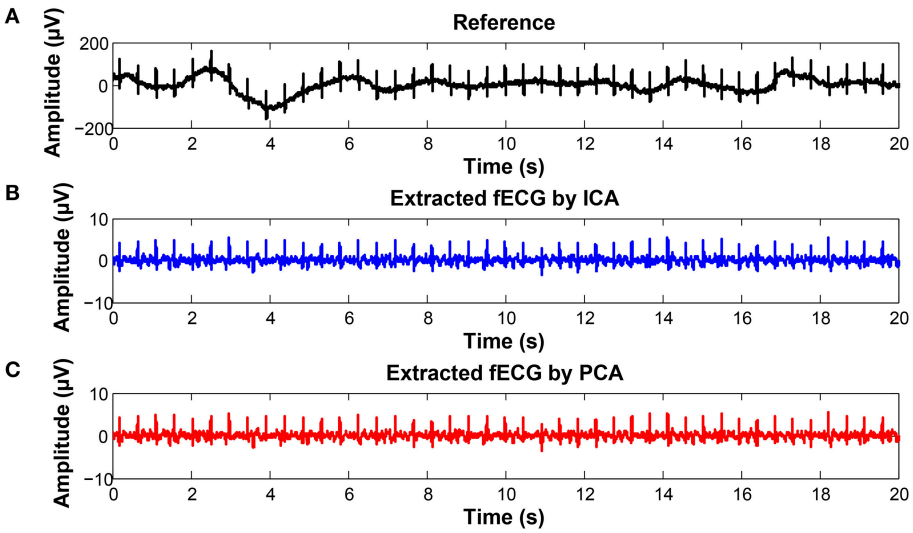

FIGURE 18 | Examples of the signals from recording real10 used for comparison: **(A)** Reference (ideal) fECG signal recorded by means of the FSE, **(B)** fECG signal extracted by the ICA method,**(C)**fECGsignal extracted by the PCA method.

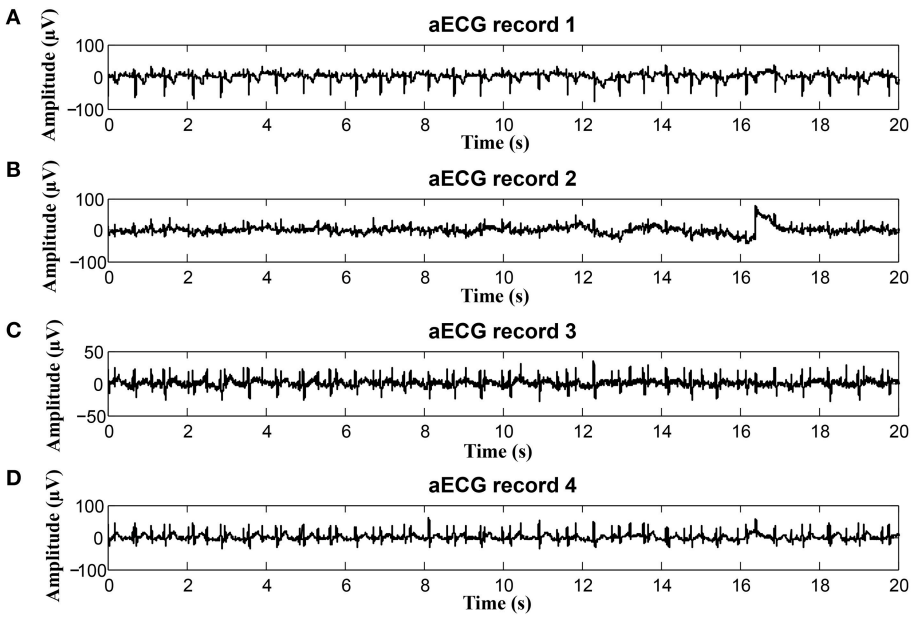

FIGURE 19 | Example of a high quality input recordings (real01) **(A)** abdominal record1; **(B)** abdominal record2; **(C)** abdominal record3; **(D)** abdominal record4.

source of information and that using advanced signal processing methods, such as ICA and PCA, could enable the utility of this type of monitoring in clinical practice as an alternative to the conventional Doppler-based technique. Our statistical analysis results revealed that these non-adaptive methods did not perform very well for some of the recordings (real04, real06, real07, real10, and real11). The results of some unsatisfactory examples (recordings real04 and real10) are depicted in **Figure 26**. A possible explanation for such inferior results is that the magnitude of the fetal component in the abdominal signals is very low in comparison with the maternal one, especially in the case of the abdominal signal denoted as Abdomen_4, shown in the bottom of the figure. Here we are of the opinion that the gestation age was too low for accurate fHR determination. On the contrary, the results for recordings real01 and real08 were satisfactory. Note that the ratio between maternal and fetal components was significantly lower than those in other recordings. An interesting fact that can be observed in recording real10 is that the polarity of the maternal component is the inverse of the polarity in the rest of the recordings. This may

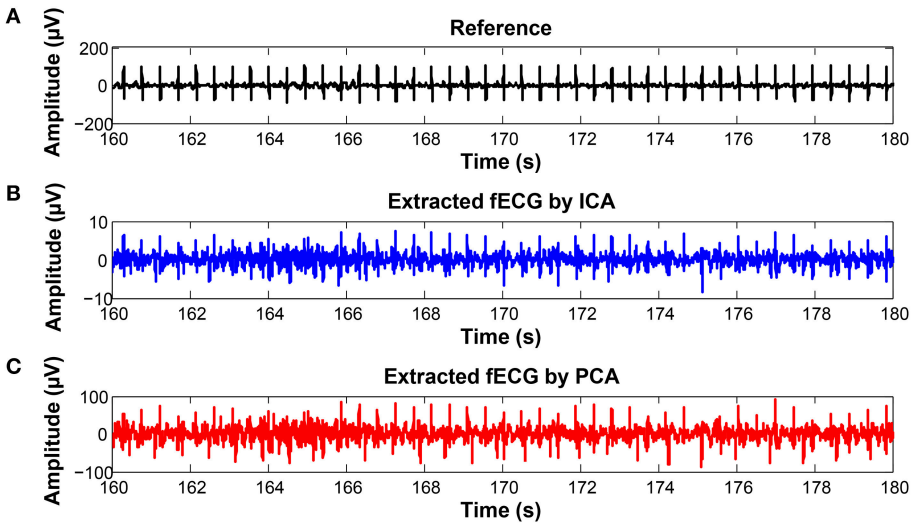

FIGURE 20 | Examples of the signals producing unsatisfactory results in fHR determinantion from recording realX: **(A)** Reference (ideal) fECG signal recorded by means of the FSE, **(B)** fECG signal extracted by the ICA method, **(C)** fECG signal extracted by the PCA method.

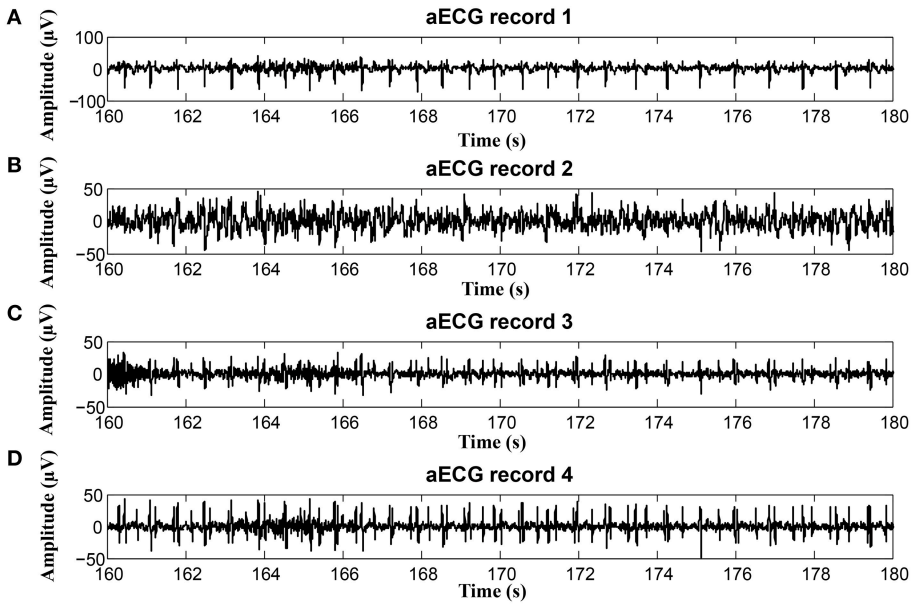

FIGURE 21 | Examples of input signals for the fHR waveform interval with values lower than the reference: **(A)** abdominal record1; **(B)** abdominal record2; **(C)** abdominal record3; **(D)** abdominal record4.

be due to a different electrode placement, which could in turn negatively influence the performance of the tested algorithms. Nevertheless, the quality of the estimated signals is high enough to follow the trend of the fHR waveform, which is a key factor for accessing the fetal condition according to FIGO guidelines (Ayres-De-Campos et al., 2015).

We also need to emphasize that for reliable Morphological Analysis (for example, STAN), the quality of the analyzed fECG signal is of paramount importance and must be adequately high. For this reason STAN is currently performed exclusively on the fECG signals acquired invasively. Such recordings have higher Signal-to-Noise Ratios and therefore the amplitude and shape of the essential components of the fECG signals (T-waves and QRS complexes) are not distorted by contaminating signals. Considering these facts, the only records that could be used for NI-STAN in our work were real01, real02, real05, real08, and real09.

There are two main options for achieving sufficient signal quality of fECGs that is sufficient for NI-STAN: (1) by improving the quality of the input recordings (as discussed in chapter 6.4), or

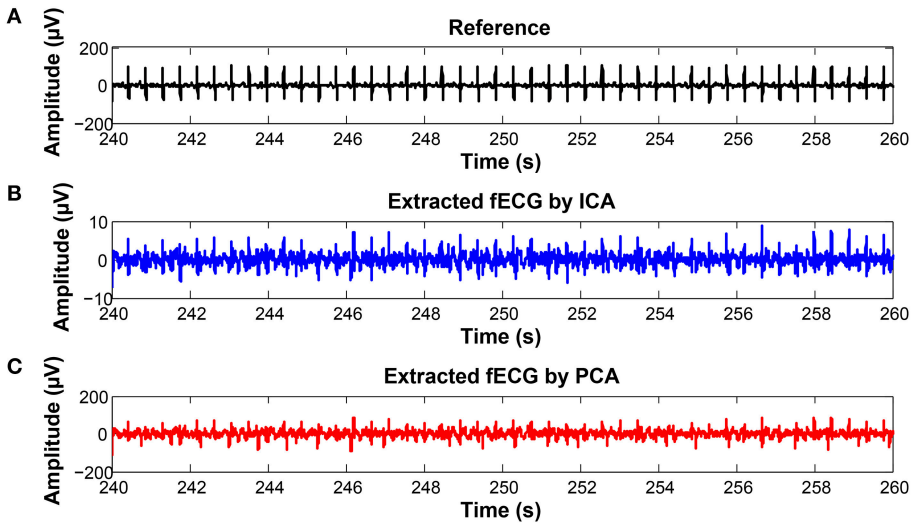

FIGURE 22 | Examples of the signals producing unsatisfactory results in fHR determinantion from recording realX: **(A)** Reference (ideal) fECG signal recorded by means of the FSE, **(B)** fECG signal extracted by the ICA method, **(C)** fECG signal extracted by the PCA method.

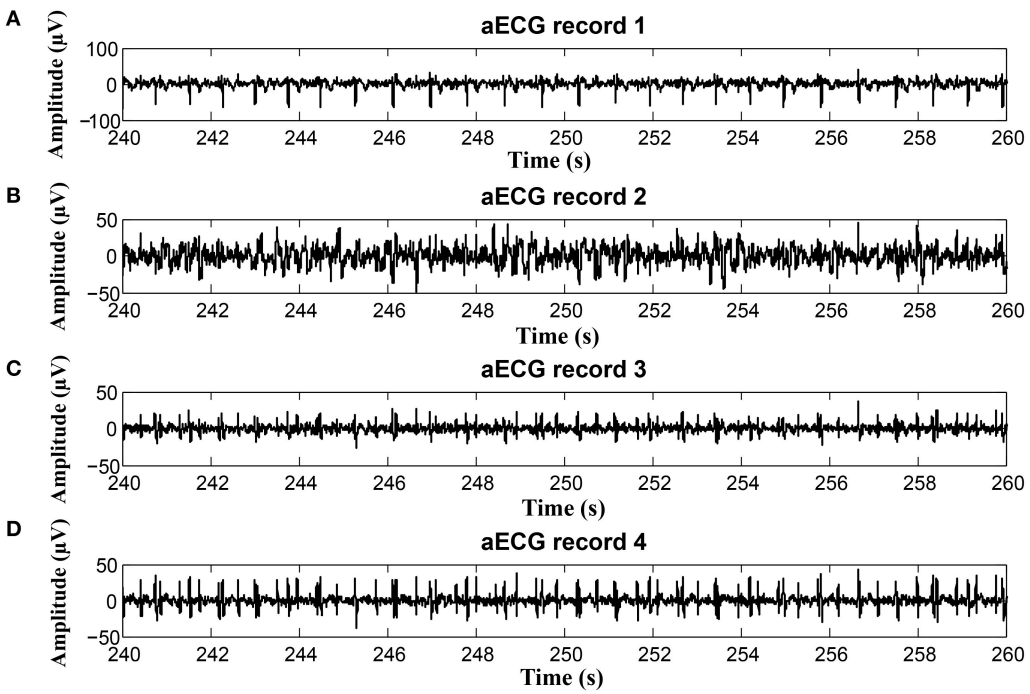

FIGURE 23 | Examples of input signals for the fHR waveform interval with values exceeding the reference: **(A)** abdominal record1; **(B)** abdominal record2; **(C)** abdominal record3; **(D)** abdominal record4.

(2) utilizing more robust techniques, such as the aforementioned hybrid methods leveraging the combined capabilities and advantages of non-adaptive and adaptive methods. For NI-STAN, the key to success is the standardization (optimization) of the electrode placements that has to accommodate varying circumstances, especially gestation age and fetal position in the uterus.

This article is focused on two popular non-adaptive signal processing methods, even though the adaptive techniques have proven to be effective tools for fECG signal extraction from aECG signals. The adaptive methods are theoretically more suitable but have their drawbacks, mainly the need for the additional thoracic electrodes and leads (which restrict the pregnant woman's movements) and thus limit the utility of

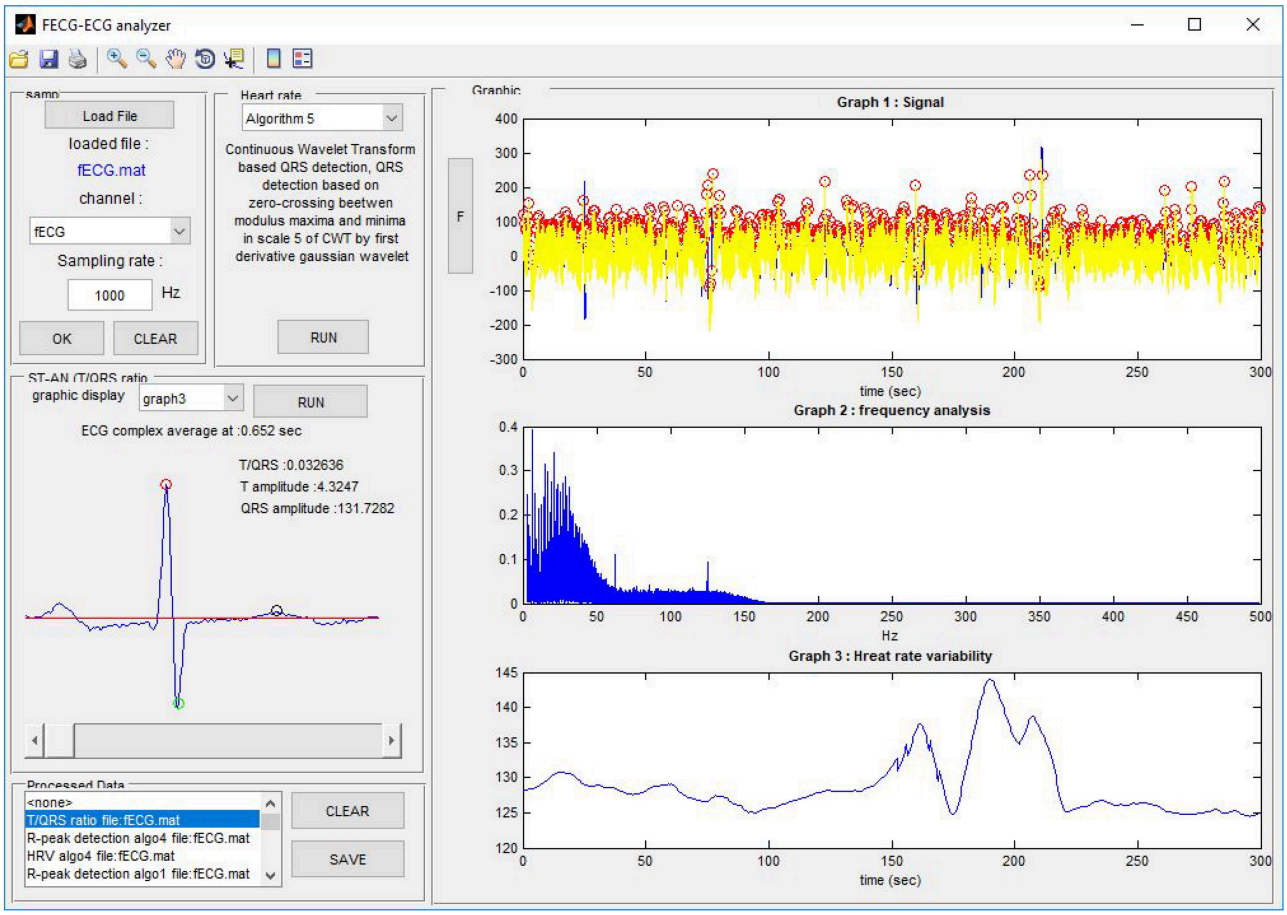

FIGURE 24 | The Graphical User Interface (GUI) of our FECG-ECG Analyzer.

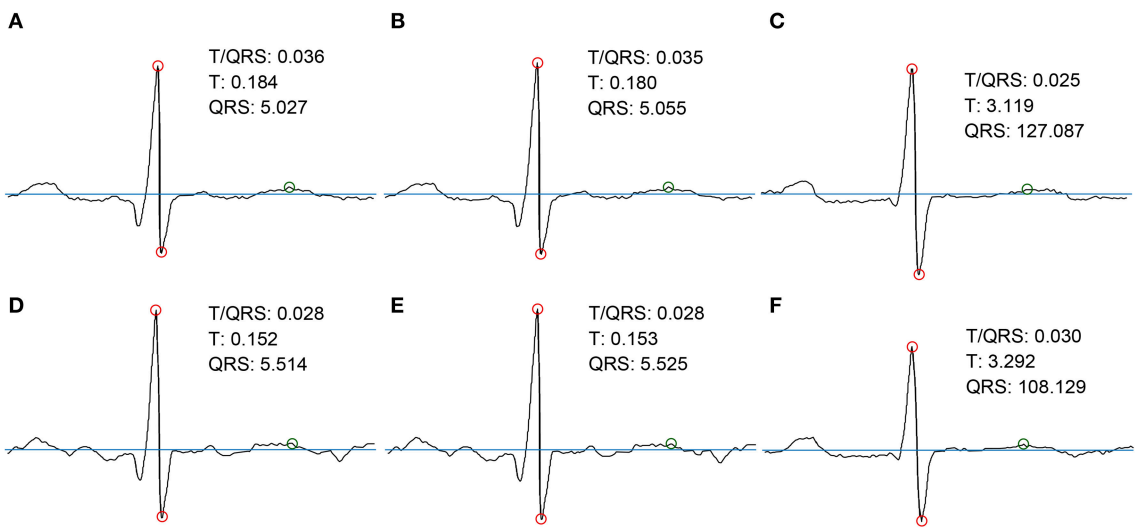

FIGURE 25 | Examples of the morphological analysis of estimated and the reference fECG signals. **(A,D)** estimated signals using PCA method; **(B,E)** estimated signals using ICA method; **(C,F)** reference signals recorded by means of FSE.

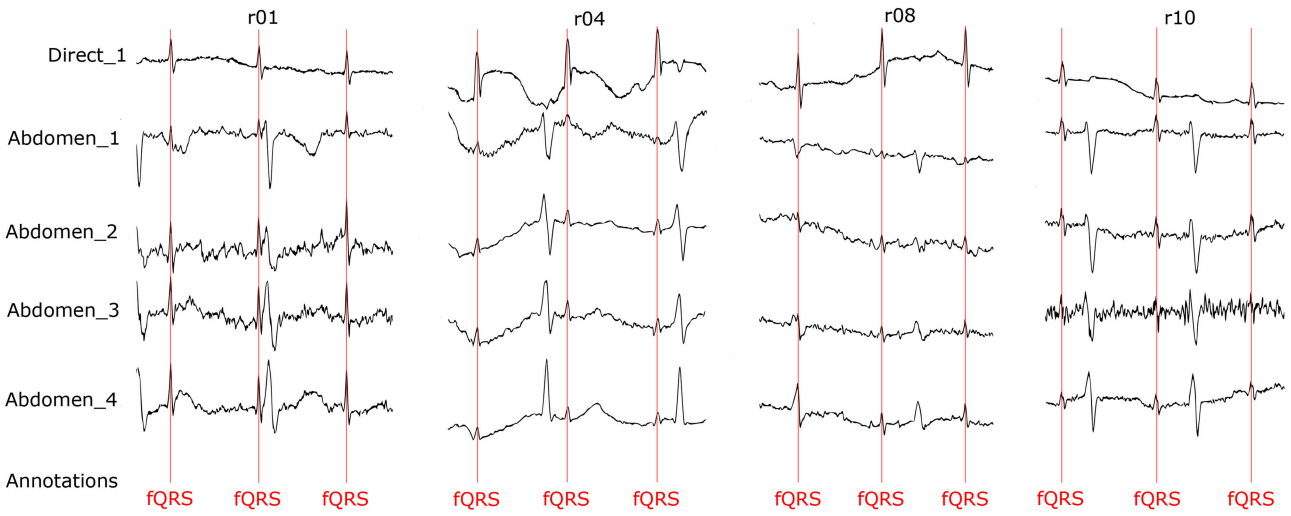

FIGURE 26 | Quality assessment of the recordings used for our comparisons.

such methods in clinical practice. Furthermore, the efficiency of the adaptive methods is closely dependent on the adaptive filter's settings. The optimal filter settings vary with gestational age, fetal position in the uterus, etc. (Kahankova et al., 2017c). Adaptive methods have already been tested by our research group (Martinek and Zidek, 2012; Martinek et al., 2016a, 2017a,b; Fajkus et al., 2017) and others (Kam and Cohen, 1999; Reaz and Wei, 2004; Al-Zaben and Al-Smadi, 2006; Poularikas and Zayed, 2006; Assaleh, 2007; Czabanski et al., 2008; Shadaydeh et al., 2008; Jia et al., 2010; Swarnalatha and Prasad, 2010; Talha et al., 2010; Amin et al., 2011; Niknazar et al., 2013; Wei et al., 2013; Martinek et al., 2016c; Kahankova et al., 2017d, 2018). We need to emphasize that to achieve Morphological Analysis of fECG signals, adaptive methods appear to be more suitable. However, for clinical applications, non-adaptive methods offer the advantage of solely using abdominal electrodes without the need for thoracic electrodes and leads. In addition, there is a trend in SMART technologies in medicine to use a multisource system, where the electrodes are embedded within a garment (one electrode grid/strip for the abdominal area). Such a system seems to be very promising for the future of fetal monitoring. In this kind of system, the ICA and PCA methods applied and tested in our research could prove to be the most suitable for implementation. Nevertheless, our aim here was not only to determine fHR values but also to achieve Morphological Analysis of the fECG waveforms. Our experimental results proved that using advanced signal processing techniques could enable further Morphological Analysis (for example, STAN), see section 6.5.

In our future research, we will focus on leveraging the utility of the combined adaptive and non-adaptive (hybrid) methods. With this approach we would benefit from the advantages offered by both methods. The hybrid methods would be more accurate for detailed Morphological Analysis while making use of the abdominal recordings alone. Our approach would be based on extracting the reference fECG signals from the aECG signals using the ICA and PCA methods. However, we needed to test adaptive and non-adaptive methods separately at first before reaching that goal.

The evaluation of our results was based on comparing the estimated signals with the reference fECG signals recorded by means of the FSE. Five of the recordings used in our experimentation are currently available from the Abdominal and Direct Fetal Electrocardiogram Database Jezewski et al. (2012). The other 7 are new and are not publicly available yet. It is important to emphasize that for the acquisition of data recorded in the entire Database, the type of measurements, sampling frequency, and other details changed. For this reason, we thought it would be beneficial to our readers to describe the details of these measurements. Professor Jezewski, a member of our team and our co-author, intends to make the rest of the Database acquired at ITAM in Poland available to the public by means of PhysioNet.

We obtained the reference fECG signals from raw data in the Database and subsequently processed and annotated them in cooperation with a team of experts including both engineers and clinicians. The R-wave peak detection was semi-automatic. First, we used the Continuous Wavelength Transform to detect the R-waves. Subsequently, we went through all the recordings and visually inspected the detection of the RR intervals to eliminate any automatic errors, see **Figure 26**. This visual quality-assurance step was important for the initial phase of our research not only to ensure the accurate detection of any errors (due to fetal movements in the uterus, incorrect electrode placement, and others); but to find solutions for eliminating them (see Supplementary Material for all figures and tables).

7. CONCLUSION AND FUTURE WORK

In this paper, we compared the effectiveness of two popular non-adaptive signal separation techniques, the ICA and PCA methods, to extract fECG signals from aECG signals noninvasively. The performance of these conventionally

used methods was improved by an adaptive algorithm, compensating amplitude difference and time shift between the estimated components. Currently, the non-adaptive methods are successfully used for fHR determination. However, there are still great research opportunities and scope for improvements, especially in terms of further Morphological Analysis. We provided the performance evaluation results on real data based on comparing the extracted signals with the reference fECG signals recorded by means of the FSE. The novelty in our work is centered around obtaining the reference signals from raw data that were subsequently processed and annotated by a team of experts. Thus, in contrast to the other results reported in the field (see Kahankova et al., 2017c; Martinek et al., 2017a), we were not limited by the lack of gold standards (fQRS annotations in the abdominal signals) as we could use our own reference data for further investigation. We have developed a software tool for Morphological Analysis (for example STAN) of the fECG waveforms. Since we have both reference and estimated fECG signals available, we are able to apply more sophisticated analysis by means of our software tool. For this reason, we could evaluate the robustness of the extraction algorithms for fHR determination and further Morphological Analysis.

The results demonstrated the effectiveness of the improved conventional methods, ICA and PCA, for fHR determination and further Morphological Analysis. The performance of the methods was influenced by several factors. The inferior performance of the methods may be attributable to the impact of the fetal position in the uterus or fetal and maternal movements. Moreover, the electrode placement varies during pregnancy and it is influenced by the Gestation Age (GA). The ICA and PCA methods have the potential to be utilized as early as the 20th week of pregnancy since the signals are too weak for the extraction before that period. As a fundamental limitation in the utility of the ICA and PCA methods for extracting fECG signals, the case of multiple pregnancy must be mentioned since these non-adaptive methods may have problems in extracting the components with same frequencies (fHRs of each fetus in the uterus). Similarly, problems could arise in pathological cases when the maternal and fetal heart rates increase/decrease by the same amount. Generally, the fetal beating frequency is about 2 times greater than the maternal rate. However, in case of fetal bradycardia or maternal tachycardia, these frequencies might have almost the same value.

At present, a great deal of attention is being paid to single-channel methods. It is obvious that for more non-invasive STAN, multichannel recordings are needed. A Single-channel signal is likely to be of low quality due to several factors such as changes in the fetal position and others. Single-channel methods are sufficient to determine the fHR, but for deeper Morphological Analysis they are rather inadequate.

We envision that a multichannel system is essential for the advanced analysis of non-invasively acquired fECG signals. In our future research, we aim to explore the combined utility of non-adaptive and adaptive signal processing methods in order to achieve better results. This approach could lead to the development of a new diagnostic method: non-invasive STAN (NI-STAN).

ETHICS STATEMENT

The study protocol was approved by the Ethical Committee of the Silesian Medical University, Katowice, Poland (NN-013-345/02). Subjects read the approved consent form and gave written informed consent to participate in the study.

AUTHOR CONTRIBUTIONS

RM, RK, JJ, RJ, JM, MF, JN, PJ, and HN proposed the system idea, wrote, and edited the manuscript. RM, MF, and JN performed the experiments, developed, tested, and validated the software. HN, JJ, and PJ critically evaluated the scientific validity of the proposed system and the acquired vital data, wrote the manuscript, and performed its final edits.

FUNDING

This article was supported by the Ministry of Education of the Czech Republic (Project No. SP2018/170). This work was supported by the European Regional Development Fund in the Research Centre of Advanced Mechatronic Systems project, project number CZ.02.1.01/0.0/0.0/16_019/0000867 within the Operational Programme Research, Development and Education.

SUPPLEMENTARY MATERIAL

The Supplementary Material for this article can be found online at: https://www.frontiersin.org/articles/10.3389/fphys.2018.00648/full#supplementary-material

REFERENCES

(2014). *Non-Invasive Fetal Ecg Analysis*. Available online at: https://physionet.org/lightwave/?db=challenge/2013/set-a

Abburi, R., and Chandrasekhara Sastry, A. S. (2012). Fpga based fetal ecg feature extraction for prenatal monitoring using hybrid method. *J. Adv. Res. Dyn. Control Syst.* 9, 69–90.

Al-Zaben, A., and Al-Smadi, A. (2006). Extraction of foetal ECG by combination of singular value decomposition and neuro-fuzzy inference system. *Phys. Med. Biol.* 51,137–143. doi: 10.1088/0031-9155/51/1/010

Amer-Wåhlin, I., Hellsten, C., Norén, H., Hagberg, H., Herbst, A., Kjellmer, I., Lilja, H., et al. (2001). Cardiotocography only versus cardiotocography plus ST analysis of fetal electrocardiogram for intrapartum fetal monitoring: a Swedish randomised controlled trial. *Lancet* 358, 534–538. doi: 10.1016/S0140-6736(01)05703-8

Amin, M., Mamun, M., Hashim, F., and Husain, H. (2011). Separation of fetal electrocardiography (ECG) from composite ECG using adaptive linear neural network for fetal monitoring. *Int. J. Phys. Sci.* 6, 5871–5876. doi: 10.5897/IJPS11.1432

Assaleh, K. (2007). Extraction of fetal electrocardiogram using adaptive neuro-fuzzy inference systems. *IEEE Trans. Biomed. Eng.* 54, 59–68. doi: 10.1109/TBME.2006.883728

Ayres-De-Campos, D., Spong, C., and Chandraharan, E. (2015). FIGO consensus guidelines on intrapartum fetal monitoring: Cardiotocography. *Int. J. Gynecol. Obstet.* 131, 13–24. doi: 10.1016/j.ijgo.2015.06.020

Behar, J., Oster, J., and Clifford, G. (2013). "Non-invasive FECG extraction from a set of abdominal sensors," in *Computing in Cardiology*, *Vol. 40* (Zaragoza).

Behar, J., Oster, J., and Clifford, G. (2014). Combining and benchmarking methods offoetal ecg extraction without maternal or scalp electrode data. *Physiol. Meas.* 35, 1569–1589. doi: 10.1088/0967-3334/35/8/1569

Bensafia, K., Mansour, A., and Haddab, S. (2017). "Blind source subspace separation and classification of ECG signals," in *ATS 2017*, (Sousse).

Bernardes, J., Costa-Pereira, A., Ayres-De-Campos, D., Van Geijn, H., and Pereira-Leite, L. (1997). Evaluation of interobserver agreement of cardiotocograms. *Int. J. Gynecol. Obstet.* 57, 33–37. doi: 10.1016/S0020-7292(97)02 846-4

Billeci, L., and Maurizio, V. (2017). A combined independent source separation and quality index optimization method for fetal ecg extraction from abdominal maternal leads. *Sensors* 17:1135. doi: 10.3390/s17051135

Blackwell, S., Grobman, W., Antoniewicz, L., Hutchinson, M., and Bannerman, C. (2011). Interobserver and intraobserver reliability of the NICHD 3-Tier Fetal Heart Rate Interpretation System. *Am. J. Obstet. Gynecol.* 205, 378.e1-5. doi: 10.1016/j.ajog.2011.06.086

Blix, E., Sviggum, O., Koss, K., and Øian, P. (2003). Inter-observer variation in assessment of 845 labour admission tests: comparison between midwives and obstetricians in the clinical setting and two experts. *BJOG* 110, 1–5. doi: 10.1046/j.1471-0528.2003.t01-1-02105.x

Bsoul, A. (2015). "A simple noninvasive approach for fetal electrocardiogram extraction based on wavelet transform," in *2015 International Conference on Advances in Biomedical Engineering, ICABME 2015* (Beirut).

Burattini, L., Agostinelli, A., Grillo, M., Biagini, A., Giuliani, C., Burattini, L., et al. (2015). Noninvasive fetal electrocardiography: an overview of the signal electrophysiological meaning, recording procedures, and processing techniques. *Ann. Noninvasive Electrocardiol.* 20, 303–313. doi: 10.1111/anec.12259

Castillo, E., Morales, D., Botella, G., García, A., Parrilla, L., and Palma, A. (2013). Efficient wavelet-based ecg processing for single-lead fhr extraction. *Digital Signal Process.* 23, 1897–1909. doi: 10.1016/j.dsp.2013.07.010

Černošek, A., Krajča, V., Mohylová, J., Petránek, S., Matoušek, M., and Paul, K. (2000). *Estimation of the Time Delay of Epileptic Spikes by ICA*, Berlin, Heidelberg: Springer Berlin Heidelberg. 34–42.

Chandraharan, E., and Arulkumaran, S. (2007). Prevention of birth asphyxia: responding appropriately to cardiotocograph (CTG) traces. *Best Pract. Res. Clin. Obstet. Gynaecol.* 21, 609–624. doi: 10.1016/j.bpobgyn.2007.02.008

Czabanski, R., Jezewski, M., Wrobel, J., Horoba, K., and Jezewski, J. (2008). "A neuro-fuzzy approach to the classification of fetal cardiotocograms," in *IFMBE Proceedings*, *Vol. 20* (Berlin; Heidelberg: IFMBE).

Datian, Y., and Xuemei, O. (1996). "Application of wavelet analysis in detection of fetal ECG," in *Annual International Conference of the IEEE Engineering in Medicine and Biology-Proceedings*, *Vol. 3* (Amsterdam).

De Araujo, D., Barros, A., Estombelo-Montesco, C., Zhao, H., Da Silva Filho, A., Baffa, O., et al. (2005). Fetal source extraction from magnetocardiographic recordings by dependent component analysis. *Phys. Med. Biol.* 50, 4457–4464. doi: 10.1088/0031-9155/50/19/002

De Lathauwer, L., De Moor, B., and Vandewalle, J. (2000). Fetal electrocardiogram extraction by blind source subspace separation. *IEEE Trans. Biomed. Eng.* 47, 567–572. doi: 10.1109/10.841326

Diamantaras, K. I., and Kung, S. Y. (1996). *Principal Component Neural Networks: Theory and Applications*. New York, NY: John Wiley & Sons, Inc.

Fajkus, M., Nedoma, J., Martinek, R., Vasinek, V., Nazeran, H., and Siska, P. (2017). A non-invasive multichannel hybrid fiber-optic sensor system for vital sign monitoring. *Sensors (Switzerland)* 17:111. doi: 10.3390/s17 010111

Fatemi, M., and Sameni, R. (2017). An online subspace denoising algorithm for maternal ecg removal from fetal ecg signals. *Iran. J. Sci. Technol. Trans. Electr. Eng.* 41, 65–79. doi: 10.1007/s40998-017-0018-4

Gurve, D., Pant, J. K., and Krishnan, S. (2017). "Real-time fetal ecg extraction from multichannel abdominal ecg using compressive sensing and ica," in *2017 39th Annual International Conference of the IEEE Engineering in Medicine and Biology Society (EMBC)* (Seogwipo), 2794–2797.

Hasan, M., Ibrahimy, M., and Reaz, M. (2009a). Fetal ECG extraction from maternal abdominal ECG using neural network. *J. Softw. Eng. Appl.* 2, 330–334. doi: 10.4236/jsea.2009.25043

Hasan, M., Reaz, M., Ibrahimy, M., Hussain, M., and Uddin, J. (2009b). Detection and processing techniques of FECG signal for fetal monitoring. *Biol. Proced. Online* 11, 263–295. doi: 10.1007/s12575-009-9006-z

Hassanpour, H., and Parsaei, A. (2007). "Fetal ECG extraction using wavelet transform," in *CIMCA 2006: International Conference on Computational Intelligence for Modelling, Control and Automation, Jointly with IAWTIC 2006: International Conference on Intelligent Agents Web Technologies* (Pune).

Hon, E., and Lee, S. (1963). NOISE REDUCTION IN FETAL ELECTROCARDIOGRAPHY. II. AVERAGING TECHNIQUES. *Am. J. Obstet. Gynecol.* 87, 1086–1096. doi: 10.1016/0002-9378(63)90104-2

Hon, E., and Lee, S. (1964). Averaging techniques in fetal electrocardiography. *Med. Electr. Biol. Eng.* 2, 71–76. doi: 10.1007/BF02474362

Hruban, L., Spilka, J., Chudáček, V., Janků, P., Huptych, M., Burša, M., et al. (2015). Agreement on intrapartum cardiotocogram recordings between expert obstetricians. *J. Eval. Clin. Pract.* 21, 694–702. doi: 10.1111/jep.12368

Hyvärinen, A., and Oja, E. (1997). A fast fixed-point algorithm for independent component analysis. *Neural Comput.* 9, 1483–1492. doi: 10.1162/neco.1997.9.7.1483

Hyvarinen, A., and Oja, E. (2000). Independent component analysis: algorithms and applications. *Neural Networks* 13, 411–430. doi: 10.1016/S0893-6080(00)00026-5

Ivanushkina, N., Ivanko, K., Lysenko, E., Borovskiy, I., and Panasiuk, O. (2014). "Fetal electrocardiogram extraction from maternal abdominal signals," in *2014 IEEE 34th International Scientific Conference on Electronics and Nanotechnology, ELNANO 2014-Conference Proceedings* (Kyiv).

Jezewski, J., Horoba, K., Roj, D., Wrobel, J., Kupka, T., and Matonia, A. (2016). Evaluating the fetal heart rate baseline estimation algorithms by their influence on detection of clinically important patterns. *Biocybern. Biomed. Eng.* 36, 562–573. doi: 10.1016/j.bbe.2016.06.003

Jezewski, J., Matonia, A., Kupka, T., Roj, D., and Czabanski, R. (2012). Determination of fetal heart rate from abdominal signals: Evaluation of beat-to-beat accuracy in relation to the direct fetal electrocardiogram. *Biomed. Tech.* 57, 562–573. doi: 10.1515/bmt-2011-0130

Jezewski, J., Wrobel, J., Horoba, K., Gacek, A., and Sikora, J. (2002). "Fetal heart rate variability: clinical experts versus computerized system interpretation," in *Annual International Conference of the IEEE Engineering in Medicine and Biology-Proceedings*, *Vol. 2* (Houston, TX).

Jezewski, J., Wrobel, J., Matonia, A., Horoba, K., Martinek, R., Kupka, T., et al. (2017). Is abdominal fetal electrocardiography an alternative to doppler ultrasound for FHR variability evaluation? *Front. Physiol.* 8:305. doi: 10.3389/fphys.2017.00305

Jia, W., Yang, C., Zhong, G., Zhou, M., and Wu, S. (2010). "Fetal ECG extraction based on adaptive linear neural network," in *Proceedings-2010 3rd International Conference on Biomedical Engineering and Informatics, BMEI 2010*, *Vol. 2* (Yantai).

Jolliffe, I. T. (2002). "Principal component analysis and factor analysis," in *Principal Component Analysis and Factor Analysis* (New York, NY).

Kahankova, R., Jaros, R., Martinek, R., Jezewski, J., Wen, H., Jezewski, M., et al. (2017a). Non-adaptive methods of fetal ecg signal processing. *Adv. Electr. Electron. Eng.* 15:476. doi: 10.15598/aeee.v15i3.2196

Kahankova, R., Jaros, R., Martinek, R., Jezewski, J., Wen, H., Jezewski, M., et al. (2017b). Non-adaptive methods of fetal ECG signal processing. *Adv. Electr. Electron. Eng.* 15, 476–490. doi:10.15598/aeee.v15i3.2196

Kahankova, R., Jezewski, J., Nedoma, J., Jezewski, M., Fajkus, M., Kawala-Janik, A., et al. (2017c). Influence of gestation age on the performance of adaptive systems for fetal ECG extraction. *Adv. Electr. Electron. Eng.* 15, 491–501. doi: 10.15598/aeee.v15i3.2207

Kahankova, R., Martinek, R., and Bilik, P. (2017d). "Fetal ecg extraction from abdominal ecg using rls based adaptive algorithms," in *2017 18th International Carpathian Control Conference (ICCC)* (Sinaia), 337–342.

Kahankova, R., Martinek, R., and Bilik, P. (2018). *Non-invasive Fetal ECG Extraction from Maternal Abdominal ECG Using LMS and RLS Adaptive Algorithms*, Cham: Springer International Publishing. 258–271.

Kam, A., and Cohen, A. (1999). "Detection of fetal ecg with iir adaptive filtering and genetic algorithms," in *1999 IEEE International Conference on Acoustics,*

Speech, and Signal Processing. Proceedings. ICASSP99 (Cat. No.99CH36258), *Vol. 4* (Phoenix, AZ) 2335–2338.

Kanjilal, P., Palit, S., and Saha, G. (1997). Fetal ecg extraction from single-channel maternal ecg using singular value decomposition. *IEEE Trans. Biomed. Eng.* 44, 51–59. doi: 10.1109/10.553712

Karhunen, J. (1996). *Neural Approaches to Independent Component Analysis and Source Separation*. Bruges:ESANN, 249–266.

Karvounis, E., Papaloukas, C., Fotiadis, D., and Michails, L. (2004). "Fetal heart rate extraction from composite maternal ECG using complex continuous wavelet transform," in *Computers in Cardiology*, *Vol. 31* (Chicago, IL).

Lee, T., Girolami, M., and Sejnowski, T. (1998). *Independent Component Analysis, Theory and Applications*. Boston, MA: Kluwer Academic Publishers.

Lhotská, L., Krajca, V., Mohylová, J., Petránek, S., and Gerla, V. (2009). "EEG data mining using PCA" in *Data Mining and Medical Knowledge Management: Cases and Applications* (IGI Global), 161–180.

Marossero, D., Erdogmus, D., Euliano, N., Principe, J., and Hild, K. (2003). "Independent components analysis for fetal electrocardiogram extraction: a case for the data efficient mermaid algorithm," in *Neural Networks for Signal Processing-Proceedings of the IEEE Workshop*, *Vol. 2003* (Toulouse).

Martín-Clemente, R., Camargo-Olivares, J., Hornillo-Mellado, S., Elena, M., and Román, I. (2011). Fast technique for noninvasive fetal ECG extraction. *IEEE Trans. Biomed. Eng.* 58, 227–230. doi: 10.1109/TBME.2010.2059703

Martinek, R., Kahankova, R., Nazeran, H., Konecny, J., Jezewski, J., Janku, P., etal. (2017a). Non-invasive fetal monitoring: a maternal surface ECG electrode placement-based novel approach for optimization of adaptive filter control parameters using the LMS and RLS algorithms. *Sensors* 17:E1154. doi: 10.3390/s17051154

Martinek, R., Kahankova, R., Skutova, H., Koudelka, P., Zidek, J., and Koziorek, J. (2016a). "Adaptive signal processing techniques for extracting abdominal fetal electrocardiogram," in *2016 10th International Symposium on Communication Systems, Networks and Digital Signal Processing, CSNDSP 2016* (Prague).

Martinek, R., Kelnar, M., Koudelka, P., Vanus, J., Bilik, P., Janku, P., et al. (2016b). A novel LabVIEW-based multi-channel non-invasive abdominal maternal-fetal electrocardiogram signal generator. *Physiol. Meas.* 37, 238–256. doi: 10.1088/0967-3334/37/2/238

Martinek, R., Kelnar, M., Vanus, J., Bilik, P., and Zidek, J. (2015a). A robust approach for acoustic noise suppression in speech using ANFIS. *J. Electr. Eng.* 66, 301–310. doi: 10.2478/jee-2015-0050

Martinek, R., Kelnar, M., Vojcinak, P., Koudelka, P., Vanus, J., Bilik, P., et al. (2015b). Virtual simulator for the generation of patho-physiological foetal ECGs during the prenatal period. *Electron. Lett.* 51, 1738–1740. doi: 10.1049/el.2015.2291

Martinek, R., Nedoma, J., Fajkus, M., Kahankova, R., Konecny, J., Janku, P., et al. (2017b). A phonocardiographic-based fiber-optic sensor and adaptive filtering system for noninvasive continuous fetal heart rate monitoring. *Sensors* 17:E890. doi: 10.3390/s17040890

Martinek, R., Skutova, H., Kahankova, R., Koudelka, P., Bilik, P., and Koziorek, J. (2016c). "Fetal ECG extraction based on adaptive neuro-fuzzy interference system," in *2016 10th International Symposium on Communication Systems, Networks and Digital Signal Processing, CSNDSP 2016* (Prague).

Martinek, R., Vanus, J., Kelnar, M., Bilik, P., and Zidek, J. (2015c). "Application of recursive least square algorithm to adaptive channel equalization," in *XXI IMEKO World Congress "Measurement in Research and Industry"* (Prague).

Martinek, R., and Zidek, J. (2012). Refining the diagnostic quality of the abdominal fetal electrocardiogram using the techniques of artificial intelligence | Poprawa jakości sygnału elektrokardiogramu płodu przy wykorzystaniu narze{ogonek}dzi sztucznej inteligencji. *Przeglad Elektrotechniczny (Electr. Rev.)* 88, 155–160.

Martinek, R., and Zidek, J. (2014). The real implementation of ANFIS channel equalizer on the system of software-defined radio. *IETE J. Res.* 60, 83–193. doi: 10.1080/03772063.2014.914698

Matonia, A., Jezewski, J., Kupka, T., Horoba, K., Wrobel, J., and Gacek, A. (2006). The influence of coincidence of fetal and maternal QRS complexes on fetal heart rate reliability. *Med. Biol. Eng. Comput.* 44, 393–403. doi: 10.1007/s11517-006-0054-0

Mochimaru, F., Fujimoto, Y., and Ishikawa, Y. (2004). The fetal electrocardiogram by independent component analysis and wavelets. *Jpn J. Physiol.* 54, 457–463. doi: 10.2170/jjphysiol.54.457

Mohylova, J., Cernosek, A., and Krajca, V. (2001). "Application independent component analysis in biomedical practice," in *24th Seminar on Fundamentals of Electrotechnics and Circuit Theory*, 489–492.

Myles, P., and Cui, J. (2007). I. Using the Bland-Altman method to measure agreement with repeated measures. *Br. J. Anaesth.* 99, 309–311. doi: 10.1093/bja/aem214

Najafabadi, F., Zahedi, E., and Mohd Ali, M. (2006). Fetal heart rate monitoring based on independent component analysis. *Comput. Biol. Med.* 36, 241–252. doi: 10.1016/j.compbiomed.2004.11.004

Neilson, J. (2006). Fetal electrocardiogram (ECG) for fetal monitoring during labour. *Cochrane Database Syst. Rev.* 3:CD000116. doi: 10.1002/14651858.CD000116.pub2

Niknazar, M., Rivet, B., and Jutten, C. (2013). Fetal ECG extraction by extended state kalman filtering based on single-channel recordings. *IEEE Trans. Biomed. Eng.* 60, 1345–1352. doi: 10.1109/TBME.2012.2234456

Pan, J., and Tompkins, W. J. (1985). A real-time qrs detection algorithm. *IEEE Trans. Biomed. Eng.* 32, 230–236. doi: 10.1109/TBME.1985.325532

Peters, M., Crowe, J., Piéri, J.-F., Quartero, H., Hayes-Gill, B., James, D., et al. (2001). Monitoring the fetal heart non-invasively: a review of methods. *J. Perinat. Med.* 29, 408–416. doi: 10.1515/JPM.2001.057

Poularikas, A., and Zayed, M. (2006). *Adaptive Filtering Primer with MATLAB*. CRC Press.

Reaz, M., and Wei, L. (2004). "Adaptive linear neural network filter for fetal ECG extraction," in *Proceedings of International Conference on Intelligent Sensing and Information Processing, ICISIP 2004* (Chennai).

Reinhard, J., Hayes-Gill, B., Schiermeier, S., Hatzmann, H., Heinrich, T., and Louwen, F. (2013). Intrapartum heart rate ambiguity: a comparison of cardiotocogram and abdominal fetal electrocardiogram with maternal electrocardiogram. *Gynecol. Obstet. Invest.* 75, 101–108. doi: 10.1159/000345059

Reinhard, J., Hayes-Gill, B., Schiermeier, S., Hatzmann, W., Herrmann, E., Heinrich, T., et al. (2012). Intrapartum signal quality with external fetal heart rate monitoring: a two way trial of external Doppler CTG ultrasound and the abdominal fetal electrocardiogram. *Arch. Gynecol. Obstet.* 286, 1103–1107. doi: 10.1007/s00404-012-2413-4

Rosen, K., Arulkumaran, S., Greene, K., Lilja, H., Lindecrantz, K., Seneviratne, H., et al. (1992). Clinical validity of fetal ecg waveform analysis. *Perinatology* 26, 95–110.

Sameni, R., and Clifford, G. D. (2010). A Review of fetal ECG signal processing; issues and promising Directions. *Open Pacing Electrophysiol. Ther. J.* 1, 4–20. doi: 10.2174/1876536X01003010004

Sameni, R., Jutten, C., and Shamsollahi, M. (2007). "What ICA provides for ECG processing: application to noninvasive fetal ECG extraction," in *Sixth IEEE International Symposium on Signal Processing and Information Technology, ISSPIT* (Vancouver, BC).

Samuel, O., Asogbon, G., Sangaiah, A., Fang, P., and Li, G. (2017). An integrated decision support system based on ann and fuzzy-ahp for heart failure risk prediction. *Exp. Syst. Appl.* 68, 163–172. doi: 10.1016/j.eswa.2016.10.020

Shadaydeh, M., Xiao, Y., and Ward, R. (2008). "Extraction of fetal ECG using adaptive Volterra filters," in *European Signal Processing Conference* (Lausanne).

Soong, A., and Koles, Z. (1995). Principal-component localization of the sources of the background eeg. *IEEE Trans. Biomed. Eng.* 42, 59–67. doi: 10.1109/10.362918

Swarnalatha, R., and Prasad, D. (2010). A novel technique for extraction of FECG using multi stage adaptive filtering. *J. Appl. Sci.* 10, 319–324. doi: 10.3923/jas.2010.319.324

Sweha, A., Hacker, T., and Nuovo, J. (1999). Interpretation of the electronic fetal heart rate during labor. *Am. Family Phys.* 59, 2487–2500.

Talha, M., Guettouche, M., and Bousbia-Salah, A. (2010). "Combination of a FIR filter with a genetic algorithm for the extraction of a fetal ECG," in *Conference Record-Asilomar Conference on Signals, Systems and Computers* (Pacific Grove, CA).

Tsui, S.-Y., Liu, C.-S., and Lin, C.-W. (2017). Modified maternal ecg cancellation for portable fetal heart rate monitor. *Biomed. Signal Proc. and Control* 32, 76–81. doi: 10.1016/j.bspc.2016.11.001

Vayssière, C., Arnaud, C., Pirrello, O., and Goffinet, F. (2010). Inter-observer agreement in clinical decision-making for abnormal cardiotocogram during labour: a comparison between CTG and CTG plus STAN. *BJOG* 117, 1081–1087. doi: 10.1111/j.1471-0528.2009.02392.x

Vintzileos, A., Nochimson, D., Guzmana, E., Knuppel, A., Lake, M., and Schifrin, B. (1995). Intrapartum electronic fetal heart rate monitoring versus intermittent auscultation: a meta-analysis. *Obstet. Gynecol.* 85, 149–155. doi: 10.1016/0029-7844(94)00320-D

Viunytskyi, O., and Shulgin, V. (2017). "Signal processing techniques for fetal electrocardiogram extraction and analysis," in *2017 IEEE 37th International Conference on Electronics and Nanotechnology (ELNANO)* (Kiev), 325–328.

Vrins, F., Jutten, C., and Verleysen, M. (2004). *Sensor Array and Electrode Selection for Non-invasive Fetal Electrocardiogram Extraction by Independent Component Analysis*, Berlin, Heidelberg: Springer Berlin Heidelberg. 1017–1024. doi: 10.1007/978-3-540-30110-3_128

Wei, Z., Xueyun, W., Jian, Z., and Hongxing, L. (2013). Noninvasive fetal ECG estimation using adaptive comb filter. *Comput. Methods Programs Biomed.* 112, 125–134. doi: 10.1016/j.cmpb.2013.07.015

Williams, B., and Arulkumaran, S. (2004). Cardiotocography and medicolegal issues. *Best Pract. Res. Clin. Obstet. Gynaecol.* 18, 457–466. doi: 10.1016/j.bpobgyn.2004.02.005

Wróbel, J., Horoba, K., Pander, T., Jezewski, J., and Czabański, R. (2013). Improving fetal heart rate signal interpretation by application of myriad filtering. *Biocybernet. Biomed. Eng.* 33, 211–221. doi: 10.1016/j.bbe.2013.09.004

Wrobel, J., Roj, D., Jezewski, J., Horoba, K., Kupka, T., and Jezewski, M. (2015). Evaluation of the robustness of fetal heart rate variability measures to low signal quality. *J. Med. Imaging Health Inform.* 5, 1311–1318. doi: 10.1166/jmihi.2015.1534

Zhang, N., Zhang, J., Li, H., Mumini, O., Samuel, O., Ivanov, K., and Wang, L. (2017). A novel technique for fetal ecg extraction using single-channel abdominal recording. *Sensors* 17:E457. doi: 10.3390/s17030457

Conflict of Interest Statement: The authors declare that the research was conducted in the absence of any commercial or financial relationships that could be construed as a potential conflict of interest.

The reviewer AF and handling Editor declared their shared affiliation.

Copyright © 2018 Martinek, Kahankova, Jezewski, Jaros, Mohylova, Fajkus, Nedoma, Janku and Nazeran. This is an open-access article distributed under the terms of the Creative Commons Attribution License (CC BY). The use, distribution or reproduction in other forums is permitted, provided the original author(s) and the copyright owner are credited and that the original publication in this journal is cited, in accordance with accepted academic practice. No use, distribution or reproduction is permitted which does not comply with these terms.

frontiers in Physiology

ORIGINAL RESEARCH
published: 19 June 2018
doi: 10.3389/fphys.2018.00759

The Impact of Variational Primary Collaterals on Cerebral Autoregulation

Zhen-Ni Guo[1,2†], Xin Sun[1†], Jia Liu[3], Huijie Sun[4], Yingkai Zhao[4], Hongyin Ma[1], Baofeng Xu[5], Zhongxiu Wang[1], Chao Li[1], Xiuli Yan[1], Hongwei Zhou[6], Peng Zhang[2], Hang Jin[1] and Yi Yang[1,2]**

[1] Department of Neurology, The First Hospital of Jilin University, Changchun, China, [2] Department of Neurology, Clinical Trial and Research Center for Stroke, The First Hospital of Jilin University, Changchun, China, [3] Shenzhen Institutes of Advanced Technology, Chinese Academy of Sciences, University Town of Shenzhen, Shenzhen, China, [4] Cadre Ward, The First Hospital of Jilin University, Changchun, China, [5] Department of Neurosurgery, The First Hospital of Jilin University, Changchun, China, [6] Department of Radiology, The First Hospital of Jilin University, Changchun, China

OPEN ACCESS

Edited by:
Thomas Heldt,
Massachusetts Institute of Technology, United States

Reviewed by:
Steffen Schulz,
Institut für Innovative Gesundheitstechnologien (IGHT), Germany
Stephen Michael Moore,
IBM Research, Australia

***Correspondence:**
Hang Jin
doctorjinhang@hotmail.com;
hangjin@jlu.edu.cn
Yi Yang
doctoryangyi@163.com;
yang_yi@jlu.edu.cn

† These authors have contributed equally to this work.

Specialty section:
This article was submitted to Computational Physiology and Medicine, a section of the journal Frontiers in Physiology

Received: 24 March 2018
Accepted: 30 May 2018
Published: 19 June 2018

Citation:
Guo Z-N, Sun X, Liu J, Sun H, Zhao Y, Ma H, Xu B, Wang Z, Li C, Yan X, Zhou H, Zhang P, Jin H and Yang Y (2018) The Impact of Variational Primary Collaterals on Cerebral Autoregulation. Front. Physiol. 9:759. doi: 10.3389/fphys.2018.00759

The influence of the anterior and posterior communicating artery (ACoA and PCoA) on dynamic cerebral autoregulation (dCA) is largely unknown. In this study, we aimed to test whether substantial differences in collateral anatomy were associated with differences in dCA in two common types of stenosis according to digital subtraction angiography (DSA): either isolated basal artery and/or bilateral vertebral arteries severe stenosis/occlusion (group 1; group 1A: with bilateral PCoAs; and group 1B: without bilateral PCoAs), or isolated unilateral internal carotid artery severe stenosis/occlusion (group 2; group 2A: without ACoA and with PCoA; group 2B: with ACoA and without PCoAs; and group 2C: without both ACoA and PCoA). The dCA was calculated by transfer function analysis (a mathematical model), and was evaluated in middle cerebral artery (MCA) and/or posterior cerebral artery (PCA). Of a total of 231 non-acute phase ischemic stroke patients who received both dCA assessment and DSA in our lab between 2014 and 2017, 51 patients met inclusion criteria based on the presence or absence of ACoA or PCoA, including 21 patients in the group 1, and 30 patients in the group 2. There were no significant differences in gender, age, and mean blood pressure between group 1A and group 1B, and among group 2A, group 2B, and group 2C. In group 1, the PCA phase difference values (autoregulatory parameter) were significantly higher in the subgroup with patent PCoAs, compared to those without. In group 2, the MCA phase difference values were higher in the subgroup with patent ACoA, compared to those without. This pilot study found that the cross-flow of the ACoA/PCoA to the affected area compensates for compromised dCA in the affected area, which suggests an important role of the ACoA/PCoA in stabilizing cerebral blood flow.

Keywords: dynamic cerebral autoregulation, cerebrovascular stenosis, anterior communicating artery, posterior communicating artery, digital subtraction angiography

INTRODUCTION

Primary collaterals include the anterior and posterior communicating arteries (ACoA and PCoA), are crucial to maintaining adequate cerebral perfusion, and their anatomic variants could pose a challenge for individuals during ischemic demand. Several studies have reported the influence of the ACoA and PCoA on cerebral hemodynamics (van Everdingen et al., 1998;

Kluytmans et al., 1999; Fabbri et al., 2014; Lin et al., 2015; Ren et al., 2015). For example, Kluytmans et al. (1999) found that in patients with a unilateral internal carotid artery occlusion, collateral flow via the ACoA is a sign of well-preserved cerebral hemodynamic status, whereas no collateral flow via the circle of Willis or flow via only the PCoA is a sign of deteriorated cerebral perfusion. In addition to directly modulating cerebral hemodynamics, the influence of ACoA and PCoA on the intrinsic ability of the cerebral vasculature to maintain cerebral hemodynamics also needs further study.

Cerebral autoregulation not only regulates cerebral hemodynamics, but also acts as a predictor for clinical occurrence and prognosis of several neurological disorders, such as cerebrovascular diseases (Guo et al., 2014a; Ma et al., 2016), Alzheimer's disease (Claassen and Zhang, 2011), and patent foramen ovale (Guo et al., 2014b). Previous studies reported that collaterals may influence cerebral autoregulation (Reinhard et al., 2003a,c; Long et al., 2008). However, the extent of the influence of the ACoA and PCoA on cerebral autoregulation is not clear. Identifying the influence of collaterals on cerebral autoregulation both qualitatively and quantitatively may help us further understand the characteristics of cerebral vessels and help us select treatment strategies to improve cerebral hemodynamics. This is especially important in the management and secondary prevention of stroke in patients with stenosis in key cerebral arteries.

Accordingly, we determined the impact of the ACoAs and PCoAs on dynamic cerebral autoregulation (dCA) in a series of stroke patients with cerebral arterial stenosis/occlusion in our hospital. We found that the presence of ACoA/PCoA was associated with better dCA in the affected cerebral arteries and thus provided direct evidence for the important role of ACoA/PCoA during cerebral hemodynamics.

MATERIALS AND METHODS

The study design was approved by the ethics committee of the First Hospital of Jilin University. The data come from the departmental dCA database in the department of Neurology. All participants gave written informed consent.

Participants

Non-acute ischemic stroke patients who underwent both dCA and digital subtraction angiography (DSA) examinations from September 2014 to July 2017 were searched in our dCA database. Inclusion criteria included: (1) either isolated basal artery and/or bilateral vertebral arteries severe stenosis/occlusion (group 1), or isolated unilateral internal carotid artery severe stenosis/occlusion (group 2) according to DSA by two neurologists. Exclusion criteria included: (1) acute phase of cerebral infarction (<15 days from onset); (2) received thrombolytic, interventional, or surgical treatment; and (3) other cerebral diseases (arterial aneurysm, intracranial tumors, and brain trauma). Patients in each group were further divided into subgroups according to presence or absence of ACoA or PCoA. The details of subgroups were as follows (**Table 1**):

Groups 1A and 1B: (1) severe stenosis or occlusion of the basal artery and/or bilateral vertebral arteries; (2) without stenosis/occlusion of the internal carotid artery, the middle cerebral artery (MCA), and the anterior cerebral artery; (3) with/without ACoA; (4) with cross-flow from anterior circulation to posterior circulation via the bilateral PCoAs (group 1A, **Figure 1A**); without bilateral PCoAs (group 1B, **Figure 1B**).

Group 2A: (1) severe stenosis or occlusion of a unilateral internal carotid artery; (2) without ACoA; (3) without stenosis/occlusion of the basal artery and/or vertebral artery; (4) with cross-flow from posterior circulation to anterior circulation via the PCoA of the affected side (**Figure 2A**).

Group 2B: (1) severe stenosis or occlusion of a unilateral internal carotid artery; (2) without PCoAs; (3) without stenosis/occlusion of the basal artery and/or vertebral artery; (4) with cross-flow from the contralateral side to the affected side via the ACoA (**Figure 2B**).

Group 2C: (1) severe stenosis or occlusion of a unilateral internal carotid artery; (2) without stenosis/occlusion of the basal artery and/or vertebral artery; (3) without both ACoA and PCoA (**Figure 2C**).

DCA Examination

For stenosis/occlusion of the basal artery and/or bilateral vertebral arteries, we conducted the dCA examination from both the bilateral middle cerebral arteries and bilateral posterior cerebral arteries. For stenosis/occlusion of the internal carotid artery, we conducted the dCA examination only from the bilateral middle cerebral arteries.

This method was reported previously (Guo et al., 2015; Ma et al., 2016). Briefly, continuous cerebral blood flow velocity was recorded non-invasively using transcranial Doppler (MultiDop X2, DWL, Sipplingen, Germany) in the bilateral middle cerebral artery at a depth of 45 to 60 mm and the bilateral posterior cerebral artery at a depth of 60 to 70 mm. Spontaneous arterial blood pressure was recorded using a servo-controlled plethysmograph (Finometer PRO, Netherlands) on one middle finger. Continuous data were recorded for 5–10 min and then were stored for further dCA analysis.

DCA Analysis

The analog output of the continuous arterial blood pressure measurement device was plugged into the A/D convertor of the transcranial Doppler device for recording the digitized arterial blood pressure and cerebral blood flow velocity simultaneously. Two digital signals were then aligned to remove the time lags calculated by a cross-correlation function. In this study, with all recordings less than 10 min, we did not find any evident data drifting after the alignment. The dCA analysis was performed as previously reported using MATLAB (MathWorks, Natick, MA, United States) (Guo et al., 2015; Ma et al., 2016). Briefly, beat-to-beat alignment of the data was achieved with a cross-correlation function to eliminate possible time lags. The relationship between dynamic changes in spontaneous arterial blood pressure and bilateral middle cerebral artery blood flow/bilateral posterior cerebral artery blood flow was assessed with a transfer function analysis (Claassen et al., 2016). For each recording, arterial blood

TABLE 1 | Baseline characteristics, phase difference, and gain values in each group.

	Male	Age (years)	Mean blood pressure (mmHg)	Right (affected) phase difference (degree)	Left (unaffected) phase difference (degree)	Right (affected) gain (cm/s/mmHg)	Left (affected) gain (cm/s/mmHg)
Group 1A (n = 11)	9 (81.8%)	58.09 ± 7.38	95.36 ± 8.91				
MCA	/	/	/	17.95 ± 6.10	20.68 ± 12.08	0.88 ± 0.38	1.11 ± 0.49
PCA	/	/	/	32.92 ± 10.54	34.09 ± 11.50	0.72 ± 0.32	0.76 ± 0.36
Group 1B (n = 10)	9 (90.0%)	62.20 ± 7.89	96.80 ± 11.07				
MCA	/	/	/	34.66 ± 12.23	35.23 ± 12.63	1.01 ± 0.28	1.20 ± 0.55
PCA	/	/	/	23.19 ± 10.15	24.85 ± 12.76	0.65 ± 0.34	0.71 ± 0.40
Group 2A (n = 9)	7 (77.8%)	55.89 ± 11.06	98.78 ± 8.93	20.95 ± 17.90	33.70 ± 17.67	0.66 ± 0.30	0.90 ± 0.44
Group 2B (n = 10)	10 (100%)	55.60 ± 13.66	93.10 ± 13.58	28.21 ± 6.13	35.07 ± 5.76	0.88 ± 0.33	0.76 ± 0.29
Group 2C (n = 11)	11 (100%)	53.18 ± 7.70	95.55 ± 10.42	14.94 ± 13.52	32.07 ± 7.73	0.79 ± 0.39	0.77 ± 0.48

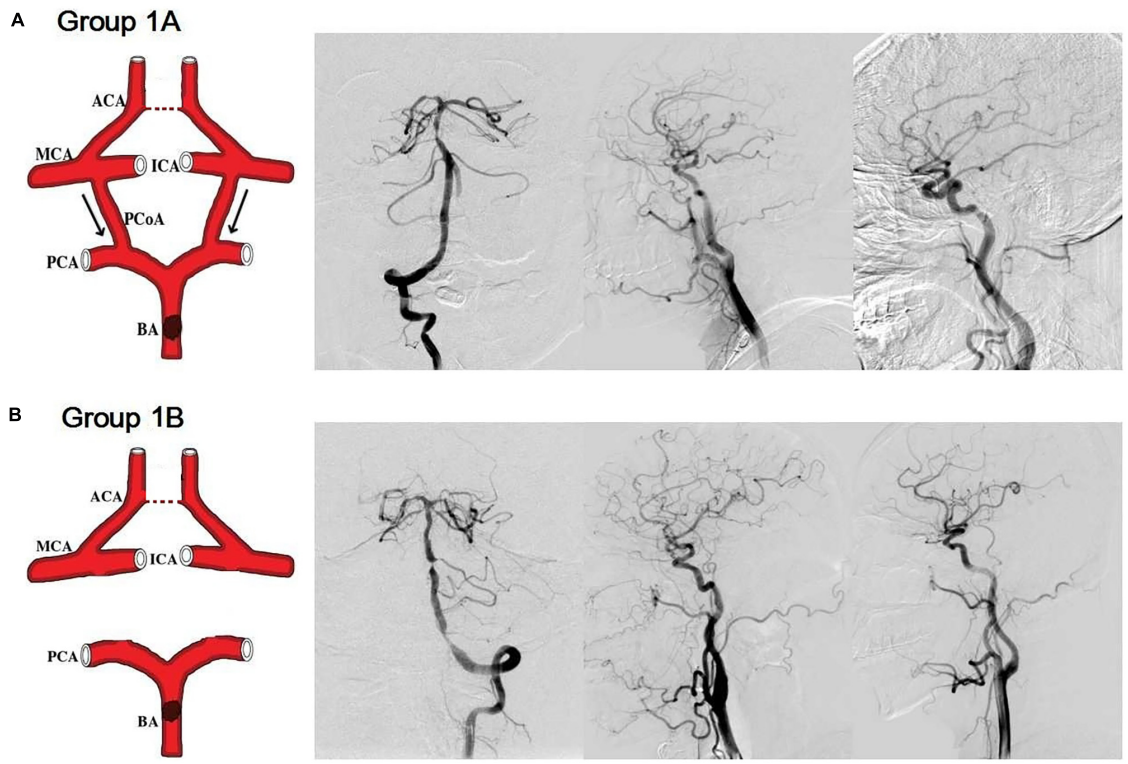

FIGURE 1 | Simulation anatomic drawing, and representative digital subtraction angiography (DSA) manifestation of group 1A and group 1B. Severe stenosis of the basal artery, with/without anterior communicating artery, with cross-flow from anterior circulation to posterior circulation via the bilateral posterior communicating arteries (group 1A, **A**); without bilateral posterior communicating arteries (group 1B, **B**).

pressure and bilateral cerebral artery blood flow velocity were divided into a number of data segments by a 60-s window with 30-s overlap. For one segment of arterial blood pressure and bilateral cerebral artery blood flow velocity, the transfer function analysis was implemented as,

$$H(f)=\frac{S_{pv}(f)}{S_{pp}(f)} \quad (1)$$

where $H(f)$ denotes the frequency response. $S_{pp}(f)$ is the auto-spectrum of arterial blood pressure and $S_{pv}(f)$ is the cross-spectrum between arterial blood pressure and cerebral artery blood flow velocity. For each subject, $S_{pp}(f)$ and $S_{pv}(f)$ were averaged over the segments to improve statistical reliability. The phase difference $\phi(f)$ can then be computed as,

$$\phi(f)=\tan^{-1}\left[\frac{H_I(f)}{H_R(f)}\right] \quad (2)$$

where $H_R(f)$ and $H_I(f)$ are the real and imaginary parts of $H(f)$, respectively. In the frequency domain, because previous studies of dCA suggested that autoregulatory parameters in a low frequency band (0.06–0.12 Hz) is more meaningful than in the other frequency bands (Reinhard et al., 2003b, 2004), thus

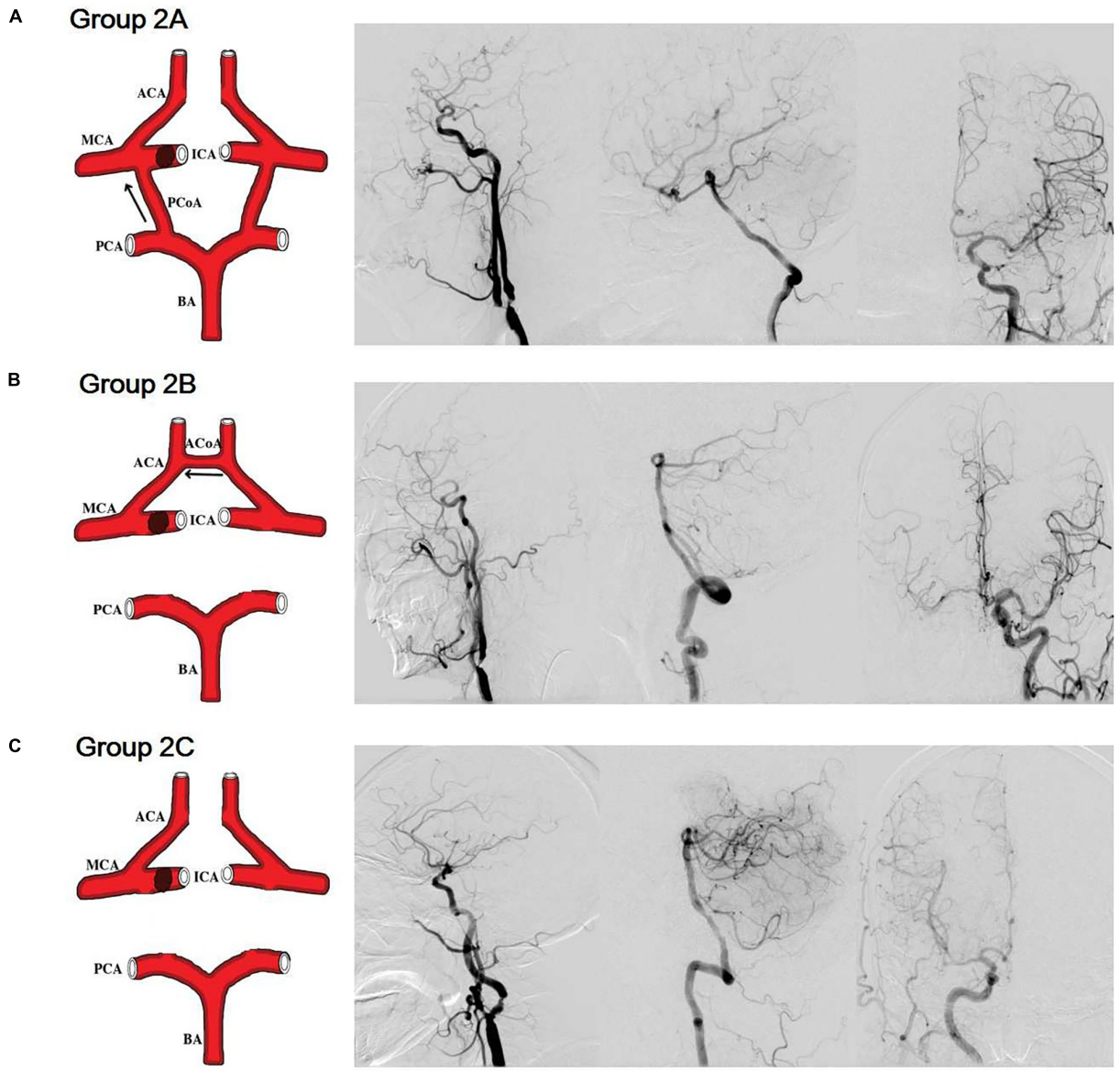

FIGURE 2 | Simulation anatomic drawing, and representative digital subtraction angiography manifestation of group 2A, group 2B, and group 2C. **(A)** Severe stenosis of a unilateral internal carotid artery, without anterior communicating artery, with cross-flow from posterior circulation to anterior circulation via the posterior communicating artery of the affected side. **(B)** Severe stenosis of a unilateral internal carotid artery, without posterior communicating arteries, with cross-flow from the contralateral side to the affected side via the anterior communicating artery. **(C)** Severe stenosis of a unilateral internal carotid artery, without both anterior communicating artery and posterior communicating artery.

the phase difference and coherence function within 0.06–0.12 Hz were estimated to evaluate dCA. A coherence threshold of >0.4 was chosen to define a lower limit of the linearity between arterial blood pressure and cerebral blood flow velocity so as to apply the transfer function analysis (Zhang et al., 1998).

Statistical Analysis

The Statistical Package for the Social Sciences Version 17.0 (SPSS, IBM, West Grove, PA, United States) was used to analyze the data. Continuous data are expressed as mean ± standard deviation and were analyzed using Student's *t*-tests. The discrete variables are expressed as the rate (percentage) and were analyzed using chi-squared and Fisher's exact tests. *P*-values < 0.05 were considered statistically significant.

RESULTS

Participant Characteristics

A total of 231 patients who underwent both dCA and DSA examinations were identified in the departmental database. Most

of these patients had a combination of multiple cerebral vascular stenosis and thus were excluded. A subtotal of 51 patients were selected, including 21 patients in the group 1, and 30 patients in the group 2. The group 1A included 11 patients; group 1B included 10 patients; group 2A included 9 patients; group 2B included 10 patients; group 2C included 11 patients.

There were no significant differences in gender, age, and mean blood pressure between group 1A and group 1B (**Table 1**, $P > 0.055$; **Supplementary Data Sheet S1**), and among group 2A, group 2B, and group 2C (**Table 1**, all $P > 0.05$; **Supplementary Data Sheet S1**).

Protective Effect of PCoAs on dCA in Patients With Isolated Basal Artery and/or Bilateral Vertebral Artery Severe Stenosis/Occlusion

In Group 1, patients with severe stenosis/occlusion of the basal artery and/or bilateral vertebral arteries, the phase difference values (autoregulatory parameter) of the right posterior cerebral artery in group 1A (with PCoAs) were significantly higher than those of right posterior cerebral artery in group 1B (without PCoAs, $P = 0.045$, **Figure 3**). The phase difference values of

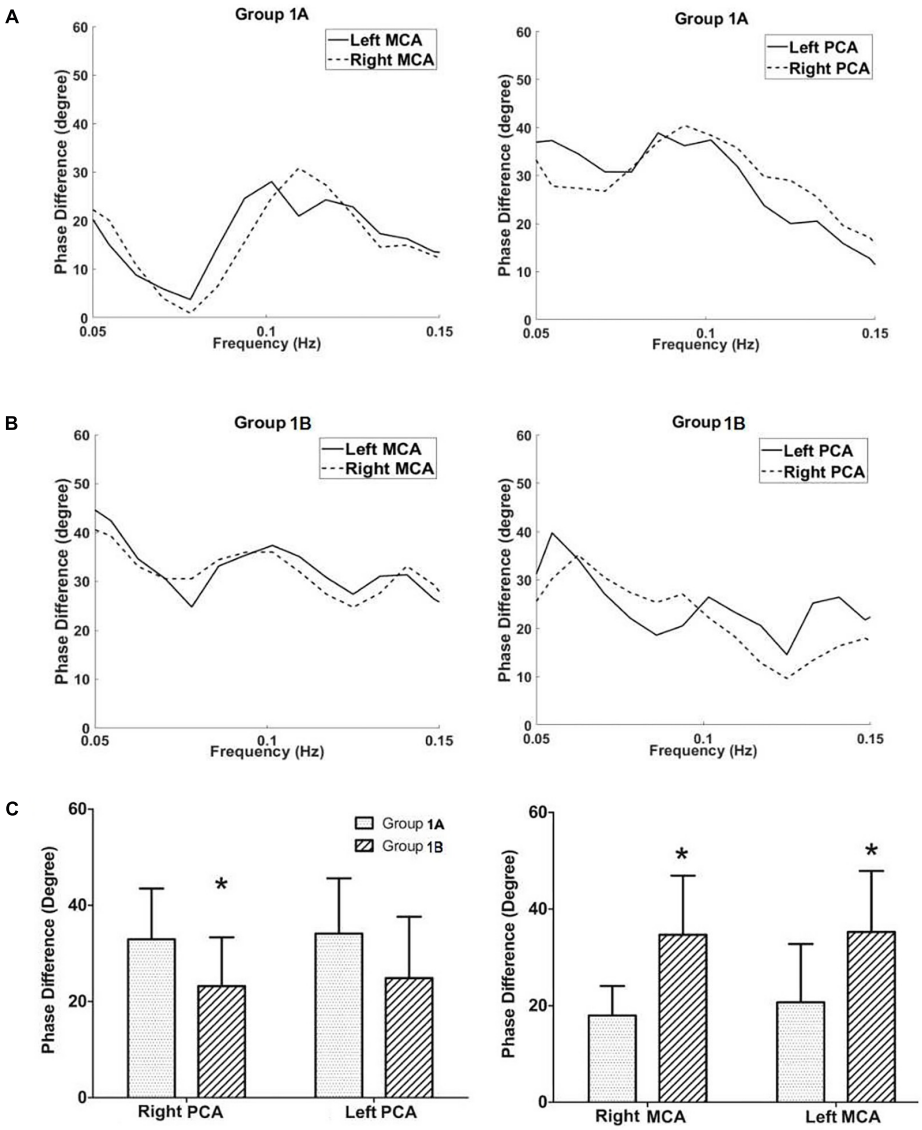

FIGURE 3 | Dynamic cerebral autoregulation analysis in subgroups of groups 1. The autoregulatory parameter (phase difference) of the bilateral middle cerebral arteries and bilateral posterior communicating arteries derived from the transfer function in group 1A **(A)**, and group 1B **(B)**. **(C)** Statistical analysis of groups 1A and 1B. Left half of **(C)**: the phase difference values of the right posterior cerebral arteries in group 1A were significantly higher than those at the same side of group 1B. The phase difference values of the left posterior cerebral arteries in group 1A tended to be higher compared with group 1B, although the value was not statistically significant. Right half of **(C)**: the phase difference values of the bilateral middle cerebral arteries in the group 1A were significantly lower than those at the corresponding side of the group 1B. $^*P < 0.05$ for comparison with group 1A.

the left posterior cerebral arteries in group 1A tended to be higher compared with group 1B, although the *P*-value was not statistically significant ($P = 0.097$, **Figure 3**).

On the contrast, the phase difference values of the bilateral middle cerebral arteries in the group 1A were significantly lower than those at the corresponding side of the group 1B (right: $P = 0.001$; left: $P = 0.014$; **Figure 3** and **Table 1**). There was no difference in gain values (another autoregulatory parameter) between group 1A and group 1B in both posterior cerebral arteries and middle cerebral arteries.

Protective Effect of ACoA or PCoA on dCA in Patients With Isolated Unilateral Internal Carotid Artery Severe Stenosis/Occlusion

In Group 2, patients with isolated unilateral internal carotid artery severe stenosis/occlusion, the phase difference values in the middle cerebral artery of the affected side in group 2A (with PCoA, but without ACoA) tended to be lower compared with the group 2B (with ACoA, but without PCoA, $P = 0.275$) whereas they tended to be higher compared with the group 2C (without both ACoA and PCoA, $P = 0.403$), though neither of these was statistically significant.

The phase difference values in the middle cerebral artery of the affected side in the group 2B were significantly higher than those in the group 2C ($P = 0.011$, **Figure 4** and **Table 1**). The phase difference values of the unaffected side were similar in each group. There was no difference of gain values in each group.

DISCUSSION

In this study, combining dCA and DSA in non-acute stroke patients with posterior circulation arteries/a unilateral internal carotid artery severe stenosis/occlusion, we found the cross-flow of the ACoA/PCoA to the affected area appears to compensate for potentially compromised dCA in the affected area via providing blood flow. These findings suggest an important role of the ACoA/PCoA in dCA regulation.

The dCA analysis reveals information about the intrinsic ability of the cerebral vasculature to maintain sufficient blood

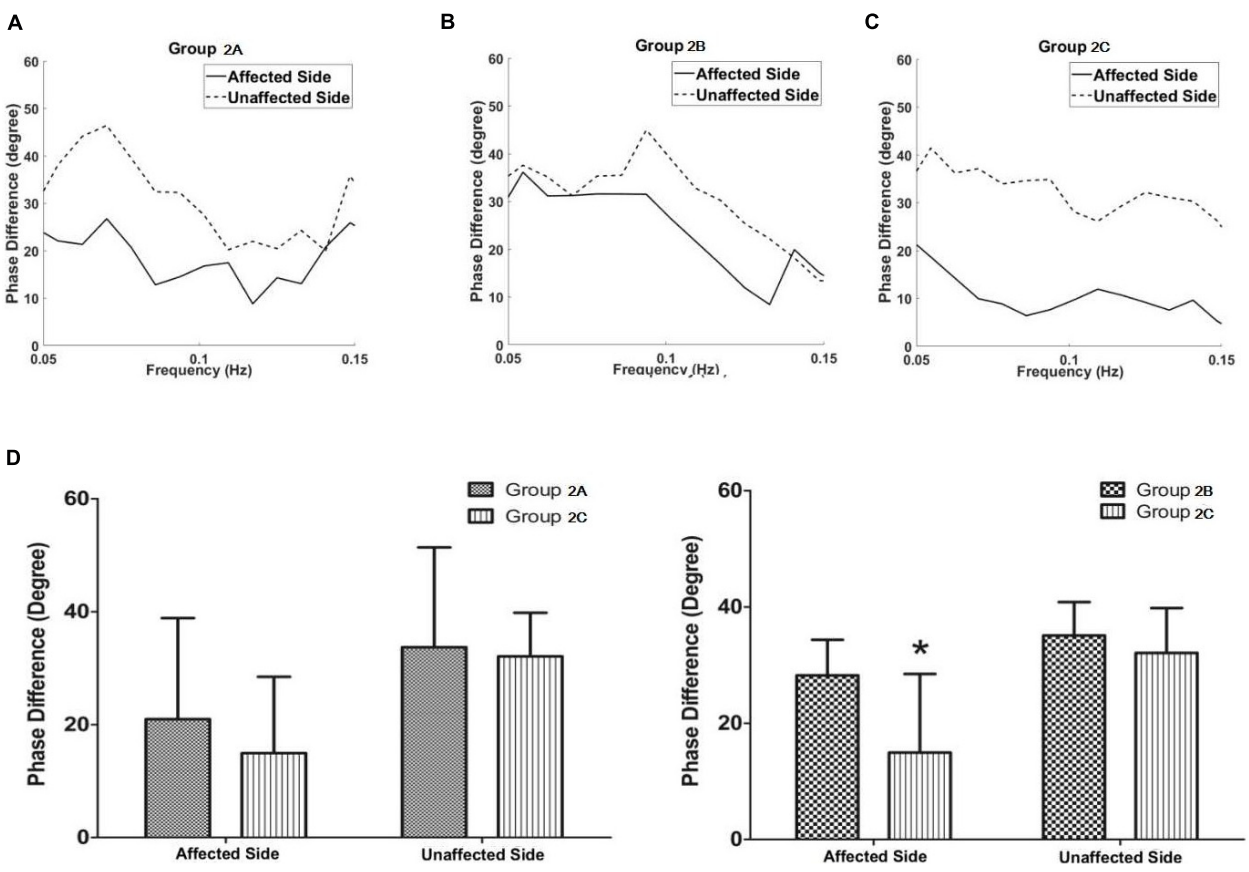

FIGURE 4 | Dynamic cerebral autoregulation analysis in subgroups of groups 2. The autoregulatory parameter (phase difference) of the bilateral middle cerebral arteries derived from the transfer function in group 2A **(A)**, group 2B **(B)**, and group 2C **(C)**. **(D)** Statistical analysis of groups 2A and 2C; and groups 2B and 2C. Left half of **(D)**: the phase difference values in the middle cerebral artery at the affected side in group 2A tended to be higher compared with the group 2C, although the value was not statistically significant. Right half of **(D)**: the phase difference values in the middle cerebral artery at the affected side in the group 2B were significantly higher than those in the group 2C. *$P < 0.05$ for comparison with group 2C.

supply, which might be a more appropriate method for evaluating cerebral hemodynamic impairment (Reinhard et al., 2003a). Pathophysiologically, insufficient collateral blood supply leads to a reduced perfusion pressure in the area downstream of the stenosis/occlusion site, causing dilation of downstream cerebral arterioles, and resulting in the impairment of dCA (Reinhard et al., 2003a). In the present study, we found that in cases of severe stenosis/occlusion of the basal artery and/or bilateral vertebral arteries, the dCA of the posterior cerebral artery (PCA) was higher in patients with PCoA than those without PCoA. This may be because sufficient blood flow results from anterior to posterior circulation via the PCoA to compensate for impaired posterior circulation. However, this may cause relatively insufficient blood supply within the anterior circulation, as reflected by the lower dCA of the middle cerebral artery in the presence of PCoA. When the middle cerebral artery and its branches are dilated in response to dCA, the remaining dCA in the middle cerebral artery is lower.

In patients with severe stenosis/occlusion of a unilateral internal carotid artery, we found the dCA of the middle cerebral artery in the affected side was significantly better in patients with ACoA than those without ACoA. This is consistent with cross-flow compensation of anterior communicating artery from the unaffected to the affected side. Kluytmans et al. (1999) found that in patients with a unilateral internal carotid artery occlusion, collateral flow via the ACoA is a sign of well-preserved hemodynamic status (Kluytmans et al., 1999). Our findings support their results, as well as the results of Reinhard et al. (2003a,c). Their studies found that in patients with severe unilateral carotid stenosis/occlusion with ACoA, dCA at the affected side did not differ significantly from the dCA at the contralateral side. All these studies demonstrated an important role of the ACoA in regulating the dCA. In addition, in group 2 patients, we found that the dCA tended to be higher among patients with PCoA compared to those without PCoA, although the difference did not reach statistical significance probably due to low numbers of patients. We considered this phenomenon may be due to the compensatory cross-flow from posterior circulation to anterior circulation through PCoA. It's worth mentioning that, following the development of 3D computational modeling, other groups also found the potential important role of circle of Wills on cerebral autoregulation (Moore et al., 2005; Long et al., 2008).

Though not every patient possesses integrated collateral circulation, it's shown that the communicating arteries play important roles in maintaining adequate perfusion status during ischemic demand (van Seeters et al., 2015; Goksu et al., 2017).

Our study here suggested a regulatory role of communicating arteries on dCA, which subsequently may modulate the occurrence and outcomes of ischemic stroke. Furthermore, our findings increased understanding of the cerebral hemodynamic characteristics in stroke patients with and without communicating arteries.

The study has several limitations which may have compromised the internal and external validity. Firstly, this study was a retrospective not prospective study. While we sought to exclude stroke patients in acute phase, the post-stroke time range was relatively wide, from 15 days to 2 months. Thus, we cannot completely exclude the time-course effects of the disease. Secondly, the statistical power of our findings was limited by the relatively small sample size of our study, which also possibly caused that the difference of several subgroups did not reach statistical significance. Thirdly, our study is based on our experience within one large tertiary care center in one province of China. The extent to which our results could be generalized to other different or broader patient populations is therefore unknown.

CONCLUSION

The present study suggests that cross-flow of the ACoA/PCoA to areas affected by severe stenosis and/or occlusion can compensate for compromised dCA in that area, consistent with an important protective function of the ACoA/PCoA in dCA compensation.

AVAILABILITY OF DATA AND MATERIALS

All datasets or this study are included in the manuscript and the supplementary files.

AUTHOR CONTRIBUTIONS

YY and HJ conceived and overseed study. HS, YZ, ZW, XY, XS, CL, and HJ performed data collection. JL and HM performed data analysis. Z-NG and PZ performed statistical analysis. BX and HZ read the DSA. Z-NG and XS wrote manuscript.

FUNDING

The authors disclosed receipt of the following financial support for the research, authorship, and/or publication of this article: the National Key R&D Program of China (Grant Nos. 2016YFC1301603 and 2016YFC1301600), the National Natural Science Foundation of China (Grant No. 81571123), and the Program for JLUSTIRT (2017TD-12) to YY.

ACKNOWLEDGMENTS

The authors are grateful to Dr. Marco D. Huesch for his insightful discussions.

SUPPLEMENTARY MATERIAL

The Supplementary Material for this article can be found online at: https://www.frontiersin.org/articles/10.3389/fphys.2018.00759/full#supplementary-material

DATA SHEET S1 | Gender, age, mean blood pressure and phase difference in each group.

REFERENCES

Claassen, J. A., Meel-van, den Abeelen, A. S., Simpson, D. M., and Panerai, R. B. (2016). Transfer function analysis of dynamic cerebral autoregulation: a white paper from the International Cerebral Autoregulation Research Network. *J. Cereb. Blood Flow Metab.* 36, 665–680. doi: 10.1177/0271678X15626425

Claassen, J. A., and Zhang, R. (2011). Cerebral autoregulation in Alzheimer's disease. *J. Cereb. Blood Flow Metab.* 31, 1572–1577. doi: 10.1038/jcbfm.2011.69

Fabbri, D., Long, Q., Das, S., and Pinelli, M. (2014). Computational modelling of emboli travel trajectories in cerebral arteries: influence of microembolic particle size and density. *Biomech. Model. Mechanobiol.* 13, 289–302. doi: 10.1007/s10237-014-0561-0

Goksu, E. O., Koc, P., Kucukseymen, E., Unal, A., Genc, F., Gencer, E. S., et al. (2017). The association of the circle of Willis anomaly and risk of stroke in patients with carotid artery disease. *Arq. Neuropsiquiatr.* 75, 429–432. doi: 10.1590/0004-282X20170054

Guo, Z. N., Liu, J., Xing, Y., Yan, S., Lv, C., Jin, H., et al. (2014a). Dynamic cerebral autoregulation is heterogeneous in different subtypes of acute ischemic stroke. *PLoS One* 9:e93213. doi: 10.1371/journal.pone.0093213

Guo, Z. N., Xing, Y., Liu, J., Wang, S., Yan, S., Jin, H., et al. (2014b). Compromised dynamic cerebral autoregulation in patients with a right-to-left shunt: a potential mechanism of migraine and cryptogenic stroke. *PLoS One* 9:e104849. doi: 10.1371/journal.pone.0104849

Guo, Z. N., Xing, Y., Wang, S., Ma, H., Liu, J., and Yang, Y. (2015). Characteristics of dynamic cerebral autoregulation in cerebral small vessel disease: diffuse and sustained. *Sci. Rep.* 5:15269. doi: 10.1038/srep15269

Kluytmans, M., van der Grond, J., van Everdingen, K. J., Klijn, C. J., Kappelle, L. J., and Viergever, M. A. (1999). Cerebral hemodynamics in relation to patterns of collateral flow. *Stroke* 30, 1432–1439. doi: 10.1161/01.STR.30.7.1432

Lin, W., Ma, X., Deng, D., and Li, Y. (2015). Hemodynamics in the circle of Willis with internal carotid artery stenosis under cervical rotatory manipulation: a finite element analysis. *Med. Sci. Monit.* 21, 1820–1826. doi: 10.12659/MSM.892822

Long, Q., Luppi, L., Konig, C. S., Rinaldo, V., and Das, S. K. (2008). Study of the collateral capacity of the circle of Willis of patients with severe carotid artery stenosis by 3D computational modeling. *J. Biomech.* 41, 2735–2742. doi: 10.1016/j.jbiomech.2008.06.006

Ma, H., Guo, Z. N., Liu, J., Xing, Y., Zhao, R., and Yang, Y. (2016). Temporal course of dynamic cerebral autoregulation in patients with intracerebral hemorrhage. *Stroke* 47, 674–681. doi: 10.1161/STROKEAHA.115.011453

Moore, S. M., Moorhead, K. T., Chase, J. G., David, T., and Fink, J. (2005). One-dimensional and three-dimensional models of cerebrovascular flow. *J. Biomech. Eng.* 127, 440–449. doi: 10.1115/1.1894350

Reinhard, M., Muller, T., Guschlbauer, B., Timmer, J., and Hetzel, A. (2003a). Dynamic cerebral autoregulation and collateral flow patterns in patients with severe carotid stenosis or occlusion. *Ultrasound Med. Biol.* 29, 1105–1113.

Reinhard, M., Muller, T., Guschlbauer, B., Timmer, J., and Hetzel, A. (2003b). Transfer function analysis for clinical evaluation of dynamic cerebral autoregulation–a comparison between spontaneous and respiratory-induced oscillations. *Physiol. Meas.* 24, 27–43.

Reinhard, M., Muller, T., Roth, M., Guschlbauer, B., Timmer, J., and Hetzel, A. (2003c). Bilateral severe carotid artery stenosis or occlusion - cerebral autoregulation dynamics and collateral flow patterns. *Acta Neurochir.* 145, 1053–1059; discussion 1059–1060. doi: 10.1007/s00701-003-0137-8

Reinhard, M., Roth, M., Muller, T., Guschlbauer, B., Timmer, J., Czosnyka, M., et al. (2004). Effect of carotid endarterectomy or stenting on impairment of dynamic cerebral autoregulation. *Stroke* 35, 1381–1387. doi: 10.1161/01.STR.0000127533.46914.31

Ren, Y., Chen, Q., and Li, Z. Y. (2015). A 3D numerical study of the collateral capacity of the Circle of Willis with anatomical variation in the posterior circulation. *Biomed. Eng. Online* 14(Suppl. 1):S11. doi: 10.1186/1475-925X-14-S1-S11

van Everdingen, K. J., Visser, G. H., Klijn, C. J., Kappelle, L. J., and van der Grond, J. (1998). Role of collateral flow on cerebral hemodynamics in patients with unilateral internal carotid artery occlusion. *Ann. Neurol.* 44, 167–176. doi: 10.1002/ana.410440206

van Seeters, T., Hendrikse, J., Biessels, G. J., Velthuis, B. K., Mali, W. P., Kappelle, L. J., et al. (2015). Completeness of the circle of Willis and risk of ischemic stroke in patients without cerebrovascular disease. *Neuroradiology* 57, 1247–1251. doi: 10.1007/s00234-015-1589-2

Zhang, R., Zuckerman, J. H., Giller, C. A., and Levine, B. D. (1998). Transfer function analysis of dynamic cerebral autoregulation in humans. *Am. J. Physiol.* 274(1 Pt 2), H233–H241. doi: 10.1152/ajpheart.1998.274.1.H233

Conflict of Interest Statement: The authors declare that the research was conducted in the absence of any commercial or financial relationships that could be construed as a potential conflict of interest.

Copyright © 2018 Guo, Sun, Liu, Sun, Zhao, Ma, Xu, Wang, Li, Yan, Zhou, Zhang, Jin and Yang. This is an open-access article distributed under the terms of the Creative Commons Attribution License (CC BY). The use, distribution or reproduction in other forums is permitted, provided the original author(s) and the copyright owner are credited and that the original publication in this journal is cited, in accordance with accepted academic practice. No use, distribution or reproduction is permitted which does not comply with these terms.

frontiers in Physiology

ORIGINAL RESEARCH
published: 31 July 2018
doi: 10.3389/fphys.2018.00926

Influence of the KCNQ1 S140G Mutation on Human Ventricular Arrhythmogenesis and Pumping Performance: Simulation Study

*Da Un Jeong and Ki Moo Lim**

Computational Medicine Lab, Department of IT Convergence Engineering, Kumoh National Institute of Technology, Gumi, South Korea

The KCNQ1 S140G mutation, which is involved in I_{Ks} current, affects atrial fibrillation. However, little is known about its effect on the mechanical behavior of the heart. Therefore, we assessed the influence of the KCNQ1 S140G mutation on ventricular electrophysiological stability and mechanical pumping performance using a multi-scale model of cardiac electromechanics. An image-based electromechanical model was used to assess the effect on electrical propagation and arrhythmogenesis of the KCNQ1 S140G mutation. In addition, it was used to compare the mechanical response under the wild-type (WT) and S140G mutation conditions. The intracellular calcium transient obtained from the electrophysiological model was applied as an input parameter to a mechanical model to implement excitation–contraction coupling. The I_{Ks} current equation was modified to account for expression of the KCNQ1 S140G mutation, and it included a scaling factor (ϕ) for mutant expressivity. The WT and S140G mutation conditions were compared at the single-cell and three-dimensional (3D) tissue levels. The action potential duration (APD) was reduced by 60% by the augmented I_{Ks} current under the S140G mutation condition, which resulted in shorter QT interval. This reduced the 3D sinus rhythm wavelength by 60% and the sustained re-entry by 56%. However, pumping efficiency of mutant ventricles was superior in sinus rhythm condition. In addition, the shortened wavelength in cardiac tissue allowed a re-entrant circuit to form and increased the probability of sustaining ventricular tachycardia and ventricular fibrillation. In contrast, under the WT condition, a normal wavelength (20.8 cm) was unlikely to initiate and sustain re-entry in the cardiac tissue. Subsequently, the S140G mutant ventricles developed a higher dominant frequency distribution range (2.0–5.3 Hz) than the WT condition (2.8–3.7 Hz). In addition, stroke volume of mutant ventricles was reduced by 65% in sustained re-entry compared to the WT condition. In conclusion, signs of the S140G mutation might be difficult to identify in sinus rhythm even though the mutant ventricles show shortened QT interval. This suggests that the KCNQ1 S140G mutation increases the risk of death by sudden cardiac arrest. In addition, the KCNQ1 S140G mutation can induce ventricular arrhythmia and lessen ventricular contractility under re-entrant conditions.

Keywords: KCNQ1 S140G mutation, ventricular arrhythmia, pumping performance, electromechanical simulation, sinus rhythm response, reentry response, dominant frequency

OPEN ACCESS

Edited by:
Thomas Heldt, Massachusetts Institute of Technology, United States

Reviewed by:
Arun V. Holden, University of Leeds, United Kingdom
Minki Hwang, Yonsei University Health System, South Korea

****Correspondence:***
Ki Moo Lim
kmlimphd@gmail.com

Specialty section:
This article was submitted to Computational Physiology and Medicine, a section of the journal Frontiers in Physiology

Received: *31 December 2017*
Accepted: *25 June 2018*
Published: *31 July 2018*

Citation:
Jeong DU and Lim KM (2018) Influence of the KCNQ1 S140G Mutation on Human Ventricular Arrhythmogenesis and Pumping Performance: Simulation Study. Front. Physiol. 9:926. doi: 10.3389/fphys.2018.00926

INTRODUCTION

Atrial fibrillation is a common cardiac arrhythmia that has been the focus of recent studies aiming to reveal the correlation between atrial fibrillation and KCNQ1 S140G mutations (Kharche et al., 2012). According to animal studies and clinical data, atrial fibrillation is mainly caused by the occurrence of re-entry due to a shortened action potential duration (APD) and decreased effective refractory period (ERP) (Nattel, 2002). The S140G gain-of-function KCNQ1 mutation, which is involved in I_{Ks} channels, induces atrial fibrillation. The KCNQ1 S140G mutation in myocardial cells results in rapid development of a substantial outward K^+ current during depolarization (Hong et al., 2005). The changes in the I_{Ks} channels caused by the KCNQ1 S140G mutation in myocardial cells increase the current through I_{Ks} channels, reducing APD and ERP, and thereby inducing atrial fibrillation (Chen et al., 2003; Kharche et al., 2012).

The electrophysiological effects of the KCNQ1 S140G mutation on myocardial cells and transgenic mouse have been investigated. Chen et al. used patch clamps and electrocardiograms (ECG) data to assess the effect of the gain-of-function S140G mutation on the KCNQ1/KCNE1 and KCNQ1/KCNE2 currents and found that this mutation caused development of atrial fibrillation by reducing APD and ERP in atrial myocytes. Therefore, the S140G mutation substantially increased the inward K^+ current at hyperpolarization, thereby stabilizing the resting membrane potential and shortening the atrial ERP (Chen et al., 2003). Bellocq et al. reported that a gain-of-function mutation affecting I_{Ks} also results in shortening of the QT interval. Abbreviation of the action potential (AP), particularly when occurring heterogeneously, facilitates development of re-entrant arrhythmias (Bellocq et al., 2004). Hong et al. reported that I_{Ks} channels containing S140G KCNQ1 subunits were constitutively open, and exhibited instantaneous activation in response to membrane depolarization and that a gain-of-function mutation can cause atrial fibrillation and short AT syndrome (Hong et al., 2005).

The KCNQ1 S140G mutation may also affect the electrophysiology of ventricular cells. Using voltage clamps, El Harchi et al. found that the S140G mutation substantially augments the repolarizing current both early and throughout the atrial AP *in vitro* and this mutation influences ventricular AP repolarization (El Harchi et al., 2010). Furthermore, Bellocq et al. suggested that ventricular fibrillation may be induced by short QT syndrome due to the S140G mutation, which has gain-of-function characteristics (Bellocq et al., 2004). Yang et al. reported that the S140G mutation is likely responsible for atrioventricular blocks. Therefore, this mutation may be associated with other cardiac arrhythmias (Yang et al., 2007).

The above studies were performed at the cellular level, not in tissue or organs. Several computational studies have predicted the effect of mutations on cardiac tissue. Kharche et al. used computer modeling to investigate the mechanism by which the KCNQ1 S140G mutation, promotes and perpetuates atrial fibrillation. I_{Ks} was increased by the S140G mutation, which enhances atrial susceptibility to arrhythmia, facilitating initiation, and maintenance of re-entry (Kharche et al., 2012). In addition, Hancox et al. employed ventricular AP clamp experiments and ventricular APD simulation to investigate not only the mechanism by which the S140G mutation modulates the risk of atrial arrhythmia, but its effect on ventricular electrophysiology by; this mutation resulted in an abbreviated ventricular AP (Hancox et al., 2014).

These studies predicted variations in cardiac responses due to the KCNQ1 S140G mutation in atria and ventricles from an electrophysiological standpoint. However, they did not predict the effects of this mutation on cardiac mechanical responses. It is important to consider cardiac mechanical phenomena as well as electrical phenomena because cardiac mechanical contraction, which is triggered by electrical excitation, is the ultimate purpose of the heart. Also, cardiac mechanical contraction affects electrophysiological phenomena. For instance, stretch-activated channels cause changes in electrogenic pump currents or flux of specific ions through mechanical stretching of the heart (Hu and Sachs, 1997).

We recently developed a three-dimensional (3D) electromechanical model of ventricles together with a lumped parameter model of the circulatory system, and investigated ventricular electromechanical responses under various pathological conditions (Lim et al., 2012, 2013, 2015). In this study, we incorporated the KCNQ1 S140G mutation into our ventricular model to predict its effect on ventricular mechanics during the normal sinus rhythm and in the presence of re-entrant arrhythmia.

METHODS

Model of Cellular Electrophysiology and Cross-Bridge Dynamics

To investigate the electromechanical effects of the KCNQ1 S140G mutation, we used an excitation–contraction coupling model, which is a human ventricular model with electrophysiological conduction and mechanical contraction. A model of electrophysiological conduction characteristics consisted of a circuit of concentrated circulation that simulated the mechanism of ion exchange through the plasma membrane of myocardial cells (**Figure 1**). We used a modified version of the validated ventricular ion model proposed by Ten Tusscher et al. (2004). To mimic the conduction of AP in myocardial cells, we applied continuum mechanics based on an electrical conduction equation (Equation 1),

$$\frac{dV_m}{dt} = -\frac{I_{ion}+I_{stim}}{C_m} \tag{1}$$

where V_m is the cell membrane potential, t is time, I_{ion} is the sum of the transmembrane currents, I_{stim} is the current due to external stimuli, and C_m is the capacitance of the cell membrane.

To express the conduction phenomenon of myocardial tissue in 3D space, we combined the ordinary differential equation for electrical propagation through the ion channel with the

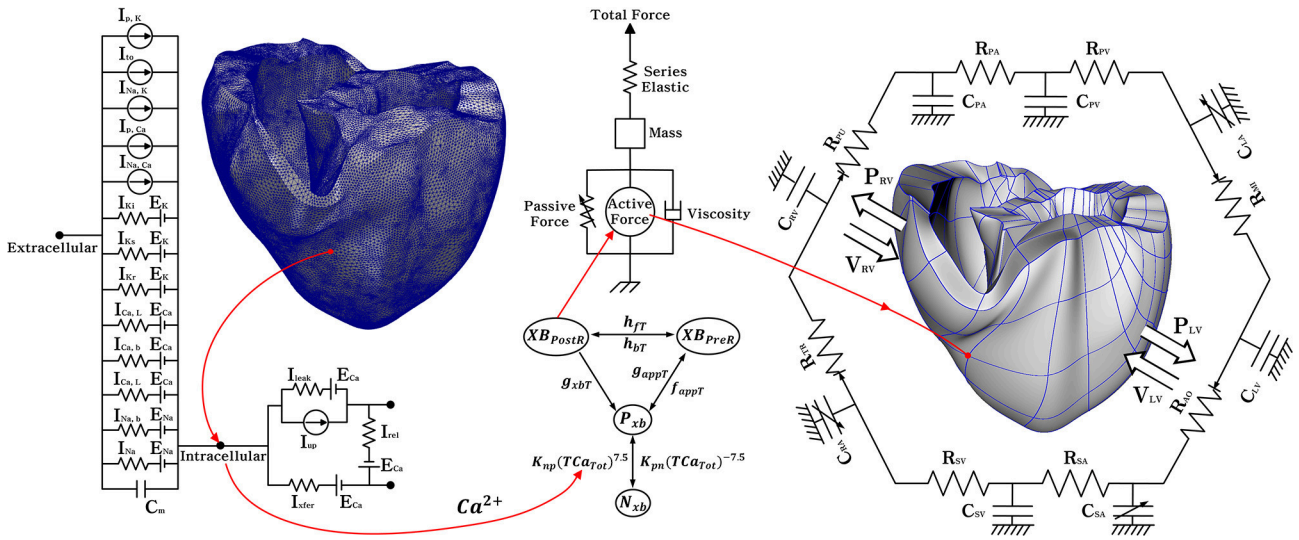

FIGURE 1 | Schematic diagram of the ventricular electromechanical model. The left side of the circuit diagram is a ventricular model of electrophysiological simulation with 214,319 nodes. The electrical components of the schematic represent the current, pump, and ion exchanger from the Ten Tusscher ion model, which emulates the cell membrane for ion transport and the sarcoplasmic reticulum within cardiac cells. $I_{p,\ k}$ is the current due to the K^+ pump, I_{to} denotes the transient outward K^+ current, $I_{Na,\ K}$ is the Na^+ $-K^+$ ion exchange current, $I_{p,\ Ca}$ is the current of the sarcoplasmic Ca^{2+} pump, and $I_{Na,\ Ca}$ means the current mediated by the Na^+ $-Ca^{2+}$ ion exchange pump. E_K, E_{Ca}, and E_{Na} are the equilibrium potentials of K^+, Ca^{2+}, and Na^+ ions, respectively, whereas C_m denotes the membrane capacitance due to the phospholipid bilayer in ventricular cells. I_{k1} is the inward rectifier K_1 current, I_{Ks} is the K^+ current due to the slow delayed rectifier, $I_{Ca,\ L}$ is the L-type inward Ca^{2+} current, and $I_{Ca,\ b}$ denotes the background Ca^{2+} current. $I_{Na,\ b}$ is the background Na^+ current, and I_{Na} is the fast inward Na^+ current. I_{rel} is the Ca^{2+} current released from the junctional sarcoplasmic reticulum (JSR), I_{leak} denotes the Ca^{2+} current that leaks from the ISR, and I_{up} is the Ca^{2+} uptake current into the network sarcoplasmic reticulum (NSR). The mechanical components on the right are the myofilament models proposed by Rice et al. N_{xB} and P_{xB} are non-permissive and permissive confirmations of regulatory proteins, and XB_{PreR} is the pre-rotated state of the myosin head in relation to binding, which contributes to stiffness but does not generate force in the absence of net motion. XB_{PostR} denotes a strongly bound myosin head and represents the isomerization that induces strain in the extensible neck region. G_{xbT} is the ATP-consuming detachment transition rate, h_{fT} and h_{bT} are the forward and backward transition rates, respectively; f_{aapT} is the cross-bridge attachment rate of transition to the first strongly-bound state XB_{PreR}, and g_{aapT} is the reverse rate. K_{np} and K_{pn} are transition rates, $K_{np}(TCa_{Tot})^{7.5}$ is the forward rate of the nonpermissive-to-permissive transition, in the opposite direction, and $K_{pn}(TCa_{Tot})-7.5$ is the backward rate of the permissive-to-nonpermissive transition. The force due to the cross-bridge can be subdivided into an active force and passive force. The active force induces the action of the cycling cross-bridge, and the passive force induces a complete muscle response with viscoelastic elements. Mass prevents instantaneous changes in muscle-shortening velocity for quick-release protocols, whereas a linear elastic element is intended to simulate the effects of the compliant end connections that take place in real muscle preparations. The model coupled with the circulatory; C_{PA}, pulmonary artery compliance; R_{PA}, pulmonary artery resistance; C_{PV}, pulmonary vein compliance; R_{PV}, pulmonary vein resistance; C_{LA}, left atrium compliance; R_{MI}, mitral valve resistance; C_{LV}, left ventricular compliance; R_{AO}, aortic valve resistance; R_{SA}, systemic artery resistance; C_{SA}, systemic artery compliance; R_{SV}, systemic vein resistance; C_{SV}, systemic vein compliance; C_{RA}, right atrium compliance; R_{TR}, tricuspid valve resistance; C_{RV}, right ventricular compliance; R_{PU}, pulmonary valve resistance; P_{RV}, right ventricular pressure; V_{RV}, right ventricular volume; P_{LV}, left ventricular pressure; V_{LV}, left ventricular volume.

partial differential equation for electrical stimulation in tissue (Equation 2):

$$\frac{dV_m}{dt} = -\frac{I_{ion} + I_{stim}}{C_m} + \frac{1}{\rho_x S C_m}\frac{\partial^2 V}{\partial^2 x^2} + \frac{1}{\rho_y S C_m}\frac{\partial^2 V}{\partial^2 y^2} + \frac{1}{\rho_z S C_m}\frac{\partial^2 V}{\partial^2 z^2} \quad (2)$$

where ρ_x, ρ_y, and ρ_z represent the cell resistance in x, y, and z directions, and S represent the ratio of the volume to the surface. Following Ten Tusscher et al., the sum of the transmembrane currents, I_{ion}, was calculated by Equation (3):

$$I_{ion} = I_{Na} + I_{K1} + I_{to} + I_{Kr} + I'_{Ks} + I_{Ca,L} + I_{Na,\ Ca} + I_{Na,K} + I_{p,Ca} + I_{p,K} + I_{b,Ca} + I_{b,Na} \quad (3)$$

where I_{Na} represents the Na^+ current, I_{K1}, I_{to}, and I_{Kr} are the K^+ currents, namely the inward rectifier K^+ current, transient outward K^+ current, and rapid delayed rectifier K^+ current, respectively. I'_{Ks} is the slow delayed rectifier K^+ current due to KCNQ1 S140G mutation. This is explained in detail in the following paragraphs. $I_{Ca,\ L}$ is the L-type inward Ca^{2+} current, $I_{Na,\ Ca}$ is the Na^+-Ca^{2+} exchange current, $I_{Na,\ k}$ denotes the Na^+-K^+ exchange current, $I_{p,\ Ca}$ is the current of the Ca^{2+} pump, $I_{p,\ K}$ is the current of the K^+ pump, $I_{b,\ Ca}$ is the background Ca^{2+} current, and $I_{b,\ Na}$ represents the background Na^+ current.

To confirm the electrophysiological changes in ventricular cells caused by the KCNQ1 S140G mutation, we used the I_{Ks} current equation (Equation 4) proposed by the Ten Tusscher ion model and the mutant I_{Ks} current equation (Equation 5) of Kharche et al. (Ten Tusscher et al., 2004; Kharche et al., 2012):

$$I'_{Ks} = I_{Ks} + \varphi G_{Ks}(V - E'_{rev}) \quad (4)$$

$$I_{Ks} = G_{Ks} x_s^2 (V - E_{Ks}) \quad (5)$$

where G_{Ks} denotes the conductance of the K^+ ion channel, which was set to 0.392·1.3 mS/μF in this study. E'_{rev} is the mutant reversal potential due to the instantaneous component of the K^+ ion channel, which was set at −75.3 mV. ϕ is the scaling factor for the S140G mutation expressivity, which was set to 0.1. This is the value used for observing the state of the ventricles, which is intermediate mutation. This value was established based on clinical studies that showed rapid changes in protein channels depending on the expression levels of the S140G mutation (Kharche et al., 2012). x_s is the activated gate variable, which was set to 0.00357 to represent K^+ channels in a steady state. E_{Ks} is the equilibrium potential of the K^+ channel, in which the initial value was set to zero (Ten Tusscher et al., 2004; Kharche et al., 2012).In particular, we used transient calcium information of electrophysiological simulation as an input for excitation–contraction coupling. Therefore, we applied the calcium dynamics equation of the Ten Tusscher ion model to induce contraction of the myofilaments and generate tension through the Ca^{2+}-induced Ca^{2+}-released (CICR) current.

$$I_{leak} = V_{leak}(Ca_{sr} - Ca_i) \tag{6}$$

$$I_{up} = \frac{V_{maxup}}{1 + K_{up}^2/Ca_i^2} \tag{7}$$

$$I_{rel} = \left(a_{rel}\frac{Ca_{sr}^2}{b_{rel}^2 + Ca_{sr}^2} + c_{rel}\right) dg \tag{8}$$

$$\frac{dCa_{itotal}}{dt} = -\frac{I_{Ca,L} + I_{b,Ca} + I_{p,Ca} - 2I_{Na,Ca}}{2V_C F} + I_{leak} - I_{up} + I_{rel} \tag{9}$$

$$\frac{dCa_{srtotal}}{dt} = \frac{V_c}{V_{SR}}(-I_{leak} + I_{up} - I_{rel}) \tag{10}$$

where I_{leak}, I_{up}, and I_{rel} denote leakage current from sarcoplasmic reticulum to cytoplasm, pump current taking up calcium in sarcoplasmic reticulum, and CICR current, respectively. V_{leak} is maximal I_{leak}, V_{maxup} is maximal I_{up}. Ca_i and Ca_{sr} are for the free calcium concentration in cytoplasm and in sarcoplasmic reticulum. K_{up} is half-saturation constant of I_{up}. a_{rel}, b_{rel}, and c_{rel} are maximal Ca_{sr}-dependent I_{rel}, Ca_{sr} half-saturation constant of I_{rel}, and maximal Ca_{sr}-independent I_{rel}, respectively. d is the activation gate of I_{rel}, and g is the calcium-dependent inactivation gate of I_{rel}. Ca_{itotal} refers to the amount of Ca^{2+} in the cytoplasm and $Ca_{srtotal}$ denotes the total amount of Ca^{2+} in the sarcoplasmic reticulum. V_c and V_{SR} are the volume of cytoplasmic and sarcoplasmic reticulum, respectively. F is Faraday constant.

In addition, to mimic cardiac muscle contraction, we referenced a mechanical cross-bridge cycling model of the myofilament, suggested by Rice et al. (2008). To express myofilament contraction, we used the equation of normalized active force (Equation 11),

$$F_{active}(x) = SOVF_{thick}(x) \times \frac{xXB_{PreR} \times XB_{PreR} + xXB_{PostR} \times XB_{PostR}}{x_0 \times XB_{PostR}^{Max}} \tag{11}$$

where $SOVF_{thick}$ is the single-overlap function for the thick filament, XB_{PreR} is state of cross-bridge pre-rotated, XB_{PostR} is state of cross-bridge post-rotated, which represents the isomerization to induce strain in the extensible neck region, xXB_{PreR} is the average distortion of XB_{PreR}, xXB_{PostR} is the average distortion of XB_{PostR}, XB_{PostR}^{Max} is scaling factors for state occupancy computed under optimal conditions, x_0 is cross-bridge distortion length.

Three-Dimensional Ventricular Electromechanical Models

In this study, we used the 3D human ventricular finite element model, which has a concentrated physiological circulatory system based on a Windkessel element. The electrophysiological simulation model consisted of 214,319 finite elements of a tetrahedral structure. The model for mechanical contraction simulation consists of 14,720 finite elements, based on Hermite, to represent the natural 3D curve of the heart surface.

For 3D electrophysiology simulation under sinus rhythm conditions, we used the ventricular model with Purkinje fibers mesh, which are distributed on the sub-endocardial surface. This model mimics conduction of electrical simulation from the AV node through the ends of the Purkinje fibers to the entire ventricle (Berenfeld and Jalife, 1998). In addition, considering differences in ventricle structural characteristics and thickness, we assumed that the ventricle tissue was heterogeneous, and that the conductance varied among the parts of the ventricle; namely, endocardium, mid-myocardium, and epicardium. A detailed description of each conductance value can be found in the simulation protocols section. For distinguish each parts of the ventricle, we applied electrical stimulation to the sub-endocardial surface and the endocardial surface, respectively. The tissues that propagated for 2 ms were determined to be endocardium and epicardium. In addition, we determined the mid-myocardium as the middle tissue, which was neither endocardium nor epicardium.

Mathematical description of mechanical contraction in cardiac tissue is based on continuum mechanics, where it is assumed for myocardium to be hyper-elastic and nearly incompressible material, and to have the passive mechanical properties defined by an exponential strain (W) function (Guccione et al., 1995; Usyk et al., 2002).

$$W = \frac{C}{2}(e^Q - 1) \tag{12}$$

$$Q = b_1 E_{ff}^2 \pm b_2\left(E_{rr}^2 + E_{cc}^2 + 2E_{rc}^2\right) + 2b_3(E_{fr}^2 + E_{fc}^2) \tag{13}$$

$$E_{\alpha\beta} = \frac{1}{2}\left(\frac{\partial x^k}{\partial \nu^\alpha}\frac{\partial x^k}{\partial \nu^\beta} - \delta_{\alpha\beta}\right) \tag{14}$$

where C is the material constants and set to 2 kPa, b_1 is 8, b_2 is 2, and b_3 is 4, which are determined with the orthotropic electrical conductivity and passive mechanical properties of the myocardium by the laminar sheet-norminal direction and fiber orientation information (For more information, see Supplementary Material). The Langian Green's strains $E_{\alpha\beta}$ are referred to the local fiber coordinate system. x^k is transformed rectangular Cartesian coordinates, and $\delta_{\alpha\beta}$ is the Kronecker delta.

For simulate hemodynamic responses, the interactions between the blood and ventricles, the finite element

electromechanical model of the human ventricle was coupled with a circulatory model using coupling method of Gurev et al. (2011) as in **Figure 1**.The circulatory model used in this study was developed based on cardiovascular model of Kerckhoffs et al. (2007). Therefore, it can derive the blood characterized by pressure, volume, and flow of ventricles. In particular, the ventricular pressure expressed by the following time-varying mathematical equation.

$$Pressure = C^{-1}(t)(V - V_{rest}(t)) \quad (15)$$

$$C = y_v\,(C_{\max} - C_{\min}) + C_{\min} \quad (16)$$

where C is time-varying compliance matrix. C_{max} and C_{min} are compliance for ventricular fully activate state and passive state, respectively. y_v denotes ventricular active function. V is ventricular volume and V_{rest} is ventricular volume at zero pressure.

$$V_{LV} = -R_{LA}\dot{Q}_{LA} + \frac{1}{C_{LA}}Q_{LA} \quad (17)$$

$$V_{rest} = \left(1 - y_v\right)^* \begin{bmatrix} V_{L,rest,d} & V_{L,rest,s} \\ V_{R,rest,d} & V_{R,rest,s} \end{bmatrix} + \begin{bmatrix} V_{L,rest,s} \\ V_{R,rest,d} \end{bmatrix} \quad (18)$$

where $V_{L,rest,d}$, $V_{L,rest,s}$, $V_{R,rest,d}$, and $V_{R,rest,s}$ are diastolic volume and systolic volume of the left and right ventricle, respectively.

Simulation Protocols

First, we investigated the effect of the KCNQ1 S140G mutation on cellular electrophysiology and the APD restitution curve. Second, we performed 3D simulation to assess the effect of the S140G mutation on the sinus rhythm response. Third, we evaluated induction of arrhythmogenesis due to the KCNQ1 S140G mutation. Fourth, we compared cardiac pumping efficiency under the WT and S140G mutation conditions with sustained re-entry.

In the cellular electrophysiological simulation, we compared the I_{Ks} current and APD_{90} between the S140G mutation and WT conditions. In addition, using a dynamic restitution protocol, we compared the action potential duration-basic cycle length (APD-BCL) curves and action potential duration-diastolic interval (APD-DI) curves; the BCL was 1,000 and 20 ms under the S140G mutation and WT conditions, respectively. In addition, we investigated the electrical phenomena caused by the S140G mutation in the ventricular endocardium, midmyocardium, and epicardium cells. For this purpose, we applied electrical conductivity as follows: for the endocardium, G_{ks} = 0.392*1.3 mS/μF and G_{to} = 0.073 mS/μF; for the midmyocardium, G_{ks} = 0.098*2.0 mS/μF and G_{to} = 0.294 mS/μF; for the epicardium, G_{ks} = 0.392*1.3 mS/μF and G_{to} = 0.294 mS/μF. These conductance values were derived from the human ventricular model of Ten Tusscher et al., which is a validated ventricular model (Ten Tusscher et al., 2004).

In the 3D simulation, we compared the cardiac pumping efficiency of the sinus rhythm under the WT and S140G mutation conditions. We first performed a 3D electrophysiological simulation and extracted the transient Ca^{2+} information. To mimic cardiac excitation–contraction coupling, we used the Ca^{2+} data, which is extracted from electrophysiological simulation, as an input in the mechanical contraction simulation. We set the BCL for sinus rhythm to 600 ms. To evaluate the mechanical behavior of ventricular tissue in steady state, we used only the result of the last cycle of the electrophysiological simulation (12 s).

We introduced the concepts of electrical activation time (EAT) and electrical deactivation time (EDT) to quantitatively confirm the electrophysiological changes caused by the KCNQ1 S140G mutation. EAT is defined as the time at which depolarization begins in ventricle myocardial cells. In this study, EAT was the time at which the AP reached −30 mV. EDT was defined as the time at which repolarization was terminated in ventricle myocardial cells. Here, EDT was the time at which the AP reached −75 mV.

To quantitatively assess the effect on pumping efficiency of the changes in I_{Ks} channels and AP caused by the S140G mutation, we used the following mechanical analysis methods: pressure–volume loop (PV loop), stroke volume, ejection fraction, and ATP consumption.

Finally, we evaluated the effect of the S140G mutation on the occurrence of ventricular fibrillation by conducting a re-entry generation simulation. We performed a sustained re-entry response simulation to compare the mechanical contraction efficiency when the re-entry wave reached steady state under the WT and S140G mutation conditions. In the re-entry generation simulation, re-entry was generated at a conduction velocity of 65 cm/s under normal conditions using S1–S2 protocols. In S1–S2 protocols, the S1 stimulus was applied three times at 600 ms intervals, and the S2 stimulus was applied when the tail of the third wave reached the middle of the ventricle. We compared arrhythmogenesis and maintenance of re-entry between the S140g mutation and WT conditions.

To generate re-entrant wave in the sustained re-entry simulation, the S1–S2 protocol was applied with a very low conduction velocity (20 cm/s). When re-entry was generated under the S140G mutation and WT conditions, we saved all dependent variables of the cellular state at the moment at which the re-entry waves were maintained. These saved cellular state variables were used as the initial values in the next simulation, which involved a normal conduction velocity (70 cm/s).

We calculated the dominant frequency of each node in the ventricular model to quantitatively compare the electrophysiological changes due to the KCNQ1 S140G mutation during re-entry. The dominant frequency was determined using the fast Fourier transform (FFT) function of MATLAB, with the sampling rate set to 0.01. The dominant frequency is defined as the frequency corresponding to the maximum power calculated by FFT. Additionally, to quantitatively assess cardiac mechanical behavior according to the electrophysiological changes caused by the S140G mutation during sustained re-entry, we evaluated ventricular pressure, volume, and ATP consumption rate.

RESULTS

Effect on Electrophysiological Activity of the S140G Mutation

We assessed the effect of the KCNQ1 S140G mutation on I_{Ks} current and the effect of the variation in I_{Ks} on the shape of the AP. Under the S140G mutation condition, I_{Ks} currents were significantly higher in the early phase of the pacing cycle compared to under the WT condition in endocardial, mid-myocardial, and epicardial cells (**Figures 2A–C**). However, I_{Ks} channels under the S140G mutation condition closed more rapidly than under the WT condition, which resulted in early termination of I_{Ks} currents. In endocardial cells, I_{Ks} currents were sustained for 284 ms under the WT condition (average current 0.27 mA/pF) and 80 ms under the S140G mutation condition (0.64 mA/pF). In mid-myocardial cells, I_{Ks} currents were sustained for 332 ms under the WT condition (average current 0.19 mA/pF) and 180 ms under the S140G mutation condition (0.50 mA/pF). In epicardial cells, I_{Ks} currents were sustained for 284 ms under the WT condition (average current 0.25 mA/pF) and 76 ms under the S140G mutation condition (60 mA/pF).

Due to these changes in I_{Ks} currents, the APD_{90} under the S140G mutation condition was significantly reduced compared to that under the WT condition. In endocardial cells, the APD_{90} was 55 ms under the S140G mutation condition, but 284 ms under the WT condition. In mid-myocardial cells, the APD_{90} was 166 ms under the S140G mutation condition, but 365 ms under the WT condition. In epicardial cells, the APD_{90} was 55 ms under the S140G mutation condition, but 280 ms under the WT condition (**Figures 2D–F**).

To observe the rate dependency of APD and wave-front stability, APD restitution curves were generated using the dynamic restitution protocol under WT and S140G mutation conditions in three cell types. The APD restitution curves under the WT condition matched the results reported by Ten Tusscher et al. (2004). The maximum slope of the APD restitution curve was >1 and <1 under the WT and S140G mutation conditions, respectively (**Figures 2J–L**). According to Ten Tusscher et al., cells under the S140G mutation condition, which have maximum APD restitution curve slopes of <1, experience the alternans phenomenon at lower BCL values than they do under the WT condition (Ten Tusscher and Panfilov, 2006). Alternans under the S140G mutation condition occurred at 50 ms in the endocardium, 100 ms in the mid-myocardium, and 50 ms in the epicardium; in contrast, they occurred at 244 ms in the endocardium, 310 ms in the mid-myocardium, and 235 ms in the epicardium under the WT condition.

3D Electromechanical Simulation

The changes in electrophysiological activity due to the KCNQ1 S140G mutation described above were detected in single-cellular levels. We thus investigated the effect of these electrophysiological variations on cardiac mechanical behavior using an image-based 3D ventricular electromechanical model.

3D Sinus Rhythm

It is assumed that in sinus rhythm, electrical impulse propagates from the AV node through the Purkinje fiber mesh. Because the conduction velocity through the Purkinje fibers is identical under the S140G mutation and WT conditions (100 cm/s), electrical depolarization of cardiac muscle from the Purkinje terminal node was triggered at the same time. Although electrical depolarization was applied simultaneously under the WT and S140G mutation conditions, electrical repolarization spread through the ventricular tissue at different velocities (**Figures 3A,B**). The transmural distribution of membrane potential also differed between the two conditions due to the differently shaped action potentials. APD_{90} was 309 ms under the WT condition compared to 126 ms under the S140G mutation condition. The conduction velocity from the apex to the top of the ventricles was 67.4 and 64.7 cm/s under the WT and S140G mutant conditions, respectively. Accordingly, the conduction wavelength was 20.8 cm under the WT and 8.2 cm under the S140G mutation condition.

Figure 3C shows the transmural distribution of the EAT and EDT under the WT and S140G mutation condition. The EAT was similar, but the EDT differed significantly between the WT and S140G mutation conditions. The EDT was 337–470 ms under the WT and 30–183 ms under the S140G mutation condition. The difference between the maximum and minimum EAT, which reflects the QRS width in ECG, was 140 ms under both conditions. The difference between the maximum EDT and minimum EAT, which reflects the QT interval was 460 and 290 ms under the WT and S140G mutation conditions, respectively.

We assessed the effect of the electrophysiological changes caused by the KCNQ1 S140G mutation on ventricular mechanical contraction in sinus rhythm (**Figure 4**). During sinus rhythm, the pressure in the left ventricle (LV) and the systemic artery was slightly decreased under the S140G mutation condition (**Figure 4A**). The pressure–volume loop of the LV was shifted to the right, which resulted in an increased LV end-diastolic volume under the S140G mutation condition (**Figure 4B**). Therefore, the LV ejection fraction under the S140G mutation condition was significantly smaller than that under the WT condition (47.6 and 54.2%, respectively), despite the slight difference in LV stroke volumes (58.6 and 58.3 mL under the WT and S140G mutation conditions, respectively) (**Table 1**).

Under the S140G mutation condition, ventricles did less stroke work (5,685 and 5,768 mm Hg·mL under the S140G mutation and WT conditions) and consumed less contractile ATP (36 /BCL in S140G and 47.6 /BCL in WT) than under the WT condition. Ventricular pumping efficacy, i.e., LV stroke work divided by contractile ATP consumption, was 157.9 and 121.2 mm Hg·mL/BCL under the S140G mutation and WT conditions, respectively.

3D Re-entrant Dynamics

To investigate the effect of the KCNQ1 S140G mutation on ventricular arrhythmogenesis, we performed a re-entrant wave dynamics simulation using an image-based 3D ventricle model under the WT and S140G mutation conditions. Under the S140G

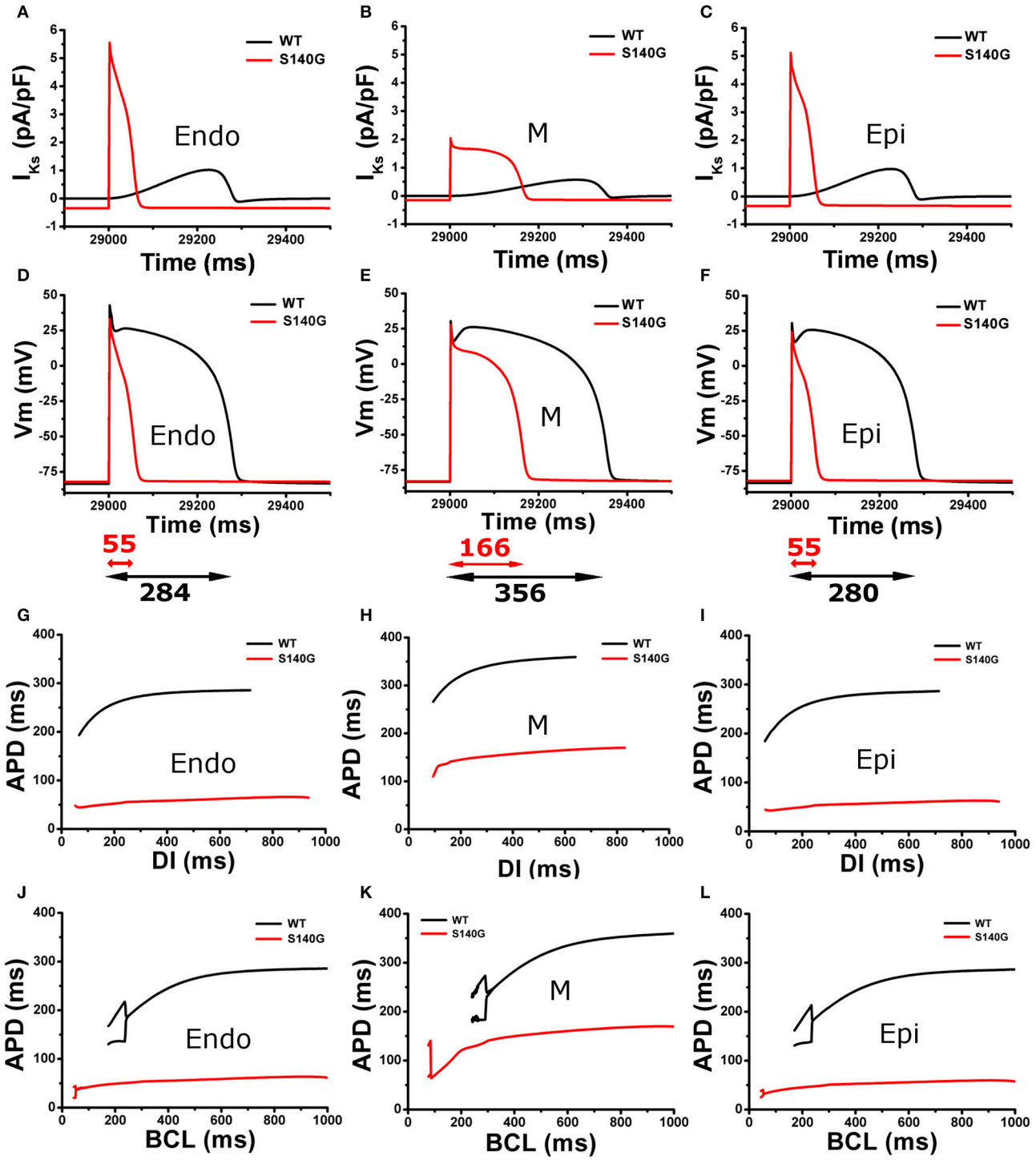

FIGURE 2 | Single-cell simulations using various myocardial cell types under the WT and S140G mutation conditions. I_{Ks} currents **(A–C)**, the corresponding AP shapes **(D–F)**, and APDR curves **(G–L)** under the WT and KCNQ1 S140G mutation conditions in ventricular endocardium (Endo), mid-myocardium (M), and epicardium (Epi) cells. APD, action potential duration; DI, diastolic interval and; BCL, basic cycle length.

mutation condition, a re-entrant wave was generated with the S1–S2 protocol and sustained re-entry occurred at a 65 cm/s conduction velocity and 5 Hz rotation rate (lower panel in **Figure 5A**). Under the WT condition, no re-entrant wave was generated, and wave propagation terminated at 3.050 ms (upper panel in **Figure 5A**) with identical tissue conductivity (65 cm/s).

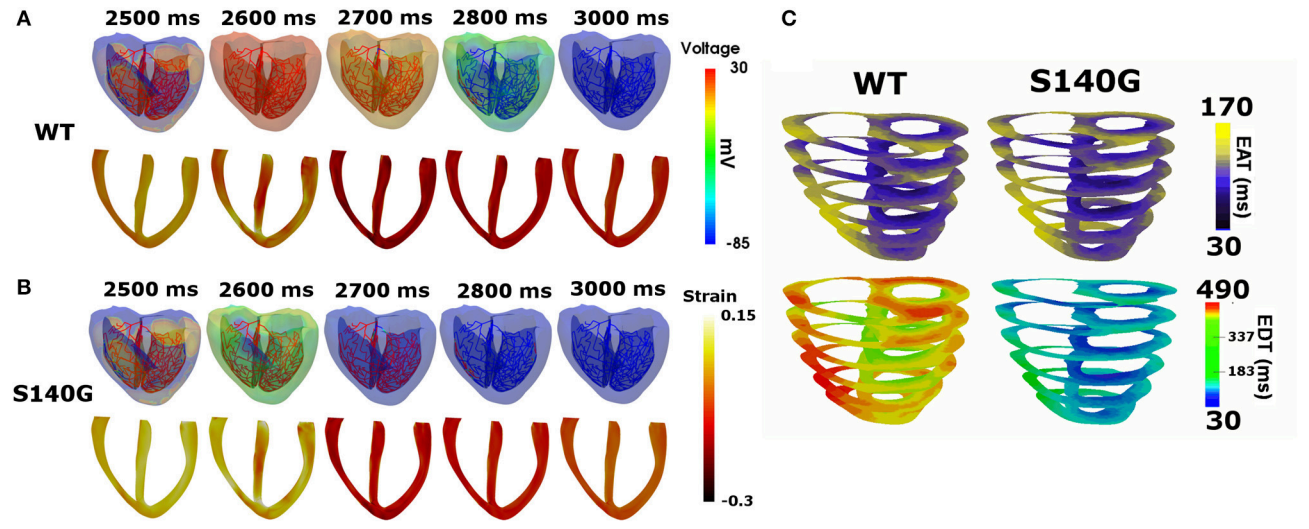

FIGURE 3 | Sinus rhythm response in the 3D ventricular tissue model under the WT and S140G mutation conditions. Snapshots of the transmural distribution of membrane potential (top), strain (bottom) **(A,B)** and electrical activation time (EAT) and electrical deactivation time (EDT) during one cycle of sinus pacing under the WT and KCNQ1 S140G mutation condition **(C)**. The anisotropy ratio of CV (longitudinal to transverse) is 1.5.

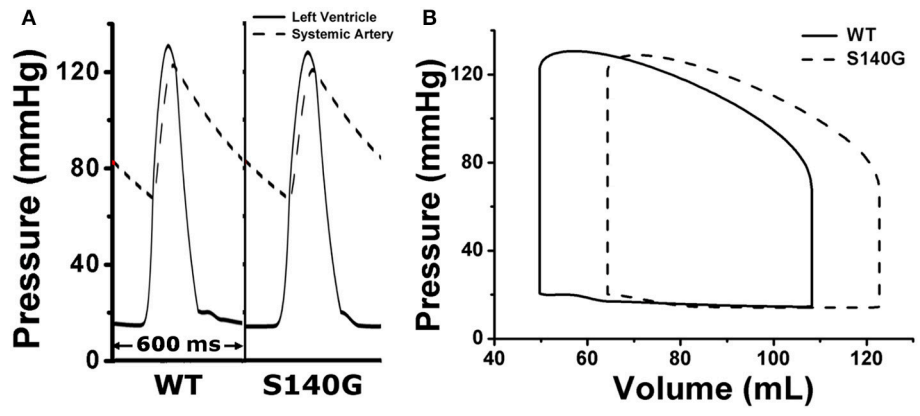

FIGURE 4 | Pressure in the left ventricle and systemic artery **(A)** and the pressure–volume (PV) loop of the left ventricle **(B)** under the WT and S140G mutation conditions.

Spikes of 5 Hz in the action potential began at 2 s under the S140G mutation condition (**Figure 5C**). whereas no action potential was evident after 3 s under the WT condition (**Figure 5B**).

Figure 6 shows the electrical wave propagation patterns under the WT and S140G mutation conditions with sustained re-entry. In epicardial cells, the estimated average APD was 106 and 240 ms under the S140G mutation and WT conditions, respectively. The estimated wavelength was 7 and 16 cm under the S140G mutation and WT conditions, respectively. Therefore, the rotation rate was significantly higher under the S140G mutation than under the WT conditions (4.9 and 3 Hz, respectively).

Figure 7 shows the dominant frequency of each node during re-entry under the WT and S140G mutation conditions. The distribution of the dominant frequency under the WT condition was 2.8 to 3.7 Hz (0.9 Hz bandwidth). However, the distribution of the dominant frequency under the S140G mutation condition was 2.0–5.3 Hz (3.3 Hz bandwidth). Therefore, the dominant frequency of all nodes was more widely distributed under the S140G mutant condition. The average dominant frequency was 3.3 and 5.0 Hz under the WT and S140G mutation conditions, respectively. The lowest dominant frequency under the WT condition was 2.875 Hz, compared to 2.0 Hz under the S140G mutation condition. The probability of alternans was lower in the lower than in the higher range of the dominant frequency under the WT and S140G mutation conditions.

Figure 8 shows the mechanical responses, which are coupled to the electrical responses (**Figure 6**). The rate of fluctuation in pressure in the LV and aorta were identical to the rotation rate of re-entry in **Figure 6**. LV peak pressure and average aortic pressure were lower under the S140G mutation condition than

TABLE 1 | Ventricular mechanical responses under the WT and S140G mutation conditions.

	Sinus rhythm response		Re-entry response	
	WT	**S140G**	**WT**	**S140G**
Stroke volume (mL)	58.6	58.3	3.2	1.1
Ejection fraction (%)	54.2	47.6		
Stroke work (mm Hg·mL)	5,768	5,685		
Contractile ATP consumption rate (s^{-1})	47.6	36.0		
Stroke work/Contractile ATP consumption (mm Hg·mL/BCL)	121.2	157.9		

WT, wild type condition; S140G, KCNQ1 S140G mutation condition.

under the WT condition (**Figure 8A**). Variation in LV volume according to the rate of fluctuation in LV pressure was observed under the WT condition, but was less clear under the S140G mutation condition (**Figure 8B**). Accordingly, the average stroke volume during the meaningful period (2.778–7.254 ms) under the WT condition was 3.2 mL, while that from 4.970 to 6.924 ms under the S140G mutation condition was 1.1 mL (**Table 1**). Here, "meaning period" indicates the period during which blood is pumped in and out of the ventricle. Accordingly, the LV pressure–volume loop under the S140G mutation condition was shifted to the right, and the area of the loop was smaller than under the WT condition (**Figure 8C**). In addition, during re-entry, the contractile ATP consumption rate was lower under the S140G mutation condition than under the WT condition (**Figure 8D**).

DISCUSSION

We evaluated the effect of the KCNQ1 S140G mutation on ventricular arrhythmogenesis and mechanical behavior during normal sinus rhythm and re-entrant arrhythmia using an image-based finite element electromechanical model. This is the first study of cardiac electrophysiology and mechanics in the presence of the KCNQ1 S140G mutation. The main findings of this study were as follows:

1) In a cellular electrophysiology simulation, the KCNQ1 S140G mutation increased the I_{Ks} current density and reduced the APD in ventricular endocardium, mid-myocardium, and epicardium cells (**Figure 2**).
2) In sinus rhythm, ventricles repolarized more rapidly under the KCNQ1 S140G mutation condition, which decreased the EDT distribution range compared to the WT condition (**Figure 3**).
3) Mutant ventricles exhibited similar stroke volumes and stroke work levels under the KCNQ1 S140G mutation and WT conditions, but consumed significantly less contractile ATP under the former condition (**Figure 4** and **Table 1**). Thus, pumping efficiency was superior under the KCNQ1 S140G mutation condition.
4) In the presence of a normal conduction velocity (70 cm/s), only mutant ventricles generated and maintained a stable re-entrant wave (**Figure 5**). This observation is consistent with the findings of Kharche et al.
5) In 3D simulation, spiral break-up occurred under both the WT and S140G mutation conditions (**Figure 6**). The conduction wavelength was reduced under the KCNQ1 S140G mutation condition. Ventricles developed a higher dominant frequency distribution range (4–5.5 Hz) (**Figure 7**) and a higher frequency of pressure fluctuation in the ventricle and aorta (**Figure 8**) under the S140G mutation condition. These results are in agreement with findings of Stiles et al. (2008).

The KCNQ1 S140G gain-of-function mutation results in more rapid opening of I_{Ks} channels. Therefore, considerable I_{Ks} current was generated at the early phase of depolarization in endocardium, mid-myocardium, and epicardium cells. This induced rapid repolarization and reduced the APD and ERP. Because APD under the KCNQ1 S140G mutation condition in 1 s BCL is markedly shorter than that under the WT condition (5-fold shorter in the endo-and epicardium and 2.5-fold shorter in the mid-myocardium), alternans occurred at a lower BCL range compared to under the WT condition (**Figure 2**). These characteristics of restitution due to S140G mutation denote loss of rate-dependent adaptation of APD, which is usually observed in chronic fibrillation patients. In addition, it suggests that ability of cell increases to support high rate electrical excitations, which can be pro-arrhythmic (Kim et al., 2002; Kharche et al., 2012).

The minimum EAT is the starting time of ventricular depolarization, and the maximum EAT is the time at which the entire ventricle is depolarized. The maximum EDT is the time required for repolarization of the entire ventricle. Accordingly, the difference between the maximum and minimum EAT, which is identical to the QRS width, was identical under the WT and S140G mutation conditions. However, the difference between the maximum EDT and minimum EAT, which is equivalent to the QT interval, was, due to the shortened APD, markedly shorter under the S140G mutation condition than under the WT condition (**Figure 3C**). These results correspond to the clinical findings of Chen et al. (2003).

The shortened APD caused by the KCNQ1 S140G mutation decreased the intracellular Ca^{2+} concentration during the depolarization period by reducing the duration of opening of voltage-dependent L-type Ca^{2+} channels. This reduces Ca^{2+} influx (the Ca^{2+}-induced Ca^{2+}-released current) from the sarcoplasmic reticulum. The released Ca^{2+} binds to troponin and forms a cross-bridge by structurally modifying tropomyosin. This leads to concentration of the ventricles. However, the reduced Ca^{2+} concentration during the depolarization period caused by the KCNQ1 S140G mutation reduced both active tension and contractile ATP consumption in the ventricles by suppressing cross-bridge formation in myofilaments (**Table 1**).

The reduced myofilament active tension decreased the ventricular contractile force, which resulted in an increase in LV volume. Accordingly, the stroke volume of the LV was slightly decreased in the S140G mutation condition. However,

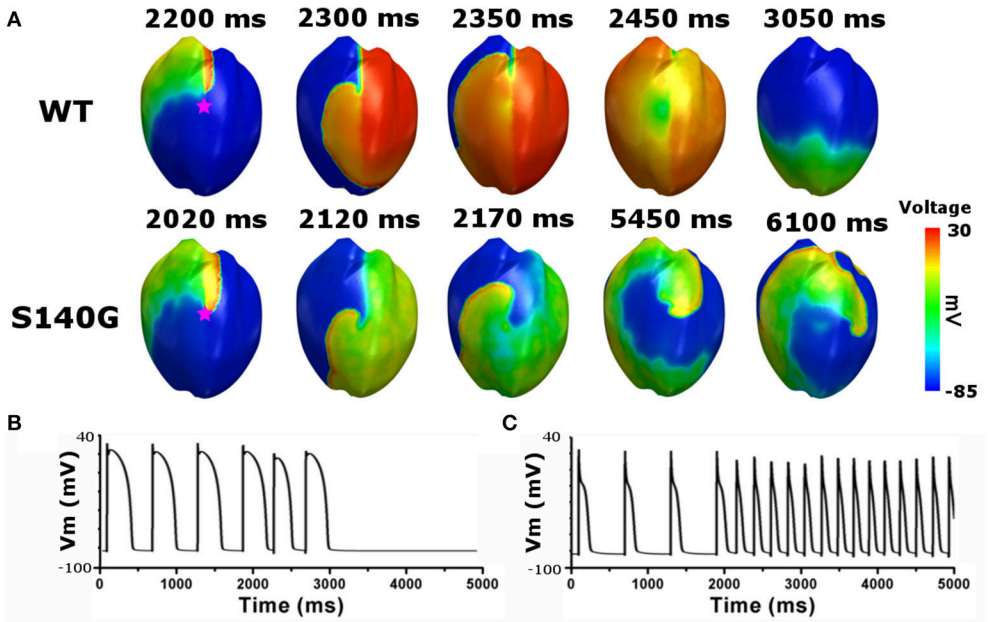

FIGURE 5 | Membrane distribution of 3D electrical re-entry generation simulation under the WT and S140G mutation conditions. Snapshots of the transmural distribution of membrane potential over time **(A)**, and AP shapes for re-entry generation under the WT **(B)**, and S140G mutation **(C)** conditions. AP shapes were obtained at the points marked by red stars.

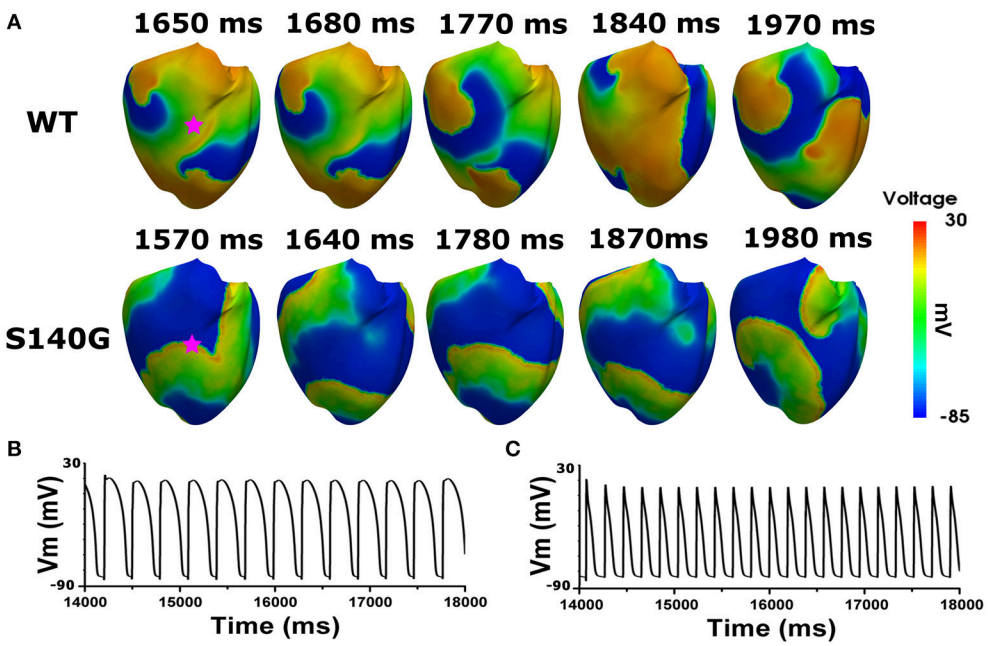

FIGURE 6 | Membrane distribution of 3D electrical simulation during sustained re-entry under the WT and S140G mutation conditions. Snapshots of the transmural distribution of membrane potential over time during re-entry **(A)**, and AP shapes during re-entry under the WT **(B)**, and S140G **(C)** conditions. AP shapes were obtained at the points marked by red stars.

there was no significant difference. That is, the effect of KCNQ1 S40G mutation on LV pressure was minor in the sinus rhythm despite significant reduction in APD under the S140G mutation condition compared to the WT condition. Therefore, the pressure–volume loop shifted to the right (**Figure 4**). As the diastolic capacity increased, the ejection fraction, i.e., the ratio

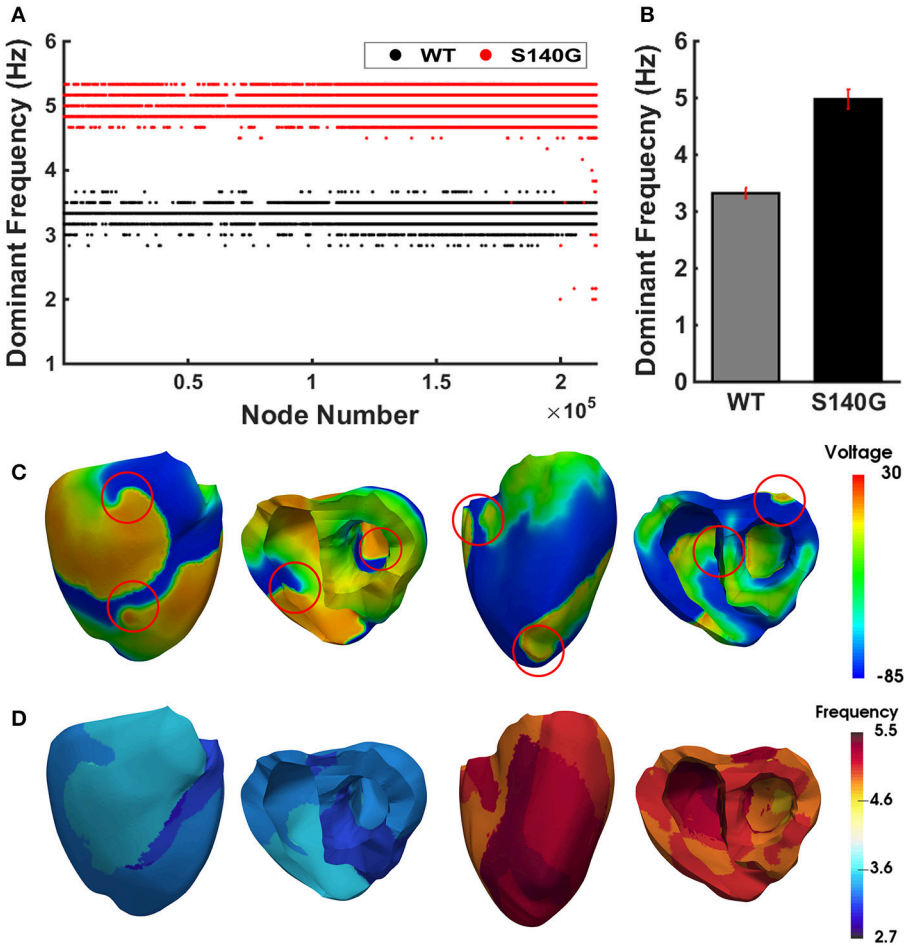

FIGURE 7 | The re-entrant dynamics response under the WT and S140G mutation conditions. Dominant frequency **(A)** of each node in the 3D ventricle model and frequency variance **(B)** under the WT and S140G mutation conditions. Contour of the transmural distribution of re-entrant dynamic wave in the 3D ventricular model under the WT and S140G mutation conditions **(C)**. Contour of the dominant frequency in each node under the WT and S140G mutation conditions **(D)**.

of stroke volume to end-diastolic volume, decreased under the S140G mutation condition as compared with the WT condition. In addition, the decreased intracellular Ca^{2+} concentration caused by the KCNQ1 S140G mutation resulted in a slight reduction in work by the left ventricle. However, the amount of ventricular work per unit contractile ATP consumption was increased under the S140G mutation condition (**Table 1**). In other words, the KCNQ1 S140G mutation increases pumping efficiency. However, the variation in sinus rhythm was neither statistically significant nor clinical important in the KCNQ1 S140G mutation compared to the WT condition. Thus, it is difficult to observe the expression of S140G mutation through specific signs in the normal sinus rhythm.

The shortened APD caused by the KCNQ1 S140G mutation resulted in a short action potential wavelength, and a short action potential wavelength reportedly creates a re-entry wave by including a large number of wavelets (Rensma et al., 1988). Similarly, the reduced cardiac action potential wavelength caused by the KCNQ1 S140G mutation resulted in initiation and maintenance of re-entrant waves in the ventricles under normal electrical conductivity conditions (**Figure 5**). Therefore, under the KCNQ1 S140G mutation condition, ventricular arrhythmogenesis is facilitated by increased tissue spatial vulnerability.

This study compared cardiac efficiency when the re-entry reached a steady state under the WT and S140G mutation conditions. Under sustained re-entry, the reduced wavelength under the S140G mutation condition increased the rotational rate of re-entry (**Figure 6**); this led to an elevated action potential firing frequency. In addition, the dominant frequency distribution was wider under the KCNQ1 S140G mutation condition compared to the WT condition (**Figure 7**). The dominant frequencies were higher and more varied in regions in which the re-entrant rotors remain for a prolonged period than in regions where they do not under both the WT and KCNQ1 S140G mutation conditions (Supplementary Figures 1, 2). These results correspond to those of a prior ventricular fibrillation study using rotor dynamics (Samie et al., 2001).

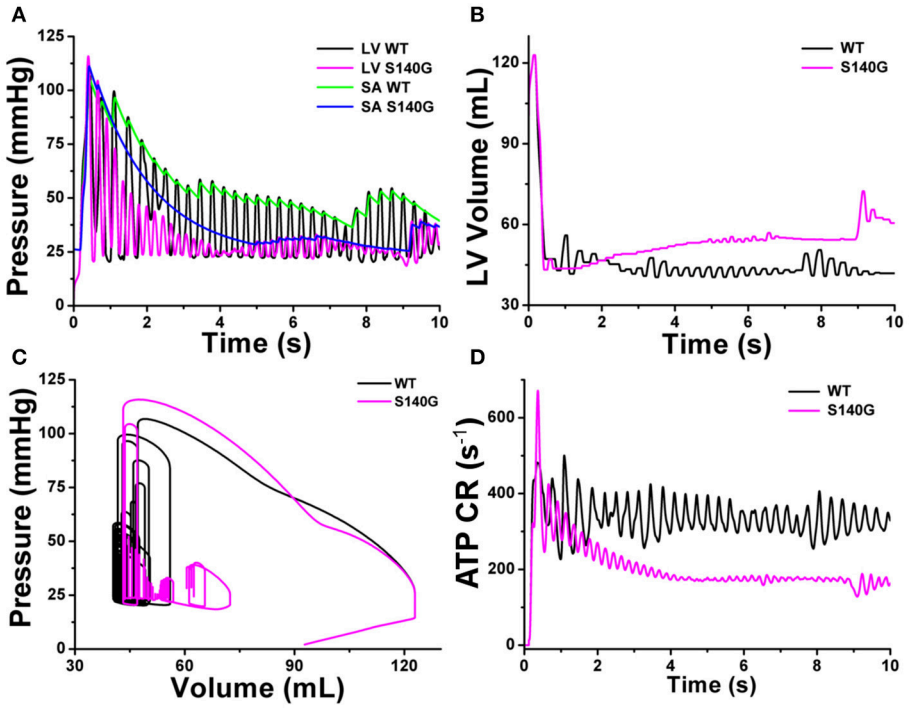

FIGURE 8 | Cardiac mechanical response of a 3D re-entrant dynamics simulation under the WT and S140G mutation conditions. Pressure in the left ventricle and aorta **(A)**, volume of the left ventricle **(B)**, PV loop **(C)**, and ATP CR (consumption rate) **(D)** under the WT and KCNQ1 S140G mutation conditions.

A high rotational rate of re-entry resulted in an increased rate of fluctuation in LV and aorta pressure under the S140G mutation condition compared to the WT condition (**Figure 8A**). In addition, during sustained re-entry, the reduced Ca^{2+} concentration caused by the S140G mutation decreased both the formation of cross-bridges in myofilaments and the contractile ATP consumption rate (**Figure 8D**) by diminishing myofilament active tension. Therefore, the LV pressure–volume loop was shifted to the right under the S140G mutation condition compared to the WT condition (**Figure 8B**). This reduced the average stroke volume according to Poiseuille's law (**Table 1** and **Figure 8C**). In the presence of re-entry waves, the reduction in the ventricular mechanical pumping function was greater under the KCNQ1 S140G mutation condition than under the WT condition.

Genetic publications have reported gain-of-function pathogenic mutations mainly in three different potassium channels such as KCNQ1, KCNH2, and KCNJ2 (Sarquella-Brugada et al., 2015). Patients with these mutations have shortened atrial and ventricular refractory periods and shortened QT intervals in ECG signal. Short QT syndrome due to these mutation, including KCNQ1 S140G mutation, is an inherited, rare, potential lethal disease characterized by ventricular repolarization alternans, predisposing to atrial fibrillation, syncope, and high incidence of sudden cardiac death. Therefore, the results of this research reflect these clinical results and can be used as a reference for clinical outcomes.

The model in this study has been used for electromechanical computational prediction in several heart failure conditions. Recently, our research group quantitatively predicted the effect of intra-aortic balloon pump function on cardiovascular responses in patients with aortic regurgitation and mitral regurgitation using this electromechanical ventricular model. As such, we successfully computed the reason for the clinical contraindication of intra-aortic balloon pump in patients with aortic regurgitation (Kim et al., 2018). In addition, it is possible to predict the effect of the G229D gene mutation on cardiac performance (Zulfa et al., 2016; Rahma et al., 2018). Therefore, our ventricular model can be used to quantitatively compute the mechanical response in several ventricular assist device conditions as well as in cardiac fibrillation conditions.

There were several limitations to this study that should be addressed. We used "one-way coupling" in which the mechanical stretch do not affect the electrophysiology, although there has been found that mechanoelectric feedback is caused by stretch-activated channels. Second, we considered only the contractile ATP consumption of the myocardium, although ATP is used in other ways, which are sarcoplasmic/endocardium reticulum ATPase (SERCA), plasma membrane Ca^{2+}-ATPase circulation. However, there limitations are not expected to greatly alter the main findings of the present study.

CONCLUSION

The KCNQ1 S140G mutation, which causes atrial fibrillation, is expressed in ventricular tissue and affects the I_{Ks} current, reducing the APD and ERP. This decreases the conduction wavelength of ventricular tissue, but it also increases cardiac

pumping efficiency slightly during sinus pacing. However, the reduced conduction wavelength caused by the S140G mutation increases spatial vulnerability and arrhythmogenesis in ventricular tissue. Furthermore, the short wavelength resulted in many rotors, high rotational rate of rotors, and wide rotor distribution with dominant frequency. Many rotors and their high rotational rates in KCNQ1 S140G mutation can induce difference in systolic timing among ventricular tissue (ventricular dyssynchrony), which can reduce ventricular pumping performance during ventricular fibrillation. In conclusion, we found that although detecting the S140G mutation is difficult in the presence of a normal sinus rhythm, the S140G mutation reduced cardiac mechanical efficiency during sustained re-entry, which increases the risk of cardiac arrest and sudden cardiac death.

AUTHOR CONTRIBUTIONS

This paper is the intellectual product of the entire team. All of the authors contributed (to varying degrees) to the analytical methods used, research concept, simulation design, simulation source code, simulation process, and writing of the manuscript.

FUNDING

This research was partially supported by the MSIT (Ministry of Science, ICT), under the ITRC (Information Technology Research Center) support program (IITP-2018-2014-0-00639) supervised by the IITP, and NRF (National Research Foundation) under basic engineering research project (2016R1D1A1B0101440) and the EDISON (NRF-2011-0020576) Programs.

SUPPLEMENTARY MATERIAL

The Supplementary Material for this article can be found online at: https://www.frontiersin.org/articles/10.3389/fphys.2018.00926/full#supplementary-material

REFERENCES

Bellocq, C., van Ginneken, A. C. G., Bezzina, C. R., Alders, M., Escande, D., Mannens, M. M., et al. (2004). Mutation in the KCNQ1 gene leading to the short QT-interval syndrome. *Circulation* 109, 2394–2397. doi: 10.1161/01.CIR.0000130409.72142.FEy

Berenfeld, O., and Jalife, J. (1998). Purkinje-muscle reentry as a mechanism of polymorphic ventricular arrhythmias in a 3-dimensional model of the ventricles. *Circ. Res.* 82, 1063–1077. doi: 10.1161/01.RES.82.10.1063

Chen, Y.-H., Xu, S.-J., Bendahhou, S. D., Wang, X.-L., Wang, Y., Xu, W.-Y., et al. (2003). KCNQ1 gain-of-function mutation in familial atrial fibrillation. *Science* 299, 251–254. doi: 10.1126/science.1077771

El Harchi, A., Zhang, H., and Hancox, J. (2010). The S140G KCNQ1 atrial fibrillation mutation affects 'I (KS)'profile during both atrial and ventricular action potentials. *J. Physiol. Pharmacol.* 61, 759–764.

Guccione, J. M., Costa, K. D., and McCulloch, A. D. (1995). Finite element stress analysis of left ventricular mechanics in the beating dog heart. *J. Biomech.* 28, 1167–1177. doi: 10.1016/0021-9290(94)00174-3

Gurev, V., Lee, T., Constantino, J., Arevalo, H., and Trayanova, N. A. (2011). Models of cardiac electromechanics based on individual hearts imaging data. *Biomech. Model. Mechanobiol.* 10, 295–306. doi: 10.1007/s10237-010-0235-5

Hancox, J. C., Kharche, S., El Harchi, A., Stott, J., Law, P., and Zhang, H. (2014). *In silico* investigation of a KCNQ1 mutation associated with familial atrial fibrillation. *J. Electrocardiol.* 47, 158–165. doi: 10.1016/j.jelectrocard.2013.12.004

Hong, K., Piper, D. R., Diaz-Valdecantos, A., Brugada, J., Oliva, A., Burashnikov, E., et al. (2005). *De novo* KCNQ1 mutation responsible for atrial fibrillation and short QT syndrome in utero. *Cardiovasc. Res.* 68, 433–440. doi: 10.1016/j.cardiores.2005.06.023

Hu, H., and Sachs, F. (1997). Stretch-activated ion channels in the heart. *J. Mol. Cell. Cardiol.* 29, 1511–1523. doi: 10.1006/jmcc.1997.0392

Kerckhoffs, R. C. P., Neal, M. L., Gu, Q., Bassingthwaighte, J. B., Omens, J. H., and McCulloch, A. D. (2007). Coupling of a 3D finite element model of cardiac ventricular mechanics to lumped systems models of the systemic and pulmonic circulation. *Ann. Biomed. Eng.* 35, 1–18. doi: 10.1007/s10439-006-9212-7

Kharche, S., Adeniran, I., Stott, J., Law, P., Boyett, M. R., Hancox, J. C., et al. (2012). Pro-arrhythmogenic effects of the S140G KCNQ1 mutation in human atrial fibrillation - insights from modelling. *J. Physiol.* 590, 4501–4514. doi: 10.1113/jphysiol.2012.229146

Kim, B.-S., Kim, Y.-H., Hwang, G.-S., Pak, H.-N., Lee, S. C., Shim, W. J., et al. (2002). Action potential duration restitution kinetics in human atrial fibrillation. *J. Am. Coll. Cardiol.* 39, 1329–1336. doi: 10.1016/S0735-1097(02)01760-6

Kim, C.-H., Song, K.-S., Trayanova, N. A., and Lim, K. M. (2018). Computational prediction of the effects of the intra-aortic balloon pump on heart failure with valvular regurgitation using a 3D cardiac electromechanical model. *Med. Biol. Eng. Comput.* 56, 853–863. doi: 10.1007/s11517-017-1731-x

Lim, K. M., Constantino, J., Gurev, V., Zhu, R., Shim, E. B., and Trayanova, N. A. (2012). Comparison of the effects of continuous and pulsatile left ventricular-assist devices on ventricular unloading using a cardiac electromechanics model. *J. Physiol. Sci.* 62, 11–19. doi: 10.1007/s12576-011-0180-9

Lim, K. M., Hong, S.-B., Lee, B. K., Shim, E. B., and Trayanova, N. (2015). Computational analysis of the effect of valvular regurgitation on ventricular mechanics using a 3D electromechanics model. *J. Physiol. Sci.* 65, 159–164. doi: 10.1007/s12576-014-0353-4

Lim, K. M., Lee, J. S., Gyeong, M.-S., Choi, J.-S., Choi, S. W., and Shim, E. B. (2013). Computational quantification of the cardiac energy consumption during intra-aortic balloon pumping using a cardiac electromechanics model. *J. Korean Med. Sci.* 28, 93–99. doi: 10.3346/jkms.2013.28.1.93

Nattel, S. (2002). New ideas about atrial fibrillation 50 years on. *Nature* 415, 219–226. doi: 10.1038/415219a

Rahma, Y. A., Febrian, S., Aroli, M., Jeong, H. H., Wook, C. S., Natalia, T., et al. (2018). Effect of KCNQ1 G229D mutation on cardiac pumping efficacy and reentrant dynamics in ventricles: computational study. *Int. J. Num. Methods Biomed. Eng.* 34:e2970. doi: 10.1002/cnm.2970

Rensma, P. L., Allessie, M. A., Lammers, W. J., Bonke, F. I., and Schalij, M. J. (1988). Length of excitation wave and susceptibility to reentrant atrial arrhythmias in normal conscious dogs. *Circ. Res.* 62, 395–410. doi: 10.1161/01.RES.62.2.395

Rice, J. J., Wang, F., Bers, D. M., and de Tombe, P. P. (2008). Approximate model of cooperative activation and crossbridge cycling in cardiac muscle using ordinary differential equations. *Biophys. J.* 95, 2368–2390. doi: 10.1529/biophysj.107.119487

Samie, F. H., Berenfeld, O., Anumonwo, J., Mironov, S. F., Udassi, S., Beaumont, J., et al. (2001). Rectification of the background potassium current: a determinant of rotor dynamics in ventricular fibrillation. *Circ. Res.* 89, 1216–1223.

Sarquella-Brugada, G., Campuzano, O., Iglesias, A., Grueso, J., Bradley, D. J., Kerst, G., et al. (2015). Short QT and atrial fibrillation: A KCNQ1 mutation–specific disease. Late follow-up in three unrelated children. *Heartrhythm Case Rep.* 1, 193–197. doi: 10.1016/j.hrcr.2015.02.005

Stiles, M. K., Brooks, A. G., John, B., Wilson, L., Kuklik, P., Dimitri, H., et al. (2008). The effect of electrogram duration on quantification of complex fractionated

atrial electrograms and dominant frequency. *J. Cardiovasc. Electrophysiol.* 19, 252–258. doi: 10.1111/j.1540-8167.2007.01034.x

Ten Tusscher, K. H. W. J., and Panfilov, A. V. (2006). Alternans and spiral breakup in a human ventricular tissue model. *Am. J. Physiol. Heart Circ. Physiol.* 291, H1088–H1100. doi: 10.1152/ajpheart.00109.2006

Ten Tusscher, K., Noble, D., Noble, P., and Panfilov, A. (2004). A model for human ventricular tissue. *Am. J. Physiol. Heart Circ. Physiol.* 286, H1573–H1589. doi: 10.1152/ajpheart.00794.2003

Usyk, T. P., LeGrice, I. J., and McCulloch, A. D. (2002). Computational model of three-dimensional cardiac electromechanics. *Comput. Visual. Sci.* 4, 249–257. doi: 10.1007/s00791-002-0081-9

Yang, Y., Liu, Y., Dong, X., Kuang, Y., Lin, J., Su, X., et al. (2007). Human KCNQ1 S140G mutation is associated with atrioventricular blocks. *Heart Rhythm* 4, 611–618. doi: 10.1016/j.hrthm.2007.01.029

Zulfa, I., Shim, E. B., Song, K.-S., and Lim, K. M. (2016). Computational simulations of the effects of the G229D KCNQ1 mutation on human atrial fibrillation. *J. Physiol. Sci.* 66, 407–415. doi: 10.1007/s12576-016-0438-3

Conflict of Interest Statement: The authors declare that the research was conducted in the absence of any commercial or financial relationships that could be construed as a potential conflict of interest.

Copyright © 2018 Jeong and Lim. This is an open-access article distributed under the terms of the Creative Commons Attribution License (CC BY). The use, distribution or reproduction in other forums is permitted, provided the original author(s) and the copyright owner(s) are credited and that the original publication in this journal is cited, in accordance with accepted academic practice. No use, distribution or reproduction is permitted which does not comply with these terms.

frontiers in Physiology

ORIGINAL RESEARCH
published: 10 September 2018
doi: 10.3389/fphys.2018.01252

Potts Shunt to Be Preferred Above Atrial Septostomy in Pediatric Pulmonary Arterial Hypertension Patients: A Modeling Study

Tammo Delhaas[1], Yvette Koeken[1], Heiner Latus[2], Christian Apitz[3] and Dietmar Schranz[4]*

[1] Department of Biomedical Engineering, CARIM School for Cardiovascular Diseases, Maastricht University, Maastricht, Netherlands, [2] Department of Paediatric Cardiology and Congenital Heart Defects, German Heart Centre, Munich, Germany, [3] Division of Pediatric Cardiology, University Children's Hospital Ulm, Ulm, Germany, [4] Pediatric Heart Center, Justus Liebig University Giessen, Giessen, Germany

Aims: To quantitatively evaluate the basic pathophysiological process involved in the creation of Eisenmenger syndrome in pediatric pulmonary arterial hypertension (PAH) patients by either atrial septostomy (AS) or Potts shunt (PS) as well as to predict the effects of AS or PS in future PAH patients.

Methods: The multi-scale lumped parameter CircAdapt model of the cardiovascular system was used to investigate the effects of AS and PS on cardiovascular hemodynamics and mechanics, as well as on oxygen saturation in moderate to severe PAH. The reference simulation, with cardiac output set to 2.1 l/min and mean systemic pressure to 61 mmHg, was used to create a compensated moderate PAH simulation with mPAP 50 mmHg. Thereupon we created a range of decompensated PAH simulations in which mPAP was stepwise increased from 50 to 80 mmHg. Then we simulated for each level of mPAP the acute effects of either PS or AS with connection diameters ranging between 0–16 mm.

Results: For any mPAP level, the effect on shunt flow size is much larger for the PS than for AS. Whereas right ventricular pump work in PS is mainly dependent on mPAP, in AS it depends on both mPAP and the size of the defect. The effects on total cardiac pump work were similar for PS and AS. As expected, PS resulted in a drastic decrease of lower body oxygen saturation, whereas in AS both the upper and lower body oxygen saturation decreased, though not as drastically as in PS.

Conclusion: Our simulations support the opinion that a PS can transfer suprasystemic PAH to an Eisenmenger physiology associated with a right-to-left shunt at the arterial level. Contrary to the current opinion that PS in PAH will decompress and unload the right ventricle, we show that while a PS does lead to a decrease in mPAP toward mean systemic arterial pressure, it does not unload the right ventricle because it mainly diverts flow from the pulmonary arterial system toward the lower body systemic arteries.

Keywords: computer modeling, pulmonary arterial hypertension, Potts shunt, atrial septostomy, exercise, pump work, shunt flow, oxygen saturation

OPEN ACCESS

Edited by:
Chae Hun Leem,
University of Ulsan College of Medicine, South Korea

Reviewed by:
Seiryo Sugiura,
UT-Heart Inc., Japan
Ki Moo Lim,
Kumoh National Institute of Technology, South Korea

****Correspondence:***
Tammo Delhaas
tammo.delhaas@maastrichtuniversity.nl

Specialty section:
This article was submitted to Computational Physiology and Medicine, a section of the journal Frontiers in Physiology

Received: *31 May 2018*
Accepted: *20 August 2018*
Published: *10 September 2018*

Citation:
Delhaas T, Koeken Y, Latus H, Apitz C and Schranz D (2018) Potts Shunt to Be Preferred Above Atrial Septostomy in Pediatric Pulmonary Arterial Hypertension Patients: A Modeling Study. Front. Physiol. 9:1252. doi: 10.3389/fphys.2018.01252

INTRODUCTION

Idiopathic pulmonary arterial hypertension (iPAH) is a rare, progressive, and ultimately devastating disease if left untreated. The disease will lead to a gradual increase in right ventricular (RV) pressure, right heart failure, functional incapacity, and death. Though recent advances in medical treatment have improved survival and quality of life in both adult and children, the mortality rate is still high. Currently freedom from death or transplantation in pediatric iPAH patients is less than 60% at 5 years (Moledina et al., 2010), highlighting the need for novel therapeutic approaches.

Life expectancy of patients with Eisenmenger syndrome, representing the end stage of an untreated left-to-right shunt in which pulmonary arterial hypertension (PAH) prohibits intracardiac repair, is significantly superior to that of iPAH patients. The median survival in Eisenmenger syndrome is estimated between 40 and 60 years, depending on the underlying cardiac defect (Hoffman, 2009). Converting cardiovascular features of iPAH patients to features typical of Eisenmenger syndrome by means of atrial septostomy (AS) is therefore an additional strategy in both adult and pediatric iPAH patients with recurrent syncope or significant right heart failure refractory to medical treatment (Barst, 2000; Micheletti et al., 2006). The created atrial septal defect (ASD) permits a right-to-left shunting that results in RV unloading and maintenance or increase of systemic flow despite severe pulmonary disease. Though AS improves symptoms and quality of life in adults and children with severe iPAH, the sizing of the defect is critical since too much right-to-left shunt at the atrial level could be immediately life threatening because of insufficient pulmonary blood flow as well as severe desaturation in the brain and in the coronary circulation, and too less shunting may require repeated procedures because of spontaneous closure of the defect (Micheletti et al., 2006). Another approach to convert iPAH patients to Eisenmenger physiology arose a decade ago and calls for the creation of an anastomosis between the descending aorta and the left pulmonary artery (Blanc et al., 2004). This so-called Potts shunt (PS) has the advantages that it does not provoke oxygen desaturation in the upper part of the body and that it directly limits pulmonary pressures to isosystemic values. The sparse literature on surgical creation of PS in pediatric iPAH patients report a success rate in the order of 75% (Blanc et al., 2004; Baruteau et al., 2012, 2015; Petersen et al., 2013). Transcatheter creation of PS by stenting a patent ductus arteriosus (PDA) in pediatric iPAH patients had a comparable clinical success rate outcome (Boudjemline et al., 2013; Esch et al., 2013; Latus et al., 2014; Boudjemline et al., 2017).

The very sparse literature on the creation of Eisenmenger syndrome in pediatric iPAH patients by either AS or PS does not quantitatively evaluate the basic pathophysiological process involved, nor can it be used to predict the effects of AS or PS in future iPAH patients. We therefore applied CircAdapt, our lumped-parameter mathematical model of the heart and circulation, to quantitatively evaluate the acute hemodynamic effects of AS and PS in pulmonary hypertension. Simulations were performed for shunt sizes with diameters ranging from 0 to 16 mm, while using the average patient as reported by Baruteau et al. (2012) as reference, albeit that mean pulmonary arterial pressures (mPAPs) ranged from 3/4 to 4/3 mean systemic arterial pressure.

MATERIALS AND METHODS

Lumped Parameter Modeling Approach

We applied the multi-scale lumped parameter CircAdapt model of the cardiovascular system to investigate the effects of AS and PS on cardiovascular hemodynamics and mechanics, as well as on oxygen saturation in pulmonary hypertension with mPAPs ranging from 3/4 to 4/3 mean systemic arterial pressure. The CircAdapt hemodynamic model of the heart and circulation (Arts et al., 2005; Lumens et al., 2009; Koeken et al., 2012; Walmsley et al., 2015) allows simulation of beat-to-beat mechanics and hemodynamics of the human cardiovascular system for both research and educational purposes[1]. CircAdapt is built on physiological and physical principles, described in brief below; more detailed theoretical descriptions of the CircAdapt model have been published previously (Arts et al., 2005, 2011, 2012; Lumens et al., 2009; Koeken et al., 2012; Walmsley et al., 2015). The model consists of modules for myofibre stress and strain, atrial and ventricular pressure, flow across cardiac valves, blood pressure within major veins and arteries, and systemic and pulmonary resistances. The right and left ventricles are mechanically coupled through the inter-ventricular septum (Lumens et al., 2009). Mean aortic pressure and cardiac output can be controlled through changes to systemic peripheral resistance and total blood volume, mimicking homeostatic control mechanisms. CircAdapt uses physiological structural remodeling rules in response to mechano-sensed signals to produce a realistic geometry of the heart and circulation (Arts et al., 2012). The dynamic behavior of the CircAdapt model allows blood to move in both directions through all cavities, shunts, and vessels during the complete cardiac cycle. Mixing of flows with different oxygen concentrations and saturations is described by differential equations that take in- and outlet blood flow sizes and oxygen concentrations into account (Koeken et al., 2012). Oxygen uptake in the lungs is assumed to render an oxygen saturation of 98% in the pulmonary veins, whereas oxygen consumption for the body as a whole can be prescribed and for the various organs can be made dependent on their size and/or work.

Modeling principles key to this simulation study include that time-depending pulmonary circulating blood flow is defined a function of a reference flow and a (normalized) pulmonary pressure drop:

$$q_{pulm}(t) = \frac{q_{pulm,ref}}{\Delta p_{pulm,ref}} \Delta p_{pulm}(t),$$

with $q_{pulm,ref}$ and q_{pulm} the (reference) pulmonary circulating flow and $\Delta p_{pulm,ref}$, and Δp_{pulm} the (reference) pulmonary pressure drop. Based on this relation, mPAP can be modulated by adjusting the reference pulmonary pressure drop ($\Delta p_{pulm,ref}$).

[1] www.circadapt.org

To create PAH with mPAPs ranging from 50 to 80 mmHG, $\Delta p_{pulm,ref}$ was varied between 44.3 and 77.5 mmHg.

Furthermore, the CircAdapt's cardiac valve module is utilized for creation of an ASD or PS. Briefly, for an ASD a valve element is incorporated connecting the left- and right atria, whereas for a PS, a valve element is incorporated connecting the pulmonary arteries to the descending aorta. In contrast to cardiac valves, however, the valves forming either a ASD or an PS, are characterized by having a constant diameter over time.

Simulation Protocol

Specific input parameters for our modeling study were derived from data presented in the paper by Baruteau et al. (2012) on the short and long term effects of a PS in eight children diagnosed with iPAH. For the reference simulation we set systemic blood flow (2.1 l/min) and mean arterial pressure (61 mmHg) to the average values of the iPAH children studied, whereas mPAP was set to 15 mmHg. Thereafter, cardiac wall sizes and blood vessel diameters were adapted to the mechanical load of the tissues during exercise with a threefold increase in cardiac output and a twofold increase in heart rate. Thereafter we simulated moderate PAH with an mPAP of 50 mmHg in rest with adaptation of heart and vessels to exercise with a twofold increase in cardiac output and a 1.8-fold increase in heart rate. Using this compensated moderate PAH simulation as a starting point, and keeping cardiac output at 2.1 l/min, we created two matrices of simulations. First we created a range of decompensated PAH simulations by stepwise increasing pulmonary resistance in absence of structural cardiovascular adaptation. This resulted in a range of simulations with 5 mmHg increases in mPAP from 50 till 80 mmHg, the mPAP-level of the average "Baruteau-child." Then we simulated for each level of mPAP the acute effects of either an ASD or a PS which diameter ranged between 0–16 mm. Our simulation protocol finally yielded two sets of 119 (=7 × 17) simulations.

RESULTS

Pressure-volume relations (pV-loops) for the left atrium (LA) and ventricle (LV) as well as the right atrium (RA) and ventricle (RV) are shown in the left panels of **Figure 1** for the reference child (**Figure 1A**), child with compensated moderate PAH (**Figure 1B**), the average "Baruteau-child" with decompensated PAH and a suprasystemic mPAP of 80 mmHg (**Figure 1C**), as well as for the average "Baruteau-child" with either a 7 mm PS (**Figure 1D**) or a 7 mm ASD (**Figure 1E**). With increasing mPAP, RV pV-loops shifted to the right, most prominently in the "Baruteau-child" with decompensated PAH. The concomitant interventricular septal bowing to the left caused a decrease in left ventricular (LV) volumes, leading to a leftward shift of the LV pV-loops (**Figures 1A–C**). After creation of a 7 mm PS (**Figure 1D**), the RV pV-loop shows an increased stroke volume but lower RV systolic pressure. This results in approximately the same pV-loop area as before the PS, indicating that RV workload is hardly affected. The LV pV-loop shows an increased systolic pressure and a slightly smaller stroke volume, albeit that the loop is shifted to the right. Also LV pV-loop area is approximately the same as before the PS. Creation of a 7 mm ASD shunt (**Figure 1E**) resulted in a right-left shunt at atrial level with concomitantly decreased RV and increased LV stroke volume, whereas systolic pressures were hardly affected at both sides. Consequently, RV workload decreased slightly whereas LV workload increased. The right panels of **Figure 1** show time curves of pressures and flows for the average "Baruteau-child" with mPAP of 80 mmHg (**Figures 1F–H**) as well as of right heart pressures for the "Baruteau-child" with either a 7 mm PS (**Figure 1I**) or a 7 mm ASD (**Figure 1J**). The latter panels clearly show that whereas a PS results in lowering of mPAP toward mean systemic arterial pressure, an ASD barely influences right heart pressures.

Figure 2 shows heatmaps for the ratio of pulmonary to systemic flow (Qp/Qs), RV-, LV-, and total pump work, as well as lower body oxygen saturation under various levels of mPAP before shunt creation and with shunt sizes ranging from 0 to 16 mm. The left panels show the immediate effect of PSs, while the results for AS are displayed in the right panels. For PS sizes up to 7 mm, the size and the direction of the shunt flow depend both on mPAP and shunt size. For shunt diameters over 7 mm, Qp/Qs is only proportional to the extent of pulmonary hypertension. AS shows qualitatively the same relation between defect size, mPAP and Qp/Qs, though changes in Qp/Qs are less. In the absence of shunts, RV pump work increased with increasing mPAP. The effects of shunt size on RV pump work are not similar for PSs and AS. Whereas RV pump work was barely influenced by PS sizes (only PSs with diameters of 4 to 5 mm resulted in a small increase in RV pump work), increasing AS defect sizes clearly resulted in a proportional decrease in RV pump work. LV pump work was barely influenced by small AS defects and small PS sizes. As of shunt sizes of 3 mm, PS and AS had opposite effects on LV pump work. In the presence of PS over 3 mm diameter in size, LV pump work decreased with suprasystemic mPAP and increased when mPAP was below mean systemic pressure. In the presence of AS defect sizes over 3 mm diameter, LV pump work increased with suprasystemic mPAP and decreased when mPAP was below mean systemic pressure. Heat maps for total pump work showed that mPAP strongly determines total pump work. For each level of mPAP, PSs up to 5 mm diameter barely influenced total pump work, whereas total pump work increased with roughly 2% when PS sizes increased from 5 to 16 mm diameter. AS defect sizes were inversely related to total pump work at each level of mPAP, with total pump work on average 2% lower when AS defect size increased to 16 mm. Whereas PS did not influence upper body arterial oxygen saturation (results not shown), it induced a decrease in lower body arterial oxygen saturation, especially for high mPAP and small shunt diameters. AS led to a decrease in both upper and lower body arterial oxygen saturation that was proportional to both mPAP and defect size.

DISCUSSION

The CircAdapt model of the human heart and circulation has been used to evaluate the effect of PS and AS on both hemodynamics and oxygen saturation for the average PAH patient that underwent a PS in the original report by

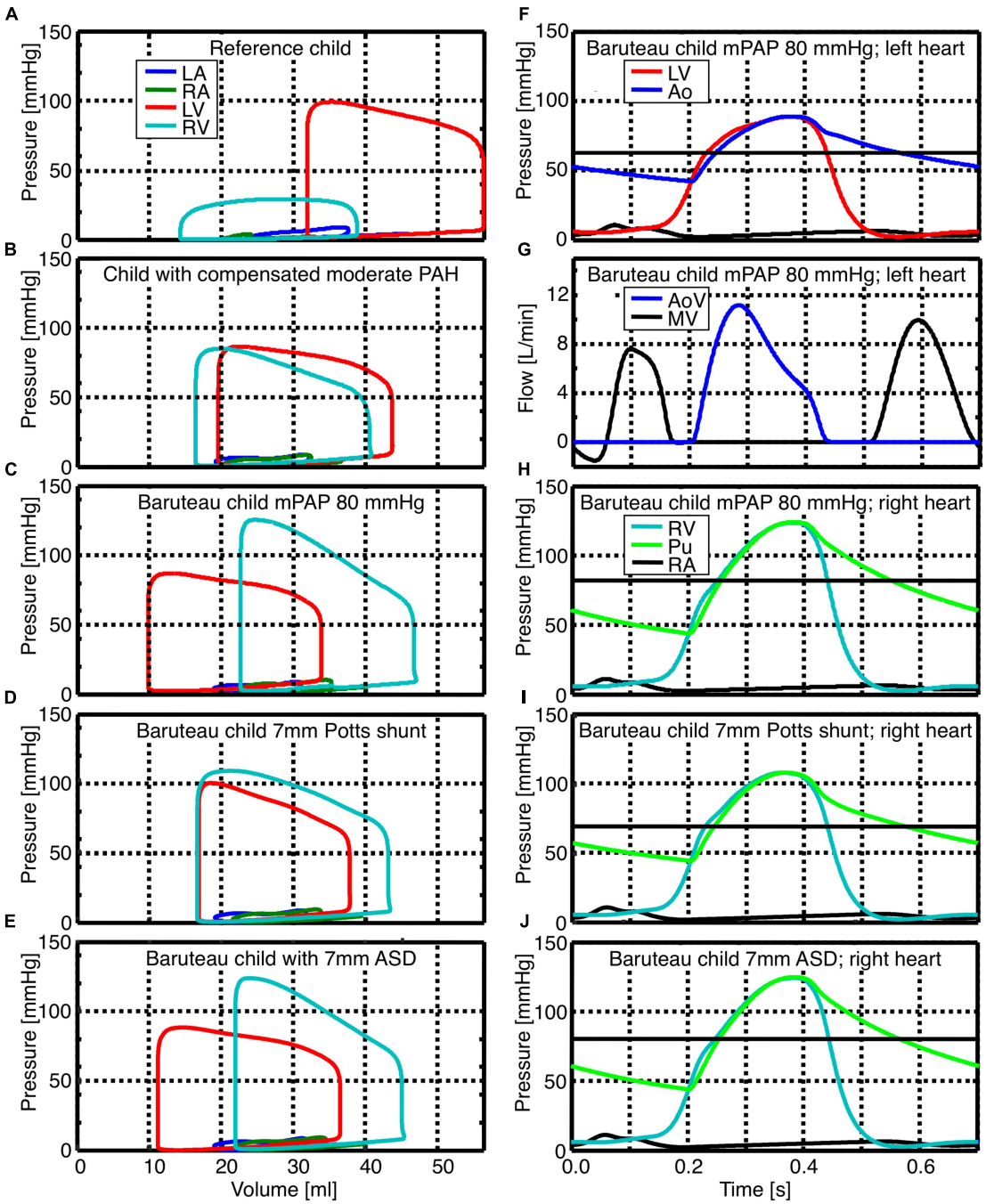

FIGURE 1 | Simulated pressure-volume loops as well as pressure and flow curves for reference child (panel **A**), child with compensated moderated pulmonary hypertension (panel **B**), the average "Baruteau child" with suprasystemic mean pulmonary artery pressure of 80 mmHg (panels **C**, **F**, **G**, and **H**), as well as the "Baruteau-child" with either a 7 mm Potts shunt (panels **D** and **I**) or a 7 mm ASD (panels **E** and **J**). Horizontal solid black line in panels with pressure curves indicates the mean systemic (panel **F**) or mean pulmonary arterial pressure (panels **H**, **I**, and **J**). Abbreviations: Ao, aorta; AoV, aortic valve; LA, left atrium; LV, left ventricle; mPAP, mean pulmonary arterial pressure; PAH, pulmonary arterial hypertension; Pu, Pulmonary artery; RA, right atrium; RV, right ventricle.

Baruteau et al. (2012). We show that for any mPAP level, the effect on shunt flow size is much larger for the PS than for the created ASD. Whereas RV pump work in PS is mainly dependent on mPAP, in AS it depends on both mPAP and the size of the created ASD. Though the effect on total cardiac pump work were similar for PS and AS, the effect on upper and lower body oxygen saturation were not. In PS, upper body oxygen saturations were not effected and remained at pulmonary venous levels, whereas lower body oxygen saturation drastically decreased. In AS, the effect of shunt size on decrease of oxygen saturation were

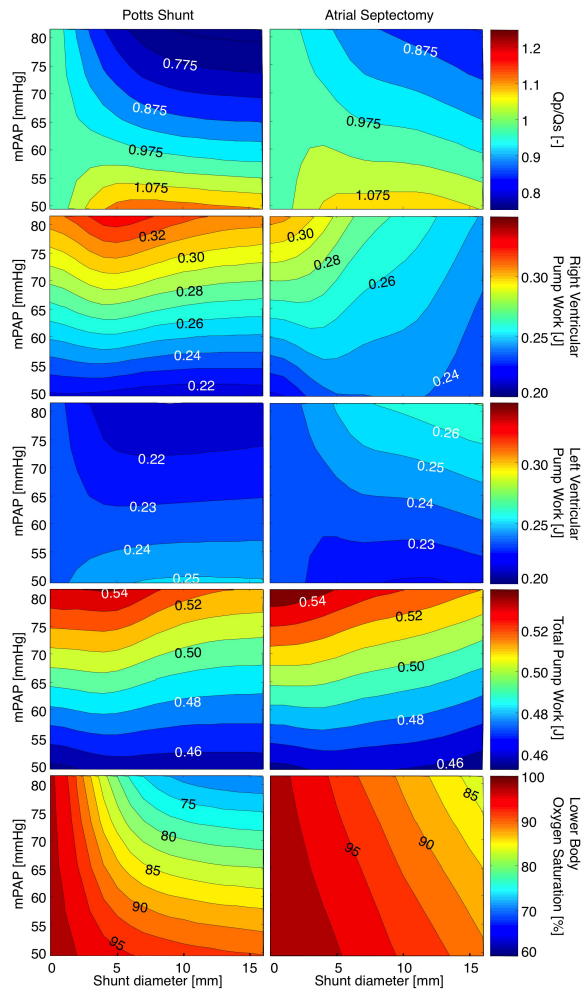

FIGURE 2 | Heatmaps for the ratio of pulmonary to systemic flow (Qp/Qs), right ventricular-, left ventricular-, and total pump work, as well as lower body oxygen saturation under various levels of mean pulmonary arterial pressure (mPAP) with shunt diameters ranging from 0 to 16 mm. The left panels show the immediate effects of Potts shunts, while the results for atrial septostomy are displayed in the right panels.

similar for the upper and lower body, though not as drastically as in PS.

Because the size of the PS is thought to be critical for the extent of right-to-left or left-to-right shunt, measures have been taken in clinical practice to limit the size of the created connection. Surgically created PS sizes are aimed for to be in the order of the diameter of the descending aorta (Baruteau et al., 2012, 2015), which is approximately 10 mm for children with a body surface area of 0.75 m^2 (Kaiser et al., 2008). If the PS is created by stenting a PDA, the diameter of the ductal stent connection is gradually increased by sequential balloon inflations with the aim of equalizing the PA and aortic systolic pressures, maintaining pulmonary blood flow and limiting the desaturation of the inferior limbs (Baruteau et al., 2015). In our simulations, however, we didn't see hardly any change in Qp/Qs above PS diameters of 7 mm. From 0 to 7 mm, shunt flow was positively related to the shunt diameter as well as to the difference between mPAP and sPAP. Therefore it seems safe to aim immediately for a PS size in the order of the descending aorta diameter, be it surgically created or by means of stenting the PDA.

In patients with (infra)systemic level of pulmonary artery pressures, creation of a Potts anastomosis bears the risk of turning the interarterial right-to-left shunt into a left-to-right shunt, that on it's turn presumably can lead to a volume overload of the pulmonary circulation, increased pulmonary artery pressures and a steal phenomenon from systemic to pulmonary circulations (Baruteau et al., 2015). We show that with infrasystemic mPAP, Qp/Qs rises in the acute situation, but that neither the RV nor the LV have additional load. However, because Qp rises on the expense of Qs, patients with infrasystemic PAH bears the risk of developing syncope upon creation of a PS. We therefore advocate the use of unidirectional valved Potts anastomosis, of which promising results have been shown in an animal model of PPH (Bui et al., 2011) as well as in the first human case ever (Baruteau et al., 2015).

In our simulations, the diversion of pump work from the RV to the LV was more pronounced in AS than in PS. However, since AS also results in coronary artery oxygen desaturation, the cardiac exercise capacity of PS will be well above the one in AS. In PAH patients with PS, the needed increases in systemic flow with exercise will not be on the expense of diminished oxygen transport to the myocardium. In a follow-up study on 24 PAH patients with PS, none of them had syncope or right heart failure (Baruteau et al., 2015). Hence, a permanent post-cardiac right-to-left shunt is to be preferred above an intra-cardiac one.

Modeling studies can provide valuable mechanistic insights in cardiovascular function dynamics before and after PS or AS in PAH patients. In a previous modeling study we provided evidence that AS might only be beneficial to patients with severe PH and that this benefit originates from an increase of LV preload and not from an increase in oxygen delivery to the tissue, as stated in previous studies (Kerstein et al., 1995; Sandoval et al., 1998; Rothman et al., 1999; Micheletti et al., 2006; Kurzyna et al., 2007; Galie et al., 2009; Zierer et al., 2009). In the current study, our simulations indicate that a PS in PAH will lead to a decrease in mPAP toward mean systemic arterial pressure, but that the PS does not unload the RV because it mainly diverts flow from the pulmonary arterial system toward the lower body systemic arteries. Whereas the current study assessed the effects of shunt type and size in an average child with PAH, we foresee an inverse modeling approach, in which the model is personalized by fitting simulated hemodynamics to a set of patient-specific data, to predict outcome of intended interventions, albeit that detailed cardiac morphology and flow dynamics, which could exert significant influences on the outcome, are not taken into consideration in our modeling approach.

CONCLUSION

Our simulations support the opinion that a PS can transfer suprasystemic PAH to an Eisenmenger physiology associated with a right-to-left shunt at the arterial level. Contrary

to the current opinion that PS in PAH will decompress and unload the right ventricle, we show that while a PS does lead to a decrease in mPAP toward mean systemic arterial pressure, it does not unload the right ventricle because it mainly diverts flow from the pulmonary arterial system toward the lower body systemic arteries.

DATA AVAILABILITY STATEMENT

The simulation software used for this study can be found at www.circadapt.org.

AUTHOR CONTRIBUTIONS

TD, CA, and DS conceived and designed the study. TD and YK performed the simulations and created the figures. TD wrote the first draft of the manuscript. All authors contributed to manuscript revision, read, and approved the submitted version.

FUNDING

This work was supported by the Dutch Heart Foundation Grant 2007B203.

REFERENCES

Arts, T., Delhaas, T., Bovendeerd, P., Verbeek, X., and Prinzen, F. W. (2005). Adaptation to mechanical load determines shape and properties of heart and circulation: the CircAdapt model. *Am. J. Physiol. Heart Circ. Physiol.* 288, H1943–H1954. doi: 10.1152/ajpheart.00444.2004

Arts, T., Lumens, J., Kroon, W., and Delhaas, T. (2012). Control of whole heart geometry by intramyocardial mechano-feedback: a model study. *PLoS Comput. Biol.* 8:e1002369. doi: 10.1371/journal.pcbi.1002369

Arts, T., Reesink, K., Kroon, W., and Delhaas, T. (2011). Simulation of adaptation of blood vessel geometry to flow and pressure: implications for arterio-venous impedance. *Mech. Res. Commun.* 42, 15–21. doi: 10.1016/j.mechrescom.2011.10.005

Barst, R. J. (2000). Role of atrial septostomy in the treatment of pulmonary vascular disease. *Thorax* 55, 95–96. doi: 10.1136/thorax.55.2.95

Baruteau, A. E., Belli, E., Boudjemline, Y., Laux, D., Lévy, M., Simonneau, G., et al. (2015). Palliative Potts shunt for the treatment of children with drug-refractory pulmonary arterial hypertension: updated data from the first 24 patients. *Eur. J. Cardiothorac. Surg.* 47, e105–e110. doi: 10.1093/ejcts/ezu445

Baruteau, A. E., Serraf, A., Lévy, M., Petit, J., Bonnet, D., Jais, X., et al. (2012). Potts shunt in children with idiopathic pulmonary arterial hypertension: long-term results. *Ann. Thorac. Surg.* 94, 817–824. doi: 10.1016/j.athoracsur.2012.03.099

Blanc, J., Vouhe, P., and Bonnet, D. (2004). Potts shunt in patients with pulmonary hypertension. *N. Engl. J. Med.* 350:623. doi: 10.1056/NEJM200402053500623

Boudjemline, Y., Patel, M., Malekzadeh-Milani, S., Szezepanski, I., Levy, M., and Bonnet, D. (2013). Patent ductus arteriosus stenting (transcatheter Potts shunt) for palliation of suprasystemic pulmonary arterial hypertension: a case series. *Circ. Cardiovasc. Interv.* 6, e18–e20. doi: 10.1161/CIRCINTERVENTIONS.112.000091

Boudjemline, Y., Sizarov, A., Malekzadeh-Milani, S., Mirabile, C., Lenoir, M., Khraiche, D., et al. (2017). Safety and feasibility of the transcatheter approach to create a reverse Potts shunt in children with idiopathic pulmonary arterial hypertension. *Can. J. Cardiol.* 33, 1188–1196. doi: 10.1016/j.cjca.2017.06.004

Bui, M. T., Grollmus, O., Ly, M., Mandache, A., Fadel, E., Decante, B., et al. (2011). Surgical palliation of primary pulmonary arterial hypertension by a unidirectional valved Potts anastomosis in an animal model. *J. Thorac. Cardiovasc. Surg.* 142, 1223–1228. doi: 10.1016/j.jtcvs.2010.10.060

Esch, J. J., Shah, P. B., Cockrill, B. A., Farber, H. W., Landzberg, M. J., Mehra, M. R., et al. (2013). Transcatheter Potts shunt creation in patients with severe pulmonary arterial hypertension: initial clinical experience. *J. Heart Lung Transplant.* 32, 381–387. doi: 10.1016/j.healun.2013.01.1049

Galie, N., Hoeper, M. M., Humbert, M., Torbicki, A., Vachiery, J. L., Barbera, J. A., et al. (2009). Guidelines for the diagnosis and treatment of pulmonary hypertension: the Task Force for the Diagnosis and Treatment of Pulmonary Hypertension of the European Society of Cardiology (ESC) and the European Respiratory Society (ERS), endorsed by the International Society of Heart and Lung Transplantation (ISHLT). *Eur. Heart J.* 30, 2493–2537. doi: 10.1093/eurheartj/ehp297

Hoffman, J. I. E. (2009). *The Natural and Unnatural History of Congenital Heart Disease*. Oxford: Wiley-Blackwell. doi: 10.1002/9781444314045

Kaiser, T., Kellenberger, C. J., Albisetti, M., Bergstrasser, E., and Valsangiacomo Buechel, E. R. (2008). Normal values for aortic diameters in children and adolescents–assessment in vivo by contrast-enhanced CMR-angiography. *J. Cardiovasc. Magn. Reson.* 10:56. doi: 10.1186/1532-429X-10-56

Kerstein, D., Levy, P. S., Hsu, D. T., Hordof, A. J., Gersony, W. M., and Barst, R. J. (1995). Blade balloon atrial septostomy in patients with severe primary pulmonary hypertension. *Circulation* 91, 2028–2035. doi: 10.1161/01.CIR.91.7.2028

Koeken, Y., Kuijpers, N. H., Lumens, J., Arts, T., and Delhaas, T. (2012). Atrial septostomy benefits severe pulmonary hypertension patients by increase of left ventricular preload reserve. *Am. J. Physiol. Heart Circ. Physiol.* 302, H2654–H2662. doi: 10.1152/ajpheart.00072.2012

Kurzyna, M., Dabrowski, M., Bielecki, D., Fijalkowska, A., Pruszczyk, P., Opolski, G., et al. (2007). Atrial septostomy in treatment of end-stage right heart failure in patients with pulmonary hypertension. *Chest* 131, 977–983. doi: 10.1378/chest.06-1227

Latus, H., Apitz, C., Moysich, A., Kerst, G., Jux, C., Bauer, J., et al. (2014). Creation of a functional Potts shunt by stenting the persistent arterial duct in newborns and infants with suprasystemic pulmonary hypertension of various etiologies. *J. Heart Lung Transplant.* 33, 542–546. doi: 10.1016/j.healun.2014.01.860

Lumens, J., Delhaas, T., Kirn, B., and Arts, T. (2009). Three-wall segment (TriSeg) model describing mechanics and hemodynamics of ventricular interaction. *Ann. Biomed. Eng.* 37, 2234–2255. doi: 10.1007/s10439-009-9774-2

Micheletti, A., Hislop, A. A., Lammers, A., Bonhoeffer, P., Derrick, G., Rees, P., et al. (2006). Role of atrial septostomy in the treatment of children with pulmonary arterial hypertension. *Heart* 92, 969–972. doi: 10.1136/hrt.2005.077669

Moledina, S., Hislop, A. A., Foster, H., Schulze-Neick, I., and Haworth, S. G. (2010). Childhood idiopathic pulmonary arterial hypertension: a national cohort study. *Heart* 96, 1401–1406. doi: 10.1136/hrt.2009.182378

Petersen, C., Helvind, M., Jensen, T., and Andersen, H. O. (2013). Potts shunt in a child with end-stage pulmonary hypertension after late repair of ventricular septal defect. *World J. Pediatr. Congenit. Heart Surg.* 4, 286–289. doi: 10.1177/2150135113482739

Rothman, A., Sklansky, M. S., Lucas, V. W., Kashani, I. A., Shaughnessy, R. D., Channick, R. N., et al. (1999). Atrial septostomy as a bridge to lung transplantation in patients with severe pulmonary hypertension. *Am. J. Cardiol.* 84, 682–686. doi: 10.1016/S0002-9149(99)00416-6

Sandoval, J., Gaspar, J., Pulido, T., Bautista, E., Martínez-Guerra, M. L., Zeballos, M., et al. (1998). Graded balloon dilation atrial septostomy in

severe primary pulmonary hypertension. A therapeutic alternative for patients nonresponsive to vasodilator treatment. *J. Am. Coll. Cardiol.* 32, 297–304. doi: 10.1016/S0735-1097(98)00238-1

Walmsley, J., Arts, T., Derval, N., Bordachar, P., Cochet, H., Ploux, S., et al. (2015). Fast simulation of mechanical heterogeneity in the electrically asynchronous heart using the multipatch module. *PLoS Comput. Biol.* 11:e1004284. doi: 10.1371/journal.pcbi.1004284

Zierer, A., Melby, S. J., Voeller, R. K., and Moon, M. R. (2009). Interatrial shunt for chronic pulmonary hypertension: differential impact of low-flow vs. high-flow shunting. *Am. J. Physiol. Heart Circ. Physiol.* 296, H639–H644. doi: 10.1152/ajpheart.00496.2008

Conflict of Interest Statement: The authors declare that the research was conducted in the absence of any commercial or financial relationships that could be construed as a potential conflict of interest.

Copyright © 2018 Delhaas, Koeken, Latus, Apitz and Schranz. This is an open-access article distributed under the terms of the Creative Commons Attribution License (CC BY). The use, distribution or reproduction in other forums is permitted, provided the original author(s) and the copyright owner(s) are credited and that the original publication in this journal is cited, in accordance with accepted academic practice. No use, distribution or reproduction is permitted which does not comply with these terms.

frontiers in Physiology

ORIGINAL RESEARCH
published: 04 October 2018
doi: 10.3389/fphys.2018.01402

Human Atrial Arrhythmogenesis and Sinus Bradycardia in *KCNQ1*-Linked Short QT Syndrome: Insights From Computational Modelling

Dominic G. Whittaker[1,2], Michael A. Colman[1], Haibo Ni[2,3], Jules C. Hancox[2,4] and Henggui Zhang[2,5,6,7]**

[1] School of Biomedical Sciences, Faculty of Biological Sciences, University of Leeds, Leeds, United Kingdom, [2] Biological Physics Group, School of Physics and Astronomy, The University of Manchester, Manchester, United Kingdom, [3] Department of Pharmacology, University of California, Davis, Davis, CA, United States, [4] School of Physiology, Pharmacology and Neuroscience, and Cardiovascular Research Laboratories, School of Medical Sciences, University of Bristol, Bristol, United Kingdom, [5] School of Computer Science and Technology, Harbin Institute of Technology, Harbin, China, [6] Space Institute of Southern China, Shenzhen, China, [7] Key Laboratory of Medical Electrophysiology, Ministry of Education, Collaborative Innovation Center for Prevention and Treatment of Cardiovascular Disease/Institute of Cardiovascular Research, Southwest Medical University, Luzhou, China

OPEN ACCESS

Edited by:
Thomas Heldt,
Massachusetts Institute of Technology, United States

Reviewed by:
Mohammed Saeed,
University of Michigan, United States
Richard Gray,
United States Food and Drug Administration, United States

***Correspondence:**
Jules C. Hancox
jules.hancox@bristol.ac.uk
Henggui Zhang
henggui.zhang@manchester.ac.uk

Specialty section:
This article was submitted to Computational Physiology and Medicine, a section of the journal Frontiers in Physiology

Received: 27 June 2018
Accepted: 14 September 2018
Published: 04 October 2018

Citation:
Whittaker DG, Colman MA, Ni H, Hancox JC and Zhang H (2018) Human Atrial Arrhythmogenesis and Sinus Bradycardia in KCNQ1-Linked Short QT Syndrome: Insights From Computational Modelling. Front. Physiol. 9:1402. doi: 10.3389/fphys.2018.01402

Atrial fibrillation (AF) and sinus bradycardia have been reported in patients with short QT syndrome variant 2 (SQT2), which is underlain by gain-of-function mutations in *KCNQ1* encoding the α subunit of channels carrying slow delayed rectifier potassium current, I_{Ks}. However, the mechanism(s) underlying the increased atrial arrhythmogenesis and impaired cardiac pacemaking activity arising from increased I_{Ks} remain unclear. Possible pharmacological interventions of AF in the SQT2 condition also remain to be elucidated. Using computational modelling, we assessed the functional impact of SQT2 mutations on human sinoatrial node (SAN) pacemaking, atrial repolarisation and arrhythmogenesis, and efficacy of the anti-arrhythmic drug quinidine. Markov chain formulations of I_{Ks} describing two *KCNQ1* mutations – V141M and V307L – were developed from voltage-clamp experimental data and then incorporated into contemporary action potential (AP) models of human atrial and SAN cells, the former of which were integrated into idealised and anatomically detailed tissue models. Both mutations shortened atrial AP duration (APD) through distinct I_{Ks} 'gain-of-function' mechanisms, whereas SAN pacemaking rate was slowed markedly only by the V141M mutation. Differences in APD restitution steepness influenced re-entry dynamics in tissue – the V141M mutation promoted stationary and stable spiral waves whereas the V307L mutation promoted non-stationary and unstable re-entrant waves. Both mutations shortened tissue excitation wavelength through reduced effective refractory period but not conduction velocity, which served to increase the lifespan of re-entrant excitation in a 3D anatomical human atria model, as well as the dominant frequency (DF), which was higher for the V141M mutation. Quinidine was effective at terminating arrhythmic excitation waves

associated with the V307L but not V141M mutation, and reduced the DF in a dose-dependent manner under both mutation conditions. This study provides mechanistic insights into different AF/bradycardia phenotypes in SQT2 and the efficacy of quinidine pharmacotherapy.

Keywords: anti-arrhythmic, arrhythmia, short QT syndrome, atrial fibrillation, KCNQ1 mutations, sinus bradycardia, quinidine

INTRODUCTION

The short QT syndrome (SQTS) is a rare but important cardiac disorder characterised by a shortened QT interval, increased incidence of ventricular and atrial arrhythmias, and risk of sudden death in affected patients (Schimpf et al., 2005). Variants 1–3 of the SQTS are caused by gain-of-function mutations to genes encoding different K^+ channel subunits, which carry currents responsible for phase 3 repolarisation of the cardiac action potential (AP) (Hancox et al., 2018). Mutations to the *KCNQ1* (*KvLQT1*, *Kv7.1*) gene product which, along with auxiliary subunits encoded by *KCNE1*, encodes slow delayed rectifier potassium current, I_{Ks}, underlie SQTS variant 2 (SQT2). To date, four missense mutations have been identified in *KCNQ1*-linked SQTS: V307L (Bellocq et al., 2004), V141M (Hong et al., 2005), R259H (Wu et al., 2015), and F279I (Moreno et al., 2015), all of which result in a gain-of-function of I_{Ks}.

There is mounting evidence for a role of I_{Ks} in atrial arrhythmogenesis (Christophersen and Ellinor, 2016). Upregulation of I_{Ks} has been identified in patients with chronic atrial fibrillation (AF) (Caballero et al., 2010; González de la Fuente et al., 2013), and mutations to *KCNQ1* have been shown to underlie lone AF (Chen et al., 2003; Lundby et al., 2007; Das et al., 2009). These findings suggest that enhanced I_{Ks} may play a role in the pathogenesis of AF. In some SQT2 patients, cardiac arrhythmia including AF has been reported (Hong et al., 2005; Villafañe et al., 2014; Righi et al., 2016). However, the mechanism(s) underlying atrial arrhythmogenesis and maintenance arising from increased potassium channel currents, including I_{Ks}, remain to be fully established. The SQTS thus represents a valuable paradigm for investigating the role of K^+ channels in AF.

Atrial fibrillation can be the first clinical presentation of the SQTS, particularly in patients diagnosed with lone AF (Hasdemir, 2016). Furthermore, the incidence of AF has been reported to be higher in patients with SQT2 than other forms of SQTS (63% vs. 21%, $p = 0.012$ (Harrell et al., 2015)). The first reported SQT2 mutation, V307L KCNQ1 (Bellocq et al., 2004), was shown to shift the voltage-dependence of *KCNQ1* + *KCNE1* activation toward less depolarised potentials and accelerate channel activation, causing a gain-of-function to I_{Ks}. The proband presented with a shortened QTc interval and idiopathic ventricular fibrillation (Bellocq et al., 2004) – whether or not this mutation is able also to promote AF is not yet known. The subsequently discovered V141M KCNQ1 mutation differs from the V307L KCNQ1 mutation in that it induces an instantaneous, voltage-independent K^+-selective current component (Hong et al., 2005). This form of SQT2 is associated with abnormally short QT intervals in affected patients, as well as multiple reports of a mixed AF and sinus bradycardia phenotype (Hong et al., 2005; Villafañe et al., 2014; Righi et al., 2016).

At present, there are no phenotypically accurate experimental models of genetic forms of SQTS. Computational modelling offers a viable way of investigating how SQTS-linked K^+ channelopathies affect organ scale electrical propagation and arrhythmogenesis. Previous studies have investigated the functional impact of SQT2 variants on ventricular arrhythmogenesis (Zhang et al., 2008; Adeniran et al., 2017), which can be attributed to abbreviated ventricular AP duration (and therefore excitation wavelength), increased transmural dispersion of repolarisation, and increased vulnerability of tissue to initiation of unidirectional conduction block. However, the mechanism(s) by which SQT2 variants promote atrial arrhythmogenesis has not been elucidated – it is possible that the interaction between genetic mutations and intrinsic electrical heterogeneities in the human atria may form an important determinant of arrhythmogenic mechanisms, as shown in previous studies (Colman et al., 2017; Whittaker et al., 2017b). Consequently, the first aim of this study was to dissect underlying mechanisms of increased susceptibility to development of AF associated with SQT2 using both idealised and anatomically-detailed, heterogeneous multi-scale tissue models of human atrial electrophysiology. We chose to study the V141M KCNQ1 mutation, which has been linked with multiple reports of AF (Hong et al., 2005; Villafañe et al., 2014; Righi et al., 2016), and use the V307L KCNQ1 mutation as a comparator, which has distinct kinetics and has been demonstrated to promote ventricular arrhythmogenesis in our previous computational modelling study (Adeniran et al., 2017).

Effective pharmacological management of AF in KCNQ1-linked SQTS conditions is an unmet challenge. Quinidine – an established inhibitor of SQTS mutant hERG channels (Gaita et al., 2004; Hu et al., 2017) has shown some efficacy in the ventricles in non-hERG-linked SQTS (e.g., Giustetto et al., 2011). However, its anti-AF effects in the context of SQT2 remain unclear. The second aim of this study was thus to assess the effects of quinidine on arrhythmic atrial excitation waves in SQT2 using cellular and tissue level simulations that incorporated drug binding kinetics and multi-channel pharmacology.

MATERIALS AND METHODS

Markov Chain Models of I_{Ks}

A Markov chain (MC) formulation of human cardiac I_{Ks} (Silva and Rudy, 2005; Adeniran et al., 2017) was used to

simulate I_{Ks} in wild type (WT) and SQT2 mutation conditions (MC scheme shown in **Supplementary Figure S1**). The V307L KCNQ1 mutation MC formulation has been described and validated previously (Adeniran et al., 2017); nonetheless, for completeness, the response of WT and V307L mutant currents to simulated voltage clamps – namely the *I–V* relation and steady state activation – and human atrial AP clamp is shown in **Supplementary Figure S2**.

The MC formulation of I_{Ks} was subsequently employed to develop a model of the V141M mutation in *KCNQ1*, first described by Hong et al. (2005). Multi-objective fitting to experimental data (Restier et al., 2008), namely the *I–V* relation, steady state activation, and voltage clamp current traces, was performed using a bounded Nelder–Mead simplex algorithm (Moreno et al., 2016). As experimental data were acquired at room temperature, a Q_{10} correction value of 3.5 (Seebohm et al., 2001) was applied in order to represent kinetics at physiological temperature. An additional voltage-independent parameter, ξ, was introduced to account for the constitutively active component of I_{Ks} observed in *KCNQ1* V141M mutant channels (Hong et al., 2005; Restier et al., 2008). The response of V141M mutant currents to simulated voltage clamps and corresponding *I–V* relation and steady state activation is shown in **Figure 1**. The V141M mutant I_{Ks} formulation reproduced accurately the experimentally measured *I–V* relationship and voltage dependence of activation under voltage clamp conditions, as well as faster activation and slower deactivation (Restier et al., 2008). For both mutations, in order to mimic the heterozygous state of probands, a heterozygous mutation formulation consisting of 50% WT and 50% mutant subunit channels was constructed (Adeniran et al., 2017). For more details of the MC scheme, see **Supplementary Method 1.1**.

Modelling Electrophysiology of the Human Atria and Sinoatrial Node

The Colman et al. (2013) family human atrial cell models incorporating regional heterogeneity, recently updated by Ni et al. (2017), was used to simulate human atrial electrophysiology in this study, and is hereinafter referred to as the CNZ (Colman-Ni-Zhang) model. For all single cell, 1D, and 2D simulations the baseline right atrium (RA) model was used. The equations for I_{Ks} – which are native to the parent Courtemanche-Ramirez-Nattel (CRN) model (Courtemanche et al., 1998) – were replaced with that of the WT MC formulation, with a current density within the range measured in human atrial myocytes (Caballero et al., 2010) – **Supplementary Figure S4**. Furthermore, as a theoretical consideration, the effects of AF-induced electrical remodelling (**Supplementary Figure S6**) were incorporated into supplementary CNZ model simulations, to assess the combined influence of *KCNQ1* mutations and AF remodelling. A recently developed human sinoatrial node (SAN) model (Fabbri et al., 2017), hereinafter referred to as the FS (Fabbri-Severi) model, was used to simulate the AP of primary pacemaker cells in the human heart. The native equations for I_{Ks} were replaced by the WT MC I_{Ks} formulation – **Supplementary Figure S7** shows the agreement between the modified FS model AP and published experimental recordings from human SAN myocytes (Verkerk et al., 2007). Full details of the CNZ and FS models, including definitions of quantitative AP biomarkers used, the effects of the new I_{Ks} formulation on the AP, regional human atrial electrophysiology models, AF remodelling, and parasympathetic modulation with acetylcholine (ACh), can be found in **Supplementary Method 1.2–1.4**.

Modelling Pharmacological Actions of Quinidine

In our recent prior study (Whittaker et al., 2017a), state-dependent binding of quinidine to hERG and sodium channels was simulated in human ventricle models. Secondary blocking actions of quinidine on other affected ionic currents were described using a simple pore block approach. The actions of quinidine on human atrial cells in this study were represented using the same formulations and IC_{50} (half maximal inhibitory concentration) values (Whittaker et al., 2017a). Additionally, quinidine block of the atrial-specific ultra-rapid delayed rectifier potassium current, I_{Kur}, was incorporated into CNZ simulations with an IC_{50} of 6.6 μM (Nenov et al., 1998), as measured in human atrial myocytes. Concentrations of 1, 2, and 5 μM quinidine, which likely represent realistic maximal unbound concentrations (Whittaker et al., 2017a), were used. A summary of IC_{50} values for quinidine inhibition of multiple ion channels is given in **Supplementary Table S4**. Further details regarding kinetics, parameters, and equations can be found in **Supplementary Method 1.5**, as well as our previous study (Whittaker et al., 2017a).

Tissue Simulations

The effects of SQT2 mutations on human atrial electrophysiology were further investigated using a hierarchy of tissue models. One-dimensional (1D) models of human atrial strands were used to assess the effects of *KCNQ1* mutations on the effective refractory period (ERP), conduction velocity (CV), and excitation wavelength (WL). In order to characterise re-entrant excitation wave dynamics, an isotropic 2D sheet of human atrial tissue was used, wherein spiral waves were initiated using an S1–S2 cross-field protocol (Whittaker et al., 2017b). In order to characterise the lifespan and dominant frequency (DF) of arrhythmic excitation waves, as well as the response to quinidine, a 3D anatomical model of the human atria (Seemann et al., 2006; Colman et al., 2013) with heterogeneity of electrophysiology, rule-based fibre orientations (Krueger et al., 2011), and validated activation times was used (**Supplementary Figure S10**). Scroll waves were initiated proximal to the SAN in the RA using the phase distribution method (Biktashev and Holden, 1998; Colman et al., 2017; Whittaker et al., 2017b), which developed into functional and/or anatomical re-entries in the 3D anatomical human atria model. The rate of electrical activation during re-entrant excitation was determined from pseudo-ECG (pECG) signals. It should be noted that the SAN region was modelled electrically as CT tissue in 3D simulations for simplicity (Colman et al., 2013, 2017). Further

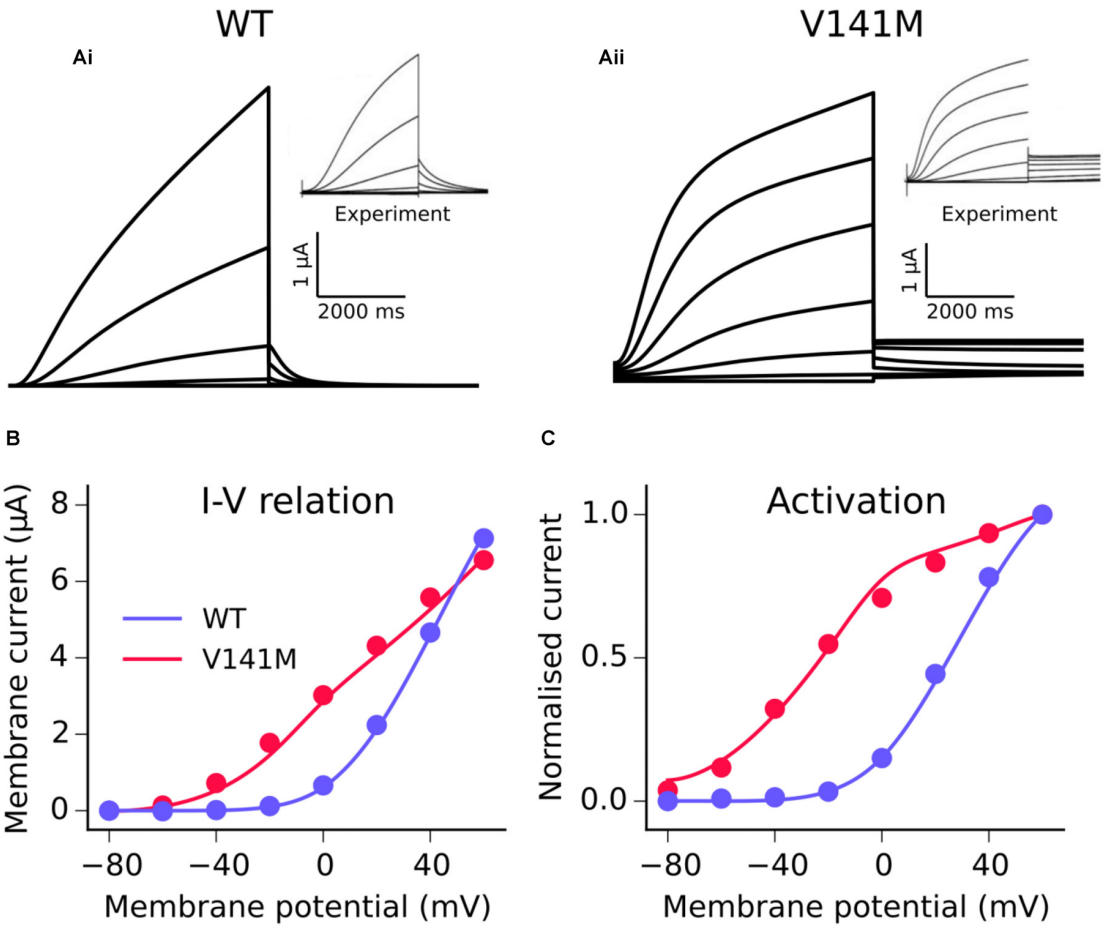

FIGURE 1 | Kinetics of the V141M KCNQ1 mutant I_{Ks} model. A comparison of simulated voltage clamp current traces in WT **(Ai)** and V141M **(Aii)** conditions at 22°C. Experimental traces inset are reproduced with permission from Restier et al. (2008), which describes the protocols used. Simulated (solid lines) *I–V* relation **(B)** and voltage dependence of activation **(C)** under WT and V141M mutation conditions, compared with experimental data (points).

descriptions of tissue models and simulation protocols are given in **Supplementary Methods 1.6–1.9**.

RESULTS

Modification of Human SAN Cell Pacemaking by SQT2 Mutant I_{Ks}

The effects of *KCNQ1* V141M and V307L gain-of-function mutations on I_{Ks} were first investigated in the FS SAN model (**Figure 2**). The heterozygous form of the V141M mutation decreased the diastolic depolarisation rate (DDR) due to increased repolarising current at potentials negative to the take-off (threshold) potential, which extended the pacemaker potential and reduced the beating rate of single SAN cells from 73 bpm in the WT condition to 50 bpm. The homozygous condition abolished pacemaking, as increased repolarising I_{Ks} prevented the membrane potential from reaching the take-off potential. The APD_{90} in the WT-V141M condition was reduced from 151.4 ms in the WT condition to 143.4 ms. The effects of the V307L mutant were comparatively modest; the WT-V307L and V307L mutation conditions reduced the beating rate to 69 bpm and 64 bpm, respectively. Furthermore, the reduction in APD_{90} was less substantial, being reduced to 149.7 ms and 148.1 ms in the WT-V307L and V307L conditions, respectively.

In addition to reduced beating rate due to decreased DDR, the maximum upstroke velocity was reduced by the WT-V141M mutation condition and to a lesser extent by the homozygous form of the V307L mutation. Under simulated parasympathetic modulation by 10 nM ACh, the reduction in beating rate in V307L mutation conditions was still relatively minor (**Figure 2Bii**), whereas pacemaking rate was reduced to 22 bpm in WT-V141M mutation conditions and was abolished completely by the homozygous V141M expression condition.

Modification of Human Atrial Action Potentials by SQT2 Mutant I_{Ks}

Action potential shortening occurred under all SQT2 mutant conditions in the baseline CNZ RA model at 1 Hz (**Figure 3**), as well as other atrial sub-regions (**Supplementary Figure S5**). The

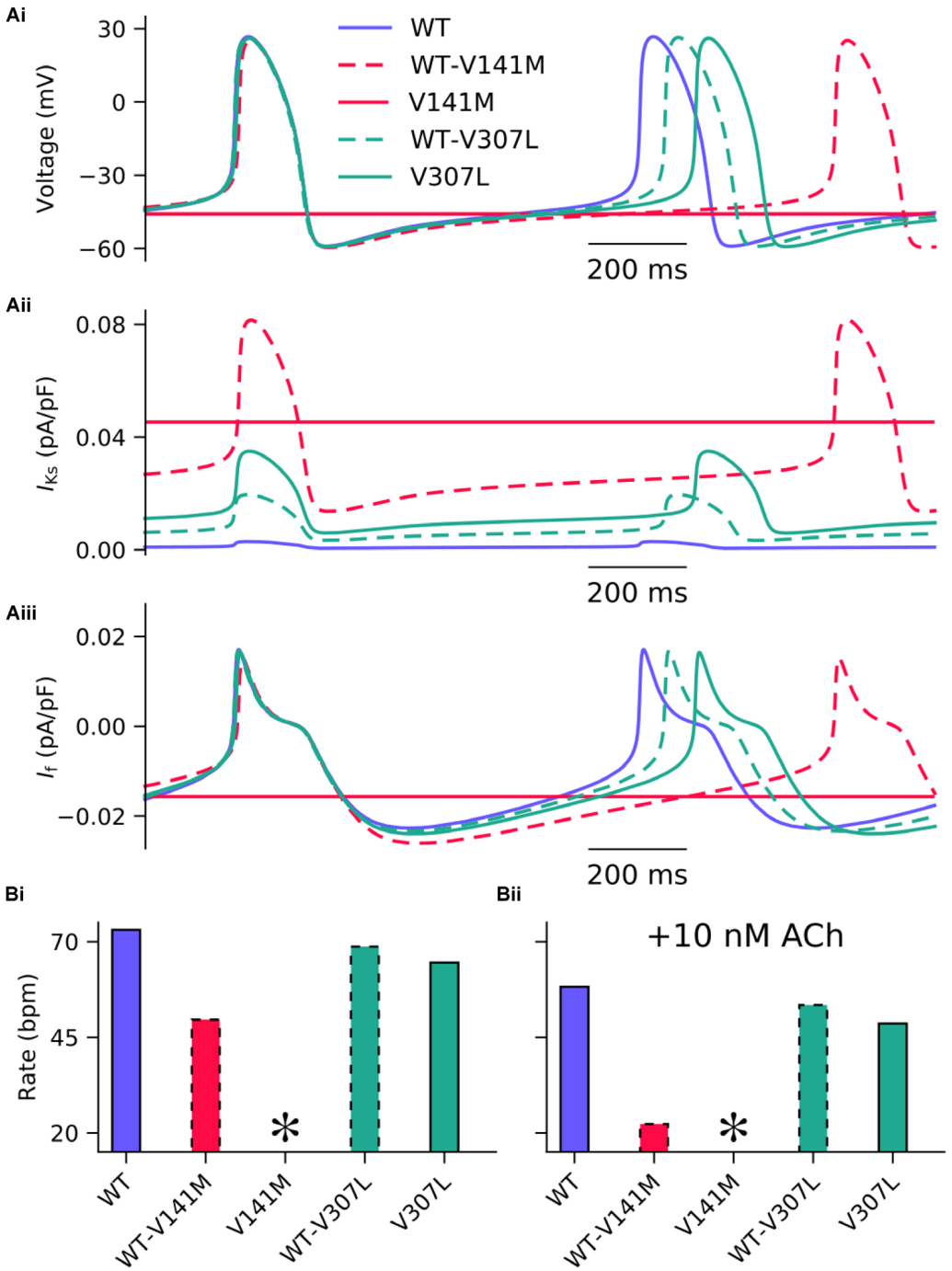

FIGURE 2 | Simulated AP profiles and current traces under WT and SQT2 mutant conditions in human SAN myocytes. Spontaneous pacemaker APs under WT (lilac, solid line), WT-V141M (red, dashed line), V141M (red, solid line), WT-V307L (turquoise, dashed line), and V307L (turquoise, solid line) conditions **(Ai)** in the absence of autonomic modulation, with corresponding current traces for I_{Ks} **(Aii)** and I_f **(Aiii)**. The beating rate is summarised as a bar chart, without autonomic modulation **(Bi)**, and with addition of 10 nM acetylcholine (ACh) **(Bii)**. *Denotes pacemaking abolished.

V141M mutation abolished the AP plateau phase and reduced the APD_{90} from 250.0 ms in the WT condition to 124.7 ms and 85.5 ms under heterozygous and homozygous forms, respectively (**Figure 3Ai**). In contrast, the 'spike and dome' morphology of the AP was preserved under V307L mutant conditions, as these mutations exerted their effects mainly during the terminal phase of repolarisation. The heterozygous and homozygous forms of these mutants abbreviated the APD_{90} to 207.6 ms and 185.4 ms, respectively. The V141M mutation induces a constitutively active voltage-independent component of I_{Ks} (Hong et al., 2005;

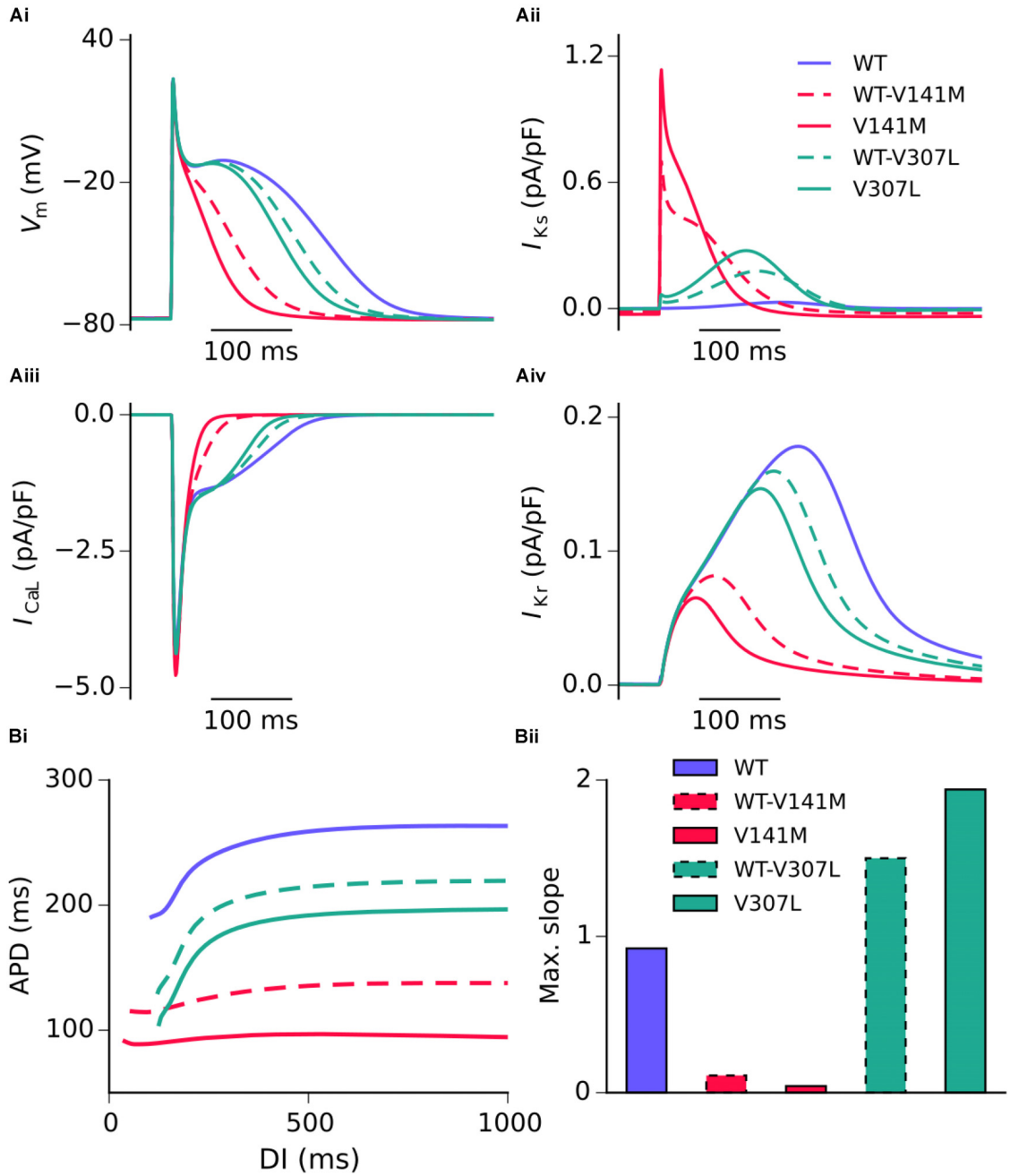

FIGURE 3 | Simulated AP profiles and current traces under WT and SQT2 mutant conditions in human atrial myocytes. AP profiles in WT, WT-V141M, V141M, WT-V307L, and V307L conditions at 1 Hz **(Ai)**, as well as corresponding I_{Ks} **(Aii)**, I_{CaL} **(Aiii)**, and I_{Kr} **(Aiv)**. APD at −70 mV plotted against diastolic interval (DI), measured using an S1–S2 protocol **(Bi)**, and a bar chart showing maximal slope of restitution **(Bii)**.

Restier et al., 2008). The combination of this and significantly slowed deactivation resulted in a large outward current during membrane depolarisation (**Figure 3Aii**). The V307L mutation, in contrast, augmented I_{Ks}, but did not fundamentally change its profile.

Figure 3 shows secondary effects of SQT2 *KCNQ1* mutants on L type calcium current, I_{CaL} (**Figure 3Aiii**) and rapid delayed rectifier potassium current, I_{Kr} (**Figure 3Aiv**) during APs. The balance of ionic currents which maintains the plateau phase was largely abolished in V141M mutation conditions, as the increase in repolarising I_{Ks} overpowered inward I_{CaL}. This also had the effect of activating I_{Kr} to a lesser extent, thus considerably decreasing its peak current density and contribution to AP repolarisation. The effects of the V307L mutation on I_{Ks} were less pervasive, with the current profiles of I_{CaL} and I_{Kr} being altered to a smaller extent. Aside from the APD, alterations

TABLE 1 | Single cell AP properties in WT and SQT2 mutant conditions in the FS human SAN model (autorhythmic) and CNZ human atrial cell model (paced at 1 Hz).

Sinoatrial node (SAN) cells					
	WT	**WT-V141M**	**V141M**	**WT-V307L**	**V307L**
Beating rate (bpm)	73.1	49.6	–	68.7	64.5
APD_{90} (ms)	151.4	143.4	–	149.7	148.1
APD_{50} (ms)	125.5	118.1	–	123.9	122.5
MUV (V/s)	7.5	7.2	–	7.5	7.4
DDR (mV/s)	35.5	21.5	–	32.6	29.9
Atrial cells					
	WT	**WT-V141M**	**V141M**	**WT-V307L**	**V307L**
APD_{90} (ms)	250.0	124.7	85.5	207.6	185.4
APD_{50} (ms)	145.9	45.7	30.1	120.0	105.4
APA (mV)	103.0	103.1	102.9	103.3	103.4
MUV (V/s)	212.4	214.7	214.6	214.2	214.4

Abbreviations are as follows: beats per minute (bpm); action potential duration at 50% and 90% repolarisation (APD_{50} and APD_{90}, respectively); maximum upstroke velocity (MUV); diastolic depolarisation rate (DDR); and action potential amplitude (APA).

to other AP parameters induced by the SQT2 mutations were minimal. A summary of single cell simulations (SAN and RA) is given in **Table 1**.

All SQT2 mutations investigated shortened the APD across a range of diastolic intervals (DIs; **Figure 3Bi**). However, the V141M and V307L KCNQ1 mutations produced opposing effects on the maximum slope of restitution. Both heterozygous and homozygous V141M mutant conditions showed almost no rate adaptation, with significantly reduced maximal slope of restitution. In contrast, the V307L mutation conditions increased the maximal slope of restitution, markedly so in the homozygous V307L condition. Furthermore, whereas the APD measured in the WT-V141M condition was considerably shorter than that measured for the V307L mutation at 1 Hz (124.7 ms vs. 185.4 ms), at fast pacing rates the restitution curves crossed over, indicating greater rate adaptation for the V307L mutation.

Tissue Restitution Properties

Restitution curves for the CV, ERP, and WL measured in the 1D strand are shown in **Figure 4**. None of the SQT2 mutation conditions investigated considerably affected the CV at pacing rates slower than 2 Hz, whereas all mutation conditions reduced the ERP across all basic cycle lengths (BCLs) investigated. As the excitation WL is given by CV × ERP, the WL was thus also decreased by SQT2 mutations across all BCLs, indicating that higher frequency excitations can be supported by SQT2 mutant tissue (investigated in **Scroll wave dynamics in 3D anatomical human atria geometry**). The V307L mutation conditions (the homozygous form in particular) induced beat-to-beat AP alternans at fast pacing rates, which was evident in restitution curves for the CV, ERP, and WL.

Spiral Wave Dynamics in Idealised 2D Sheets of Human Atrial Tissue

The functional impact of *KCNQ1*-linked SQT2 mutations on re-entry dynamics was first investigated using an idealised 2D sheet of human atrial tissue. In the WT condition, an S2 stimulus delivered at 259 ms following a train of S1 stimuli with a BCL of 400 ms induced a spiral wave which meandered over a large area for ∼3.7 s before meeting a tissue boundary and terminating (**Figure 5A** and **Supplementary Video S1**). Both heterozygous and homozygous forms of the V141M mutation showed qualitatively similar meandering patterns in tissue. S2 stimuli delivered at 135 ms and 114 ms in WT-V141M and V141M conditions, respectively, produced spiral waves with more stationary trajectories (meandering over a smaller area) which sustained for the complete 5.0 s duration of the simulation (**Figures 5B,C** and **Supplementary Videos S2, S3**). In the WT-V307L condition, an S2 stimulus applied at 219 ms produced a spiral wave which also sustained for 5.0 s, meandering with a hypocycloidal trajectory over a considerably larger area than under V141M mutation conditions (**Figure 5D** and **Supplementary Video S4**). In the homozygous V307L mutation condition, however, the S2 stimulus delivered at 201 ms induced a non-stationary and unstable spiral wave which spontaneously degenerated into multiple, regenerative wavelets (**Figure 5E** and **Supplementary Video S5**), resembling AF-like electrical excitations.

Scroll Wave Dynamics in 3D Anatomical Human Atria Geometry

Use of the phase distribution method resulted in scroll waves which developed into functional and/or anatomical re-entries in the 3D anatomical human atria model (**Figure 6**). In the WT condition, the initiated scroll wave developed into a transient re-entry, completing two circuits in the RA before self-terminating at ∼0.6 s (**Supplementary Video S6**). This precluded accurate computation of the DF. In the heterozygous WT-V141M mutation condition, the stationary re-entrant wave pattern mirrored that observed in the 2D sheet, with re-entry being driven by a single scroll wave in the RA with a high frequency of rotation (9.1 Hz; **Supplementary Video S7**). In the homozygous

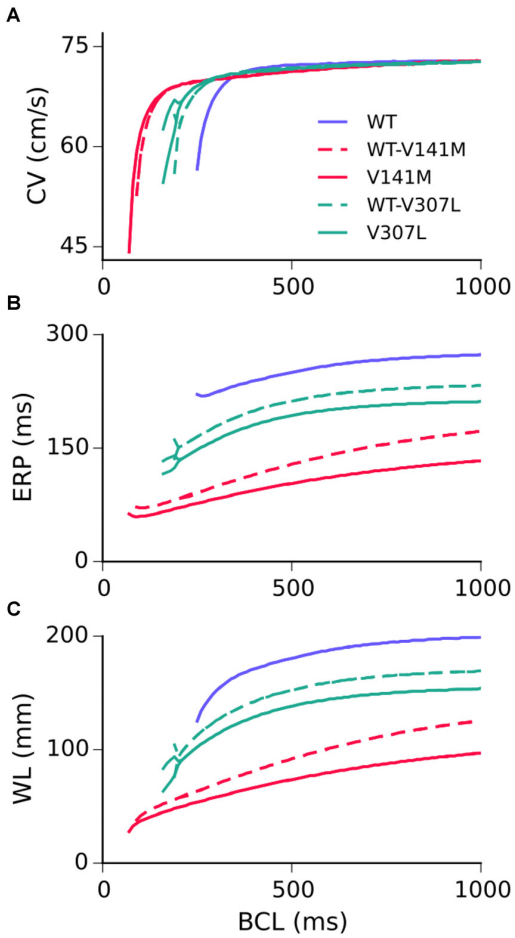

FIGURE 4 | Tissue restitution properties in WT and mutation conditions. Steady-state restitution of the conduction velocity (CV) **(A)**, effective refractory period (ERP) **(B)**, and excitation wavelength (WL) **(C)** against a range of basic cycle lengths (BCL), measured in the 1D tissue model.

V141M mutation condition, re-entry was driven by a single stationary scroll wave in the right atrial appendage (RAA), which had an even higher frequency (10.1 Hz; **Supplementary Video S8**). In both cases the re-entry was stable and persistent (lasting for the full 10.0 s duration of the simulation), and showed no signs of wave break.

In V307L mutation conditions, re-entrant excitation waves meandered to a much larger extent than under the V141M mutation, consistent with observations in the idealised 2D sheet. In the heterozygous WT-V307L condition, the initiated scroll wave developed into an irregular excitation pattern, which eventually anchored to the boundary of the inferior vena cava (IVC) and sustained for 10.0 s (**Supplementary Video S9**). Although the IVC re-entry was persistent, occasional transient micro re-entrant circuits developed around the RAA. In the homozygous V307L condition, the initiated scroll wave moved unpredictably, occasionally breaking and forming multiple wavelets which meandered and collided, as observed in the 2D sheet. This also ultimately degenerated into a persistent circuit around the IVC, sustaining for the full 10.0 s of the simulation (**Supplementary Video S10**). The DF of re-entry under heterozygous and homozygous V307L mutation conditions was 5.3 and 5.8 Hz, respectively.

Effects of Quinidine on APD, ERP, and Organ-Scale Re-entry Dynamics

As SQTS mutant subunits are expressed heterozygously *in vivo*, the effects of different concentrations of the class Ia anti-arrhythmic drug quinidine were simulated on the cellular APD/ERP and organ scale re-entry dynamics in WT-V141M and WT-V307L mutant conditions only. Quinidine restored the APD to that of the WT level in the WT-V307L but not WT-V141M condition. However, in both mutation conditions quinidine prolonged the ERP in a concentration-dependent manner due to actions on I_{Na}, especially in the WT-V307L mutation condition in which APD was also prolonged. **Supplementary Table S7** gives a summary of APD and ERP prolongation at 1 and 2 Hz, including that observed in additional simulations in which AF remodelling was considered.

In 3D re-entry simulations, quinidine was applied after 2.5 s under heterozygous SQT2 mutation conditions in which re-entry sustained for 10.0 s in the absence of the drug. Under WT-V141M conditions, all concentrations of quinidine tested failed to terminate re-entry, but decreased its frequency of rotation. Application of both 2 and 5 μM quinidine was sufficient to terminate re-entrant excitations in the WT-V307L condition (termination of re-entry by 2 μM quinidine is shown in **Supplementary Video S11**), reducing the lifespan of re-entrant excitation to 7.5 and 4.0 s, respectively. The mechanism underlying re-entry termination in this condition was increased ERP by quinidine, which reduced the excitable gap for anatomically driven re-entry in the anatomical human atria model. The effects of 2 μM quinidine on re-entry dynamics and the pECG in WT-V141M and WT-V307L conditions are shown in **Figure 7**, as well as the DF for a range of quinidine concentrations. A summary of the effects of quinidine on SQT2-mediated atrial arrhythmias under AF remodelling conditions is shown in **Supplementary Figure S13**.

DISCUSSION

Main Findings

The major findings of this study are as follows: (1) The *KCNQ1* V141M but not V307L mutation slowed human SAN pacemaking rate profoundly, through reduced DDR; (2) The V141M and V307L KCNQ1 mutations shortened the human atrial APD through distinct mechanisms – the V141M mutation induced a large instantaneous component of I_{Ks} upon membrane depolarisation which shortened the APD, whereas the V307L mutation increased I_{Ks} primarily during phase 3 repolarisation, producing more modest APD shortening. The mutations produced opposing effects on the steepness of restitution; (3) Both mutations shortened the tissue excitation wavelength through a reduction in the ERP but not CV across a wide range of pacing rates; (4) In idealised 2D sheets of human atrial tissue,

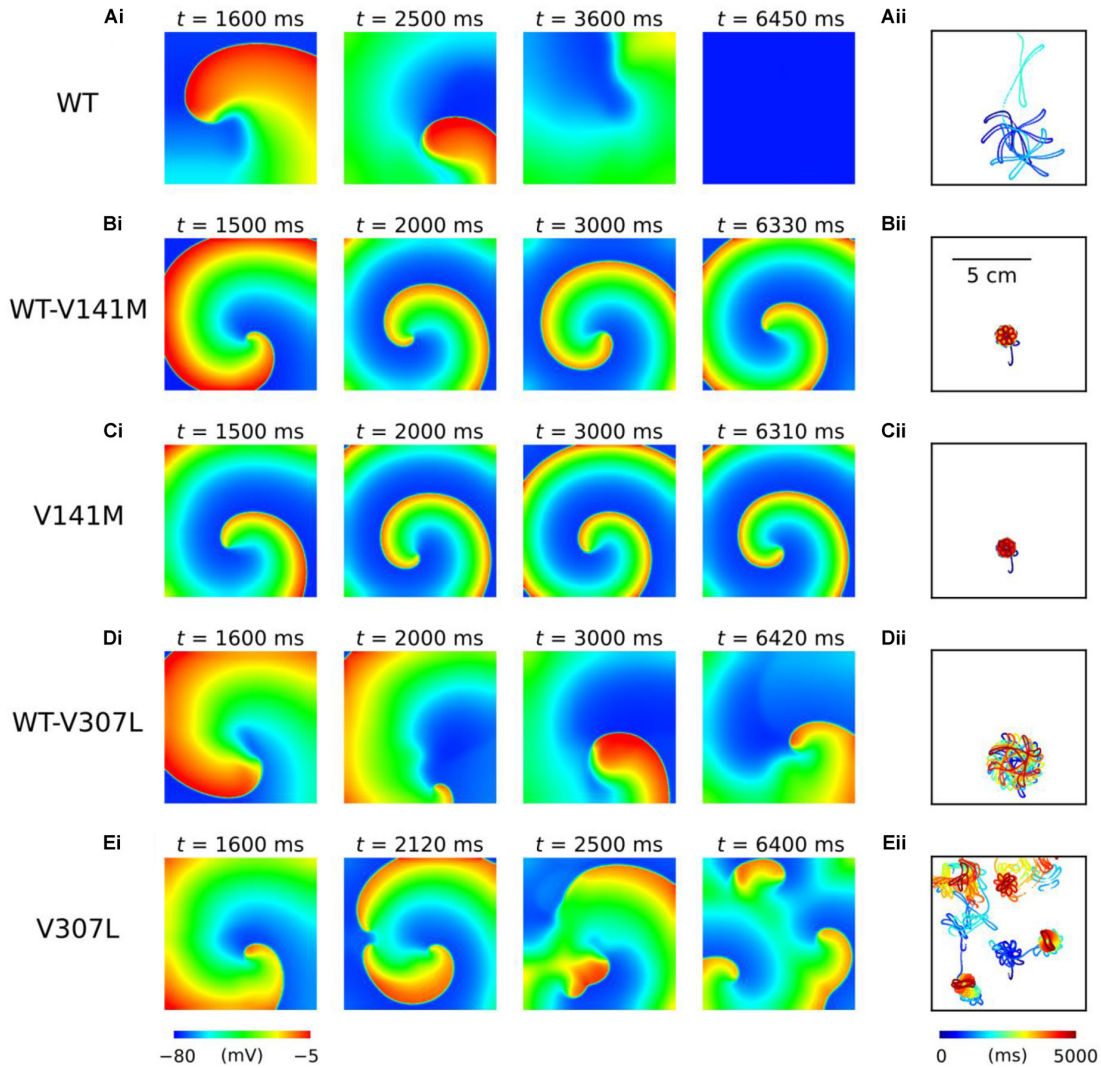

FIGURE 5 | Spiral wave dynamics in 2D human atrial tissue simulations. Snapshots of re-entry are shown at various time points after initiation of a spiral wave in WT **(A)**, WT-V141M **(B)**, V141M **(C)**, WT-V307L **(D)**, and V307L **(E)** conditions **(i)**, with corresponding spiral wave core trajectories **(ii)**. Note that the time at which snapshots were taken differs between mutation conditions.

stationary spiral waves were observed with the V141M mutation, whereas spiral waves meandered in the heterozygous V307L mutation condition and wave break occurred in the homozygous V307L condition. In the 3D anatomical human atria model, scroll waves self-terminated in the WT condition, whereas all SQT2 mutation conditions favoured sustenance of re-entry; (5) Quinidine exerted an anti-arrhythmic decrease in the DF of re-entrant excitation in heterozygous forms of the SQT2 mutations, but was effective at terminating scroll waves associated with the V307L mutation only.

The V141M but not V307L KCNQ1 Mutation Promotes Sinus Bradycardia

In the FS human SAN model, the homozygous form of the V141M mutation abolished pacemaking, whereas the heterozygous form reduced the spontaneous beating rate from 73 bpm in the WT condition to 50 bpm. This is in good agreement with 40–60 bpm (Villafañe et al., 2014) and 50 bpm (Righi et al., 2016) heart rates reported in SQT2 probands with the *KCNQ1* V141M mutation. Upon application of 10 nM ACh, pacemaking rate was further reduced to 22 bpm in the heterozygous V141M mutation condition, and was again abolished altogether in the homozygous V141M mutation condition. Previous computational modelling of the V141M mutation using a rabbit SAN cell model showed abolished pacemaking in a 1:1 WT:mutant heterozygous WT-V141M condition (Hong et al., 2005). However, the present study is the first to reproduce the sinus bradycardia phenotype associated with the V141M mutation using a biophysically detailed model of human SAN electrophysiology (Fabbri et al., 2017). Such alterations to pacemaking activity by the V141M mutation might

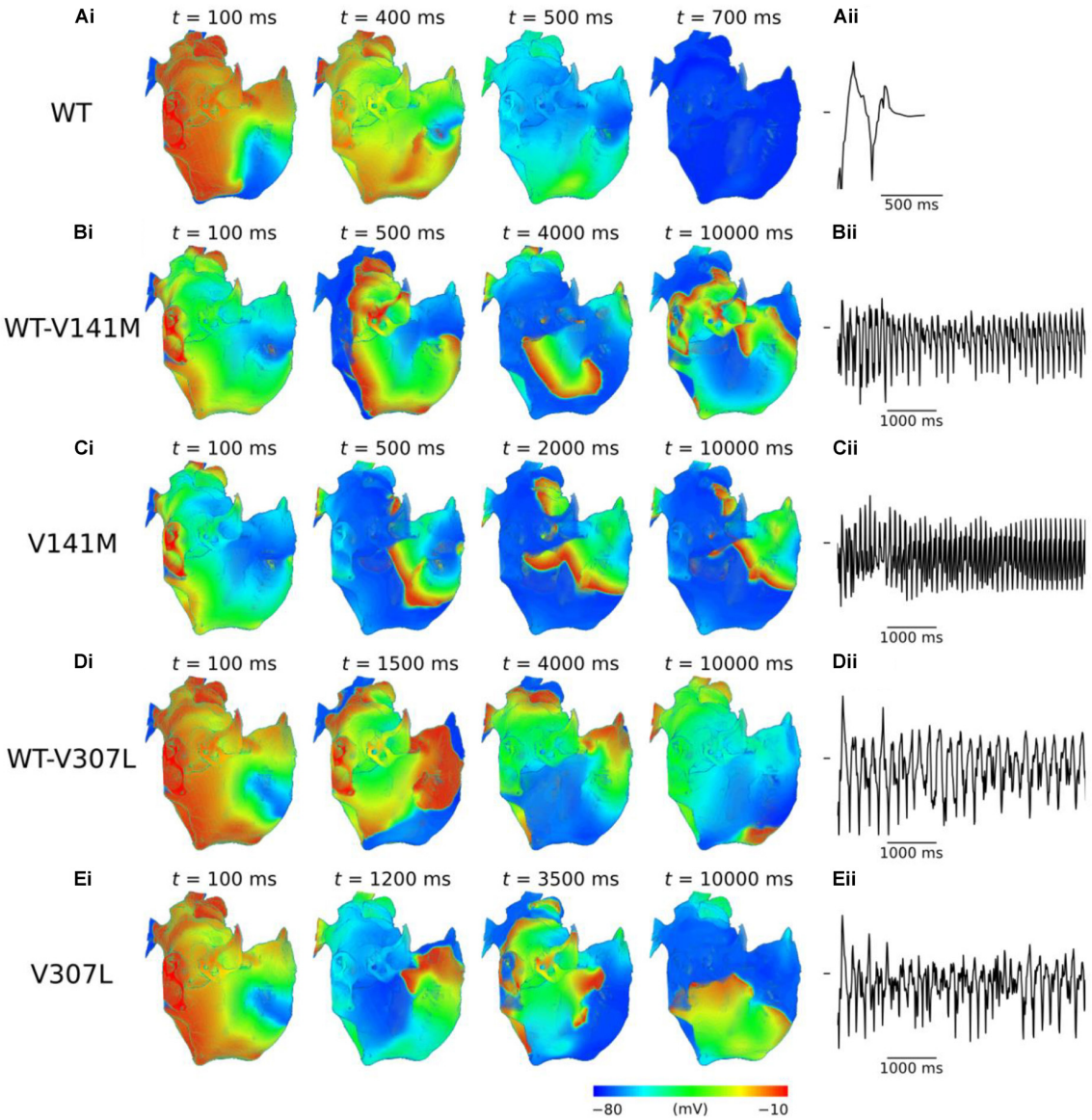

FIGURE 6 | Re-entry dynamics in 3D anatomical human atria. Snapshots of re-entry are shown at various time points after initiation of a scroll wave in WT **(A)**, WT-V141M **(B)**, V141M **(C)**, WT-V307L **(D)**, and V307L **(E)** conditions **(i)**, with corresponding first 5.0 s of pseudo ECG **(ii)**. Note that snapshot times differ between mutation conditions.

be expected to impair the ability of the SAN to pace-and-drive the surrounding atrium. In relation to this, Hong et al. (2005) suggested that electrical activity might be initiated in the atrio-ventricular node in such patients, which could potentially explain the lack of apparent P waves.

Heterozygous and homozygous forms of the V307L mutation exerted weaker effects on the SAN pacemaking rate due to less pervasive effects on I_{Ks} – the measured rates of 69 and 64 bpm, respectively, were within the normal range of heart rates in humans. It is relevant in this regard that there have been no reports of sinus bradycardia associated with the V307L mutation in *KCNQ1*, with physical examination of the first proband identified revealing no electrophysiological anomalies other than a shortened QT interval, as well as the episode of ventricular fibrillation for which he was admitted to hospital (Bellocq et al., 2004).

V141M and V307L KCNQ1 Mutations Shorten Human Atrial APD Through Different Mechanisms

The V141M and V307L KCNQ1 mutations have been shown in previous *in silico* studies to shorten the human ventricular APD (Adeniran et al., 2017; Lee et al., 2017). In this study, distinct mechanisms of APD shortening between the mutations in human atrial cells were identified. Whereas the V141M

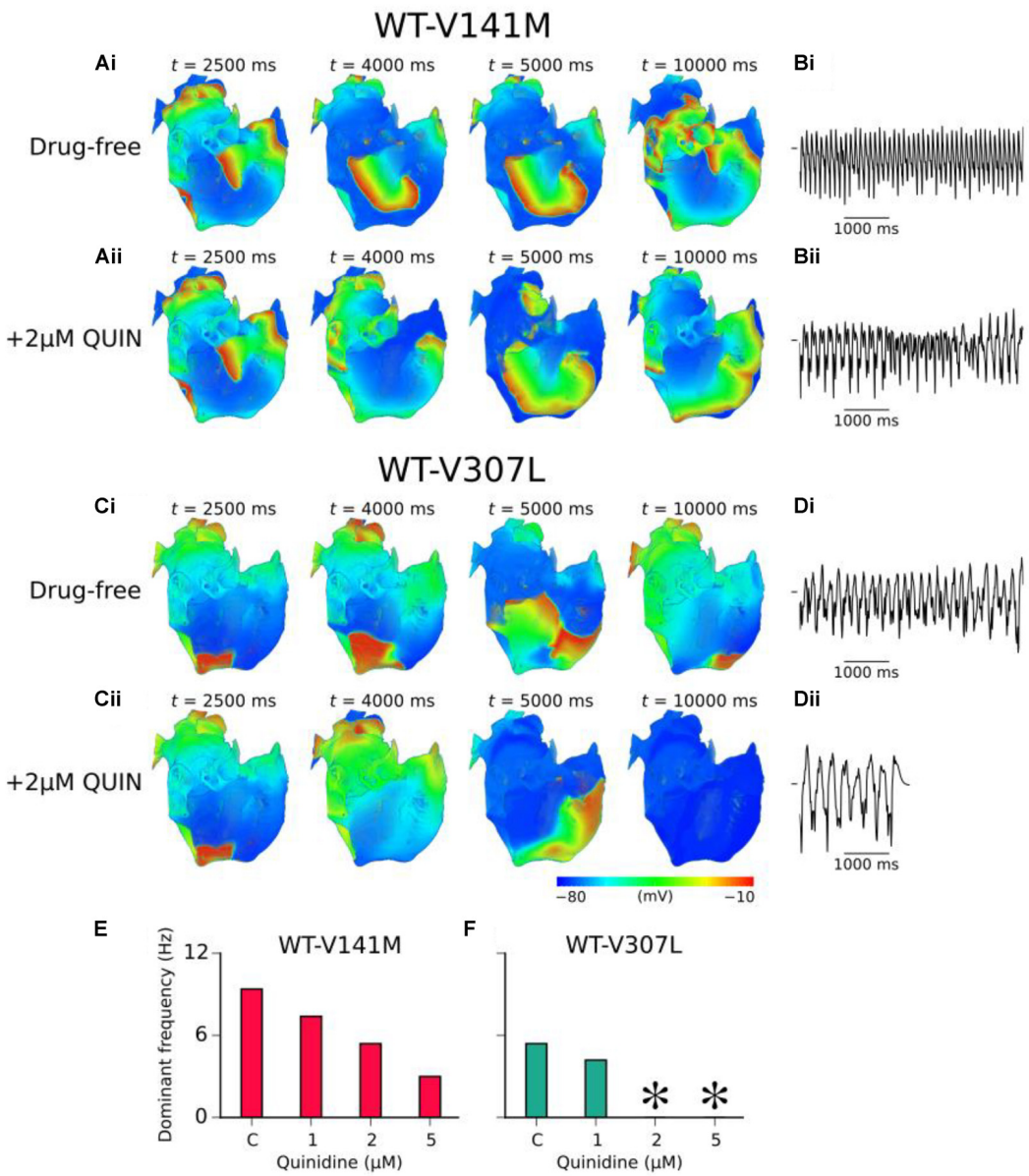

FIGURE 7 | Effects of quinidine on re-entry dynamics under SQT2 mutation conditions. **(A)** Snapshots of re-entrant scroll waves at various time points after initiation of a scroll wave in the 3D anatomical human atria under drug-free WT-V141M **(i)**, and WT-V141M + 2 μM quinidine (QUIN) **(ii)** conditions, with **(B)** corresponding pseudo ECG (pECG) recorded during the final 5.0 s. **(C)** Snapshots of re-entrant scroll waves following re-entry initiation under drug-free WT-V307L **(i)**, and WT-V307L + 2 μM QUIN **(ii)** conditions, with **(D)** corresponding pECGs recorded during the final 5.0 s. Dominant frequencies (DF) calculated from pECGs in control (c) WT-V141M **(E)** and WT-V307L **(F)** conditions and upon application of various concentrations of quinidine. In drug simulations, QUIN was applied at t = 2.5 s. *Denotes DF was not calculated as re-entry termination occurred.

mutation conditions caused a more triangular AP morphology due to increased I_{Ks} early during the AP, the V307L mutation conditions preserved the 'spike and dome' morphology of the AP due to less pervasive effects on I_{Ks} (**Figure 3** and **Supplementary Figure S5**). Furthermore, increased APD dispersion between cells of the pulmonary veins and left atrium under SQT2 mutation conditions was observed (**Supplementary Figure S5**), which may promote high frequency excitation or microreentrant sources around this junction as a mechanism of AF in this context.

Different effects of the V141M and V307L KCNQ1 mutations on the human atrial AP resulted in opposing effects on the maximum slope of APD restitution – additional simulations in **Supplementary Investigation 2.1** revealed that increased I_{Ks} conductance alone, similar to kinetic changes seen with the V307L KCNQ1 mutation, increased the slope of restitution,

whereas constitutively active I_{Ks}, as observed for the V141M KCNQ1 mutation, favoured a decrease in the maximum slope of restitution. For the *KCNQ1* V141M mutation, the slope was substantially reduced. This is consistent with the study of Kharche et al. (2012), in which the S140G KCNQ1 mutation which includes an instantaneous component of I_{Ks} similar to that induced by the V141M mutation, was shown to reduce markedly the maximum slope of restitution in the CRN human atrial cell model (Courtemanche et al., 1998). The V307L mutation, on the other hand, was shown to increase the slope of restitution, which was also reported in the investigation of the *KCNQ1* V307L mutation in human ventricles by Adeniran et al. (2017). Both of these key findings were reproduced in supplementary simulations using the human atrial model of Grandi et al. (2011) (**Supplementary Investigation 2.2**).

SQT2 Mutations Promote Human Atrial Arrhythmogenesis

Action potential duration shortening at the cellular level manifested as a reduction in the ERP across all pacing rates for both SQT2 mutations. The CV was largely unaffected, and thus the profound reduction in the excitation WL observed under SQT2 mutation conditions can be attributed almost exclusively to the reduction in ERP. This is in contrast to findings pertaining to *KCNJ2*-linked SQTS presented in our previous study (Whittaker et al., 2017b), where reduced WL was found to be mediated by a decrease in both ERP and CV; this emphasises the value of multi-scale computational modelling in elucidating phenotypic differences between different variants of the SQTS. In idealised 2D sheet simulations, WT tissue did not support a sustained spiral wave, whereas the V141M and V307L mutations both favoured sustenance of re-entry. The V141M mutation produced stationary spiral waves, which were also observed in the study of Kharche et al. (2012) for the S140G KCNQ1 mutation which similarly induces an instantaneous component of I_{Ks} (Chen et al., 2003). In contrast, the V307L mutation conditions produced spiral waves which meandered to a larger extent, spontaneously breaking and forming multiple wavelets in the homozygous condition. This mutant form showed a steep (>1) maximum slope of restitution and alternans, which are known to promote electrical instability in cardiac tissue.

In 3D human atria simulations the V141M mutation produced stationary scroll waves, even in the presence of electrical and anatomical heterogeneities. The persistent nature of re-entry in this condition compared to the WT, in which scroll waves quickly self-terminated, can be explained in terms of tissue excitation WL. Increased I_{Ks} associated with the V141M mutation abbreviated APD and ERP, which consequently reduced the excitation WL. This is a measure of the spatial requirement for a functional re-entrant circuit, and thus reduced WL facilitates conduction of high rate excitation waves within a limited atrial mass (Kharche et al., 2012; Whittaker et al., 2017b). The findings of this study thus substantiate a causative link between the *KCNQ1* V141M mutation and multiple reports of recalcitrant AF in affected patients (Hong et al., 2005; Villafañe et al., 2014; Righi et al., 2016). There have been no reported episodes of AF consequent to the V307L mutation to date. However, as the number of V307L SQTS patients is very small (Hu et al., 2017), and AF can be paroxysmal and/or asymptomatic, atrial arrhythmias arising from this mutation cannot be ruled out. The phenotypically accurate computational models in this study predicted that the V307L KCNQ1 mutation facilitates sustenance of re-entrant excitations in the human atria, albeit with decreased stability, stationarity, and DF compared to V141M mutation conditions.

Quinidine Controls Rate but not Rhythm of Arrhythmic Atrial Excitations in SQT2

To date, no specific blockers of I_{Ks} are in clinical use (Hancox et al., 2018). The current front-line pharmacological treatment for *hERG*-related SQTS patients is the class Ia anti-arrhythmic drug quinidine (Gaita et al., 2004; Hu et al., 2017) – a multi-channel blocker which exerts a mild blocking effect on I_{Ks}. Under the WT-V141M mutation condition, quinidine reduced the DF of re-entry, but did not terminate re-entrant activity at any of the concentrations tested. This is consistent with the findings of Righi et al. (2016) who reported that recurrent AF associated with the *KCNQ1* V141M mutation was unresponsive to multiple anti-arrhythmic agents (failing to revert to sinus rhythm), including (hydro)quinidine (Righi et al., 2016). Re-entrant excitations in the human atria under the WT-V307L mutation condition, on the other hand, were responsive to quinidine therapy, with concentrations of 2 and 5 μM terminating re-entry in our model. The findings of the 3D simulations were consistent with cellular level APD/ERP predictions, in which quinidine was shown to effectively restore the APD only in the WT-V307L condition, but consistently increased the ERP in a dose-dependent manner under both mutation conditions (including in the presence of AF remodelling; **Supplementary Table S7**). These results suggest that in the setting of SQT2-mediated atrial arrhythmias, quinidine may be a more effective strategy for rate control than rhythm control.

It has been reported previously that quinidine was ineffective at prolonging the QT interval in the setting of *KCNQ1* V141M-mediated SQT2 (Righi et al., 2016). As SQT2 is caused by a gain-of-function in I_{Ks}, it is likely that an anti-arrhythmic drug which blocks I_{Ks} to a larger degree is required to reverse the phenotype. In a previous computational study of SQT2 in the human ventricles by Adeniran et al. (2017), I_{Ks} block was demonstrated to effectively terminate re-entrant excitations associated with the V307L mutation in *KCNQ1*, as well as to restore the APD/QT interval in both V307L and V141M conditions. Selective I_{Ks} block as a potential therapeutic strategy has also been supported in an experimental study (Campbell et al., 2013). I_{K1} has also been suggested to be a potential therapeutic target in the context of V141M-mediated SQT2, based on the reduction in transmural APD heterogeneity and prolongation of the QT interval observed following I_{K1} block in computational models of the human ventricles (Lee et al., 2017).

Limitations

There are a number of limitations associated with the simulations presented in this study. Potential limitations of the 3D anatomical human atria, regional cell models, and drug binding models have been discussed in our previous publications (Colman et al., 2013; Ni et al., 2017; Whittaker et al., 2017a,b). Specific limitations to be considered here are as follows. (1) Previous *in vitro* experiments have shown that blocking potency of I_{Ks} blockers can be reduced for recombinant channels containing *KCNQ1*-linked SQT2 mutations, as observed for chromanol 293B (Lerche et al., 2007; El Harchi et al., 2010) but not mefloquine (El Harchi et al., 2010). Whether or not quinidine block of I_{Ks} is altered by the SQT2 mutations was not considered due to lack of experimental data, although even at the highest concentration tested (5 μM), the block of I_{Ks} was small (∼10%). (2) Late sodium current, I_{NaL}, is not present in the CNZ model. Quinidine block of I_{NaL} could potentially reduce the APD prolongation observed in this study, although the presence and contribution of I_{NaL} in human atrial myocytes at physiological temperature remains to be confirmed (Poulet et al., 2015). (3) There are currently no data on the presence or absence of electrical and/or structural remodelling in the SQTS. Inclusion of these factors was considered in the **Supplementary Material** for completeness – these additional simulations do not change the fundamental mechanistic conclusions drawn in this study. (4) The heterozygous formulations of SQT2 mutants used in this study relied on the simplifying assumption that both V141M and V307L I_{Ks} behave similarly to a 50:50 mixture of WT and mutant channels. In reality, the channel populations may be more complex, with each channel consisting of both WT and mutant *KCNQ1* subunits. In our previous study (Zhang et al., 2008), the effects of varying mutant subunit composition in SQT2 were investigated, based on different expression/co-expression ratios used by Bellocq et al. (2004) in the original paper describing the V307L KCNQ1 mutation. In that study (Zhang et al., 2008), it was found that the degree of shortening of the ventricular APD and QT interval increased progressively with the level of V307L expression. Furthermore, in our previous study (Adeniran et al., 2017), the heterozygote formulation used for V307L was shown to reproduce QT interval shortening and increased T wave associated with the SQTS phenotype, thus supporting the approach adopted in this study. (5) The effects of human atrial contraction were not considered, which could feasibly modulate the atrial AP under SQTS conditions (Whittaker et al., 2015), and thus re-entrant electrical activity. (6) Scroll wave dynamics in the 3D anatomical human atria model should be interpreted with caution, as dynamic behaviour of re-entrant excitations, including wave break, can depend critically on initial conditions, especially in such a complex geometry (Benson et al., 2007).

CONCLUSION

The multi-scale computational approach adopted in this study allowed phenotypic differences associated with two distinct *KCNQ1*-linked SQTS mutations to be assessed. Furthermore, the response of arrhythmic excitation waves to clinically relevant doses of quinidine under SQT2 conditions was probed. The simulations substantiated a causative link between the *KCNQ1* V141M mutation and an AF/sinus bradycardia phenotype which has been observed clinically. In addition, the V307L mutation in *KCNQ1* was predicted to promote human atrial arrhythmogenesis whilst not significantly affecting pacemaking function. Quinidine was shown to be useful for rate control of atrial arrhythmias associated with SQT2, but appears likely to be less reliable for rhythm control in this setting.

AUTHOR CONTRIBUTIONS

DW, JH, and HZ conceived the experiments. DW developed and validated the computer models and performed the numerical experiments and analysis. DW, MC, and HN provided the computing tools. All authors wrote the manuscript.

FUNDING

DW was supported by the British Heart Foundation (FS/14/5/30533 – HZ and JH) and is currently supported by a Wellcome Trust ISSF fellowship (204825/Z/16/Z). This work was also supported by grants from EPSRC (United Kingdom) (EP/J00958X/1 and EP/I029826/1), MC-IRSES CORDIS3D (317766), NSFC (61179009), Shenzhen Science and Technology Innovation Committee (JCYJ20151029173639477 and JSGG20160229125049615), and a Medical Research Council Strategic Skills Fellowship to MC (MR/M014967/1). The funders had no role in study design, data collection and analysis, decision to publish, or preparation of the manuscript.

ACKNOWLEDGMENTS

JH gratefully acknowledges receipt of a University of Bristol research fellowship.

SUPPLEMENTARY MATERIAL

The Supplementary Material for this article can be found online at: https://www.frontiersin.org/articles/10.3389/fphys.2018.01402/full#supplementary-material

REFERENCES

Adeniran, I., Whittaker, D. G., Harchi, A. E., Hancox, J. C., and Zhang, H. (2017). In silico investigation of a KCNQ1 mutation associated with short QT syndrome. *Sci. Rep.* 7:8469. doi: 10.1038/s41598-017-08367-2

Bellocq, C., van Ginneken, A. C. G., Bezzina, C. R., Alders, M., Escande, D., Mannens, M. M., et al. (2004). Mutation in the KCNQ1 gene leading to the short qt-interval syndrome. *Circulation* 109, 2394–2397. doi: 10.1161/01.CIR.0000130409.72142.FE

Benson, A. P., Ries, M. E., and Holden, A. V. (2007). "Effects of geometry and architecture on re-entrant scroll wave dynamics in human virtual ventricular

tissues," in *Functional Imaging and Modeling of the Heart* eds P. Mihaela and W. Graham (Berlin: Springer), 200–209. doi: 10.1007/978-3-540-72907-5-21

Biktashev, V. N., and Holden, A. V. (1998). Reentrant waves and their elimination in a model of mammalian ventricular tissue. *Chaos Interdiscip. J. Nonlinear Sci.* 8, 48–56. doi: 10.1063/1.166307

Caballero, R., de la Fuente, M. G., Gómez, R., Barana, A., Amorós, I., Dolz-Gaitón, P., et al. (2010). In humans, chronic atrial fibrillation decreases the transient outward current and ultrarapid component of the delayed rectifier current differentially on each atria and increases the slow component of the delayed rectifier current in both. *J. Am. Coll. Cardiol.* 55, 2346–2354. doi: 10.1016/j.jacc.2010.02.028

Campbell, C. M., Campbell, J. D., Thompson, C. H., Galimberti, E. S., Darbar, D., Vanoye, C. G., et al. (2013). Selective targeting of gain-of-function KCNQ1 mutations predisposing to atrial fibrillation. *Circ. Arrhythm. Electrophysiol.* 6, 960–966. doi: 10.1161/CIRCEP.113.000439

Chen, Y.-H., Xu, S.-J., Bendahhou, S., Wang, X.-L., Wang, Y., Xu, W.-Y., et al. (2003). KCNQ1 gain-of-function mutation in familial atrial fibrillation. *Science* 299, 251–254. doi: 10.1126/science.1077771

Christophersen, I. E., and Ellinor, P. T. (2016). Genetics of atrial fibrillation: from families to genomes. *J. Hum. Genet.* 61, 61–70. doi: 10.1038/jhg.2015.44

Colman, M. A., Aslanidi, O. V., Kharche, S., Boyett, M. R., Garratt, C., Hancox, J. C., et al. (2013). Pro-arrhythmogenic effects of atrial fibrillation-induced electrical remodelling: insights from the three-dimensional virtual human atria. *J. Physiol.* 591, 4249–4272. doi: 10.1113/jphysiol.2013.254987

Colman, M. A., Ni, H., Liang, B., Schmitt, N., and Zhang, H. (2017). In silico assessment of genetic variation in KCNA5 reveals multiple mechanisms of human atrial arrhythmogenesis. *PLoS Comput. Biol.* 13:e1005587. doi: 10.1371/journal.pcbi.1005587.

Courtemanche, M., Ramirez, R. J., and Nattel, S. (1998). Ionic mechanisms underlying human atrial action potential properties: insights from a mathematical model. *Am. J. Physiol. Heart Circ. Physiol.* 275, H301–H321. doi: 10.1152/ajpheart.1998.275.1.H301

Das, S., Makino, S., Melman, Y. F., Shea, M. A., Goyal, S. B., Rosenzweig, A., et al. (2009). Mutation in the S3 segment of KCNQ1 results in familial lone atrial fibrillation. *Heart Rhythm* 6, 1146–1153. doi: 10.1016/j.hrthm.2009.04.015

El Harchi, A., McPate, M. J., Zhang, Y. H., Zhang, H., and Hancox, J. C. (2010). Action potential clamp and mefloquine sensitivity of recombinant "I KS" channels incorporating the V307L KCNQ1 mutation. *J. Physiol. Pharmacol. Off. J. Pol. Physiol. Soc.* 61, 123–131.

Fabbri, A., Fantini, M., Wilders, R., and Severi, S. (2017). Computational analysis of the human sinus node action potential: model development and effects of mutations. *J. Physiol.* 595, 2365–2396. doi: 10.1113/JP273259

Gaita, F., Giustetto, C., Bianchi, F., Schimpf, R., Haissaguerre, M., Calò, L., et al. (2004). Short QT syndrome: pharmacological treatment. *J. Am. Coll. Cardiol.* 43, 1494–1499. doi: 10.1016/j.jacc.2004.02.034

Giustetto, C., Schimpf, R., Mazzanti, A., Scrocco, C., Maury, P., Anttonen, O., et al. (2011). Long-term follow-up of patients with short qt syndrome. *J. Am. Coll. Cardiol.* 58, 587–595. doi: 10.1016/j.jacc.2011.03.038

González de la Fuente, M., Barana, A., Gómez, R., Amorós, I., Dolz-Gaitón, P., Sacristán, S., et al. (2013). Chronic atrial fibrillation up-regulates β1-adrenoceptors affecting repolarizing currents and action potential duration. *Cardiovasc. Res.* 97, 379–388. doi: 10.1093/cvr/cvs313

Grandi, E., Pandit, S. V., Voigt, N., Workman, A. J., Dobrev, D., Jalife, J., et al. (2011). Human atrial action potential and Ca2+ model: sinus rhythm and chronic atrial fibrillation. *Circ. Res.* 109, 1055–1066. doi: 10.1161/CIRCRESAHA.111.253955

Hancox, J. C., Whittaker, D. G., Du, C., Stuart, A. G., and Zhang, H. (2018). Emerging therapeutic targets in the short QT syndrome. *Expert Opin. Ther. Targets.* 22, 439–451. doi: 10.1080/14728222.2018.1470621.

Harrell, D. T., Ashihara, T., Ishikawa, T., Tominaga, I., Mazzanti, A., Takahashi, K., et al. (2015). Genotype-dependent differences in age of manifestation and arrhythmia complications in short QT syndrome. *Int. J. Cardiol.* 190, 393–402. doi: 10.1016/j.ijcard.2015.04.090

Hasdemir, C. (2016). Atrial arrhythmias in inherited arrhythmogenic disorders. *J. Arrhythmia* 32, 366–372. doi: 10.1016/j.joa.2015.11.007

Hong, K., Piper, D. R., Diaz-Valdecantos, A., Brugada, J., Oliva, A., Burashnikov, E., et al. (2005). De novo KCNQ1 mutation responsible for atrial fibrillation and short QT syndrome in utero. *Cardiovasc. Res.* 68, 433–440. doi: 10.1016/j.cardiores.2005.06.023

Hu, D., Li, Y., Zhang, J., Pfeiffer, R., Gollob, M. H., Healey, J., et al. (2017). The phenotypic spectrum of a mutation hotspot responsible for the short QT syndrome. *JACC Clin. Electrophysiol.* 3, 727–743. doi: 10.1016/j.jacep.2016.11.013

Kharche, S., Adeniran, I., Stott, J., Law, P., Boyett, M. R., Hancox, J. C., et al. (2012). Pro-arrhythmogenic effects of the S140G KCNQ1 mutation in human atrial fibrillation – insights from modelling. *J. Physiol.* 590, 4501–4514. doi: 10.1113/jphysiol.2012.229146

Krueger, M. W., Schmidt, V., Tobón, C., Weber, F. M., Lorenz, C., Keller, D. U. J., et al. (2011). "Modeling atrial fiber orientation in patient-specific geometries: a semi-automatic rule-based approach," in *Functional Imaging and Modeling of the Heart Lecture Notes in Computer Science*, eds I. E. Magnin, J. Montagnat, P. Clarysse, J. Nenonen, and T. Katila (Berlin: Springer), 223–232. doi: 10.1007/978-3-642-21028-0-28

Lee, H.-C., Rudy, Y., Liang, H., Chen, C.-C., Luo, C.-H., Sheu, S.-H., et al. (2017). Pro-arrhythmogenic effects of the V141M KCNQ1 mutation in short QT syndrome and its potential therapeutic targets: insights from modeling. *J. Med. Biol. Eng.* 37, 780–789. doi: 10.1007/s40846-017-0257-x

Lerche, C., Bruhova, I., Lerche, H., Steinmeyer, K., Wei, A. D., Strutz-Seebohm, N., et al. (2007). Chromanol 293B binding in KCNQ1 (Kv7.1) channels involves electrostatic interactions with a potassium ion in the selectivity filter. *Mol. Pharmacol.* 71, 1503–1511. doi: 10.1124/mol.106.031682

Lundby, A., Ravn, L. S., Svendsen, J. H., Olesen, S.-P., and Schmitt, N. (2007). KCNQ1 mutation Q147R is associated with atrial fibrillation and prolonged QT interval. *Heart Rhythm* 4, 1532–1541. doi: 10.1016/j.hrthm.2007.07.022

Moreno, C., Oliveras, A., de la Cruz, A., Bartolucci, C., Muñoz, C., Salar, E., et al. (2015). A new KCNQ1 mutation at the S5 segment that impairs its association with KCNE1 is responsible for short QT syndrome. *Cardiovasc. Res.* 107, 613–623. doi: 10.1093/cvr/cvv196

Moreno, J. D., Lewis, T. J., and Clancy, C. E. (2016). Parameterization for in-silico modeling of ion channel interactions with drugs. *PLoS One* 11:e0150761. doi: 10.1371/journal.pone.0150761

Nenov, N. I., Crumb, W. J., Pigott, J. D., Harrison, L. H., and Clarkson, C. W. (1998). Quinidine interactions with human atrial potassium channels. *Circ. Res.* 83, 1224–1231. doi: 10.1161/01.RES.83.12.1224

Ni, H., Whittaker, D. G., Wang, W., Giles, W. R., Narayan, S. M., and Zhang, H. (2017). Synergistic anti-arrhythmic effects in human atria with combined use of sodium blockers and acacetin. *Front. Physiol.* 8:946. doi: 10.3389/fphys.2017.00946

Poulet, C., Wettwer, E., Grunnet, M., Jespersen, T., Fabritz, L., Matschke, K., et al. (2015). Late sodium current in human atrial cardiomyocytes from patients in sinus rhythm and atrial fibrillation. *PLoS One* 10:e0131432. doi: 10.1371/journal.pone.0131432

Restier, L., Cheng, L., and Sanguinetti, M. C. (2008). Mechanisms by which atrial fibrillation-associated mutations in the S1 domain of KCNQ1 slow deactivation of IKs channels. *J. Physiol.* 586, 4179–4191. doi: 10.1113/jphysiol.2008.157511

Righi, D., Silvetti, M. S., and Drago, F. (2016). Sinus bradycardia, junctional rhythm, and low-rate atrial fibrillation in short QT syndrome during 20 years of follow-up: three faces of the same genetic problem. *Cardiol. Young* 26, 589–592. doi: 10.1017/S1047951115001432

Schimpf, R., Wolpert, C., Gaita, F., Giustetto, C., and Borggrefe, M. (2005). Short QT syndrome. *Cardiovasc. Res.* 67, 357–366. doi: 10.1016/j.cardiores.2005.03.026

Seebohm, G., Lerche, C., Busch, A., and Bachmann, A. (2001). Dependence of IKs biophysical properties on the expression system. *Pflüg. Arch.* 442, 891–895. doi: 10.1007/s004240100608

Seemann, G., Höper, C., Sachse, F. B., Dössel, O., Holden, A. V., and Zhang, H. (2006). Heterogeneous three-dimensional anatomical and electrophysiological model of human atria. *Philos. Trans. R. Soc. Lond. Math. Phys. Eng. Sci.* 364, 1465–1481. doi: 10.1098/rsta.2006.1781

Silva, J., and Rudy, Y. (2005). Subunit interaction determines IKs participation in cardiac repolarization and repolarization reserve. *Circulation* 112, 1384–1391. doi: 10.1161/CIRCULATIONAHA.105.543306

Verkerk, A. O., Wilders, R., van Borren, M. M., Peters, R. J., Broekhuis, E., Lam, K., et al. (2007). Pacemaker current (If) in the human sinoatrial node. *Eur. Heart J.* 28, 2472–2478. doi: 10.1093/eurheartj/ehm339

Villafañe, J., Fischbach, P., and Gebauer, R. (2014). Short QT syndrome manifesting with neonatal atrial fibrillation and bradycardia. *Cardiology* 128, 236–240. doi: 10.1159/000360758

Whittaker, D. G., Colman, M. A., Ni, H., Hancox, J. C., and Zhang, H. (2015). "In silico investigation of short QT syndrome-linked potassium channel mutations on electro-mechanical function of human atrial cells," in *Proceedings of the 2015 Computing in Cardiology Conference (CinC)* (Nice: IEEE), 853–856. doi: 10.1109/CIC.2015.7411045

Whittaker, D. G., Ni, H., Benson, A. P., Hancox, J. C., and Zhang, H. (2017a). Computational analysis of the mode of action of disopyramide and quinidine on hERG-linked short QT syndrome in human ventricles. *Front. Physiol.* 8:759. doi: 10.3389/fphys.2017.00759

Whittaker, D. G., Ni, H., Harchi, A. E., Hancox, J. C., and Zhang, H. (2017b). Atrial arrhythmogenicity of KCNJ2 mutations in short QT syndrome: insights from virtual human atria. *PLoS Comput. Biol.* 13:e1005593. doi: 10.1371/journal.pcbi.1005593

Wu, Z.-J., Huang, Y., Fu, Y.-C., Zhao, X.-J., Zhu, C., Zhang, Y., et al. (2015). Characterization of a Chinese KCNQ1 mutation (R259H) that shortens repolarization and causes short QT syndrome 2. *J. Geriatr. Cardiol. JGC* 12, 394–401. doi: 10.11909/j.issn.1671-5411.2015.04.002

Zhang, H., Kharche, S., Holden, A. V., and Hancox, J. C. (2008). Repolarisation and vulnerability to re-entry in the human heart with short QT syndrome arising from KCNQ1 mutation—a simulation study. *Prog. Biophys. Mol. Biol.* 96, 112–131. doi: 10.1016/j.pbiomolbio.2007.07.020

Conflict of Interest Statement: The authors declare that the research was conducted in the absence of any commercial or financial relationships that could be construed as a potential conflict of interest.

Copyright © 2018 Whittaker, Colman, Ni, Hancox and Zhang. This is an open-access article distributed under the terms of the Creative Commons Attribution License (CC BY). The use, distribution or reproduction in other forums is permitted, provided the original author(s) and the copyright owner(s) are credited and that the original publication in this journal is cited, in accordance with accepted academic practice. No use, distribution or reproduction is permitted which does not comply with these terms.

frontiers in Physiology

ORIGINAL RESEARCH
published: 14 March 2019
doi: 10.3389/fphys.2019.00177

Simulation of the Perfusion of Contrast Agent Used in Cardiac Magnetic Resonance: A Step Toward Non-invasive Cardiac Perfusion Quantification

João R. Alves[1], *Rafael A. B. de Queiroz*[1], *Markus Bär*[2] *and Rodrigo W. dos Santos*[1]*

[1] Graduate Program in Computational Modeling, Universidade Federal de Juiz de Fora, Juiz de Fora, Brazil, [2] Department of Mathematical Modeling and Data Analysis, Physikalisch-Technische Bundesanstalt, Berlin, Germany

This work presents a new mathematical model to describe cardiac perfusion in the myocardium as acquired by cardiac magnetic resonance (CMR) perfusion exams. The combination of first pass (or contrast-enhanced CMR) and late enhancement CMR is a widely used non-invasive exam that can identify abnormal perfused regions of the heart via the use of a contrast agent (CA). The exam provides important information to the diagnosis, management, and prognosis of ischemia and infarct: perfusion on different regions, the status of microvascular structures, the presence of fibrosis, and the relative volume of extracellular space. This information is obtained by inferring the spatiotemporal dynamics of the contrast in the myocardial tissue from the acquired images. The evaluation of these physiological parameters plays an important role in the assessment of myocardial viability. However, the nature of cardiac physiology poses great challenges in the estimation of these parameters. Briefly, these are currently estimated qualitatively via visual inspection of images and comparison of relative brightness between different regions of the heart. Therefore, there is a great urge for techniques that can help to quantify cardiac perfusion. In this work, we propose a new mathematical model based on multidomain flow in porous media. The model is based on a system of partial differential equations. Darcy's law is used to obtain the pressure and velocity distribution. CA dynamics is described by reaction-diffusion-advection equations in the intravascular space and in the interstitial space. The interaction of fibrosis and the CA is also considered. The new model treats the domains as anisotropic media and imposes a closed loop of intravascular flow, which is necessary to reproduce the recirculation of the CA. The model parameters were adjusted to reproduce clinical data. In addition, the model was used to simulate different scenarios: normal perfusion; endocardial ischemia due to stenosis in a coronary artery in the epicardium; and myocardial infarct. Therefore, the computational model was able to correlate anatomical features, stenosis and the presence of fibrosis, with functional ones, cardiac perfusion. Altogether, the results suggest that the model can support the process of non-invasive cardiac perfusion quantification.

Keywords: myocardial perfusion imaging, contrast enhanced MRI, porous media, computational physiology and medicine, perfusion quantification

OPEN ACCESS

Edited by:
Eun Bo Shim,
Kangwon National University, South Korea

Reviewed by:
Daniel Andrew Beard,
University of Michigan, United States
Ki Moo Lim,
Kumoh National Institute of Technology, South Korea

***Correspondence:**
Rodrigo W. dos Santos
rodrigo.weber@ufjf.edu.br

Specialty section:
This article was submitted to Computational Physiology and Medicine, a section of the journal Frontiers in Physiology

Received: *25 May 2018*
Accepted: *12 February 2019*
Published: *14 March 2019*

Citation:
Alves JR, de Queiroz RAB, Bär M and dos Santos RW (2019) Simulation of the Perfusion of Contrast Agent Used in Cardiac Magnetic Resonance: A Step Toward Non-invasive Cardiac Perfusion Quantification. Front. Physiol. 10:177. doi: 10.3389/fphys.2019.00177

1. INTRODUCTION

Cardiovascular diseases have a close relation with high blood pressure, smoking, diabetes, lack of exercise, obesity, high blood cholesterol, poor diet, and excessive alcohol (Mendis et al., 2011; Mehta et al., 2015). Many of these conditions can affect *myocardial perfusion* (MP), which is the distribution process of oxygen and nutrients to the cardiac tissue. Among all the injuries related to a compromised cardiac perfusion that can evolve inside the heart, one that occurs frequently is the obstruction of a coronary artery, or stenosis. This leads to perfusion problems, the *coronary artery diseases* (CAD), also referred to as *ischemic heart diseases* (IHD) or simply as *ischemia*. Basically, the stenosis reduces the supply of oxygen and nutrients (perfusion defect) in the region of the myocardium that should be irrigated by the coronary artery in question. This condition may lead to more severe cases, like an infarct, which can provoke irreversible damages to the cardiac tissue, including death. There are several exams used to evaluate myocardial perfusion in clinical practice. Two that are widely used are *computer tomography* (CT) and the *magnetic resonance imaging* (MRI). Both consists in the administration in the patient of a *contrast agent* (CA) which, in the images generated by the chosen protocol, assume a specific contrast on poor perfused regions. The information that can be inferred with the acquired images has a fundamental role in the diagnosis, management, and prognosis of ischemia and infarct. In this work we present a new mathematical model to describe cardiac perfusion in the myocardium as acquired by cardiac magnetic resonance perfusion exams. Our results suggest that the model is an valuable tool that can support the process of non-invasive cardiac perfusion quantification. The next section gives more detailed explanations of MP and of contrast-enhanced MRI, which is the focus of this work.

1.1. Background

For the heart to have the necessary strength to pump blood throughout the body, it needs a constant supply of oxygen and nutrients. This process can be summarized as follows: the blood enters into the myocardium through the epicardial coronary arteries. As **Figure 1** summarizes, the coronary arteries branches in smaller arteries, the arterioles. These in turn, branches into even smaller vessels. This process continues down to the capillaries, which are the smallest vessels in terms of diameter. It is on this level where the leakage of oxygen and nutrients from intra to extravascular media happens. After that, the capillaries increase in size and become veins. The venous blood follows the opposite direction and arrives at the venules followed by the coronary veins, these last vessels leave the epicardium to the lungs to be filtrated. Previous studies have shown that the blood-tissue exchange on the capillary level may be a complex phenomenon. For instance, in Bassingthwaighte et al. (1989) and Dash and Bassingthwaighte (2006), a multidomain model that accounts for the blood flow in capillary, endothelium, interstitium and parenchymal cells was developed, that includes the fluid exchange between each domain. However, the present work will not take into account such level of details.

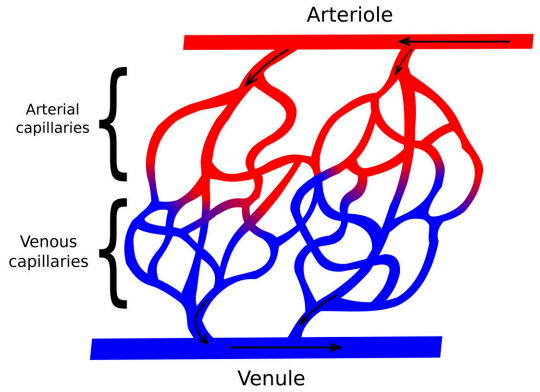

FIGURE 1 | Simplified scheme representing the relation between arteries and veins, in addition with the direction of blood flow. The coronary arteries get smaller and become arterioles, which get smaller again and become arterial capillaries. After the leak of oxygen and nutrients, the arterial capillaries now are called venous capillaries, which get bigger, becoming venules, and finally coronary veins.

In order to evaluate MP, several exams can be used. One that provides high quality images is *computer tomography* (CT). However, CT uses a harmful and allergenic substance as contrast agent (Brenner and Hall, 2007; Kroeker et al., 2011). Another option is contrast-enhanced MRI (Nikolaou et al., 2011). This one consists in the administration of a dose of *Gadolinium with diethylenetriaminepentacetate* (Gd-DTPA) in the patient that helps to identify patterns in the myocardial tissue. Contrast-enhanced MRI has different protocols. We can mention, for example, the *first pass* (FP) (Gerber et al., 2008) and the *late-enhancement* (LE) (Pop et al., 2013). As the name says, the FP uses the first passage of the CA through the circulatory system to generate the images, in which the regions that are well perfused by the CA acquire a characteristic glow, whereas dark regions indicate problems in perfusion. These problems can be related for instance with ischemia or infarct regions. The FP evaluates the myocardium for 50 s. On the other hand, LE enables the differentiation between a ischemic region, potentially still viable, and infarct. This exam evaluates the myocardium 10 min after the CA administration, and opposite to the FP, the infarct area is the one that gets brighter. Therefore, both FP and LE can be used as complementary MRI perfusion exams.

Nevertheless, the evaluation of the images acquired by the exams is a tedious and error-prone process performed by highly specialized physicians. To support and improve this process different tools that seek a more quantitative evaluation of myocardial perfusion are under development. In Chiribiri et al. (2013) and Alves et al. (2017), such process is studied using phantoms specifically designed to simulate contrast-enhanced MRI exams. In Aquaro et al. (2013), flow quantification is approached by calculating the maximum upslope of the myocardial signal. In Jerosch-Herold (2010) and Zarinabad et al. (2012), the quantification is given in terms of signal deconvolution techniques (Fermi deconvolution). In addition, several mathematical models have been developed with this goal.

In Michler et al. (2013), a model is presented that captures pressure and velocity profiles of the blood in 3D representation of the heart. In Alves et al. (2016), the authors performed simulations considering regions with low permeability, showing the behavior of the CA in different scenarios. In Cookson et al. (2014), for the purpose of reproducing the exchange of CA between intra and extravascular spaces, the authors take into account a 2-domain formulation. Although clearly substantial progress has been made, there is still room for further improvements.

Another invasive exam that indirectly evaluates perfusion is the *Fractional Flow Reserve* (FFR) (Lee et al., 2017), which gives information related to the severity of a coronary stenosis. It is important to mention that there are softwares that can estimate FFR by combining mathematical models (also PDEs) and images acquired by CT exams. These softwares are available for clinical use (Hlatky et al., 2015).

In this work, we propose a similar tool that also uses mathematical models based on PDEs and images, in this case from contrast-enhanced MRI exams. The model simulates the blood flow in a short-axis slice of the myocardium (cardiac muscle). Simulations of the model provides the dynamics of CA in the initial stage, as captured by *first pass*, and after many minutes of initial CA injection, as captured by *late enhancement*. In order to describe myocardial blood flow, Darcy approach for fluid in porous media is used, coupled to advection-diffusion-reaction equations to evaluate the CA dynamics. Clinical data were used to adjust the parameters of the model. Some specific contributions of this work are: (1) the simulation of CA dynamics in a domain that represents the short axis of the myocardium; (2) the development and test of a mathematical formulation that takes into account three domains (intravascular, extravascular, and fibrosis); (3) a model that contains a closed loop of intravascular flow, which is necessary to reproduce the recirculation of the CA; (4) the model parameters were adjusted to reproduce clinical data; and (5) analysis of the CA dynamics and its quantification for scenarios of normal perfusion, endocardial ischemia, and myocardial infarct.

In section 2 the multi-domain mathematical model is presented. Section 3 describes the numerical methods. Section 4 presents the results obtained with the simulations. Section 5 presents a general discussion of the results and the limitations of the model. Finally, section 5.3 presents the conclusions.

2. MULTI-DOMAIN MODEL FOR THE BLOOD CIRCULATION AND THE CONTRAST DYNAMICS

In this work, the blood flow in the myocardium is considered as a single-phase flow in porous media. Basically, a porous media is a solid filled with empty spaces, which are connecting each other. The fraction of empty spaces in the total sample volume, which is called *porosity*, is given by

$$\phi = \frac{V_p}{V_t}, \tag{1}$$

where V_p is the volume of the pores and V_t is the total volume of the sample. This kind of analysis is widely used in oil extraction (Taber, 1969) and aquifer contamination by organic compounds (Abriola and Pinder, 1985).

In order to better understand the complex phenomenon of myocardial perfusion and, in particular, how MRI images are related to ischemia or infarct, previous works have considered the myocardial arterial tree as a porous media (Bassingthwaighte et al., 1989; Michler et al., 2013; Cookson et al., 2014; Alves et al., 2015, 2016). This approach represents a major simplification. As presented in **Figure 1** the vessel network is discrete and involves non-trivial topological features. Therefore, a lot of information is lost when we represent it by a continuous porous media. Nevertheless, this simplified model is still able to provide useful insights about the phenomena of myocardial perfusion. For instance, in Michler et al. (2013), Darcy's law for flow in porous media was used to model the pressure field and blood velocity in the intravascular tree that perfuses the myocardium. In addition, the same work proposes the use of three different compartments, each one dealing with a diameter range of the vascular tree. In addition to this study, in Alves et al. (2015, 2016), a second equation was proposed, this was a diffusion-advection PDE used to describe the CA dynamics in scenarios of both healthy and diseased tissues. For this purpose, a small region in the domain was set with a lower permeability. In Cookson et al. (2014), a third equation was added to capture the CA dynamics in two different domains, intravascular and extravascular. In this work, we will present a new mathematical model that is able to reproduce three important scenarios: perfusion on a healthy tissue, on an ischemic region, and on an infarct. The last two can happen due to a low pressure difference between epicardial and endocardial surfaces, which can be caused by a stenosis in a coronary artery. Compared to the aforementioned previous work, the new model is more realistic:

(I) It reproduces the Gd-DTPA recirculation: the CA substance is partially washed out after the first pass in the myocardium. However, as can be seen in Lima et al. (1995) and Daly and Kwong (2013), the blood with CA returns to perfuse the heart in cycles. The new arrival of this CA wave implies in a small increase of the SI (Signal Intensity), which is captured by the new model here presented;

(II) Here, our domain is not a simple rectangle as those used before in Cookson et al. (2014) and Alves et al. (2016). In this work, we use a realist short-axis cut of the cardiac left ventricle. Therefore, the simulation results are closer to the images actually acquired by an MRI exam;

(III) The CA is confined to the interstitial (extracellular) space, since it is known that it does not to enter into the cardiac cells (intracellular space);

(IV) When the scenario of infarct is simulated, we added a sortion term in the equations to capture how CA is trapped inside the fibrosis network present in the scars (injured portion of the interstitium).

Cardiac perfusion happens together with cardiac contraction, see **Figure 2** for an example of the different phases of cardiac

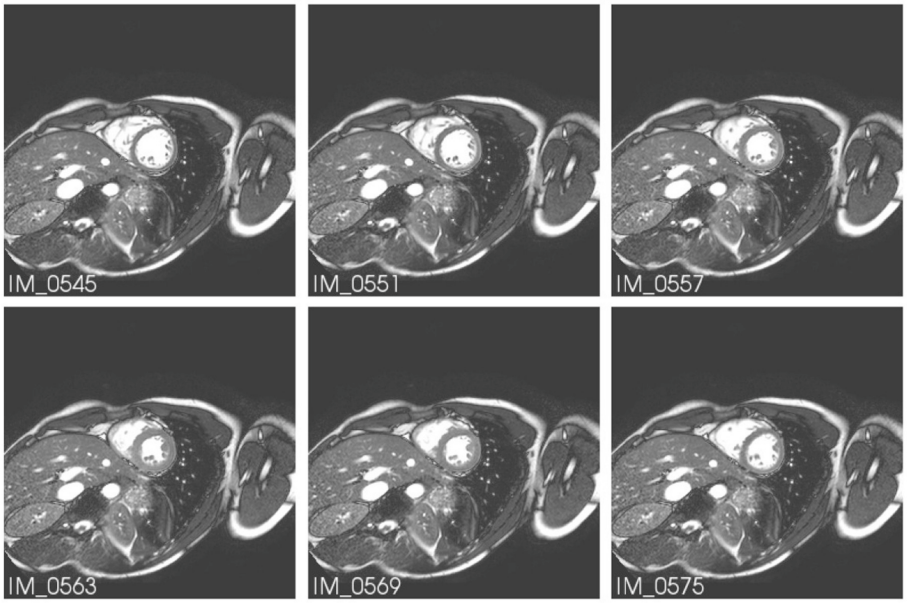

FIGURE 2 | Six MR images at different phases of cardiac cycle (it is possible to observe the movement of the myocardium). Extracted from Koch et al. (2011).

contraction as captured by cine MRI exam. However, for contrast-enhanced MRI physicians use a single phase, usually end-diastole, and analyze CA dynamics comparing these images acquired on different heart beats. Therefore, the sequence of contrast-enhanced MR images is analyzed on a non-contracting heart. It is a simplification, but serves well the purpose as most of the perfusion takes place during diastole. In this work, we will use the same hypothesis and consider CA dynamics on a non-contracting heart. Therefore, the variables of interest are myocardial pressure and CA concentration. The blood fluid is taken as incompressible, homogeneous, and Newtonian.

2.1. Mathematical Model

Figure 3 shows a framework of a multidomain model for cardiac perfusion of the left ventricle. Each domain is modeled by a porous media where the variables of interest are pressure, flow, and CA concentration. On the left side of the figure we have the domains that represent the intravascular flow in the heart: arterial domain (top), capillary domain (middle), and venous domain (bottom). On the right side of the figure we have the extravascular domain in the heart which is subdivided in interstitial space and fibrotic network (shaded area associate to an infarction). This multidomain model captures the flux between the domains as part of a closed circuit. There is an influx through the coronary arteries on the epicadial surface of the arterial domain. The blood follows to the capillary domain, where there is the exchange of plasma and CA with the extracellular domain. The flow continues from the capillary domain to the venous one, from where the coronary veins leave the heart. This outflux enters a recirculation circuit, which is a simplification of the pulmonary and systemic circulation processes.

This multidomain model can be further extended or simplified, depending on the main goals of a particular study. For instance, it could be used to reproduce the transmural perfusion and respective pressure gradients from subepicardium to subendocardium in the arterial domain as well as the outward perfusion, i.e., from subendocariaum to subepicardium, in the case of the venous domain. In addition, by setting an appropriate anisotropic permeability tensor of the vascular domain, it may be used to reproduce the preferential perfusion direction of the micro-vascular system, which follows the orientations of cardiac fibers. In this work, we have used a simplified version of the described multidomain approach by combining the arterial and capillary domains into one intravascular domain and by neglecting the venous domain. This simplification is presented in **Figure 4A**. As our results will show, this simplified model is quite successful in reproducing several aspects of CA dynamics in myocardial perfusion. In particular, it allowed the study of the influence that a coronary obstruction has in the pressure distribution and cardiac perfusion, including scenarios of ischemia and infarction.

To obtain a transmural pressure gradient, boundary conditions are prescribed, which generates a pressure gradient and therefore a blood flow from epi- to endo-cardium. This part of the model can be summarized as follows:

$$\nabla \cdot \vec{v} = 0 \quad \text{in} \quad \Omega_i, \tag{2}$$

$$\vec{v} = -\mathbf{K}\nabla p \quad \text{in} \quad \Omega_i, \tag{3}$$

where $\mathbf{K}$ is the permeability tensor; p is the pressure; $\vec{v}$ is the Darcy velocity and Ω_i is the intravascular domain. The boundary conditions for Equation 2, written in terms of pressure, are given by Dirichlet's boundary condition:

$$p = p_o \quad \text{in} \quad \Gamma_o, \tag{4}$$

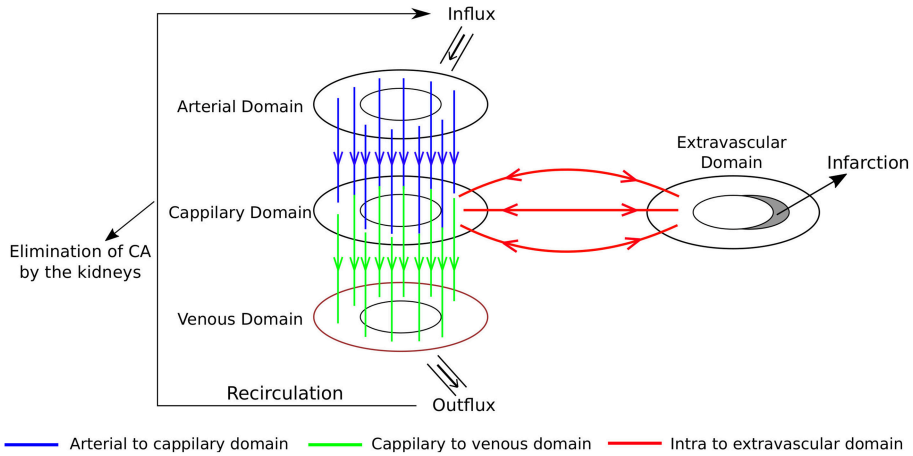

FIGURE 3 | Multidomain model for cardiac perfusion of the left ventricle. Each domain is modeled by a porous media. On the left side of the figure we have the domains that represent the intravascular flow in the heart: arterial domain **(top)**, capillary domain **(middle)**, and venous domain **(bottom)**. On the right side of the figure we have the extravascular domain in the heart which is subdivided in interstitial space and fibrotic network (shaded area associate to an infarction). A recirculation circuit, which is a simplification of the pulmonary and systemic circulation processes, enforces a closed circuit.

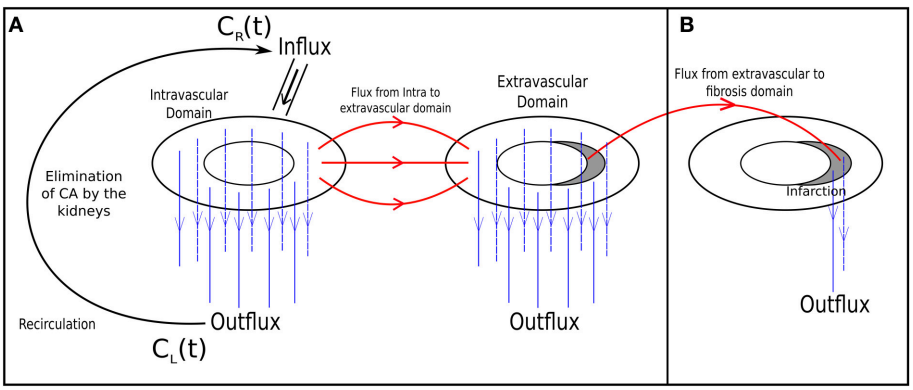

FIGURE 4 | The simplified two-domain model **(A)**, used to simulate healthy and acute ischemia cases; and the three-domain model extended by a fibrosis domain **(B)**, used to simulate an infarct region.

$$p = p_i \quad \text{in} \quad \Gamma_i, \tag{5}$$

where Γ_o and Γ_i are epicardial and endocardial boundaries, respectively. For the CA dynamics we considered advective ($\vec{v}C$) and diffusive ($-D\nabla C$) components for both the intravascular and extravascular domains. Thus, this system is given by

$$\frac{\partial(\phi C_i)}{\partial t} + \nabla \cdot \vec{v} C_i - \phi \nabla \cdot (D_i \nabla C_i) + f = 0 \quad \text{in} \quad \Omega_i, \tag{6}$$

$$\frac{\partial((1-\phi)\lambda C_e)}{\partial t} - (1-\phi)\lambda \nabla \cdot (D_e \nabla C_e) - f + (1-\phi)\lambda k_e C_e + g = 0 \text{ in } \Omega_e, \tag{7}$$

where f models the transfer between the two domains and is given by

$$f = \begin{cases} P \times (C_i - C_e), & \text{if} \quad C_i > C_e \\ 0, & \text{otherwise,} \end{cases} \tag{8}$$

where P is the endothelial permeability. This parameter is known to vary for different pathologies (Bassingthwaighte et al., 1989). Section 5 presents the sensitivity of it. ϕ is porosity, i.e., the fraction of intravascular domain, and thus $1 - \phi$ is the fraction of the extravascular domain. C_i is the concentration of CA in the intravascular domain (Ω_i), C_e is the concentration of CA in the interstitial space (Ω_e). D_i and D_e are diffusion coefficients. $-k_e C_e$ models the flux from the interstitial space to the venous system. As mentioned before, the extravascular space can be divided in interstitial (extracellular) and intracellular portions. We assume that the CA does not enter in the myocytes. Thus, λ represents the fraction of extravascular $(1-\phi)$ space that is due to the interstitium.

As mentioned before, in the case of chronic infarct, scars may develop by the increase of fibrosis to replace dead myocytes. Therefore, when performing the two protocols of *contrast-enhanced MRI perfusion*, two different situations may happen: in *first pass*, because it takes around 50 s, there is not enough

time for the CA to reach the fibrotic area. Thus, on this exam, the images provided by the MRI will indicate a dark color in the injured area, whereas the remain will be bright. On the other hand, in *late enhancement*, there is enough time for the CA to reach the area. In addition, the wash out of CA is delayed, since the network of fibrosis will behave as a trap for CA. The described phenomenon, of fluid, particles or substances been attached to a "solid phase," in physics, is called sortion. Therefore, the dynamics of the CA in the fibrosis is given by

$$\frac{\partial((1-\phi)\lambda\lambda_f C_f)}{\partial t} + (1-\phi)\lambda\lambda_f k_f C_f - g = 0, \quad \text{in} \quad \Omega_f, \quad (9)$$

where C_f is the concentration of CA in the fibrosis domain (Ω_f) and $k_f C_f$ models the flux from the fibrotic network to the venous system. g reflects the flow of CA from interstitium to the fibrotic network. It is nonzero only when we simulate the infarct scenario. It is given by

$$g = (1-\phi)\lambda\lambda_f k_{ef} C_e, \quad (10)$$

where k_{ef} is the rate in which the contrast goes from the interstitium to the fibrosis. λ_f is the fraction of the interstitium with fibrosis. See **Figure 4B**.

For the outer boundary condition (Γ_o), a prescribed flux ($\vec{v}\,Q(t)$) is used, applying a transient Gaussian formula:

$$Q(t) = \frac{1}{\sigma\sqrt{2\pi}} e^{-\frac{1}{2}\left(\frac{t-t_{peak}}{\sigma}\right)} + X(t,x,y), \quad (11)$$

where σ^2 reflects the variance of the contrast agent infusion, t_{peak} is the mean of the Gaussian which sets the time value for the peak of the gadolinium intensity. $X(t,x,y)$ is a term that must be added to simulate the CA cyclic behavior observed in experiments for the first pass and late enhancement MRI perfusion (Lima et al., 1995; Daly and Kwong, 2013). In the next section we will present more details about this term.

Homogeneous Neumann boundary conditions are used in Γ_i for both equations:

$$D_i \nabla C_i \cdot \vec{\mathbf{n}} = 0 \quad \text{in} \quad \Gamma_i, \quad (12)$$

$$D_e \nabla C_e \cdot \vec{\mathbf{n}} = 0 \quad \text{in} \quad \Gamma_i, \quad (13)$$

where $\vec{\mathbf{n}}$ is the normal vector. The same is assumed for Γ_o in Equation 7:

$$D_e \nabla C_e \cdot \vec{\mathbf{n}} = 0 \quad \text{in} \quad \Gamma_o. \quad (14)$$

As initial conditions, we have:

$$C_i(x,0) = C_{i_0}(x) \quad \text{in} \quad \Omega, \quad (15)$$

$$C_e(x,0) = C_{e_0}(x) \quad \text{in} \quad \Omega. \quad (16)$$

2.2. 1D Model to Simulate the CA Cyclic Behavior

Like Equation 6, that simulates the contrast agent dynamics in the myocardium, a similar model, however simplified to 1D, was used to capture the recirculation of contrast. **Figure 4A** uses a line to represent the recirculation. This line connects the outflux and influx via the variables $C_L(t)$ and $C_R(t)$, respectively.

Basically, the values $C_L(t)$ and $C_R(t)$ are the amount of contrast at the beginning and at the end of the recirculation, respectively. The amount $C_L(t)$ is given by

$$C_L(t) = \frac{\int_{\Omega_i} C_i \, d\Omega_i}{|\Omega_i|}. \quad (17)$$

The value given by Equation 17 represents the average of the contrast in the intravascular medium. It is considered as a Dirichlet condition in the left boundary of the 1D domain. Thus, for a given velocity, the average of contrast travels in the domain through the advection-diffusion-reaction equation

$$\frac{\partial C_{out}}{\partial t} + \nabla \cdot \vec{v}_{out} C_{out} - \nabla \cdot (D_{out} \nabla C_{out}) + k C_{out} = 0 \quad \text{in} \quad \Omega_{out}. \quad (18)$$

The amount obtained in the right boundary of the 1D domain, $C_R(t)$, is taken as the recirculation term $X(t,x,y)$ in Equation 11. Physiologically, a portion of the contrast is eliminated in the recirculation, specially by the kidneys. This is modeled by the reaction term kC_{out}. This phenomenon explains the decrease of CA in the subsequent passes in the myocardium. Although the recirculation is more complex and involves the dispersion of the CA in the whole body in different quantities, this simple 1D model captures the CA elimination and its cyclic behavior in the MRI perfusion exam, as presented in section 4.

3. NUMERICAL METHODS AND EXPERIMENTS

For the discretization, the FVM (Finite Volume Method) formulation was used, which consists in the evaluation of influx and outflux of a control volume around each node of the mesh. The FVM applied to Equation 2 (an elliptic PDE) gives us a linear system with one equation for each node. The control volumes were taken as squares of size equal to h. This system was solved by the iterative method of Jacobi (Quarteroni et al., 2010), with an error tolerance (stop criteria) set to 10^{-8}. Once the pressure field is known, Equation 3 is used to obtain the velocity in the faces of the control volumes. The velocity is used in the second term of the left side in Equation 6 and the discretization of the diffusive term follows that of the pressure equation. For the diffusive term, the central differences scheme works very well, without any major problems. But for the advective term a more sophisticated scheme must be used to ensure accuracy and convergence of the numerical method. For the numerical approximation of this term, the *third-order polynomial upwind scheme* (TOPUS) was implemented. For more details about this upwind scheme, see Ferreira et al. (2012) and Alves et al. (2016).We used the explicit

Euler method in the temporal part of the advection-diffusion-reaction equations. All the mathematical calculations in each step of the discretization can be found in Alves et al. (2016).

3.1. Numerical Simulations

We simulated the CA dynamics on a short-axis slice of a human ventricle taken from an open repository (Koch et al., 2011) (see **Figure 5**). During the segmentation process, we have included the papillary muscles as part of the myocardium (Gommans et al., 2016). However, we note that the results presented in this work are not affect by this particular short-axis or segmentation. Similar results can be obtained with different short-axis and different segmentation schemes that do not include the papillary muscles.

We discretized the segmented image using a total of 10,000 finite volumes, i.e., the resolution used for the simulations was $\Delta x = \Delta y = 0.5$mm. The MRI image used had a resolution of 1.5×1.5 mm^2 (Koch et al., 2011). Therefore, the resolution used for the simulations was three times higher than the one from the MRI image. However, as we have not processed the segmented image with any smoothing technique, our simulation domain presented in **Figure 5** is also pixel-based, with non-smooth boundaries.

In order to assess the model in different scenarios, three main simulations were performed: the first is a healthy situation, with normal values of pressure in epi- and endo-cardium. The second simulation tries to reproduce an ischemia. For this purpose, a drop of pressure is considered in the epicardium, which emulates a coronary stenosis. For the third simulation, we consider a more severe stenosis and a region with fibrosis to reproduce an infarct. The values for the prescribed pressures in the non-ischemic case are taken from Chapelle et al. (2010). For the diseased simulations, the values for the drop of pressure in a location of the epicardium (that simulates a coronary artery) were taken from works that study the FFR technique (Pijls et al., 2000; Sant'Anna et al., 2007; Lee et al., 2017). Here we present the features of each of these scenarios (see **Figure 5**):

- 1st (normal): $p(x, y) = 0.0$ kPa, $\forall (x, y) \in \Gamma_i$, and $p(x, y) = 2.0$ kPa, $\forall (x, y) \in \Gamma_o$, see **Figure 5A**;
- 2nd (ischemia): In a small region of the right-hand side of Γ_o pressure is reduced (to simulate a 30% stenosis), $p(x, y) = 1.4$ kPa. The exact location is presented by the arrow in **Figure 5B**. In the rest of Γ_o, pressure is set to its normal value, $p(x, y) = 2.0$ kPa. See the circular color bar around the epicardial surfaces that presents pressure values at the epicardial surface in **Figure 5B**. At the endocardial surface $p(x, y) = 0.0$ kPa, $\forall (x, y) \in \Gamma_i$;
- 3rd (infarct): In a small region of the right-hand side of Γ_o pressure is reduced (to simulate a 80% stenosis), $p(x, y) = 0.4$ kPa. The exact location is presented by the arrow in **Figure 5C**. In the rest of Γ_o, pressure is set to its normal value, $p(x, y) = 2.0$ kPa. See the circular color bar around the epicardial surfaces that presents pressure values at the epicardial surface in **Figure 5C**. At the endocardial surface $p(x, y) = 0.0$ kPa, $\forall (x, y) \in \Gamma_i$. In addition, this scenario also considers the presence of a fibrotic region near the endocardial surface and opposed to the simulated stenosis. This fibrotic region is called diseased, and its location and size are presented in **Figure 5D**.

The 3rd scenario has more particularities than just the pressure gradient. As mentioned before, the CA is confined to the interstitial space, and the measurements of this volume have several particularities (Al-Wakeel-Marquard et al., 2017). For the purpose of this work, we use $\lambda = 0.25$ (Arai, 2011) for the healthy and ischemic scenarios. In the case of an infarct region, many cells are dead and thus the fraction related to the interstitium is big, and we set $\lambda = 1.0$. In the same way, λ_f, the fraction of fibrosis, is zero for the healthy and ischemic cases, whereas for infarct $\lambda_f = 0.50$. Finally, for the infarct scenario the wash out of CA is delayed, since it is trapped in the fibrotic network. Therefore, the rate of CA from fibrosis to the venous system is $k_f = 0.0007\ s^{-1}$, much slower than for the cases without fibrosis, where $k_e = 0.003\ s^{-1}$.

The total porosity ϕ was assumed to be constant and equal to 0.10 (Cookson et al., 2014). The Gaussian formula (Equation 11) was applied only at the epicardium, Γ_o, with $\sigma = 7.0$ and $t_{peak} = 22$ s. The simulation time was set to 600 s, which is the average time used for the LE exam (Knowles et al., 2008; Arai, 2011). It is known that the exchange of oxygen, nutrients and CA from capillaries to the tissue is a phenomenon that involves different components of the biological system, such as the capillary, endothelium, interstitium, and parenchymal cells) (Bassingthwaighte et al., 1989). However, here we fix the endothelial permeability P of Equation 8 to $P = 0.03\ s^{-1}$, in the three scenarios. Nevertheless, section 4 presents a sensitivity analysis of this parameter. With respect to the 1D model, the parameter values were: $\vec{v} = 1.1\ mm\ s^{-1}$ (velocity), $D_{out} = 0.5 \times 10^{-1}\ mm^2\ s^{-1}$ (diffusion coefficient), $k = 0.015\ s^{-1}$ (elimination of contrast in the recirculation). **Table 1** presents a summary of the parameter values for each scenario.

3.2. Anisotropy and Heterogeneity of the Intravascular Domain

The subendocardial permeability is, in average, two times higher than the subepicardial one (Smith et al., 2014). In addition, the preferential direction of permeability, in the short-axis, is parallel to the epicardial and endocardial surfaces (Smith et al., 2014). Therefore, in order to take these features into account, a permeability tensor $\mathbf{K}(x, y)$ was generated $\forall (x, y) \in \Omega_i$. First we generate a transmural gradient of permeability by solving the Laplacian equation, $\Delta w = 0 \in \Gamma_i$, with $w = 0 \in \Gamma_o$ and $w = 1 \in \Gamma_i$, i.e., using Dirichlet boundary condition at the epicardial and endocardial boundaries, respectively. This gives us values between 0 and 1 for each node in the simulated domain. Next, we compute the pair of vectors $\{\mathbf{e_l}, \mathbf{e_t}\}$, where $\mathbf{e_l}$ is the first and $\mathbf{e_t}$ the second preferential direction of permeability by making $\mathbf{e_t} = \nabla w$, and ensuring that $\mathbf{e_l}$ is perpendicular to $\mathbf{e_t}$. With these two vectors calculated for each point (x, y) we can write the permeability tensor $\mathbf{K}(x, y)$ as follows:

$$K(x, y) = K_l(x, y)I + (K_t(x, y) - K_l(x, y))e_l(x, y)e_l(x, y)^t, \quad (19)$$

where K_l is the permeability value along e_l and K_t is the permeability along e_t (transversal to e_l). These values can be

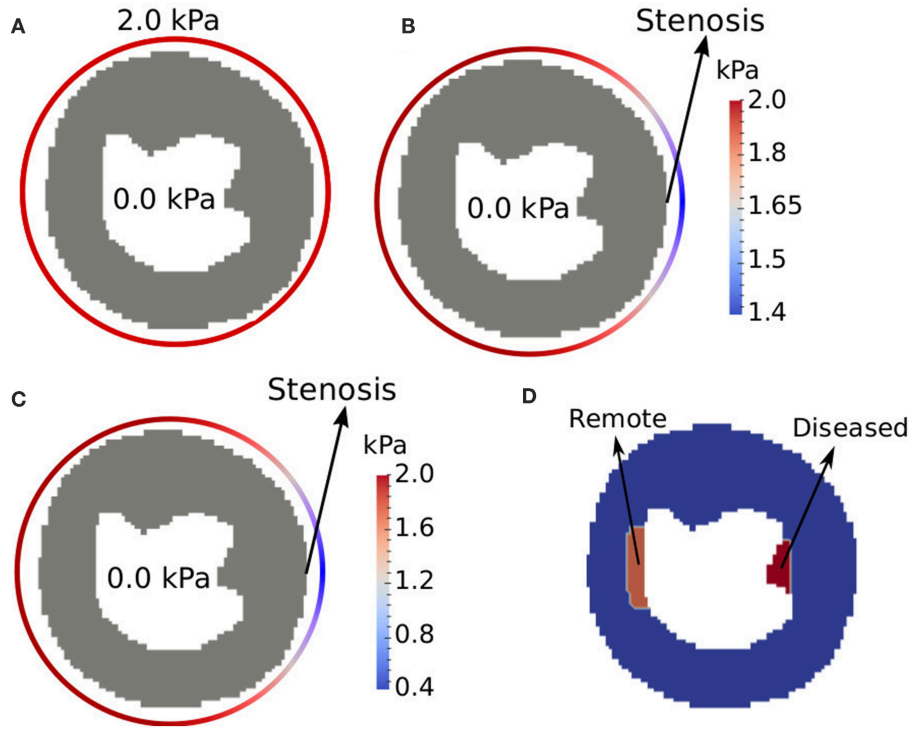

FIGURE 5 | Performed simulations: **(A)** healthy, **(B)** ischemic, and **(C)** infarct. **(D)** Shows the regions of interest for the evaluation of CA signal intensity. When simulating ischemia and infarct, we sum up the concentration of CA in these regions of interest, for each time instant. The colored circle that surrounds the epicardium represents the pressure boundary condition for each scenario. Note the different minimum values of the two color bars.

calculated using the weight w:

$$K_l(x,y) = K_1(1 - w(x,y)) + 2.0K_1 w(x,y), \quad (20)$$

$$K_t(x,y) = K_2(1 - w(x,y)) + 2.0K_2 w(x,y), \quad (21)$$

where K_1 and K_2 are the permeabilities in outer boundary, with K_1 approximately 10.8 times higher than K_2 (Smith et al., 2014); and the multiplication by 2.0 in the equation reflects that the subendocardial permeability is, in average, two times higher than the subepicardial one (Smith et al., 2014).

Table 1 presents a summary of the parameters used for each considered scenario in this work.

3.3. Computing

The simulator is an in-house code implemented in C. Simulations were executed on an Intel(R) Core(TM) i7 3 GHz 8 Gb. Each simulation of the late enhancement protocol (10 min of perfusion) takes approximately 708 s. This first version of the code was developed as a sequential one, i.e., parallel programming was not used, but it is planned for future works.

4. RESULTS

Section 4.1 presents the pressure profile obtained from the Darcy approach (Equation 2). In the sequence, we present qualitative results of the CA perfusion on a short axis. Both, first pass and late enhancement are considered for the three different scenarios (healthy, ischemic, and infarction). In section 4.2 we present quantitative results of the model, and compare the signal intensities of the CA in the first pass and in the late enhancement exams to clinical data from the literature (Knowles et al., 2008; Daly and Kwong, 2013).

TABLE 1 | Parameters used in each scenario.

Parameter (unity)	Healthy/Ischemic	Infarction
$k_e\ (s^{-1})$	0.002	0.0009
$P(s^{-1})$	0.03	0.025
$k_f(s^{-1})$	0	0.0007
$k_{ef}(s^{-1})$	0	1.0
ϕ	0.10	0.10
λ	0.25	1.0
λ_f	0	0.5
$D(mm^2s^{-1})$	10^{-3}	10^{-7}
$K(mm^2kPa^{-1}s^{-1})$	$K_1 = 1.5; K_2 = 0.75$	$K_1 = 1.5; K_2 = 0.75$
σ	7.0	7.0
$t_{peak}(s)$	25	25
$v_{out}(mm.s^{-1})$	1.0	1.0
$D_{out}(mm^2s^{-1})$	0.05	0.05
$k(s^{-1})$	0.02	0.02

4.1. Spatio-Temporal Dynamics of CA Perfusion in the Heart

Figure 6 presents the numerical solutions obtained for the pressure distribution for the three considered scenarios: (a) healthy situation; (b) for the case where a stenosis of 30% is simulated; and (c) for a stenosis of 80%. In the real phenomenon, the pressure profile changes during the cardiac cycle. As mentioned before, we use the same hypothesis as the clinicians and evaluate the dynamics of perfusion at the same instant of each cardiac cycle, i.e., heart contraction is not taken into account. The calculated pressure and velocity will be used in the transport equation (Equation 6). From the figure we observe that the stenosis decreases the trasmural gradient of pressure.

Figure 7 shows the final result, in terms of qualitative images of the myocardial short axis for the three simulated scenarios. For each scenario, we shown the concentration in the end of both first pass and late enhancement exams. The simulation domain was adapted from a real short axis MRI image (Koch et al., 2011). The model reproduces very well the qualitative behavior, for both first pass and late enhancement exams. During first pass, in a healthy heart the CA is homogeneously distributed, whereas in the cases of ischemia and infarction the affected region is revealed by low localized contrast values. At the time of late-enhancement, the CA attaches to fibrosis in the infarct region. This is reflected by the high localized contrast values at late-enhancement.

4.2. Signal Intensity of Contrast Agent

The variable of interest in this section is the signal intensity of the contrast agent in specific regions of interest (ROI). To compare the CA dynamics of the healthy and pathological cases, two regions of interest in the myocardium were marked as presented in **Figure 5D**: one captures the injured region and the other is on a remote healthy region. Each value of the time series correspond to the sum of the CA concentration in one specific ROI at a specific time.

Since we are setting a reduced pressure on the right-hand side of the epicardial surface to simulate a stenosis, we placed the diseased ROI as a subendocardial region opposite to the stenosis point. The remote ROI was placed on the subendocardial left-hand side of the short axis (see **Figure 5D**). These are common choices of ROIs to compare a diseased versus a healthy region (Hsu et al., 2006; Schuster et al., 2015). In our simulations, the remote ROI has a total area of 70 mm^2, while the diseased ROI has 55 mm^2. These sizes and locations of ROIs are commonly reported in the literature (Hsu et al., 2012; Pop et al., 2013; Schuster et al., 2015). For the third scenario that simulates an infarct, a fibrotic region was modeled at the same location of the diseased ROI.

Section 4.2.1 presents the results for the ischemic scenario. Section 4.2.2 presents the results of the infarction. Is important to remark that the fibrosis mentioned before was placed only in the *diseased* region, with a particular volume fraction, as discussed in section 2.1.

4.2.1. First Pass

Figure 8A shows the results obtained with respect to the intensity of CA signal during a first pass MRI perfusion exam in the two considered regions of interest. These results are in agreement with those found in the literature (Nagel et al., 2003; Jenson et al., 2013; Wang et al., 2015; Bakir et al., 2016). In particular, the experimental curves presented in **Figure 8A** are taken from Daly and Kwong (2013), where the first pass of healthy region is compared to a ischemic one. It is possible to observe the *second pass* of the CA, i.e., the remaining amount of it that was not eliminated by the kidneys and recirculates. **Figure 8B** presents how each domain, intra and extravascular, contributes to the total SI of CA over time for the case of ischemia. These results are also in agreement with the literature (Bogaert et al., 2005).

4.2.2. Late Enhancement

After the first pass detects a region with poor perfusion, late-enhancement is performed to study myocardial viability, i.e., to differentiate between ischemia, but yet viable tissue, or infarct. This is possible because fibrosis is present in chronic infarct and the CA is trapped in the fibrotic network, taking longer to be washed out of the myocardium. If the perfusion problem is not so severe, like under ischemia, the CA is washed out at a similar rate as a remote/healthy region. The results shown in **Figure 9** are in agreement with the late enhancement dynamics (Arai, 2011) and reproduces well the clinical data taken from Knowles et al. (2008). **Figure 9** presents the contribution of both intra- and extravascular spaces in the CA dynamics in the infarct region. The intravascular curve shows that the CA in this domain is quickly washed out if compared to the CA in the extravascular space.

5. DISCUSSION

As we present a new model for cardiac perfusion with focus on the application of contrast-enhanced MRI, this section begins by presenting sensitivity tests of the proposed models. This will contribute to the discussion regarding the importance of our main hypothesis, the positive outcomes of our model as well as its limitations.

5.1. Sensitivity of the Parameters

This section is divided in three parts. Section 5.1.1 shows the importance of the recirculation coupling in the model (Equation 18). In section 5.1.2, an effort to reproduce clinical data of LE for the infarction scenario without taking into account the domain of fibrosis is presented. In section 5.1.3, we demonstrate that the coupling of the model with a fibrotic domain and the inclusion of a sortion term provide a better alternative to model the experimental and clinical data.

5.1.1. Recirculation

Figure 10 is presented to reinforce the idea that the recirculation coupling is important to obtain results close to those obtained in clinical exams. The red curve is the clinical information from Daly and Kwong (2013) (same as in **Figure 8A**), and due to the lack of data, it stops after 50 s. The figure also shows the dynamics of the CA with the recirculation model (black, same as in **Figure 8A**) and without it (yellow) for 200 s of perfusion. As presented, if one does not take into account the recirculation

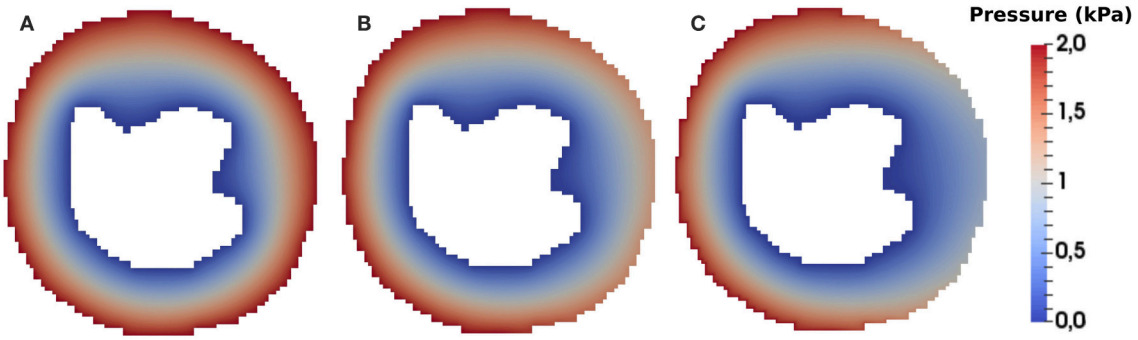

FIGURE 6 | Pressure field of the **(A)** healthy **(B)** ischemic and **(C)** infarction scenario (in *kPa*). It is possible to observe that the pressure is higher near the epicardium area and lower near endocardium, as expected. The Dirichlet boundary condition mentioned in section 3.1 generates a pressure gradient. Using the Darcy's law we obtain a velocity field that is used in the advective term of Equation 6.

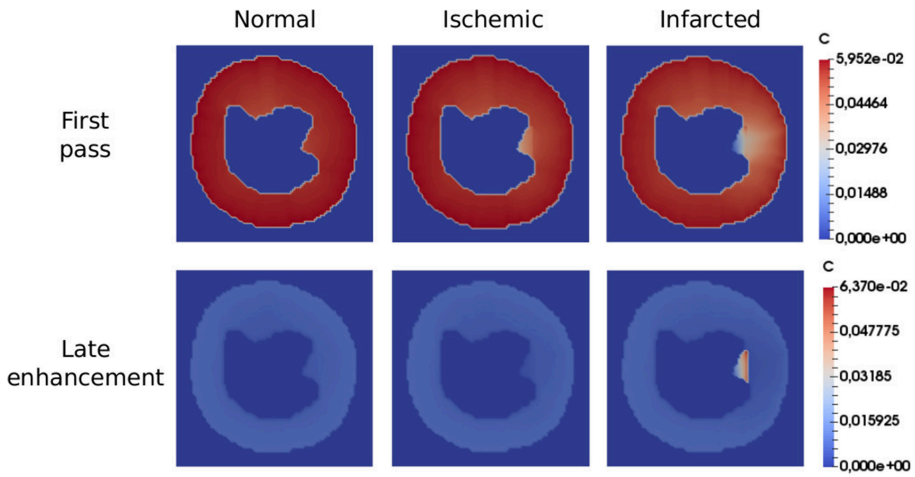

FIGURE 7 | Qualitative images in the end of first pass (50 s) and late enhancement (600 s) exams. In the first scenario (healthy), the CA is homogeneously distributed, while in the second (ischemia), the diseased region is revealed by low localized contrast values. At the time of late-enhancement, the CA gets stuck in the infarction region as reflected by the high localized contrast values. All the simulations reproduced well the characteristics seen by the clinicians in the considered scenarios.

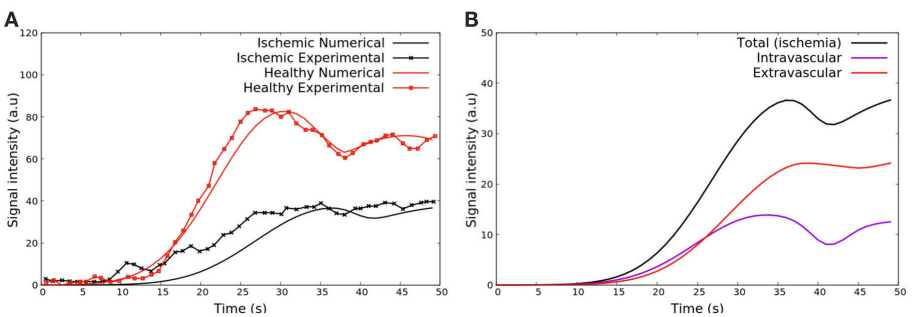

FIGURE 8 | (A) Comparison between SI of the CA during time observed in Daly and Kwong (2013) and the numerical results of this work in some ischemic area (red) and remote and healthy area (blue). The oscillatory decay is due to the Gd-DTPA recirculation. **(B)** The contribution of intra- and extravascular SI of the CA in the ischemic area: (purple) total, (red) intravascular, and (black) extravascular concentrations vs. time.

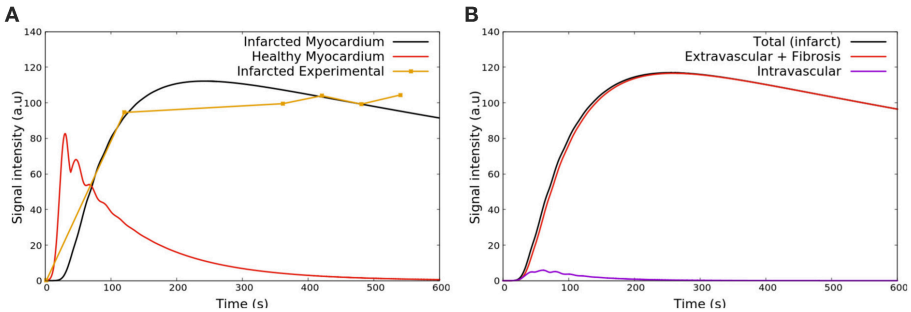

FIGURE 9 | (A) SI of the contrast agent in scenarios remote/healthy (red) and infarction (black). The yellow curve presents the clinical data taken from Knowles et al. (2008). The CA remains in the infarct area because it attaches to fibrosis, and thus takes longer to be washed out. **(B)** Contribution of both intra and extravascular spaces in the CA dynamics in the infarct region. The intravascular curve (purple) shows that the CA in this domain is quickly washed out, while the CA remains in the extravascular space (red curve) after 2 min.

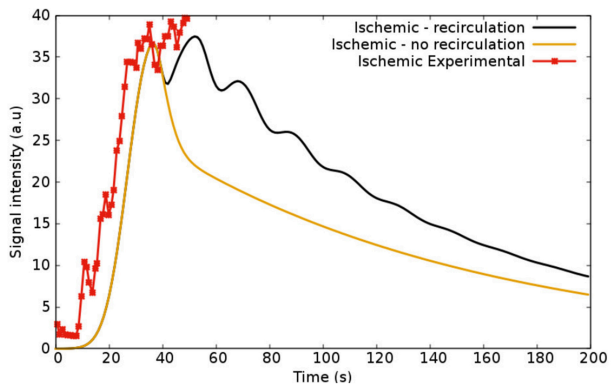

FIGURE 10 | Simulations regarding ischemic scenarios: the first (black), shows the model coupled with the recirculation part (Equation 18) and the second (yellow), without it. The red curve shows the experimental data from Daly and Kwong (2013).

model and its parameters ($\vec{v}_{out}$, D_{out} and k from Equation 18), the oscillatory decay observed in the clinical and experimental data is not captured.

The whole process of recirculation is quite complex: the kidneys, for instance, play an important role in the physiological process of elimination of CA; the constant flux velocity assumed by the model is in fact a simplification, since the flux varies and depends on the location if the body, the structure of the vessels, viscosity, and many other features. Therefore, other variables and parameters could be added in this part of the model. However, it is not in the scope of this work to go deep into this topic. The solution presented here is taking into account the blood cycle in the whole human body as a single-phase flow in a simple 1D domain, which provides good qualitative agreement with experimental data. For future works, it would be interesting to study this phenomenon and look for other solutions.

5.1.2. Modeling Perfusion Without a Mathematical Description of Fibrosis

As mentioned before, without taking into account (Equation 9), that describes fibrosis, the model captures well the scenario of ischemia and is able to reproduce clinical data (Daly and Kwong, 2013). However, here we show that without the mathematical description of fibrosis the model can not reproduce the dynamics of infaction, mainly those found in the time-scale of the late-enhancement exam.

Figure 11 presents the sensitivity analysis of the model without the coupling to Equation (9). In other words, it shows an attempt of reproduce the clinical data of infarction from Knowles et al. (2008) using just a part of the proposed mathematical model. All curves in **Figure 11** refer to the dynamics of the CA in the diseased region according to **Figure 5D**. The parameters were only varied is this ROI, and kept constant in the other regions. In addition, when varying one parameter, all the others are fixed according to the infarction column in **Table 1**.

Figure 11A presents the sensitivity of λ (fraction of interstitium in the extravascular domain). For high values of λ there is more space for the CA. Thus, more CA is hold in the interstitial domain: time-to-peak, peak value and value at 600 s increase. These are all in the correct direction to reproduce the data in **Figure 11D** (black and yellow). However, even setting $\lambda = 1$, i.e., to its maximum value, the values of **Figure 11A** are far from those of **Figure 11D** (black and yellow). **Figure 11B** shows the sensitivity of P, which models the rate of CA exchange between intra and extravascular domains. For instance, $P = 0$ s^{-1} indicates that there is no contrast agent flowing from one domain to the other, which means that it is confined to the intravascular domain. Hence, in this particular case, the CA is quickly washed out. Increasing P, the CA goes faster to the extravascular domain, hence it takes longer to be washed out to the venous system, but it is still completely washed out at 600 s. **Figure 11C** shows how the pressure gradient, which is related to the severity of coronary stenosis, influences the signal intensity of the CA in the diseased region. For example, in the case of an ischemia (this one is related with **Figure 5B**), the obstruction of 30% leads to a pressure gradient of up to 1.45 *kPa* in the right portion of the myocardium. In the worst scenario shown here, an obstruction of 80% leads to a pressure gradient of up to 0.45 *kPa* between epi- and endo-cardium (related with **Figure 5C**). As expected, the pressure gradient is directly proportional to the rate with which the CA reaches the diseased area. In **Figure 11D**,

two different values for k_e (transfer of CA from the extravascular media to the venous system) are used. As expected, decreasing the value by two order of magnitude, the CA takes longer to be washed out. However, once gain, the curves obtained are far from the goal **11D** (black and yellow).

In summary, using the formulation with only two domains (intra- and extra-vascular), it was not possible to reproduce the observed scenario of CA dynamics for a case of infarction. However, in Cookson et al. (2014), a formulation with two domains was used and some results were similar to those observed for infarction. To achieve this, however, the authors had to change the permeability of the media (**K** in Equation 3) in specific regions. Their purpose was to evaluate the CA dynamics in different scenarios, without specifying any pathology. For the cases of healthy, ischemic or infarct myocardium, the three scenarios treated here, the changes used in the permeability **K** would be difficult to justify. Thus, for the simulation of an infarction it seems to be important to model fibrosis, as we propose in our new formulation.

5.1.3. Modeling Perfusion With a Mathematical Description of Fibrosis

Figure 12 shows the dynamics of the CA in the infarct region taking into account the third domain and Equation 9. **Figure 12A** shows the dynamics of the CA for different values of λ (interstitial fraction of the extravascular media). For the healthy regions, its values is around 0.25 (Knowles et al., 2008; Arai, 2011). Once again, for all the tests, when varying one parameter, all the others are fixed according to the infarction column in **Table 1**. As in **Figure 11A**, for high values of λ there is more space for the CA. Thus, more CA is hold in the interstitial domain. However, using this model, time-to-peak, peak value, and value at 600 s are all much more sensitive to λ. And therefore, few adjustments of the parameter are enough to fit different experimental values. **Figure 12B** presents the sensitivity of k_f, the rate in which the CA goes from fibrosis to the venous system. The higher its value, the faster the CA is washed out of the myocardium. If $k_f = 0.0\ s^{-1}$, no CA is leaving the fibrotic region, hence a plateau appears. The best value that reproduces the clinical data is $k_f = 7 \times 10^{-4}\ s^{-1}$. **Figure 12C** presents the sensitivity of P. The value that best fitted the clinical data of infarction is $P = 0.025\ s^{-1}$. Once again, if $P = 0.0\ s^{-1}$, there is no communication between intra and extravascular domains, hence the CA is quickly washed out. **Figure 12D** shows results for different values of k_e (decay rate of CA). It reaches saturation at $7 \times 10^{-5}\ s^{-1}$. In summary, the presented formulation that models a third domain for fibrosis has proved to be a good alternative for the simulation of the dynamics of CA in the case of infarction. In addition, the curves generated with this model were more sensitive to many of its parameters. Therefore, a few adjustments of some parameters are enough to fit different experimental values.

5.2. Limitations and Future Works

For low doses of contrast agents, there is an approximately linear relationship between the SI of the CA and its concentration (Donahue et al., 1997). For cardiovascular imaging, the dosage is not low enough for this linearity assumption to apply (Gerber et al., 2008). To overcome this issue, several researchers have presented different solutions (Cernicanu and Axel, 2006; Engblom et al., 2017; Kellman et al., 2017). In this work, the presented models focus on the dynamics of CA concentration. In future works, we will adopt the aforementioned solutions to convert CA concentration to SI and vice-versa.

As mentioned before, in the series of images provided by the contrast enhanced MRI perfusion, the clinicians take the same image, or phase, at different cardiac cycles to analyze the perfusion of the CA. Doing so, the short axis images of the left ventricle have the same shape over time. Hence it is reasonable to assume a static configuration of pressure. However, this assumption, which does not take into account poroelastic effects, has its shortcomings. To improve this model, a general mathematical model that couples porous flows and hyperelastic formulation was developed in Chapelle and Moireau (2014). Furthermore, the same authors used a similar formulation in order to evaluate myocardial perfusion (Chapelle et al., 2010). In future works, the model presented here will be extended in this direction, in order to obtain more reliable results and to evaluate the myocardium at different scenarios and for different pathologies.

It is important to mention that the pressure and flow distributions in the intravascular tree are more complex than those obtained by our model. The fine and complex structure with its connectivity, branches and varying radius are important features that are not present in our continuum porous media model. Therefore, in the near future we will replace our continuum approach for the intravascular domain by a detailed arterial tree model. In order to generate arterial trees, we will adopt algorithms based on the CCO (Constrained Constructive Optimization) method (Karch et al., 1999; Blanco et al., 2013; Brito et al., 2017; Meneses et al., 2017). This will allow us to model stenosis in a more precise way, by directly altering the radius of a particular branch of the coronary arteries.

We have chosen to use a segmentation of the short axis that includes the papillary muscles. Indeed, recent papers show that these muscles have impact on the analysis of MR images (Gommans et al., 2016). However, this controversy is out of the scope of our work. The segmentation choice was arbitrary and our model and implementation is general enough to use any domain, short-axis, long-axis, with or without papillary muscles. The same applies for the location and shapes of the modeled infarct region.

A very important feature here presented is the simulation of fibrosis. To reproduce late-enhancement images for the case of infaction it was fundamental to couple the third domain for fibrosis to the two-domain model (intra- and extra-vascular domains). However, this brings more parameters to be adjusted. In future works, we plan to study how the numbers of parameters of the models affect the correct description of patient specific perfusion data.

A similar model to the two-domain model (intra- and extra-vascular domains) presented here has been successfully used in the quantification of myocardial perfusion with cardiac MRI (Engblom et al., 2017; Kellman et al., 2017; Brown et al., 2018). It is a simplification of the model

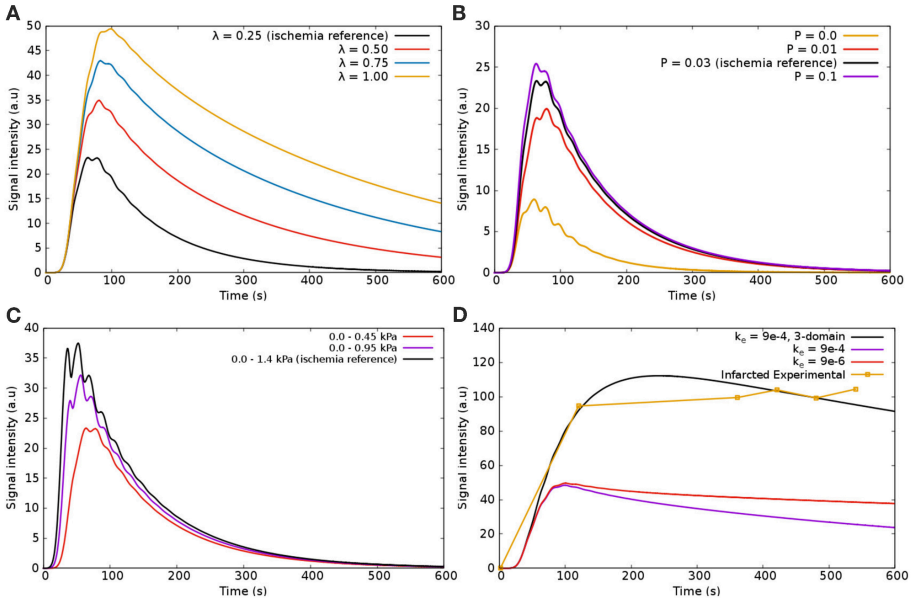

FIGURE 11 | Sensitivity analysis of the parameters using the model two domains: **(A)** λ—the fraction of extravascular media that corresponds to the interstitium; **(B)** P—the rate of CA that goes from intravascular to extravascular space; **(C)** Pressure difference between epicardium and endocardium in the infarcted region; **(D)** k_e—the rate of CA going from extravascular media to the venous domain (a term of decay). When varying one parameter, all the others are fixed according to the infarction column in **Table 1**.

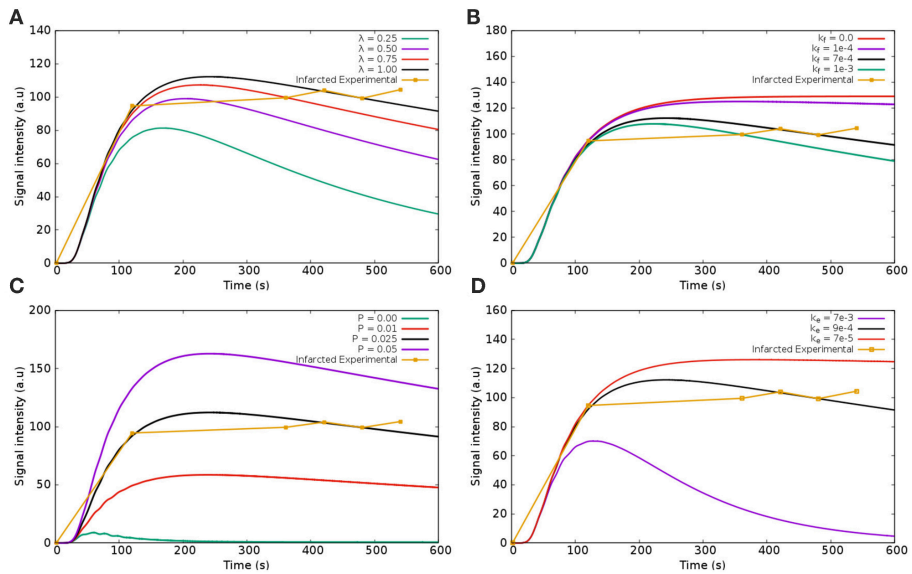

FIGURE 12 | Sensitivity analysis of the parameters in the infarcted scenario using the model with three domains: **(A)** λ—the fraction of interstitium in the infarcted area; **(B)** k_f—the exchange rate of CA going from interstitium to the venous system; **(C)** λ_f—the fraction of interstitium that has fibrosis (scars); **(D)** decay of CA from the fibrosis. When varying one parameter, all the others are fixed according to the infarction column in **Table 1**.

presented in Bassingthwaighte et al. (1989) and was called the BTEX model. This simplified model was shown to be very useful to speed up the inverse problem of parameter estimation to reproduce patient-specific CA dynamics. Here, we will show the simplification steps needed to convert our two-domain model into the BTEX model. First, the pressure equation is not taken into account, and tissue perfusion is characterized by a single scalar parameter F which replaces our vector $\vec{v} = -\mathbf{K}\nabla p$ in Equation (6). Another simplification of BTEX is that it is used as a set of independent 1D two-domain models. The perfusion F

is independently estimated for each MRI pixel via a 1D model. This approach allows a great simplification for the problem of parameter estimation. In this work, we have presented 2D models that can be easily extended to full 3D models of the heart. Finally, a very important feature here presented was the simulation of fibrosis. To reproduce late-enhancement images for the case of infarction, it was fundamental to couple the third domain for fibrosis to the two-domain model. In summary, the new models proposed in this work have some potential advantages for the process of cardiac perfusion quantification. However, the models have more equations and parameters than the simplified models that are currently used. As a consequence, parameter estimation via the solution of an associated inverse problem will be a difficult task. One solution is to use additional non-invasive information to adjust the model, such as T1 and T2 mapping from MRI exams and FFR (pressure and flux) estimations from CT exams. As future work, we plan to study how these larger number of parameters and equations may affect the correct estimation of patient-specific cardiac perfusion by performing a clinical study similar to those presented in Engblom et al. (2017), Kellman et al. (2017), and Brown et al. (2018).

5.3. Conclusion

We presented a mathematical model that describes the blood and contrast perfusion in a short axis cut of the left ventricle of the heart. The simulation results are in agreement with the observed phenomena, specifically with the MRI images obtained by the non-invasive first pass and late enhancement exams and with clinical data on the time dependence of the contrast agent (CA) in different situations. This model takes into account the flow of Gadolinium-based MRI CA (Gd-DTPA) in the arterial vascular domain, its leakage to the interstitial domain and its retention in fibrotic tissue (when simulating a scenario of infarction). Having in mind the substantial information that quantitative methods can provide for the physicians, the mathematical model proposed here and its future extensions can be considered as a first step to develop better tools to understand the complexity of the spatio-temporal CA dynamics and the relation between clinical data acquired via MRI and the underlying cardiac perfusion.

AUTHOR CONTRIBUTIONS

JA and RdS conceived the mathematical model. JA implemented the code and performed the simulations. JA and RdQ developed the numerical approximations. MB provided clinical data to validate the model. All authors evaluated the results and reviewed the manuscript.

FUNDING

The authors would like to acknowledge the financial support provided by FAPEMIG, CAPES, UFJF, FINEP, CNPq, and PTB.

ACKNOWLEDGMENTS

The authors are grateful to Tobias Schäffter for the fruitful discussions.

REFERENCES

Abriola, L. M., and Pinder, G. F. (1985). A multiphase approach to the modeling of porous media contamination by organic compounds: 1. Equation development. *Water Resour. Res.* 21, 11–18. doi: 10.1029/WR021i001p00011

Alves, J., de Queiroz, R., and dos Santos, R. (2017). Comparing myocardium perfusion data acquired by a MRI-phantom and a mathematical model. *IFMBE Proc.* 60, 308–311. doi: 10.1007/978-981-10-4086-3_78

Alves, J. R., Queiroz, R. A. B., and Santos, R. W. (2016). Simulation of cardiac perfusion by contrast in the myocardium using a formulation of flow in porous media. *J. Comput. Appl. Math.* 295, 13–24. doi: 10.1016/j.cam.2015.04.008

Alves, J. R., Santos, R. W., Novaes, G. M., and Queiroz, R. A. B. (2015). Simulating the perfusion of contrast in cardiac transmural wall. *IFMBE Proc.* 49, 837–840. doi: 10.1007/978-3-319-13117-7_213

Al-Wakeel-Marquard, N., Rastin, S., Muench, F., Yilmaz, S., Berger, F., Kuehne, T., et al. (2017). Cardiac t1 mapping in congenital heart disease: bolus vs. infusion protocols for measurements of myocardial extracellular volume fraction. *Int. J. Cardiovasc. Imaging* 33, 1961–1968. doi: 10.1007/s10554-017-1191-2

Aquaro, G. D., Todiere, G., Di Bella, G., Guiducci, L., Pingitore, A., and Lionetti, V. (2013). A fast and effective method of quantifying myocardial perfusion by magnetic resonance imaging. *Int. J. Cardiovasc. Imaging* 29, 1313–1324. doi: 10.1007/s10554-013-0220-z

Arai, A. E. (2011). The cardiac magnetic resonance (CMR) approach to assessing myocardial viability. *J. Nucl. Cardiol.* 18, 1095–1102. doi: 10.1007/s12350-011-9441-5

Bakir, M., Wei, J., Nelson, M. D., Mehta, P. K., Haftbaradaran, A., Jones, E., et al. (2016). Cardiac magnetic resonance imaging for myocardial perfusion and diastolic function - reference control values for women. *Cardiovasc. Diagn. Ther.* 6, 78–86. doi: 10.3978/j.issn.2223-3652.2015.09.03

Bassingthwaighte, J., Wang, C., and Chan, I. (1989). Blood-tissue exchange via transport and transformation by capillary endothelial cells. *Circul. Res.* 65, 997–1020. 78-86.

Blanco, P. J., Queiroz, R. A. B., and Feijóo, R. A. (2013). A computational approach to generate concurrent arterial networks in vascular territories. *Int. J. Numer. Methods Biomed. Eng.* 29, 601–614. doi: 10.1002/cnm.2547

Bogaert, J., Dymarkowski, S., and Taylor, A. M. (2005). *Clinical Cardiac MRI*. Heidelberg: Taylor & Francis.

Brenner, D. J., and Hall, E. J. (2007). Computed tomography - an increasing source of radiation exposure. *N. Engl. J. Med.* 357, 2277–2284. doi: 10.1056/NEJMra072149

Brito, P. F., Meneses, L. D. M., Rocha, B. M., Santos, R. W., and Queiroz, R. A. B. (2017). Construction of arterial networks considering the fahraeus-lindqvist effect. *IFMBE Proc.* 60, 277–280. doi: 10.1007/978-981-10-4086-3_70

Brown, L. A. E., Onciul, S. C., Broadbent, D. A., Johnson, K., Fent, G. J., Foley, J. R. J., et al. (2018). Fully automated, inline quantification of myocardial blood flow with cardiovascular magnetic resonance: repeatability of measurements in healthy subjects. *J. Cardiovasc. Magn. Reson.* 20:48. doi: 10.1186/s12968-018-0462-y

Cernicanu, A., and Axel, L. (2006). Theory-based signal calibration with single-point t1 measurements for first-pass quantitative perfusion mri studies. *Acad. Radiol.* 13, 686–693. doi: 10.1016/j.acra.2006.02.040

Chapelle, D., Gerbeau, J.-F., Sainte-Marie, J., and Vignon-Clementel, I. E. (2010). A poroelastic model valid in large strains with applications to perfusion

in cardiac modeling. *Comput. Mech.* 46, 91–101. doi: 10.1007/s00466-009-0452-x

Chapelle, D., and Moireau, P. (2014). General coupling of porous flows and hyperelastic formulations-From thermodynamics principles to energy balance and compatible time schemes. *Eur. J. Mech. B Fluids* 46, 82–96. doi: 10.1016/j.euromechflu.2014.02.009

Chiribiri, A., Schuster, A., Ishida, M., Hautvast, G., Zarinabad, N., Morton, G., et al. (2013). Perfusion phantom: An efficient and reproducible method to simulate myocardial first-pass perfusion measurements with cardiovascular magnetic resonance. *Magn. Reson. Med.* 69, 698–707. doi: 10.1002/mrm.24299

Cookson, A. N., Lee, J., Michler, C., Chabiniok, R., Hyde, E., Nordsletten, D., et al. (2014). A spatially-distributed computational model to quantify behaviour of contrast agents in MR perfusion imaging. *Med. Image Anal.* 18, 1200–1216. doi: 10.1016/j.media.2014.07.002

Daly, C., and Kwong, R. Y. (2013). Cardiac MRI for myocardial ischemia. *Method. DeBakey Cardiovasc. J.* 9, 123–131. doi: 10.14797/mdcj-9-3-123

Dash, R. K., and Bassingthwaighte, J. B. (2006). Simultaneous blood–tissue exchange of oxygen, carbon dioxide, bicarbonate, and hydrogen ion. *Ann. Biomed. Eng.* 34, 1129–1148. doi: 10.1007/s10439-005-9066-4

Donahue, K. M., Weisskoff, R. M., and Burstein, D. (1997). Water diffusion and exchange as they influence contrast enhancement. *J. Magn. Reson. Imaging* 7, 102–110. doi: 10.1002/jmri.1880070114

Engblom, H., Xue, H., Akil, S., Carlsson, M., Hindorf, C., Oddstig, J., et al. (2017). Fully quantitative cardiovascular magnetic resonance myocardial perfusion ready for clinical use: a comparison between cardiovascular magnetic resonance imaging and positron emission tomography. *J. Cardiovasc. Magn. Reson.* 19:78. doi: 10.1186/s12968-017-0388-9

Ferreira, V. G., Queiroz, R. A. B., Lima, G. A. B., Cuenca, R. G., Oishi, C. M., Azevedo, J. L. F., et al. (2012). A bounded upwinding scheme for computing convection-dominated transport problems. *Comput. Fluids* 57, 208–224. doi: 10.1016/j.compfluid.2011.12.021

Gerber, B. L., Raman, S. V., Nayak, K., Epstein, F. H., Ferreira, P., Axel, L., et al. (2008). Myocardial first-pass perfusion cardiovascular magnetic resonance: history, theory, and current state of the art. *J. Cardiovasc. Magn. Reson.* 10:18. doi: 10.1186/1532-429X-10-18

Gommans, D. H. F., Bakker, J., Cramer, G. E., Verheugt, F. W. A., Brouwer, M. A., and Kofflard, M. J. M. (2016). Impact of the papillary muscles on cardiac magnetic resonance image analysis of important left ventricular parameters in hypertrophic cardiomyopathy. *Netherlands Heart J.* 24, 326–331. doi: 10.1007/s12471-016-0805-y

Hlatky, M. A., De Bruyne, B., Pontone, G., Patel, M. R., Norgaard, B. L., Byrne, R. A., et al. (2015). Quality-of-life and economic outcomes of assessing fractional flow reserve with computed tomography angiography: Platform. *J. Am. Coll. Cardiol.* 66, 2315–2323. doi: 10.1016/j.jacc.2015.09.051

Hsu, L.-Y., Groves, D. W., Aletras, A. H., Kellman, P., and Arai, A. E. (2012). A quantitative pixel-wise measurement of myocardial blood flow by contrast-enhanced first-pass cmr perfusion imaging: microsphere validation in dogs and feasibility study in humans. *Cardiovasc. Imaging* 5, 154–166. doi: 10.1016/j.jcmg.2011.07.013

Hsu, L.-Y., Rhoads, K. L., Holly, J. E., Kellman, P., Aletras, A. H., and Arai, A. E. (2006). Quantitative myocardial perfusion analysis with a dual-bolus contrast-enhanced first-pass mri technique in humans. *J. Magn. Reson. Imaging* 23, 315–322. doi: 10.1002/jmri.20502

Jenson, S., Craig, S., York, G., and Steel, K. (2013). Review of cardiac MR perfusion imaging. *J. Am. Osteopath. Coll. Radiol.* 2, 2–7. Available online at: https://www.jaocr.org/articles/review-of-cardiac-mr-perfusion-imaging

Jerosch-Herold, M. (2010). Quantification of myocardial perfusion by cardiovascular magnetic resonance. *J. Cardiovasc. Magn. Reson.* 12:57. doi: 10.1186/1532-429X-12-57

Karch, R., Neumann, F., Neumann, M., and Schreiner, W. (1999). A three-dimensional model for arterial tree representation, generated by constrained constructive optimization. *Comput. Biol. Med.* 29, 19–38. doi: 10.1016/S0010-4825(98)00045-6

Kellman, P., Hansen, M. S., Nielles-Vallespin, S., Nickander, J., Themudo, R., Ugander, M., et al. (2017). Myocardial perfusion cardiovascular magnetic resonance: optimized dual sequence and reconstruction for quantification. *J. Cardiovasc. Magn. Reson.* 19:43. doi: 10.1186/s12968-017-0355-5

Knowles, B. R., Batchelor, P. G., Parish, V., Ginks, M., Plein, S., Razavi, R., et al. (2008). Pharmacokinetic modeling of delayed gadolinium enhancement in the myocardium. *Magn. Reson. Med.* 60, 1524–1530. doi: 10.1002/mrm.21767

Koch, H., Bousseljot, R.-D., Kosch, O., Jahnke, C., Paetsch, I., Fleck, E., et al. (2011). A reference dataset for verifying numerical electrophysiological heart models. *Biomed. Eng. Online* 10:11. doi: 10.1186/1475-925X-10-11

Kroeker, K. I., Lam, S., Birchall, I., and Fedorak, R. N. (2011). Patients with IBD are exposed to high levels of ionizing radiation through CT scan diagnostic imaging: a five-year study. *J. Clin. Gastroenterol.* 45, 34–39. doi: 10.1097/MCG.0b013e3181e5d1c5

Lee, K. E., Lee, S. H., Shin, E.-S., and Shim, E. B. (2017). A vessel length-based method to compute coronary fractional flow reserve from optical coherence tomography images. *Biomed. Eng. Online* 16:83. doi: 10.1186/s12938-017-0365-4

Lima, J. A., Judd, R. M., Bazille, A., Schulman, S. P., Atalar, E., and Zerhouni, E. A. (1995). Regional heterogeneity of human myocardial infarcts demonstrated by contrast-enhanced MRI. *Circulation* 92, 1117–1125. doi: 10.1161/01.CIR.92.5.1117

Mehta, P. K., Wei, J., and Wenger, N. K. (2015). Ischemic heart disease in women: a focus on risk factors. *Trends Cardiovasc. Med.* 25, 140–151. doi: 10.1016/j.tcm.2014.10.005

Mendis, S., Puska, P., Norrving, B., World Health Organization, and World Heart Federation. (2011). *Global Atlas on Cardiovascular Disease Prevention and Control.* Geneva: World Health Organization.

Meneses, L. D. M., Brito, P. F., Rocha, B. M., Santos, R. W., and Queiroz, R. A. B. (2017). Construction of arterial networks considering a power law with exponent dependent on bifurcation level. *IFMBE Proc.* 60, 545–548. doi: 10.1007/978-981-10-4086-3_137

Michler, C., Cookson, A. N., Chabiniok, R., Hyde, E., Lee, J., Sinclair, M., et al. (2013). A computationally efficient framework for the simulation of cardiac perfusion using a multi-compartment Darcy porous-media flow model. *Int. J. Numer. Methods Biomed. Eng.* 29, 217–232. doi: 10.1002/cnm.2520

Nagel, E., Klein, C., Paetsch, I., Hettwer, S., Schnackenburg, B., Wegscheider, L., et al. (2003). Magnetic resonance perfusion measurements for the noninvasive detection of coronary artery disease. *Circulation* 108, 432–437. doi: 10.1161/01.CIR.0000080915.35024.A9

Nikolaou, K., Alkadhi, H., Bamberg, F., Leschka, S., and Wintersperger, B. J. (2011). MRI and CT in the diagnosis of coronary artery disease: indications and applications. *Insights Imaging* 2, 9–24. doi: 10.1007/s13244-010-0049-0

Pijls, N. H., De Bruyne, B., Bech, G. J. W., Liistro, F., Heyndrickx, G. R., Bonnier, H. J., et al. (2000). Coronary pressure measurement to assess the hemodynamic significance of serial stenoses within one coronary artery. *Circulation* 102, 2371–2377. doi: 10.1161/01.CIR.102.19.2371

Pop, M., Ghugre, N., Ramanan, V., Morikawa, L., Stanisz, G., Dick, A., Wright, G., et al. (2013). Quantification of fibrosis in infarcted swine hearts by *ex vivo* late gadolinium-enhancement and diffusion-weighted MRI methods. *Phys. Med. Biol.* 58, 5009–5028. doi: 10.1088/0031-9155/58/15/5009

Quarteroni, A., Sacco, R., and Saleri, F. (2010). *Numerical Mathematics, Vol. 37.* Heidelberg: Springer Science & Business Media.

Sant'Anna, F. M., Silva, E. E., Batista, L. A., Ventura, F. M., Barrozo, C. A. M., and Pijls, N. H. (2007). Influence of routine assessment of fractional flow reserve on decision making during coronary interventions. *Am. J. Cardiol.* 99, 504–508. doi: 10.1016/j.amjcard.2006.09.097

Schuster, A., Sinclair, M., Zarinabad, N., Ishida, M., van den Wijngaard, J. P., Paul, M., et al. (2015). A quantitative high resolution voxel-wise assessment of myocardial blood flow from contrast-enhanced first-pass magnetic resonance perfusion imaging: microsphere validation in a magnetic resonance compatible free beating explanted pig heart model. *Eur. Heart J. Cardiovasc. Imaging* 16, 1082–1092. doi: 10.1093/ehjci/jev023

Smith, A. F., Shipley, R. J., Lee, J., Sands, G. B., LeGrice, I. J., and Smith, N. P. (2014). Transmural variation and anisotropy of microvascular flow conductivity in the rat myocardium. *Ann. Biomed. Eng.* 42, 1966–1977. doi: 10.1007/s10439-014-1028-2

Taber, J. (1969). Dynamic and static forces required to remove a discontinuous oil phase from porous media containing both oil and water. *Soc. Petrol. Eng. J.* 9, 3–12. doi: 10.2118/2098-PA

Wang, J., Xiang, B., Lin, H.-y., Liu, H.-y., Freed, D., Arora, R. C., et al. (2015). Collateral circulation formation determines the characteristic profiles of contrast-enhanced MRI in the infarcted myocardium of pigs. *Acta Pharmacol. Sin.* 36, 463–472. doi: 10.1038/aps.2014.158

Zarinabad, N., Chiribiri, A., Hautvast, G. L., Ishida, M., Schuster, A., Cvetkovic, Z., et al. (2012). Voxel-wise quantification of myocardial perfusion by cardiac magnetic resonance. Feasibility and methods comparison. *Magn. Reson. Med.* 68, 1994–2004. doi: 10.1002/mrm.24195

Conflict of Interest Statement: The authors declare that the research was conducted in the absence of any commercial or financial relationships that could be construed as a potential conflict of interest.

Copyright © 2019 Alves, de Queiroz, Bär and dos Santos. This is an open-access article distributed under the terms of the Creative Commons Attribution License (CC BY). The use, distribution or reproduction in other forums is permitted, provided the original author(s) and the copyright owner(s) are credited and that the original publication in this journal is cited, in accordance with accepted academic practice. No use, distribution or reproduction is permitted which does not comply with these terms.

frontiers in Physiology

ORIGINAL RESEARCH
published: 09 May 2019
doi: 10.3389/fphys.2019.00400

Prediction of Plaque Progression in Coronary Arteries Based on a Novel Hemodynamic Index Calculated From Virtual Stenosis Method

Kyung Eun Lee[1,2], Sung Woong Shin[1], Gook Tae Kim[3], Jin Ho Choi[4] and Eun Bo Shim[1]**

[1] Department of Mechanical and Biomedical Engineering, Kangwon National University, Chuncheon, South Korea, [2] Bio-Convergence Technology Group, Korea Institute of Industrial Technology, Jeju, South Korea, [3] SiliconSapiens Inc., Seoul, South Korea, [4] Department of Cardiology, Samsung Medical Center, Sungkyunkwan University, Seoul, South Korea

OPEN ACCESS

Edited by:
Joseph L. Greenstein,
Johns Hopkins University,
United States

Reviewed by:
Diego Gallo,
Politecnico di Torino, Italy
Umberto Morbiducci,
Politecnico di Torino, Italy
David S. Liebeskind,
University of California, Los Angeles,
United States

***Correspondence:**
Eun Bo Shim
ebshim@kangwon.ac.kr
Jin Ho Choi
jhchoimd@gmail.com

Specialty section:
This article was submitted to Computational Physiology and Medicine, a section of the journal Frontiers in Physiology

Received: 13 August 2018
Accepted: 22 March 2019
Published: 09 May 2019

Citation:
Lee KE, Shin SW, Kim GT, Choi JH and Shim EB (2019) Prediction of Plaque Progression in Coronary Arteries Based on a Novel Hemodynamic Index Calculated From Virtual Stenosis Method. Front. Physiol. 10:400. doi: 10.3389/fphys.2019.00400

Rationale: Predicting the sites in coronary arteries that are susceptible to plaque deposition is essential for the development of clinical treatment strategies and prevention. However, to date, no physiological biomarkers for this purpose have been developed. We hypothesized that the possibility of plaque deposition at a specific site in the coronary artery is associated with wall shear stress (WSS) and fractional flow reserve (FFR).

Background and Objective: We proposed a new biomarker called the stenosis susceptibility index (SSI) using the FFR and WSS derived using virtual stenosis method. To validate the clinical efficacy of this index, we applied the method to actual pilot clinical cases. This index non-invasively quantifies the vasodilation effects of vascular endothelial cells relative to FFR variation at a specific coronary artery site.

Methods and Results: Using virtual stenosis method, we computed maximum WSS and FFR according to the variation in stenotic severity at each potential stenotic site and then plotted the variations of maximum WSS (y-axis) and FFR (x-axis). The slope of the graph indicated a site-specific SSI value. Then we determined the most susceptible sites for plaque deposition by comparing SSI values between the potential sites. Applying this method to seven patients revealed 71.4% in per-patient basis analysis 77.8% accuracy in per-vessel basis analysis in percutaneous coronary intervention (PCI) site prediction.

Conclusion: The SSI index can be used as a predictive biomarker to identify plaque deposition sites. Patients with relatively smaller SSI values also had a higher tendency for myocardial infarction. In conclusion, sites susceptible to plaque deposition can be identified using the SSI index.

Keywords: stenosis susceptibility index, virtual stenosis method, wall shear stress, fractional flow reserve, coronary plaque deposition

Abbreviations: CAD, coronary artery disease; CFD, computational fluid dynamics; CT, computed tomography; FFR, fractional flow reserve; LAD, the left anterior descending artery; LCX, the left circumflex coronary artery; MI, myocardial infarction; PCI, percutaneous coronary intervention; RCA, the right coronary artery; SSI, stenosis susceptibility index; WSS, wall shear stress.

INTRODUCTION

Predicting what sites are susceptible to stenotic plaque deposition in coronary arteries is an important factor in the diagnosis of CAD. To date, several basic and clinical research studies have been conducted to examine the mechanism of plaque progression in coronary arteries. WSS, defined as the product of blood viscosity and the spatial gradient of blood velocity at the vascular wall, plays a critical role in plaque deposition within coronary arteries (Samady et al., 2011; Dolan et al., 2013; Nørgaard et al., 2016; Park et al., 2016; Ng et al., 2017; Hayashi et al., 2018). The contribution of WSS to the initiation and progression of atherosclerosis has been extensively studied by experimental and CFD methods (Samady et al., 2011; Nørgaard et al., 2016; Hayashi et al., 2018). These studies have revealed that coronary plaque deposition frequently happens near low WSS regions. Also, it has been shown that oscillatory WSS and a steep shear stress gradient can affect plaque progression. The molecular effects of WSS on plaque deposition at specific sites have also been widely investigated (Li et al., 2005; Lu and Kassab, 2011). However, despite the substantial progress in understanding the physiological and pathological mechanisms of plaque progression, only a few studies on what specific coronary artery sites are susceptible to coronary plaque generation or deposition have been published. Recently, Choi et al. (2015) proposed a hemodynamic index, called axial plaque stress, to assess the future risk for plaque rupture and to determine treatment strategies for patients with CAD. This index quantified the possibility of plaque rupture of coronary stenosis but was mainly limited to the evaluation of plaque rupture in an already narrowed coronary artery. In the absence of significant plaque deposition in coronary arteries, monitoring the future risk for coronary arterial stenosis is essential for early diagnosis. If it were possible to predict what sites in the coronary artery are more susceptible to plaque deposition, clinicians would be able to develop better treatment plans for their patients.

In this study, we predicted what specific coronary artery sites were vulnerable to plaque deposition in patients without severe coronary stenosis. We hypothesized that plaque deposition at a specific site of the coronary artery is associated with changes in WSS and FFR at the site according to stenosis severity. Then a novel biomarker, SSI, was developed based on these measures. To compute this index at the potential sites, we used the virtual stenosis method presented in our previous paper (Lee et al., 2016a). We validated the efficacy of the index by comparing the computed results with clinical observations in a pilot clinical study, and then assessed the utility of the index.

MATERIALS AND METHODS

The main procedures for SSI computation are shown in **Figure 1**. First, a three-dimensional (3D) patient-specific coronary model was reconstructed from CT images (Kwon et al., 2014; Lee et al., 2016a; Chung et al., 2017). We obtained CT image data from nine patients with suspicious CAD who underwent a medical examination at Samsung Seoul Medical Center in Seoul, Korea. The study was approved by the Institutional Review Board of the hospital. CT scans were performed in nine patients to observe stenotic severity in coronary arteries and the progression of stenosis. However, two patients were excluded due to severely calcified vessels that can result in incorrect image segmentation. CT image slices were 0.60 mm (512 × 512 pixels) in width and were segmented and reconstructed using a semi-automated method, as described in our previous paper (Kwon et al., 2014; Lee et al., 2016a,b; Chung et al., 2017). Each 0, 25, and 50% stenosed virtual model was merged into a potential site of the 3D patient-specific coronary model as **Figure 2** (Lee et al., 2016a). To simulate coronary hemodynamics at hyperemia, we simulated unsteady blood flow behavior by using a Navier–Stokes equations solver in Eqs 1 and 2. Pulsatile blood flows in the 3D CFD coronary model at hyperemia were simulated by using Navier–Stokes solver which was based on segregated finite element method (Kwon et al., 2014) (Eqs 1 and 2).

$$\nabla \cdot \boldsymbol{u} = 0 \tag{1}$$

$$\partial \boldsymbol{u}/\partial t + \boldsymbol{u} \cdot \nabla \boldsymbol{u} = -\nabla p/\rho + \mu/\rho \nabla^2 \boldsymbol{u} \tag{2}$$

Here, $\boldsymbol{u}$, t, p, and ρ means velocity vector, time, pressure, and blood density, respectively.

To simulate coronary hemodynamics, we used a multi-scale simulation model by coupling patient-specific boundary conditions. The waveform of arterial blood pressure was used as an inlet boundary condition of the CFD model. Here, these pressures were based on the measured systolic/diastolic blood pressure and heart rate (Kelly and Fitchett, 1992; Verbeke et al., 2005; Laurent et al., 2006; Kwon et al., 2014). For the implementation of outlet boundary conditions of the CFD model, LPM is used to represent the physiological effects of micro-scale vessel effects. Collateral circulation was also considered in the lumped parameter model by using a switching system. On-off style switch works when coronary arterial distal pressure reaches a specific level (Schaper and Schaper, 1993; Seiler, 2009; Chung et al., 2017). Technical verification for the algorithm is shown in our previous paper (Kwon et al., 2014). For the identification of LPM resistance values, we used the vessel length based method that is explained in detail in our previous paper (Lee et al., 2016b, 2017). The method is based on the physiological observation that vessels with longer length feed more muscle mass inducing less microvascular resistance. In LPM models, the resistances of LAD and LCX are represented as follows (Lee et al., 2016b) (Eqs 3 and 4):

$$R_{LAD} = k/l_{LAD} \tag{3}$$

$$R_{LCX} = k/l_{LCX} \tag{4}$$

Here, l is the summed length exceeding a specific diameter and subscript represents the target vessel.

In the equations, resistance, denoted as "R", are inversely proportional to vessel length, l, indicating that longer vessel length induces less resistance and thus more blood flow. Here, "k" is a proportional constant. In case of RCA, we divided the RCA vessels into two parts: the summed length of the RCA vessels feeding right ventricle, and the summed length of the RCA vessels

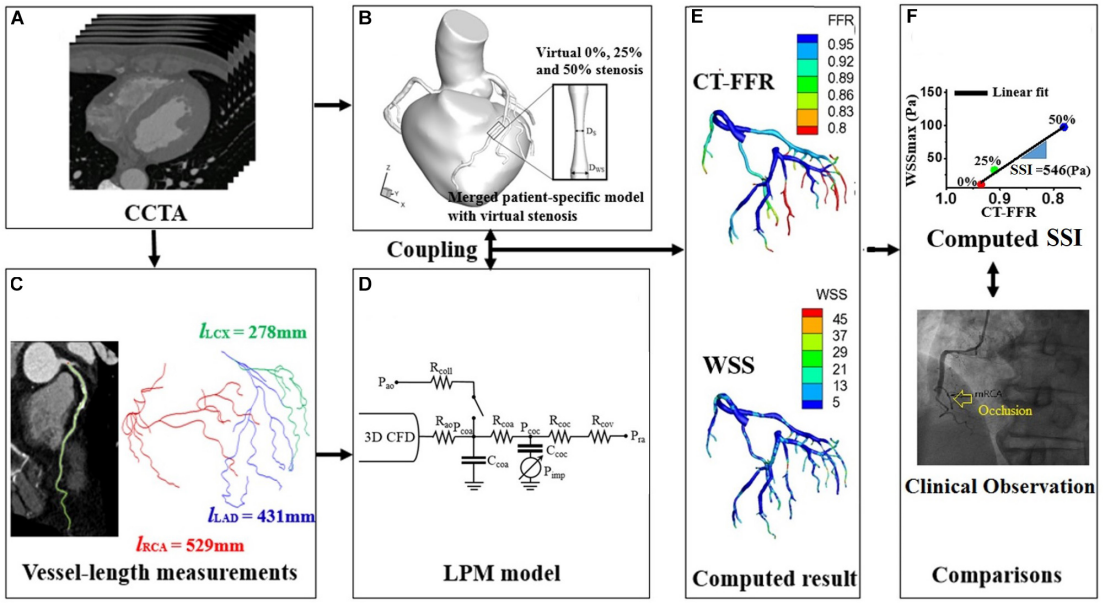

FIGURE 1 | Schematic of computer simulation procedures used to obtain the SSI using the virtual stenosis model presented in our previous paper (Lee et al., 2016b). **(A)** The acquisition of coronary computed tomography angiogram, **(B)** merged process between patient-specific coronary model and virtual stenosis model, **(C)** measurements of vessel length from coronary computed tomography angiogram, **(D)** establishment of lumped parameter model, **(E)** computation of FFR and WSS, and **(F)** comparison between clinical observation and region with the minimum of computed SSI.

feeding left ventricle. Since the summed length of the RCA vessels feeding right ventricle (RV) induces less blood flow than that of the RCA vessels feeding left ventricle (LV), the resistances of RCA are represented as follows (Lee et al., 2016b) (Eq. 5):

$$R_{LCX} = {}^{\alpha k}/_{(l_{RCA})_{RV}} + {}^{k}/_{(l_{RCA})_{LV}} \quad (\alpha > 1) \tag{5}$$

α is a constant (>1), reducing the effect of the RCA vessel length feeding RV muscle on RCA flow. Here, the value of α was set to be 3.45 which is a typical muscle volume ratio of LV to RV (Lee et al., 2016b). The proportional constant, k, in the equations, is derived from pressure-flow rate relation as explained in our previous paper (Lee et al., 2016b) (Eq. 6).

$$k = \frac{\Delta P}{Q}\left\{l_{LAD} + l_{LCX} + \frac{(l_{RCA})_{RV} \cdot (l_{RCA})_{LV}}{(l_{RCA})_{RV} + \alpha \cdot (l_{RCA})_{LV}}\right\} \tag{6}$$

In the above equation, the Q and ΔP are the total flow rate to coronary arteries and the pressure difference between the aorta and coronary veins, respectively. A more detailed description of these methods can be found in our previous papers (Kwon et al., 2014; Lee et al., 2016a,b; Chung et al., 2017).

To compute an SSI value for coronary artery sites, we used the virtual stenosis method proposed in our previous paper (Lee et al., 2016a). In details, this method constructed the virtual stenosis models with 0, 25, and 50% of stenotic severity at a potential site, and each virtual stenosis configuration was merged into the 3D patient-specific coronary model as shown in **Figure 2**. We made the three virtual stenotic models for each coronary artery site to mimic plaque growth from mild to severe states. At each stenotic level at the site, maximum WSS (WSSmax) and FFR were computed and plotted to determine the correlation as shown in **Figure 2**. In this study, SSI was designated as the slope of the linear plot. Simply expressing, SSI is represented as follows (Eq. 7).

$$\mathrm{SSI} = \frac{\mathrm{WSSmax}_{\text{stenosis mode}} - \mathrm{WSSmax}_{\text{non-stenosis mode}}}{FFR_{\text{non-stenosis mode}} - FFR_{\text{stenosis mode}}} \tag{7}$$

If we assume that WSSmax and FFR in non-stenosis model equal to zero, and one, respectively, then SSI can be expressed as (Eq. 8):

$$\mathrm{SSI} = \frac{\mathrm{WSSmax}_{\text{stenosis mode}}}{1 - FFR_{\text{stenosis mode}}} \tag{8}$$

After SSIs were computed for several potential coronary artery sites, we identified the location with the minimum SSI. We hypothesized that this location would be the most susceptible site for coronary artery stenosis. Therefore, we assumed this was where the patient was most likely to need PCI treatment due to a severe coronary artery occlusion. Based on this hypothesis, we computed SSI values from CT image data before the occurrence of severe coronary artery stenosis and identified the location with the minimum SSI value. Then we verified the validity of this hypothesis by comparing the location of the PCI with the location predicted using the smallest SSI.

RESULTS

The arterial site-specific SSI values from linear regression were obtained using three virtual stenotic models for a specific site, as

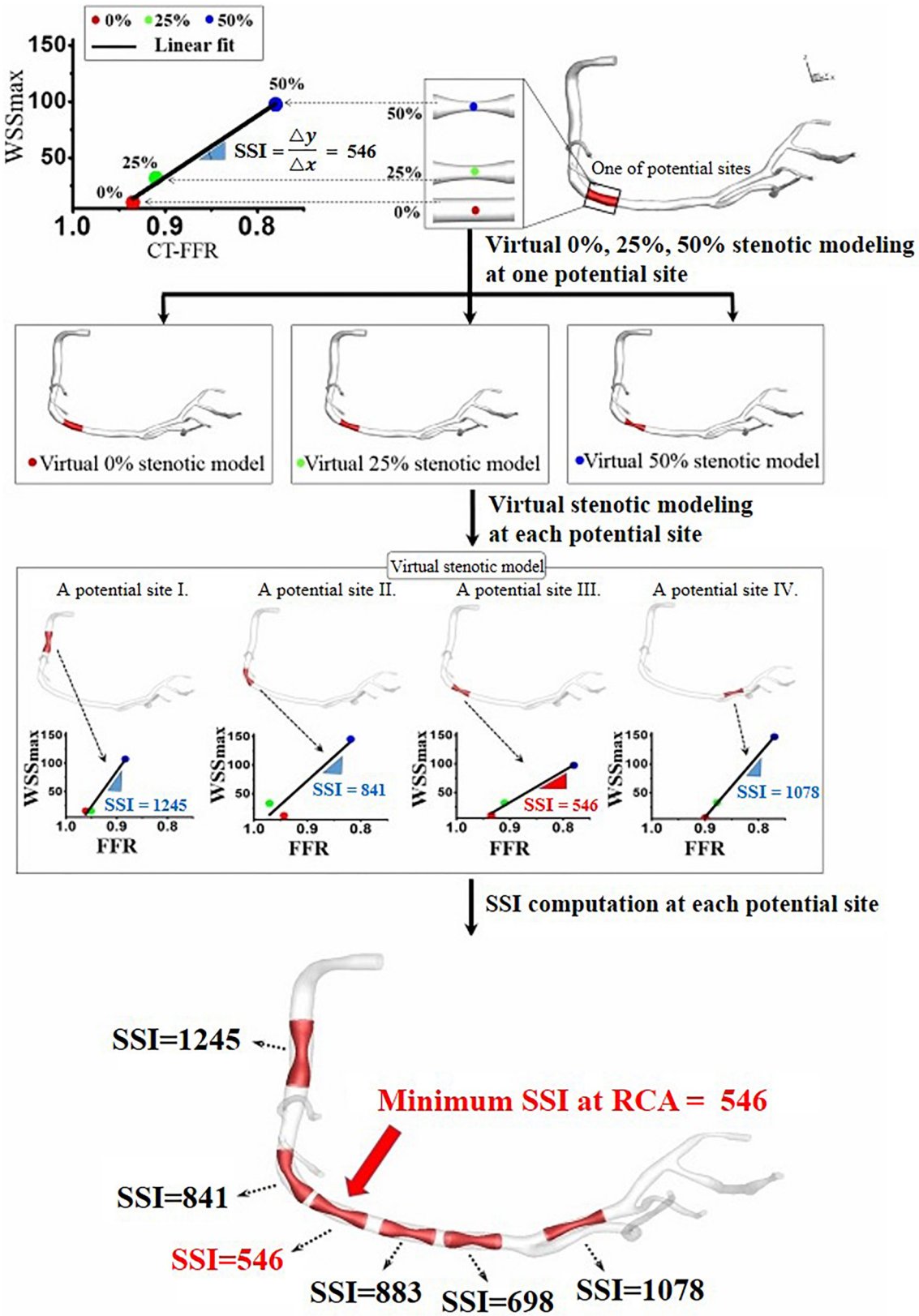

FIGURE 2 | Site-specific SSI obtained from the linear relationship between computed WSS_{max} and FFR for three virtual stenotic models with stenotic severities of 0, 25, and 50% at a selected potential site.

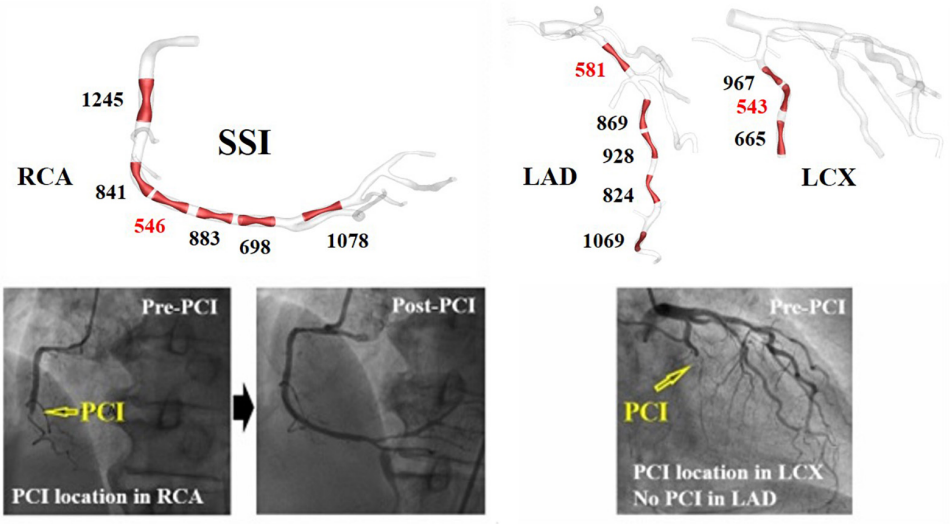

FIGURE 3 | A vessel site-specific SSI and clinically observed stenosis progression in representative case I (**Table 1**).

shown in **Figure 3**. The minimum SSI values (546, 581, and 543) were observed in RCA, LAD, and LCX, respectively, as shown in **Table 1**. Of the minimum SSI values, the values obtained in the RCA and LAD were similar, and are marked with red arrows. MI was also found upon clinical observation in this patient. Furthermore, this patient was treated at the RCA and LAD sites marked with a yellow arrow. We found that the site where the minimum SSI was observed was co-localized with the PCI treatment site in the corresponding patient.

Table 1 shows the minimum SSI value for each artery in all of the seven cases. The minimum SSI in the main arteries is written in bold. In five of seven patients, the site with the smallest SSI was identical to the site where PCI was performed due to stenosis progression, which equates to a 71.4% prediction rate. In seven of nine vessels, the site with the smallest SSI was also the site where PCI was performed, equating to a match rate of 77.8%.

TABLE 1 | Minimum SSI for each coronary artery, clinically observed MI, and matches between the minimum SSI and PCI site in nine vessels from seven patients.

	Minimum SSI per artery			Clinical observation	Match between the PCI and minimum SSI sites per artery		
	RCA	LAD	LCX	MI	RCA	LAD	LCX
Case I	**546**	581	**543**	Y	o	–	o
Case II	412	329	**239**	Y	–	o	o
Case III	792	874	**429**	N	–	–	o
Case IV	**729**	793		N	o	–	–
Case V	**468**	755	877	Y	–	×	–
Case VI	**520**	980	532	Y	–	×	–
Case VII	**1171**	1238	1400	N	o	–	–

Bold values were minimum SSI value among three main coronary arteries (RCA, LAD, and LCX).

Good matches between PCI and minimum SSI sites are marked by a red circle. Mismatches are indicated using a black cross. The artery where PCI was not yet performed is marked using a hyphen ("-"). Furthermore, MI was observed in four of seven patients, as shown in **Table 1**. Compared to the absence of MI, the minimum SSI value of LAD tended to be smaller in cases with MI for all cases except VI.

DISCUSSION

Identifying sites that are susceptible to deposition is an important factor for determining the appropriate preventive therapy for CAD. Despite significant research in this area using both clinical and computational approaches, there are currently no biomarkers that allow for identification of specific sites at risk for plaque disposition. Therefore, we developed a new biomarker to predict the sites that are susceptible to coronary stenosis and evaluated the predictive capacity of this marker using pilot clinical data to confirm validity. The biomarker, in this case, is an index obtained using virtual stenosis method (**Figure 1**).

There are three main findings. First, we presented a new index called SSI. This index was able to predict which sites in the coronary arteries were more susceptible to plaque deposition. Applying this index to seven patients showed that we could estimate the actual PCI positions of the patients with 71.4 and 77.8% accuracy in per-patient basis and per-vessel basis, respectively (**Table 1**). Stenotic plaque in coronary arteries can easily accumulate in areas with low WSS such as recirculation zones, but to date, no index has been developed to quantify this. In this study, we proposed SSI to predict sites that were susceptible to plaque disposition and showed that this index could be used for the preventive treatment of patients.

Second, a comparison of SSI in the LADs of the seven patients showed that patients with low SSI in LAD were susceptible to MI

(**Figure 3**). In clinics, stenosis of LAD causes MI, which induces severe damage to cardiac muscle. In this study, we obtained the minimum SSI values in the LADs of seven patients and investigated the relationship between the minimum SSI values and MI occurrence. Although the cut-off value of the minimum SSI value was not determined for all of the cases (only determined for case 6), the one reported MI occurred in the patient with the lowest SSI. Therefore, we can use the LAD SSI to predict the possibility of MI occurrence in a specific patient, resulting in a better-informed treatment plan for prevention. Thus, this index can become a useful clinical predictive index to prevent sudden death by MI.

Third, we presented a physiological hypothesis to show the efficacy of SSI. FFR decreases and WSSmax increases according to the increases of stenotic severity at specific sites. Here, the change in the rate of WSSmax relative to FFR change was defined as the SSI. Therefore, as shown in **Figure 2**, when the SSI was large at a specific site, WSS reached a critical value that could induce vascular vasodilation even after minimal increases in stenosis, thereby inhibiting plaque deposition. By contrast, if the SSI at a specific site was small, the critical WSS could be induced by more severe stenosis, and a stenotic plaque could easily accumulate at the location. A vasodilation effect can occur only when WSS is beyond a certain critical value; thus it is an important factor in reducing atherosclerosis, as evidenced by some physiological studies (Diamond et al., 1989; Ballermann et al., 1998; Chai et al., 2013).

However, there were still many limitations to this study. Most importantly, the pilot clinical data used in this study is small. Therefore, we have not been able to demonstrate the predictive ability of SSI in plaque progression or MI. Further validation will be the objective of future studies. Simulation of the data based on one or 2 years follow-up of patients with mild chest pain can provide the clinical evidence of SSI predictive ability in plaque progression. However, in the case of MI, because of the limited number of MI patients in one institution, SSI simulation study for large-scale retrospective data in multi-center basis will be a more plausible alternative.

Second, although the hypothesis in this study was physiologically reasonable, no *in vitro* or *in vivo* experiments were performed. Third, there are various factors (e.g., biochemical effects, vessel wall interaction, vasodilation effects, blood property effects, and lesion configurations effects) attributing to plaque progression. However, we hypothesized that the lumen geometrical factors might be a dominant factor in most cases. Furthermore, we used only symmetric plaque configurations without considering asymmetric plaque, various shapes of plaque, etc. These are also limitations in the current study. These diverse characteristics of plaque must be investigated in future research. Last, in this study, the occurrence of MI was predicted to increase when the SSI value was low, but data on the cut-off value were not available. Therefore, further in-depth studies using large-scale clinical data are required to provide criteria and data to determine the cut-off values. However, we believe that these limitations did not affect the major findings of the study.

ETHICS STATEMENT

This study is non-invasive and uses only CT data of patients. This study was approved as a retrospective study by the Institutional Review Board of Seoul Samsung Medical Center. All methods were carried out in accordance with relevant guidelines and regulations. All subjects were over 18 years old, and informed consent was obtained from all subjects.

AUTHOR CONTRIBUTIONS

KL, JC, and ES provided the main idea of this research, analyzed the data, and wrote the manuscript. SS and GK assisted for technical supports. JC designed the clinical validation and provided the clinical images and data. All authors reviewed this manuscript. ES and JC contributed as corresponding authors.

FUNDING

This research was supported by the National Research Foundation of Korea (NRF) grant (2018R1D1A1B07044528 and 2017R1A2B310918) and by the Ministry of Trade, Industry and Energy, Ministry of Science and ICT, and Ministry of Health and Welfare under Technology Development Program for Ai-Bio-Robot-Medicine Convergence (20001704).

REFERENCES

Ballermann, B. J., Dardik, A., Eng, E., and Liu, A. (1998). Shear stress and the endothelium. *Kidney Int. Suppl.* 67, S100–S108. doi: 10.1046/j.1523-1755.1998.06720.x

Chai, Q., Wang, W. L., Zeldin, D. C., and Lee, H. C. (2013). Role of caveolae in shear stress-mediated endothelium-dependent dilation in coronary arteries. *Cardiovasc. Res.* 100, 151–159. doi: 10.1093/cvr/cvt157

Choi, G., Lee, J. M., Kim, H. J., Park, J. B., Sankaran, S., Otake, H., et al. (2015). Coronary artery axial plaque stress and its relationship with lesion geometry: application of computational fluid dynamics to coronary CT angiography. *JACC Cardiovasc. Imaging* 8, 1156–1166. doi: 10.1016/j.jcmg.2015.04.024

Chung, J. H., Lee, K. E., Nam, C. W., Doh, J. H., Kim, H. I., Kwon, S. S., et al. (2017). Diagnostic performance of a novel method for fractional flow reserve computed from noninvasive computed tomography angiography (NOVEL-FLOW Study). *Am. J. Cardiol.* 120, 362–368. doi: 10.1016/j.amjcard.2017.04.057

Diamond, S. L., Eskin, S. G., and McIntire, L. V. (1989). Fluid flow stimulates tissue plasminogen activator secretion by cultured human endothelial cells. *Science* 243, 1483–1485. doi: 10.1126/science.2467379

Dolan, J. M., Kolega, J., and Meng, H. (2013). High wall shear stress and spatial gradients in vascular pathology: a review. *Ann. Biomed. Eng.* 41, 1411–1427. doi: 10.1007/s10439-012-0695-0

Hayashi, K., Makino, A., and Kakoi, D. (2018). Remodeling of arterial wall: response to changes in both blood flow and blood pressure. *J. Mech. Behav. Biomed. Mater.* 77, 475–484. doi: 10.1016/j.jmbbm.2017.10.003

Kelly, R., and Fitchett, D. (1992). Noninvasive determination of aortic input impedance and external left ventricular power output: a validation and

repeatability study of a new technique. *J. Am. Coll. Cardiol.* 20, 952–963. doi: 10.1016/0735-1097(92)90198-V

Kwon, S. S., Chung, E. C., Park, J. S., Kim, G. T., Kim, J. W., Kim, K. H., et al. (2014). A novel patient-specific model to compute coronary fractional flow reserve. *Prog. Biophys. Mol. Biol.* 116, 48–55. doi: 10.1016/j.pbiomolbio.2014.09.003

Laurent, S., Cockcroft, J., Van Bortel, L., Boutouyrie, P., Giannattasio, C., Hayoz, D., et al. (2006). Expert consensus document on arterial stiffness: methodological issues and clinical applications. *Eur. Heart J.* 27, 2588–2605. doi: 10.1093/eurheartj/ehl254

Lee, K. E., Kim, G. T., Lee, J. S., Chung, J. H., Shin, E. S., and Shim, E. B. (2016a). A patient-specific virtual stenotic model of the coronary artery to analyze the relationship between fractional flow reserve and wall shear stress. *Int. J. Cardiol.* 222, 799–805. doi: 10.1016/j.ijcard.2016.07.153

Lee, K. E., Kwon, S. S., Ji, Y. C., Shin, E. S., Choi, J. H., Kim, S. J., et al. (2016b). Estimation of the flow resistances exerted in coronary arteries using a vessel length-based method. *Pflugers. Arch.* 468, 1449–1485. doi: 10.1007/s00424-016-1831-8

Lee, K. E., Ryu, A. J., Shin, E. S., and Shim, E. B. (2017). Physiome approach for the analysis of vascular flow reserve in the heart and brain. *Pflugers. Arch.* 469, 613–628. doi: 10.1007/s00424-017-1961-7

Li, Y. S., Haga, J. H., and Chien, S. (2005). Molecular basis of the effects of shear stress on vascular endothelial cells. *J. Biomech.* 38, 1949–1971. doi: 10.1016/j.jbiomech.2004.09.030

Lu, D., and Kassab, G. S. (2011). Role of shear stress and stretch in vascular mechanobiology. *J. R. Soc. Interface* 8, 1379–1385. doi: 10.1098/rsif.2011.0177

Ng, J., Bourantas, C. V., Torii, R., Ang, H. Y., Tenekecioglu, E., Serruys, P. W., et al. (2017). Local hemodynamic forces after stenting: implications on restenosis and thrombosis. *Arterioscler. Thromb. Vasc. Biol.* 37, 2231–2242. doi: 10.1161/ATVBAHA.117.309728

Nørgaard, B. L., Leipsic, J., Koo, B. K., Zarins, C. K., Jensen, J. M., Sand, N. P., et al. (2016). Coronary computed tomography angiography derived fractional flow reserve and plaque stress. *Curr. Cardiovasc. Imaging Rep.* 9:2. doi: 10.1007/s12410-015-9366-5

Park, J. B., Choi, G., Chun, E. J., Kim, H. J., Park, J., Jung, J. H., et al. (2016). Computational fluid dynamic measures of wall shear stress are related to coronary lesion characteristics. *Heart* 102, 1655–1661. doi: 10.1136/heartjnl-2016-309299

Samady, H., Eshtehardi, P., McDaniel, M. C., Suo, J., Dhawan, S. S., Maynard, C., et al. (2011). Coronary artery wall shear stress is associated with progression and transformation of atherosclerotic plaque and arterial remodeling in patients with coronary artery disease. *Circulation* 124, 779–788. doi: 10.1161/CIRCULATIONAHA.111.021824

Schaper, W., and Schaper, J. (1993). *Collateral Circulation: Heart, Brain, Kidney, Limbs*. Berlin: Springer, 269–271. doi: 10.1007/978-1-4615-3092-3

Seiler, C. (2009). *Collateral Circulation of the Heart*. Berlin: Springer, 120–141. doi: 10.1007/978-1-84882-342-6

Verbeke, F., Segers, P., Heireman, S., Vanholder, R., Verdonck, P., and Van Bortel, L. M. (2005). Noninvasive assessment of local pulse pressure: importance of brachial-to-radial pressure amplification. *Hypertension* 46, 244–248. doi: 10.1161/01.HYP.0000166723.07809.7e

Conflict of Interest Statement: GK was employed by company SiliconSapiens Inc (Seoul, South Korea).

The remaining authors declare that the research was conducted in the absence of any commercial or financial relationships that could be construed as a potential conflict of interest.

Copyright © 2019 Lee, Shin, Kim, Choi and Shim. This is an open-access article distributed under the terms of the Creative Commons Attribution License (CC BY). The use, distribution or reproduction in other forums is permitted, provided the original author(s) and the copyright owner(s) are credited and that the original publication in this journal is cited, in accordance with accepted academic practice. No use, distribution or reproduction is permitted which does not comply with these terms.

Advantages of publishing in Frontiers

OPEN ACCESS
Articles are free to read for greatest visibility and readership

FAST PUBLICATION
Around 90 days from submission to decision

HIGH QUALITY PEER-REVIEW
Rigorous, collaborative, and constructive peer-review

TRANSPARENT PEER-REVIEW
Editors and reviewers acknowledged by name on published articles

Frontiers
Avenue du Tribunal-Fédéral 34
1005 Lausanne | Switzerland

Visit us: www.frontiersin.org
Contact us: info@frontiersin.org | +41 21 510 17 00

REPRODUCIBILITY OF RESEARCH
Support open data and methods to enhance research reproducibility

DIGITAL PUBLISHING
Articles designed for optimal readership across devices

FOLLOW US
@frontiersin

IMPACT METRICS
Advanced article metrics track visibility across digital media

EXTENSIVE PROMOTION
Marketing and promotion of impactful research

LOOP RESEARCH NETWORK
Our network increases your article's readership